ABSTRACT

Title of dissertation: DISORDER AND DOPING IN THE OXYGENATED ELECTRON-DOPED SUPERCONDUCTOR $Pr_{2-x}Ce_xCuO_{4\pm\delta}$

Joshua Scott Higgins, Doctor of Philosophy, 2006

Dissertation directed by: Professor Richard L. Greene
Department of Physics

This thesis is composed of two parts: the first part deals with the high temperature electron-doped superconductor $Pr_{2-x}Ce_xCuO_{4\pm\delta}$; the second part deals with the diluted magnetic semiconductor $Ti_{1-x}Co_xO_{2-\delta}$.

It is not clear why oxygen reduction and cerium doping are necessary to obtain superconductivity in the electron-doped $Pr_{2-x}Ce_xCuO_{4\pm\delta}$. I investigated the effects of oxygenation in this material using resistivity and Hall measurements. For various oxygen contents, I was able to determine that there is a separable doping and a disorder contribution to the superconducting transition temperature. I was able to quantitatively separate out these two effects and show that these two effects are opposite with regards to changes in T_c for overdoped thin films. The disorder component is roughly twice as large as the doping component. This analysis is also shown to be self consistent in demonstrating that the doping component of oxygen variation follows the trends of Cerium doping.

For the diluted magnetic semiconductor $Ti_{1-x}Co_xO_{2-\delta}$, I investigated the intrinsic nature of the ferromagnetism observed in thin films. Hall effect measurements were used as the technique because ferromagnetic materials exhibit an anomalous Hall effect, which is due to an interaction between the charge carriers and the magnetic moments. I found that low carrier concentration anatase phase films did not exhibit an anomalous Hall effect, whereas high carrier concentration rutile phase films do. The presence of the anomalous Hall effect at this point cannot be attributed to an intrinsic ferromagnetism as cobalt clusters are observed in these films.

DISORDER AND DOPING IN THE OXYGENATED ELECTRON-DOPED SUPERCONDUCTOR $Pr_{2-x}Ce_xCuO_{4\pm\delta}$

by

Joshua Scott Higgins

Dissertation submitted to the Faculty of the Graduate School of the
University of Maryland, College Park in partial fulfillment
of the requirements for the degree of
Doctor of Philosophy
2006

Advisory Committee:

Professor Richard L. Greene, Chair/Advisor
Professor Christopher J. Lobb
Professor Steven M. Anlage
Professor Thirumalai Venkatesan
Professor Ichiro Takeuchi

ACKNOWLEDGMENTS

There are many people who have helped me during the entire process of graduate school. Without their help and support, I do not feel that this work would have been possible. There is not enough space, nor time, to acknowledge everyone to the extent they deserve. I hope people understand the brevity of this part.

First and foremost, I would like to express deep gratitude to my advisor, Professor Richard L. Greene. His patience and compassion have helped me through many rough times, in both my private and academic affairs. I have learned a lot from Rick Greene. He has taught me how to present myself and my work, and for this I am most appreciative.

Professor Christopher J. Lobb is an interesting case for me. While I did not work with him directly, he was always available to offer support. When I started working at Maryland, I was a very shy and timid person. He took it upon himself to turn me into a confident scientist. Over the years, I believe he succeeded.

There are several post-docs, that have either worked or are currently working for Rick Greene, that I would like to mention. Patrick Fournier was my initial mentor, and it was because of him that I finally decided to enter graduate school. Amlan Biswas, Weiqiang Yu, and Alexandre Zimmers have all been supportive and willing to share their expertise with me. Yoram Dagan was an essential part of my education in the latter years, and has become a good friend.

Hamza Balci, Mumtaz Qazilbash, Pengcheng Li, and Sudeep Dutta were all graduate students (at one point of another) along with me. Their help in the lab, as well as outside the lab, has been instrumental to my survival as a graduate student. They all helped me become comfortable with presenting and defending ideas. They are also all good friends. To Matt Sullivan and Betsy Pugel, I owe a great deal. Not only have I learned a lot about physics from them, but they have also taught me a lot about life.

Several undergraduates working in Rick Greene's group have made my experience at Maryland more enjoyable. Chris Hill, Matt Barr, and William Fisher (Fish) have all made the lab fun. I always looked forward to talking and working with them.

I am also appreciative of all the help from the staff in the Center for Superconductivity Research: Belta Pollard, Brian Barnaby, Grace Sewlall, Cleopatra White, Brian Straughn, and Doug Bensen. I would like to express an extra special thanks to Brian Straughn and Doug Bensen. Not only have they helped me with the maintenance of lab equipment, but they have also offered invaluable advice in regards to my personal life.

To my parents, whose love and support have helped stabilize my life, I am thankful for all they have done for me. I would also like to thank all of my friends. They have listened to me and watched me grow throughout my graduate career. This is particularly directed towards Scott Stanley, Lex Berthelsen, and Brooke Berthelsen.

Last but not least, I would like to thank Alexandra Elizabeth Curtin, whose

love and support had helped me through the last several years of this work.

Table of Contents

List of Tables vii

List of Figures viii

1 Introduction 1
1.1 Low Temperature Superconductivity . . . 1

2 High Temperature Superconductivity 4
2.1 Structure . . . 6
2.2 Parent Compound and Electronic Structure . . . 8
2.3 Evolution of the Phase Diagram with Doping . . . 12
2.4 Magnetism and Electronic Transport in the Cuprates . . . 16
2.4.1 Motivation . . . 33

3 Transport - Theory 34
3.1 Boltzmann Transport . . . 34
3.2 Electronic Transport in Metals . . . 37
3.2.1 Matthiessen's Rule . . . 39
3.2.2 Impurity Scattering . . . 39
3.2.3 Electron-Phonon Scattering . . . 40
3.2.4 Electron-Electron Scattering . . . 41
3.3 Electronic Transport in Magnetic Fields . . . 43
3.3.1 Magnetoresistance . . . 43
3.3.2 Hall Effect . . . 49
3.4 Disorder in Superconductors . . . 52

4 Transport in the Electron-doped Cuprates 55
4.1 Resistivity . . . 55
4.2 Hall Effect . . . 58
4.3 Oxygen Non-stoichiometry . . . 59
4.3.1 Hole-doped Cuprates . . . 59
4.3.2 Electron-doped Cuprates . . . 62
4.4 Disorder and Impurity Effects . . . 71
4.4.1 Kondo Effect and 2D Weak Localization . . . 72
4.4.2 Cation Disorder . . . 77
4.4.3 Irradiation . . . 90
4.4.4 Oxygen Non-stoichiometry . . . 94

5 Sample Fabrication 98
5.1 Growth and Annealing . . . 98
5.2 Characterization . . . 105
5.3 Patterning . . . 111
5.4 Irradiation . . . 113

6 Transport Measurements and Analysis 116
6.1 Overview of the Measurements . . . 117
6.2 Oxygenation versus Ion Irradiation . . . 119
6.2.1 Data . . . 121
6.2.2 Analysis . . . 127
6.2.3 Consideration within a Two-band Model . . . 136
6.3 Magnetic Contributions to the Hall Effect . . . 143
6.4 Future Directions . . . 150

7 Introduction to Diluted Magnetic Semiconductors 154
7.1 Spintronics . . . 154
7.1.1 Magnetization and Spin Polarization . . . 155
7.1.2 Two Current Uses of Spintronics in Technology . . . 162
7.2 Diluted Magnetic Semiconductors . . . 164
7.3 Models for DMS Systems . . . 171
7.3.1 Bound Magnetic Polarons . . . 172
7.3.2 RKKY Model . . . 173

8 Samples and Measurements 174
8.1 Introduction to $Ti_{1-x}Co_xO_{2-\delta}$ . . . 174
8.2 Sample Growth and Measurements . . . 175
8.3 Possible Explanation for the Anomalous Hall Effect . . . 186
8.4 Future Directions . . . 187

9 Summary 188
9.1 $Pr_{2-x}Ce_xCuO_{4\pm\delta}$ . . . 188
9.2 $Ti_{1-x}Co_xO_{2-\delta}$ . . . 189

Bibliography 190

List of Tables

5.1 Deposition and annealing conditions for PCCO thin films used for oxygenation and irradiation 101

List of Figures

2.1 Schematic for the lattice structures for the single layer cuprates . . . 6

2.2 Schematic of band calculations hybridizing the copper and oxygen orbitals in the CuO_2 plane . . . 9

2.3 Dispersion curves for NCCO . . . 10

2.4 Schematic of the density of states for the parent compounds of the cuprates . . . 11

2.5 Generic phase diagram of the cuprates . . . 13

2.6 Alignment of the Copper spins in the antiferromagnetic state of the electron-doped cuprates . . . 14

2.7 T_N versus cerium content x in $Nd_{2-x}Ce_xCuO_{4\pm\delta}$ for oxygen reduced and as-grown crystals . . . 18

2.8 ρ_{ab} versus Temperature for optimally doped hole and electron-doped cuprates . . . 19

2.9 Normal state Resistivity versus Temperature for $Pr_{2-x}Ce_xCuO_{4\pm\delta}$ thin films . . . 21

2.10 R_H versus T for $La_{2-x}Sr_xCuO_4$ and $Nd_{2-x}Ce_xCuO_{4\pm\delta}$ . . . 23

2.11 R_H versus x for $La_{2-x}Sr_xCuO_4$ and $Pr_{2-x}Ce_xCuO_{4\pm\delta}$ . . . 24

2.12 ARPES on NCCO crystals . . . 25

2.13 Schematic of ARPES and antiferromagnetic Brillouin zones for NCCO 27

2.14 Schematic of ARPES data on overdoped NCCO . . . 28

2.15 Schematic of a quantum phase transition . . . 29

2.16 Temperature versus control parameter for a quantum phase transition 30

2.17 Hall and resistivity evidence for a QPT in $Pr_{2-x}Ce_xCuO_{4\pm\delta}$ . . . 32

3.1 Hall Schematic . . . 50

4.1 ρ_{ab} vs T for PCCO . . . 56

4.2 ρ_{ab} vs Temperature for oxygenated LCO 61

4.3 ρ_{ab} vs Temperature for various δ in $Nd_{1.85}Ce_{0.15}CuO_{4\pm\delta}$ 64

4.4 T_c, MR, and R_H as a function of oxygen in $Nd_{1.85}Ce_{0.15}CuO_{4\pm\delta}$ 65

4.5 Hall coefficient as a function of oxygen in $Nd_{1.85}Ce_{0.15}CuO_{4\pm\delta}$ 66

4.6 Logarithmic temperature divergence of ρ_{ab} in $Pr_{2-x}Ce_xCuO_{4\pm\delta}$ & $Nd_{2-x}Ce_xCuO_{4\pm\delta}$ 73

4.7 Orbital magnetoconductance in $Pr_{2-x}Ce_xCuO_{4\pm\delta}$ & $Nd_{2-x}Ce_xCuO_{4\pm\delta}$ 74

4.8 Logarithmic temperature divergence of ρ_{ab} in $La_{1.955}Ce_{0.045}CuO_{4\pm\delta}$, $Pr_{1.902}Ce_{0.098}CuO_{4\pm\delta}$, $Nd_{1.914}Ce_{0.086}CuO_{4\pm\delta}$ 75

4.9 Kondo fits to $\rho_k(B,T)$ for $La_{1.955}Ce_{0.045}CuO_{4\pm\delta}$, $Pr_{1.902}Ce_{0.098}CuO_{4\pm\delta}$, $Nd_{1.914}Ce_{0.086}CuO_{4\pm\delta}$ 76

4.10 T_c versus cation substitution for copper in $La_{1.85}Sr_{0.15}Cu_{1-y}M_yO_4$ and $Nd_{1.85}Ce_{0.15}Cu_{1-y}M_yO_{4\pm\delta}$ 80

4.11 Evolution of R_H versus Temperature in $La_{1.85}Sr_{0.15}Cu_{1-y}Zn_yO_4$ and $Nd_{1.85}Ce_{0.15}Cu_{1-y}Zn_yO_{4\pm\delta}$ 82

4.12 Abrikosov-Gor'kov theoretical fit for T_c versus Ni concentration in $Nd_{1.85}Ce_{0.15}Cu_{1-y}Ni_yO_{4\pm\delta}$ 85

4.13 T_c versus $< r_A >$ and σ^2 in the $Ln_{2-x}M_xCuO_4$ system 88

4.14 R_H versus Temperature for out-of-plane disorder in $Bi_2Sr_{1.6}Ln_{0.4}CuO_{6+\delta}$ and $La_{1.85-y}Nd_ySr_{0.15}CuO_4$ systems 89

4.15 T_c versus Sheet Resistance in the disordered $Bi_2Sr_{1.6}Ln_{0.4}CuO_{6+\delta}$ and $La_{1.85-y}Nd_ySr_{0.15}CuO_4$ systems 90

4.16 $\frac{dT_c}{d\phi}$ versus Nonionizing Energy Loss for the cuprates 91

4.17 ρ, R_H versus Temperature on He^+ irradiated $Nd_{1.86}Ce_{0.14}CuO_{4\pm\delta}$ . . . 93

4.18 c-axis lattice parameter of $Pr_{2-x}Ce_xCuO_{4\pm\delta}$ before and after post-deposition annealing 95

4.19 STM images of oxygen dopant defects in $Bi_2Sr_2CaCu_2O_{8+\delta}$ 97

5.1 Schematic for PLD film growth 102

5.2 X-ray diffraction pattern for $Pr_{1.83}Ce_{0.17}CuO_{4\pm\delta}$ . . . 106

5.3 Optical microscope images of $Pr_{2-x}Ce_xCuO_{4\pm\delta}$ thin films . . . 107

5.4 AC susceptibility probe schematic . . . 108

5.5 Typical AC susceptibility measurement . . . 110

5.6 Hall Bar Schematics . . . 112

5.7 Non-ionizing energy loss versus incident particle energy for YBCO . . 115

6.1 Schematic Hall bar voltage leg offset . . . 118

6.2 T_c versus doping phase diagram for $Pr_{2-x}Ce_xCuO_{4\pm\delta}$ (schematic) . . 120

6.3 ρ_{ab} versus Temperature for oxygenated and irradiated thin films of $Pr_{1.83}Ce_{0.17}CuO_{4\pm\delta}$ . . . 122

6.4 Low Temperature resistivity of $Pr_{1.83}Ce_{0.17}CuO_{4\pm\delta}$ thin films subjected to oxygenation or irradiation . . . 123

6.5 Example of fit to the low temperature normal state resistivity of $Pr_{1.83}Ce_{0.17}CuO_{4\pm\delta}$ thin films . . . 125

6.6 Example of the determination of T_c for the $Pr_{1.83}Ce_{0.17}CuO_{4\pm\delta}$ thin films . . . 126

6.7 ΔT_c versus $\Delta\rho_\circ$ for oxygenated and ion irradiated $Pr_{1.83}Ce_{0.17}CuO_{4\pm\delta}$ thin films . . . 127

6.8 R_H versus Temperature for oxygenated and ion irradiated thin films of $Pr_{1.83}Ce_{0.17}CuO_{4\pm\delta}$ . . . 128

6.9 ρ_{xy} versus Magnetic Induction for a $Pr_{1.83}Ce_{0.17}CuO_{4\pm\delta}$ thin film . . . 129

6.10 Supplemental plots for the analysis of oxygenation versus irradiation . 131

6.11 ΔT_c versus ΔR_H . . . 133

6.12 R_H versus Temperature for irradiated $Pr_{1.83}Ce_{0.17}CuO_{4\pm\delta}$ thin films . 139

6.13 Magnetoresistance of irradiated and oxygenated $Pr_{1.83}Ce_{0.17}CuO_{4\pm\delta}$ thin films . . . 142

6.14 Magnetoresistance of irradiated and oxygenated $Pr_{1.83}Ce_{0.17}CuO_{4\pm\delta}$ thin films, taken in high fields . . . 144

6.15 Paramagnetic (molar) susceptibility for $Pr_2CuO_{4\pm\delta}$ single crystals . . 147

6.16 Temperature dependencies for χ^* and R_H for $Pr_{2-x}Ce_xCuO_{4\pm\delta}$ 148

6.17 R_H versus χ^* for $Pr_{2-x}Ce_xCuO_{4\pm\delta}$ thin films; $x = 0.05, 0.15, 0.17$ . . . 149

7.1 Schematic of the Density of States at the Fermi surface for normal metals and ferromagnetic metals 159

7.2 Schematic $M - H$ curve for a ferromagnet 161

7.3 Schematic of a spin-valve 163

7.4 Schematic of a spin-FET 165

7.5 Schematic of diluted magnetic doping 168

7.6 Predictions for ferromagnetic transition temperatures in several semiconducting compounds with 5% magnetic substitutions 169

7.7 ρ_{xy} versus magnetic field for $Ga_{0.947}Mn_{0.053}As$ 171

7.8 Schematic of the bound magnetic polaron model 173

8.1 Lattice structure of rutile and anatase TiO_2 175

8.2 ρ_{xy} and M versus magnetic field for anatase $Ti_{1-x}Co_xO_{2-\delta}$ 176

8.3 X-ray diffraction scan of rutile $Ti_{1-x}Co_xO_{2-\delta}$ 178

8.4 Resistivity versus Temperature for rutile $Ti_{1-x}Co_xO_{2-\delta}$ 179

8.5 Hall resistivity for rutile $Ti_{1-x}Co_xO_{2-\delta}$, sample TC2-86 181

8.6 Magnetic hysteresis loops and Hall resistivity for rutile $Ti_{1-x}Co_xO_{2-\delta}$, sample TC2-86 182

8.7 Hall resistivity for rutile $Ti_{1-x}Co_xO_{2-\delta}$, sample TC2-84 183

8.8 Anomalous Hall resistivity for rutile $Ti_{1-x}Co_xO_{2-\delta}$, sample TC2-84 . 184

8.9 Cobalt clusters in highly reduced $Ti_{1-x}Co_xO_{2-\delta}$ 185

8.10 Cobalt clusters in a conducting matrix 186

Chapter 1

Introduction

1.1 Low Temperature Superconductivity

Superconductors are typically identified by two phenomena: 1) perfect conductivity, and 2) perfect diamagnetism. The first effect was discovered in 1911 when Heike Kamerlingh Onnes was investigating the low temperature electrical resistance of certain metals. He found that the dc resistance of mercury decreased rapidly towards zero at a temperature of $\simeq 4.2$ degrees above absolute zero (4.2 K, $\simeq -269°$ C, $\simeq -452°$ F) [1]. Onnes interpreted this transition into perfect dc conductivity as a new state of matter, which was eventually termed superconductivity (it was first called supraconductivity). Shortly afterwards more materials were found, in single elemental metals as well as in metallic compounds and alloys, which possessed this property. The temperature at which they became perfect dc conductors has come to be known as the critical temperature (or superconducting transition temperature) denoted by T_c, which differed among the various materials. The second effect, perfect diamagnetism, was discovered 22 years later in 1933 by Walther Meissner and Robert Ochsenfeld. They found that superconductors completely expelled internal magnetic fields below a certain critical field, H_c [2]. In fields larger than H_c, the superconductors returned to their normal, non-superconducting state. This effect demonstrated that the transition into the superconducting state was indeed a ther-

modynamic phase transition. The complete expulsion of magnetic field (coined the Meissner effect) differentiated superconductors from perfect conductors in that the latter are only able to expel *changes* in magnetic field. Therefore, perfect conductivity and perfect diamagnetism uniquely define superconductivity.

The mechanism for superconductivity was not understood at this point, but advances were made in the next 23 years which contributed vital clues. In 1935, H. London and F. London developed two phenomenological equations (the London equations) which described the behavior of the current density in superconductors subjected to electric and magnetic fields [3]. F. London pointed out that these equations could be derived from quantum theory if the superconducting wavefunction was relatively insensitive to external magnetic fields. Electronic specific heat measurements revealed an exponential temperature dependence in superconductors far below T_c [4]. This behavior implied that an energy gap existed in the superconducting state, between the ground state and the excited states. Other measurements on electromagnetic absorption [5, 6] also pointed to the existence of an energy gap and were consistent with the specific heat measurements, provided the ground state consisted of electron pairs. One important discovery, which led to the "understanding" of low temperature superconductors, was the isotope effect [7, 8]. When the T_c of different isotopes of single element low temperature superconductors was measured, it was found to decrease as the mass of the lattice atom increased ($T_c \propto M^{-1/2}$). This electron-phonon interaction implied that the interaction between the electrons and the lattice played a primary role in T_c.

Bardeen, Cooper, and Schrieffer [9] devised a theory (BCS theory) in which

pairs of electrons, of opposite spin and momentum, are attracted to each other through the exchange of virtual phonons. This attraction creates a lowered energy state for the pair, and as a result condenses the pairs into a coherent ground state below the Fermi energy (this gives an energy gap between the energy of the bound pairs and the Fermi energy). The BCS theory was one of the first to be able to calculate some of the above behaviors. The results were astounding and to this day the BCS theory is used (in one form or another) as a means to predict, calculate, and describe superconductors. The idea here is not to give a comprehensive overview of the BCS theory, but it is to introduce it as a breakthrough in the understanding of superconductors.

Chapter 2

High Temperature Superconductivity

High temperature superconductivity (HTSC) was first discovered by Bednorz and Müller in 1986 [10] in the Ba-La-Cu-O multi-phase ceramic oxide system (onset $T_c \simeq 30$ K). The high-T_c phase was later determined to be $La_{2-x}Ba_xCuO_{4-\delta}$ [11]. Superconductivity (SC) in oxides was not common, but was not unheard of at this point. It was known to occur in the oxygen deficient semiconducting $SrTiO_3$ [12] ($T_c \simeq 0.25$ K) and the metallic $Li_{1+x}Ti_{2-x}O_4$ [13] ($T_c \simeq 13$ K). The former was important because it was a doped semiconductor, the latter because it was transition metal oxide. The most significant precursor to the ceramic oxides was found in $BaPb_{1-x}Bi_xO_3$ by A. W. Sleight *et al.* [14], which superconducts at T = 13 K for $x = 0.3$. There are a few interesting features in this oxide system [15]. First, this system is composed of a mixture of the semiconducting $BaBiO_3$ and the semimetallic $BaPbO_3$ compounds, and so an insulator to metal transition can be controlled by changing x. Second, it was found that the lead and oxygen orbitals were highly hybridized, which is not typical to conductive oxides [15]. It will become clear later in this chapter how hybridized bands in oxides are important.

The discovery by Bednorz and Müller was somewhat surprising because the material was a ceramic oxide. Now, ceramics are *typically* insulators with a low carrier concentration, and it is therefore counter-intuitive to search for supercon-

ductivity in this class of materials. Because of this line of thought, the discovery of SC in the Ba-La-Cu-O system spurred vigorous research into other copper oxides. A simple replacement of Ba with Sr yielded a single-phase SC [16] $La_{2-x}Sr_xCuO_4$ (LSCO, $T_c \simeq 36$ K). These events (among others) led to, in only a *very* short time, the discovery of another multi-phase superconductor $Y_{1.2}Ba_{0.4}CuO_{4-\delta}$ [17] with a superconducting transition higher than the temperature of liquid nitrogen ($T_c \simeq 93$ K, nitrogen is liquid at $\simeq$ 77 K). Very quickly, the SC phase was shown to be $YBa_2Cu_3O_{7-\delta}$ (YBCO). These findings were significant for several reasons: 1) a widely held belief had the BCS theory predicting that phonon-mediated SC was limited to T_c's of $\simeq$ 30 K (this implies a new mechanism for SC), and 2) the relatively cheap cryogen, liquid nitrogen, could now be used to cool samples rather than the more expensive liquid helium. Subsequently, many more types of copper oxides were discovered with the highest T_c (at ambient pressure) of $\simeq$ 138 K in the mercury-based $Hg_{0.8}Tl_{0.2}Ba_2Ca_2Cu_3O_{8.33}$ [18]

The superconducting copper oxides (cuprates) are all doped insulators, where the doped carriers are holes. It wasn't until 1989 that the electron-doped counterparts were found [19, 20] in $RE_{2-x}Ce_xCuO_{4\pm\delta}$ (RE = Nd, Pr, and Sm). It is the electron-doped HTSCs which are one of the foci of this thesis.

Much has been learned over the past 20 years, but there is still a long way to go. For example, the underlying mechanism for SC in this class of materials is still unknown. The rest of this chapter is devoted to a brief summary of the lattice and electronic structures of the HTSCs, with a focus on the electron-doped HTSC as well as the similar hole-doped sister compounds.

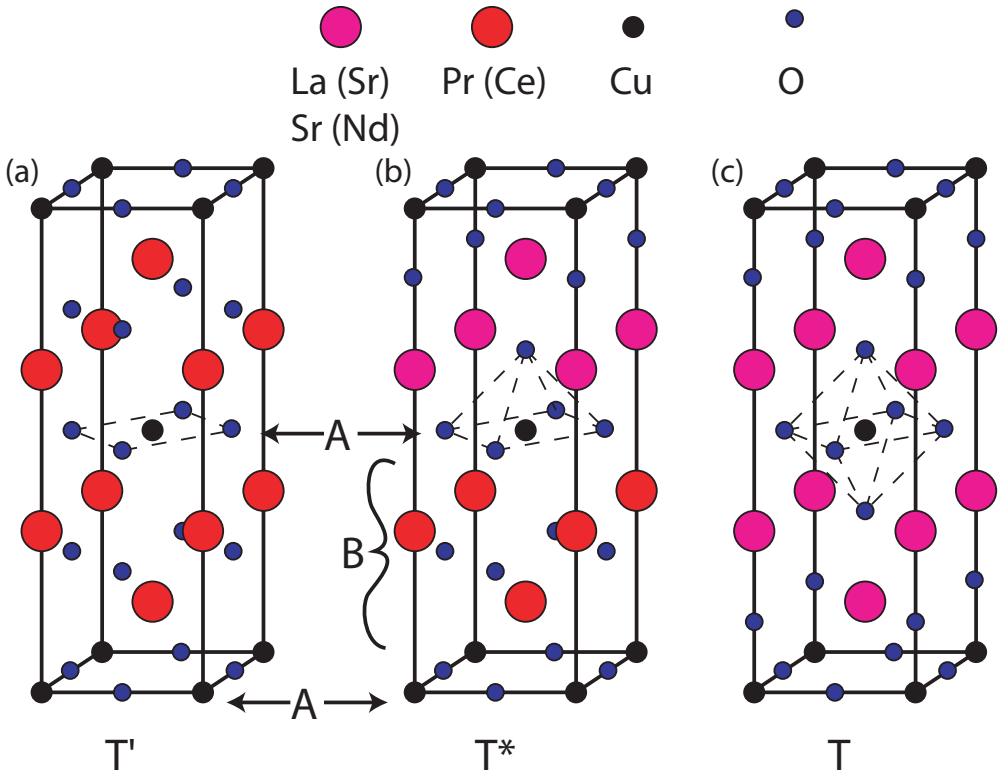

Figure 2.1: Schematic for the lattice structures for the single layer cuprates, E_2CuO_4. (a) T′ structure in which the Copper and Oxygen form a CuO_2 plane. (b) T* structure in which the Copper and Oxygen form a CuO_5 pyramid [which is a mixture of (a) and (b)]. (c) T structure in which the Copper and Oxygen form a CuO_6 octahedra. All the structures shown here are tetragonal. The label 'A' point to the CuO_2 plane, and the label 'B' points to the charge reservoirs.

2.1 Structure

The unit cell of all of these copper oxides is predominantly tetragonal and they have a structural feature in common, namely, they consist of layered planes of CuO_2. Hence, the HTSC ceramic oxides are frequently called cuprates. Figure 2.1 shows the lattice structure of several of the structurally simple E_2CuO_4 (214) cuprates, of which LSCO ($E = La_{2-x}Sr_x$) and PCCO ($E = Pr_{2-x}Ce_x$) belong. These lattices are body-centered-tetragonal. The CuO_2 planes (labeled 'A' in Fig. 2.1) are separated by a layer consisting of oxygen and the other elements in the formulary (labeled

'B' in Fig. 2.1). In the case of the electron-doped $Pr_{2-x}Ce_xCuO_{4\pm\delta}$ (PCCO), the layers between the CuO_2 planes are composed of O and Pr/Ce. These layers are charge reservoirs for the CuO_2 planes. The lattice structures in Fig. 2.1 are called the T, T′, and T* phases of the 214 cuprates. PCCO has the T′ phase, whereas LSCO has the T phase. A mixture of these two phases, T* [Fig. 2.1(b)], can be found in $Nd_{2-x-z}Ce_xSr_zCuO_4$. The main differences between these phases is in the arrangement of the oxygen. In the T′ phase (PCCO), the CuO_2 planes consist of squares of copper and oxygen, each successive CuO_2 plane is rotated 45° with respect to each other. The oxygen sites are all arranged along a line in the c direction, throughout the unit cell. The T phase (LSCO), on the other hand, consists of CuO_6 octahedral. In this phase, oxygen sits directly above and below the copper sites (apical sites). Unlike the T′ phase, the oxygen sites do not all fall along a common line. The T* phase has CuO_5 pyramids, where there is only one oxygen directly above or below the copper site. As one can see from Fig 2.1, this phase consists of half of the T′ phase and half of the T phase in the unit cell. The different oxygen positions are frequently labeled O(1) (planar sites), and O(2) (reservoir sites). The apical oxygen (mentioned above) in the T phase are a part of the reservoir. In PCCO, there is a small amount of apical oxygen present in the T′ phase (an impurity site), which are distinct from the O(2) sites, and are labeled O(3).

These phases fall into the category of single layer cuprates ($n = 1$). This nomenclature stems from the fact that there exists a single CuO_2 plane between successive reservoir layers. There are also double ($n = 2$) and triple ($n = 3$) layer cuprates, where between any two successive reservoir layers there are n CuO_2

planes. The trend also continues past $n = 3$. A little side note; many "families" of cuprates exist and they can be regarded as following the general formulary $\mathbf{A}_m\mathrm{E}_2\mathrm{Q}_{n-1}\mathrm{Cu}_n\mathrm{O}_{2n+m+2+y\pm\delta}$ [21] (abbreviated to $\mathbf{A}$-$m2(n-1)n$) [1]. $\mathbf{A}$ can be any of the elements Cu, Bi, Pb, Tl, Hg, Al, Ga, C, or B. E is typically Ba, Sr, or La. Q is Ca or one of the rare earth elements. Each family is differentiated by the atomic species at the $\mathbf{A}$ site. Within a given family of cuprates, T_c increases as n increases up to $n = 3$. For $n > 3$, T_c stays the same as $n = s$ or more frequently decreases. Take, for example, the Bi family of cuprates ($\mathrm{Bi}_m\mathrm{Sr}_2\mathrm{Ca}_{n-1}\mathrm{Cu}_n\mathrm{O}_{2n+m+2}$). As n increases, the T_c increases as follows: Bi-2201 $T_c \simeq 34$ K [22], Bi-2212 $T_c \simeq 96$ K [23], Bi-2223 $T_c \simeq 110$ K [24], Bi-2234 $T_c \simeq 110$ [25]. This trend, however, does not hold between families of cuprates. A synopsis of the cuprate structures can be found in Ref. [26], while a more detailed structural description of the cuprates can be found in Ref. [27].

2.2 Parent Compound and Electronic Structure

In the beginning of this chapter it was mentioned that the SC cuprates are doped insulators. The undoped compound, the parent compound, are thus the insulators into which carriers are doped. If we look at the electronic configurations for the elements in the parent compound $\mathrm{Pr}_2\mathrm{CuO}_4$ (PCO), we have the following: Pr, $[\mathrm{Xe}]4f^36s^2$; O, $1s^22s^22p^4$; Cu, $[\mathrm{Ar}]3d^{10}4s^1$. In PCO, $\mathrm{Pr} \rightarrow \mathrm{Pr}^{3+}$ leaving closed and

[1] This formula is not always apparent, as in the case of $\mathrm{YBa}_2\mathrm{Cu}_3\mathrm{O}_{7-\delta}$ (Y-123), which is a double layer cuprate, and is a modification of the Cu-1212 system with Y substituted for Ca. The 214 cuprates can also be described by this general formula, where $m = 0$ and $n = 1$. Within this formula, one obtains 0201.

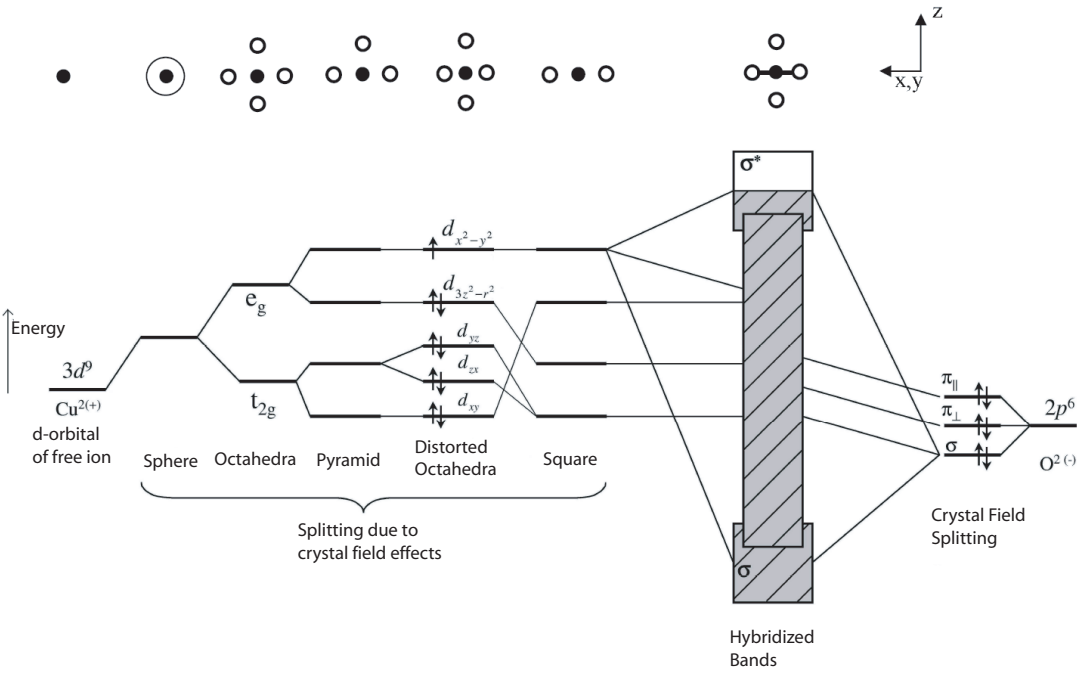

Figure 2.2: Schematic of band calculations hybridizing the copper and oxygen orbitals in the CuO_2 plane, taken from Ref. [28, 29]. The far left shows the free ion Copper site, while the far right shows the free ion Oxygen site. From left to right, the orbitals change energy based on crystal field effects from the surrounding Oxygen: spherical, octahedral coordination, pyramidal coordination, distorted octahedral coordination, and the last on the left is a planar coordination (which is the important one for PCCO). The hybridized bands, between Copper and Oxygen show that a mixing of the Cu $d_{x^2-y^2}$ orbital and the Oxygen σ orbital leave a half filled $\sigma^\star$ band, basically one free electron per copper site.

stable shells, and $O \rightarrow O^{2-}$ again leaving closed and stable shells. This leaves $Cu \rightarrow Cu^{2+}$ with a nearly filled d shell ($3d^9$). Simple band structure calculations on these parent compounds predict that they should be half-filled band metals (schematically shown in Fig. 2.2, where the half-filled Copper $d_{x^2-y^2}$ orbital hybridized with the Oxygen σ gives a Copper site which is half-filled in the CuO_2 plane). Fig. 2.2 only considers the hybridization of the planar copper and oxygen, the reason being that band calculations show these to be the only states within several eV of the Fermi energy [29] (Fig. 2.3). Experimentally, however, they are insulators. The

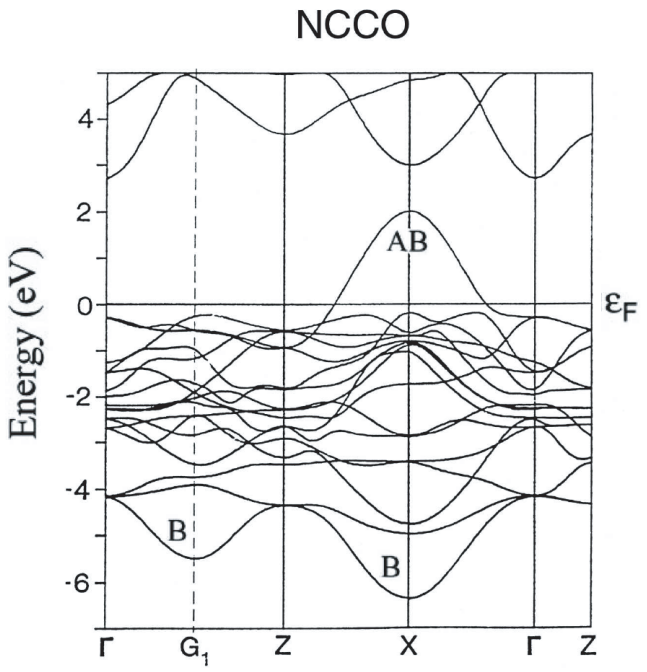

Figure 2.3: Dispersion curves for NCCO using a local density approximation, taken from Ref. [28, 29]. All the curves (E versus k) shown here are due to the CuO_2 plane. The curves labeled 'A' and 'B' correspond to antibonding and bonding of the Copper d orbital with the Oxygen p orbital.

simple band calculations do not include interactions between the quasiparticles. This phenomenon is not particular to the cuprates, but to many transition metal oxides.

When a material is predicted, by band theory, to be a metal, but it is in fact an insulator, then the material falls into the class of Mott-Hubbard insulators [30, 31]. What happens here is that a strong on-site Coulomb repulsion (U) makes a doubly occupied site (filled band) unfavorable. As a result, the band is split into an upper Hubbard band (UHB) and a lower Hubbard band (LHB) [Fig. 2.4(b)]. The gap between these two bands is typically of order U, which is on the order of several eV [29]. The cuprates are a slightly different story. There is a Cu-O charge-transfer

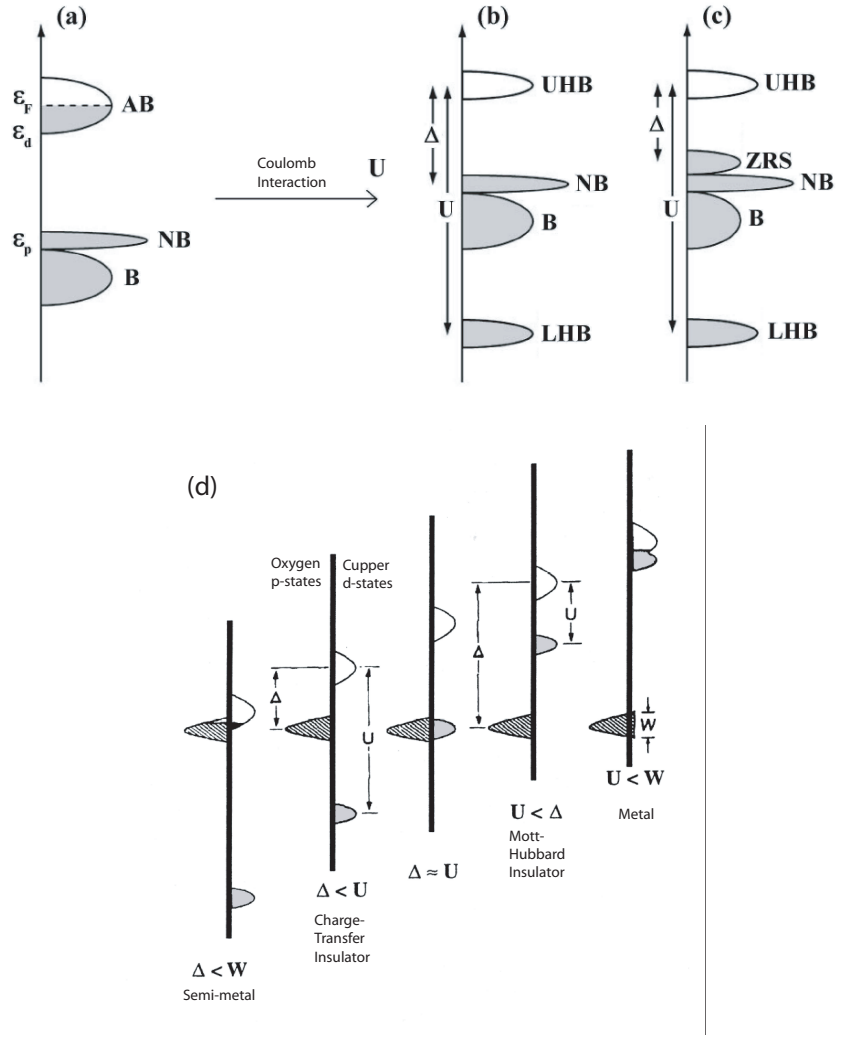

Figure 2.4: Schematic of the density of states for the parent compounds of the cuprates, taken from Ref. [28]. Similar figures can be found in Ref. [29]. (a) Schematic for the density of states without Coulomb interactions taken into account. The band crossing the Fermi Energy (antibonding band AB) is the hybridization of the Cu $d_{x^2-y^2}$ orbital and the Oxygen σ orbital. (b) Inclusion of Coulomb interactions (energy scale U) splits the AB band into an upper Hubbard band and a lower Hubbard band. The charge-transfer gap Δ is less than U and the next closest band to the Fermi Energy is the non-bonding band NB (see text). (c) Spectral weight is shifted from the upper Hubbard band and the non-bonding band to form a Zhang-Rice singlet band (mentioned in the text). This picture is effectively the same as in (b). (d) Schematic of the density of states for different ratios of U and Δ for the scenarios in (a-c). For $\Delta < W$ (W is the width of the band) and $\Delta \ll U$ there is an overlap upper Hubbard band with the non-bonding band (i.e., a semi-metal). For $W < \Delta < U$ there is a charge-transfer insulator (cuprates). For $W < \Delta \simeq U$, the non-bonding band is at the same level as the lower Hubbard band. For $W < U < \Delta$, the charge-transfer gap is larger than the Coulomb repulsion and it is easier to doubly occupy the Copper sites. This is a Mott-Hubbard insulator. For $U < W < \Delta$, the upper and lower Hubbard bands have overlap and the material is a metal.

gap Δ which is smaller than coulomb repulsion gap U [Fig. 2.4(b)]. This is the energy required to move a charged particle between the copper and oxygen sites. This implies that it is easier to move charges between sites rather than doubly occupying a single site. As a result, the cuprates are more accurately labeled charge-transfer, or Mott-like, insulators [29] (Fig. 2.4). This type of insulator is not to be confused with the typical band insulator, where the Pauli exclusion principle prevents conduction of charge carriers (Fig. 2.4).

2.3 Evolution of the Phase Diagram with Doping

It is worth briefly mentioning here how doping occurs in the cuprates. In the case of $La_{2-x}Sr_xCuO_4$ (LSCO), hole doping occurs by the partial substitution of La^{3+} by Sr^{2+}, since Sr is giving up less electrons to the conduction band. In $Pr_{2-x}Ce_xCuO_{4\pm\delta}$ (PCCO), electron doping occurs by the partial substitution of Pr^{3+} by Ce^{4+}, thereby adding more electrons into the conduction band. There is an interesting peculiarity with PCCO; oxygen reduction, along with Ce doping, is necessary in order to achieve superconductivity. This is not the case for the hole-doped cuprates. Many of the hole-doped cuprates are doped by changing the oxygen content, however adjusting oxygen in addition to another element is not a necessity for the hole-doped compound. This will become more clear in Chapter 4.

The parent compound, mentioned above, has a Cu $d_{x^2-y^2}$ band which is half filled (Fig. 2.2). Strong Coulomb repulsion breaks this band into two, resulting in a localized electron on the Cu site. This gives the Cu^{2+} ions a spin-1/2 character, and

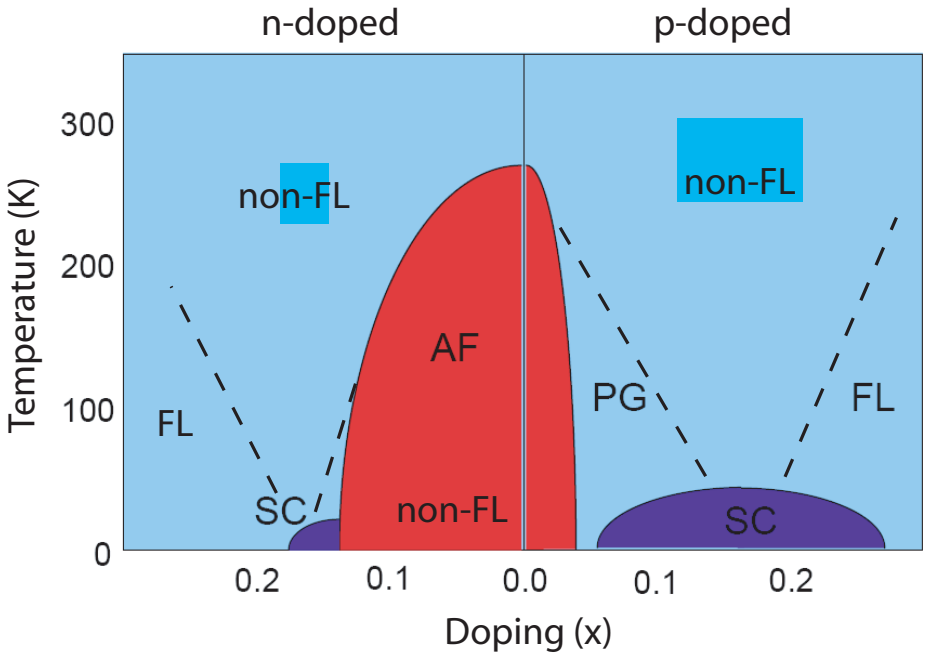

Figure 2.5: Generic phase diagram of the cuprates. The left side of the diagram is representative of the electron-doped cuprates. The long-range antiferromagnetic region (AF) persists up to (and perhaps into) the superconducting dome (SC). The dashed lines separate the AF region from the non-Fermi liquid region and the Fermi liquid region. Above the dome the material behaves in a non-Fermi like manner. The right side of the diagram shows the hole-doped cuprates. The AF region dies off relatively quickly (due to AF frustration rather than dilution as in the electron-doped cuprates). The superconducting dome extends over a broader range than in the electron-doped counter parts. The dashed lines again separate the three distinct regions around the SC dome. The pseudogap (PG) is a high-energy normal state gap which vanishes along the dashed line (as one moves to the right in the diagram).

the superexchange interaction between copper sites results in an antiferromagnetic correlation. So, the undoped parent ($x = 0$) compound is an antiferromagnetic insulator (see Fig. 2.5). In this state, the Cu spins are aligned in a static, commensurate antiferromagnetic pattern as shown in Fig. 2.6.

Several models are proposed to explain the behavior of these cuprates as the doping increases from $x = 0$. The most popular ones are the three band model [32, 33] and the one band model [34]. In these theories, the first consideration is that

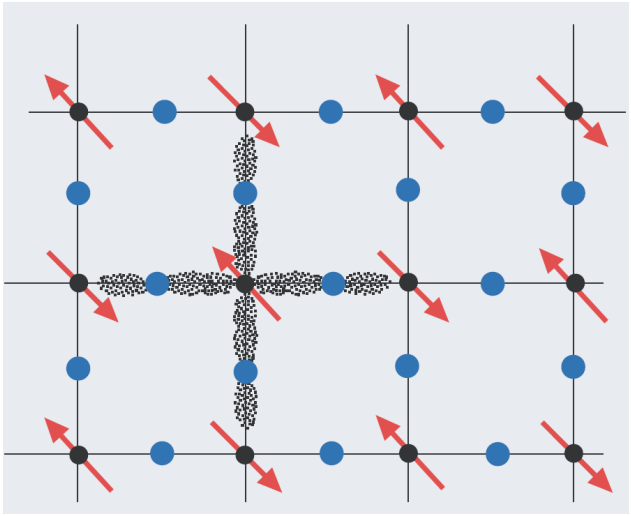

Figure 2.6: Alignment of the Copper spins in the antiferromagnetic state of the electron-doped cuprates. This is a representation of the xy plane. The Copper spins are aligned along the 45° line of the CuO_2 squares.

the important physics is occurring in the CuO_2 plane. Again, the reason is that the bands closest to the Fermi energy (as determined by band calculations) are due to the in-plane hybridization of the copper and oxygen orbitals (Fig. 2.3). The three band model incorporates all of the hybridized bands, and a competition between on-site coulomb repulsion U [2] and a hopping component between nearest neighbors (denoted as t in the literature). In this picture [charge-transfer schematic in Fig. 2.4(d)] doped holes enter into the oxygen p orbital, whereas doped electrons enter into the upper Hubbard band. Therefore, doped holes preside mostly on the oxygen sites and doped electrons are mostly on the copper sites. In the one band model, the holes doped onto the oxygen sites are thought to form singlet pairs [34] (Zhang-Rice singlets) with the lone hole on the copper site. Without loss of generality, one can consider the singlet state to be centered on the copper site. In this picture, the copper sites

[2] There is a repulsion term for all the sites; U_{dd} for Cu-Cu, U_{pp} for O-O, and U_{pd} for Cu-O (Δ in the previous section).

are primarily considered, the oxygen bands much less so, and there is only an upper Hubbard band and a lower Hubbard band, energetically separated by an effective repulsive gap U_{eff}. Similarly to the three band model, there is again a competition between U_{eff} and t. As in the three band model, electrons are doped onto the copper site, whereas doped holes are now shared between the copper and oxygen sites.

As doping increases (see Fig. 2.5), the antiferromagnetic (AF) transition temperature T_N decreases, with long-range order eventually vanishing. For the hole-doped compounds, this occurs nears $x \simeq 0.02$. In the electron-doped compounds, there is evidence to support a persistence of long-range AF order into the SC dome (more on this observation later). A decrease in the electron-electron correlations accompanies an increase in doping. At low (but non-zero) dopings, the cuprates exhibit non-Fermi liquid behaviors, with quasi-two dimensional (2D) behavior (remember the energy states within the CuO_2 plane have the energies closest to the Fermi energy and so CuO_2 plane is considered 2D). Superconductivity eventually sets in, and T_c increases with an increase in doping. T_c maximizes ($x \simeq 0.15$ for holes and electrons) and begins to decrease upon further doping. Frequently in the literature, HTSC are classified as underdoped, optimally doped, and overdoped (within a specific compound). The underdoped region corresponds to the portion of the phase diagram where T_c increases with doping. The optimal doping is where the T_c is maximal, and the overdoped region is where T_c decreases with doping. In the overdoped region, the normal state (non-superconducting state), driven by magnetic field or temperature or doping, appears to be consistent with a Fermi liquid like behavior as the electron-electron interactions become screened and significantly

weakened.

The one band and the three band models mentioned above do an adequate job of describing the electronic behavior of the cuprates, but only in the region of strong/weak electron-electron interactions ($U \gg t$, $U \ll t$). In the region of comparable interactions ($U \approx t$), the models are less representative of the experimental observations.

2.4 Magnetism and Electronic Transport in the Cuprates

The previous sections outlined the basic lattice structure and electronic structure of the cuprates. Here I would like to outline some specific measurements and properties relevant to this thesis and it's motivation.

Antiferromagnetism

As mentioned in Section 2.3, the spin 1/2 Cu^{2+} are long-range antiferromagnetically ordered with an AF transition temperature $T_N \simeq 200 - 400$ K ($\simeq 250$ K for NCCO [35]), depending on the compound. The alignment of the Cu spins are strongly ordered in the CuO_2 plane and are shown schematically in Fig. 2.6. The AF ordering is commensurate with the lattice structure in the undoped parent compounds, i.e., in rational multiples of the lattice parameters. The electron-doped cuprates show a weakening of the long-range AF order as doping increases from $x = 0$, consistent with a dilution of the spin structure. As a result, T_N steadily decreases with doping. The hole-doped cuprates, on the other hand, show a more

dramatic decrease of T_N with hole-doping (see Fig. 2.5).

Focusing on the electron-doped cuprates, commensurate long-range 3D AF order persists up to relatively high doping (at least up to the doping where SC is observed). It is still under debate as to whether long-range 3D AF order coincides with the superconducting region, or if only short-range AF order exits [36]. Nevertheless, some form of AF order persists inside the SC dome. It has been found that doping induces a modulation in the density of spins [37] (called a spin density wave, or SDW). This SDW is a quasi-2D AF, with short-range correlation along the c-axis and long-range order within the CuO_2 plane. Therefore, the effective physics within the planes should be nearly identical in either the 3D AF phase or the SDW phase. Just as with the AF order, the SDW is also commensurate with the lattice structure. These magnetic orders, AF and SDW, persist up to a doping of $x \simeq 0.16$, beyond which they become disordered paramagnetic phases [38].

Since we know that the electron-doped cuprates require oxygen reduction in order to superconduct (even if we don't know exactly why), it is interesting to see how oxygen reduction affects the AF order. Mang *et al* [37] show that AF order persists up to $x = 0.18$ for non-oxygen-reduced NCCO (as-grown NCCO). Oxygen reduction causes T_N to decrease over entire doping range [36, 37] (Fig. 2.7). This reduction induces the quasi-2D SDW phase, and results in a reduced T_N corresponding to a rigid shift in doping of $\simeq 0.03$ [37]. The reduction in T_N with a reduction in oxygen content is not surprising. Oxygen has a strong affinity for a valency of -2, thereby removing electrons from the conduction band. Removing oxygen would do the reverse and re-insert electrons into the conduction band. As already pointed

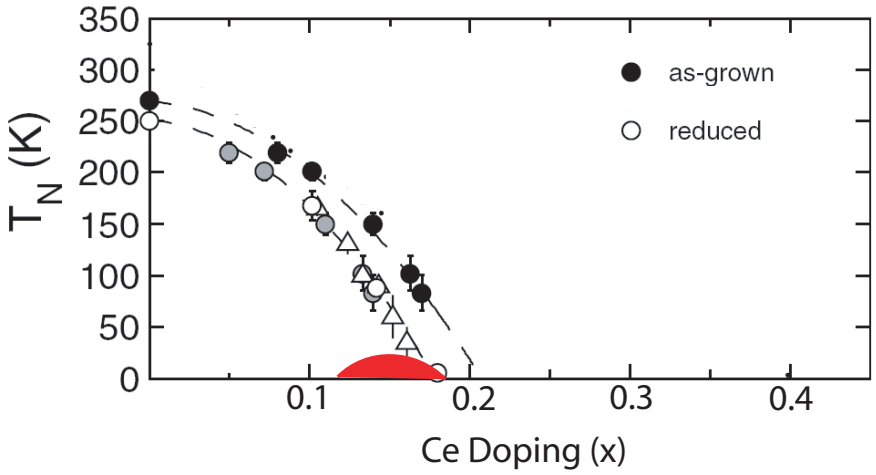

Figure 2.7: T_N versus cerium content x in $Nd_{2-x}Ce_xCuO_{4\pm\delta}$. • data are from "as-grown" crystals. ∘ data are from oxygen-reduced crystals. △ data are from Ref. [36]. The semi-circle represents the doping where SC occurs in NCCO.

out, electron-doping results in a dilution of the AF order.

Resistivity

In Section 2.2 it was shown that the CuO_2 planes contain the lowest energy states. This tells us that the electronic properties should be dominated by these planes. This is reaffirmed by measurements of the resistivity anisotropy, i.e., the resistivity perpendicular to the CuO_2 planes compared to the resistivity parallel to the planes ρ_c/ρ_{ab}. Anisotropies on the order of $10^2 - 10^4$ are found for both the hole-doped [39, 40] and the electron-doped [41, 42] cuprates. This observations means that it is much easier for electrons to move within the plane than it is to move between planes. Therefore, the cuprates are quasi-2D systems, where the electronic transport is dominated by conduction within the CuO_2 planes.

The temperature dependencies of the in-plane resistivities are also an inter-

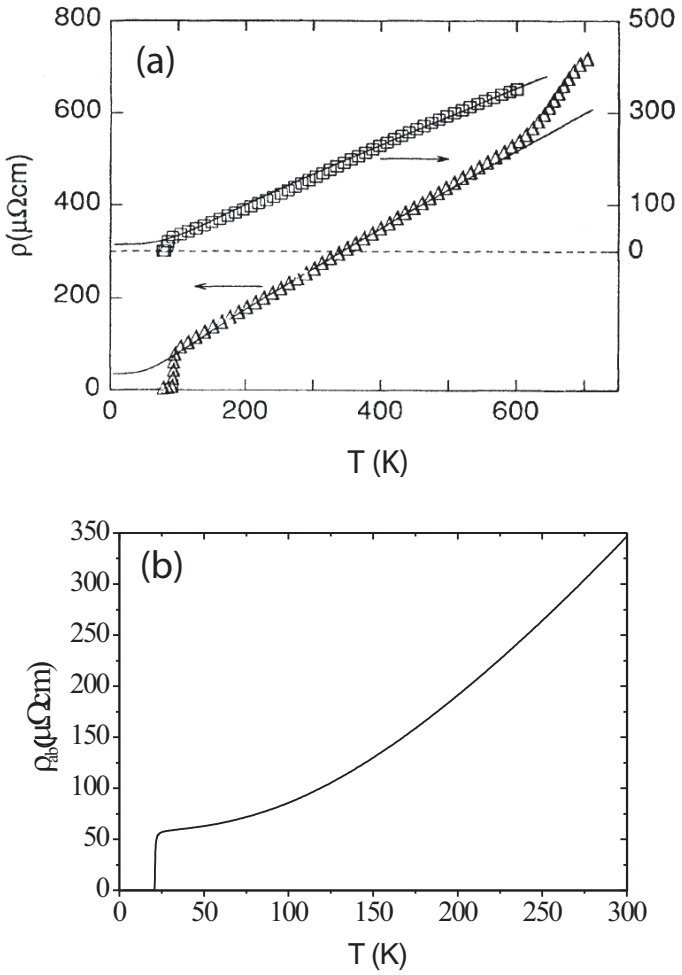

Figure 2.8: ρ_{ab} versus Temperature for optimally doped hole and electron-doped cuprates. (a) Optimally hole-doped $YBa_2Cu_3O_{7-\delta}$ ($\triangle$) and $YBa_2Cu_4O_{8\pm\delta}$ thin films, taken from Ref. [44]. (b) Optimally electron-doped ($x = 0.15$) $Pr_{2-x}Ce_xCuO_{4\pm\delta}$, taken from Ref. [45]. ρ_{ab} is linear for (a), and quadratic for (b). (a) is linear up to T = 700 K, which is frequently observed in the hole-doped cuprates. The nonlinearity at higher temperatures is attributed to a loss of oxygen

esting feature of the cuprates. One of the first things noticed about the hole-doped cuprates was that $\rho_{\rm ab} \propto$ T [43] [Fig. 2.8(a) and (b)]. The linear temperature dependence, over such a wide temperature range, is quite a peculiarity. This dependence is inconsistent with conventional Fermi liquid theory, which predicts a quadratic dependence for quasi-particle scattering at low temperature. Moderate success has

been achieved in fitting the linear dependence to the Bloch-Grüneisen theory for electron-phonon scattering [44,46] (see Chapter 3 for the formula), however, it should be stressed that the linear temperature dependence is observed in a narrow doping range around optimal doping [47]. So it seems unlikely that electron-phonon scattering is responsible for the temperature dependence of ρ [3]. As the hole-doped cuprates enter into their overdoped regime, the resistivity begins to show a $\rho \propto \mathrm{T}^2$ behavior, which is more in line with a Fermi liquid model. The electron-doped cuprates, on the other hand, show a $\rho \propto \mathrm{T}^2$ behavior over all dopings and up to relatively high temperatures ($\mathrm{T} \simeq 200$ K). While this temperature dependence is consistent with a Fermi liquid, it is still difficult to explain the experimental data. Experimentally, the coefficient A_{ee} of the T^2 resistivity term ($\rho(\mathrm{T}) = \mathrm{A}_{ee}\mathrm{T}^2$) is orders of magnitude larger than what is predicted by theory [51, 52].

As mentioned in Section 2.3, the strong electron-electron correlations weaken upon doping, allowing the system to evolve from an insulator to a metal. This is easiest to see in the field-driven normal state of the *electron*-doped cuprates. At low dopings, the resistivity of the electron-doped cuprates exhibits insulator-like behavior ($d\rho/d\mathrm{T} < 0$) at low temperatures, while it maintains metallic-like behavior ($d\rho/d\mathrm{T} > 0$) at higher temperatures. The crossover from metallic to insulator-like with temperature (denoted T_{min}) decreases as the doping increases [53] (Fig. 2.9). The doping at which T_{min} vanishes is near optimal doping in PCCO, as reported

[3] There are several side notes to point out here. Despite the lack of a significant isotope effect on T_c, an isotope effect has been reported in the phonon spectra of angle-resolved photoemission spectroscopy (ARPES) [48,49]. Several other reports are *re*-investigating some sort of inclusion of phonons in the mechanism of HTSC [50], as well as the reason for the temperature dependence of ρ [46].

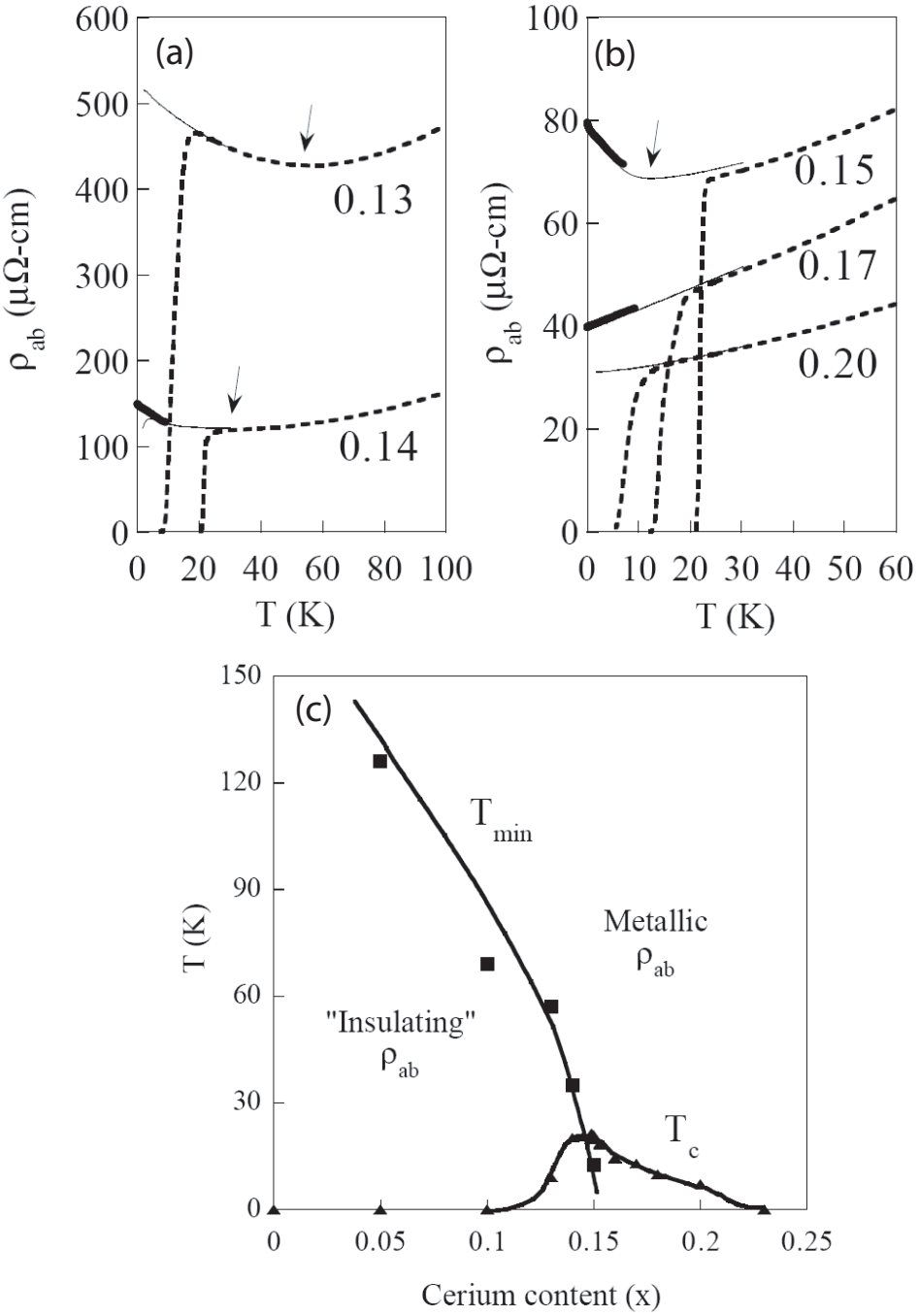

Figure 2.9: Normal state Resistivity versus Temperature for $Pr_{2-x}Ce_xCuO_{4\pm\delta}$ thin films, taken from Ref. [53]. (a) Underdoped thin films. (b) Optimal and overdoped thin films. $T_{\rm min}$ is shown by the arrows. Thin lines are data taken in 8.7 T magnetic field. Thick solid lines are taken in 12 T fields. Dashed lines are zero field data. (c) $T_{\rm min}$ versus doping for the same thin films, shown along with the SC dome. The lines connecting the data are guides to the eye. As the doping increases, the low temperature resistivity behavior evolves from an insulating-like state to a metallic state.

by Fournier *et al.* [53]. This transition from a $T = 0$ insulating to metallic state is typically called a metal-to-insulator transition (MIT). This feature is also observed in the hole-doped LSCO [54], in magnetic fields up to 60 T, also near optimal doping. This similarity, between the hole-doped LSCO and the electron-doped PCCO, has been interpreted as evidence for a symmetry in the CuO_2 planes between the hole and electron-doped cuprates [53]. The exact cause of the MIT, however, is not understood. With this "symmetry", one would expect the conduction within the planes, i.e., ρ_{ab}(T), to be similar. Yet, as shown above, there does not seem to be an obvious connection between the resistivities of the hole-doped and the electron-doped cuprates, as of the current state of understanding.

Hall Effect

The Hall effect is another transport property that is inconsistent with a Fermi liquid model. For both hole and electron-doped cuprates, the Hall coefficient R_H shows significant temperature dependence (see Fig. 2.10), whereas the Fermi liquid model predicts a temperature independent Hall coefficient, for single-band conduction. Due to this peculiarity in the Hall coefficient, it is rather difficult to make a simple relation to carrier density [57], and rarely is one able to determine the carrier density from R_H alone.

In addition to the temperature dependence is the interesting doping dependence of R_H in the cuprates. Now, the sign of R_H is conventionally determined by the sign of the charge carriers: it is positive for holes and negative for electrons.

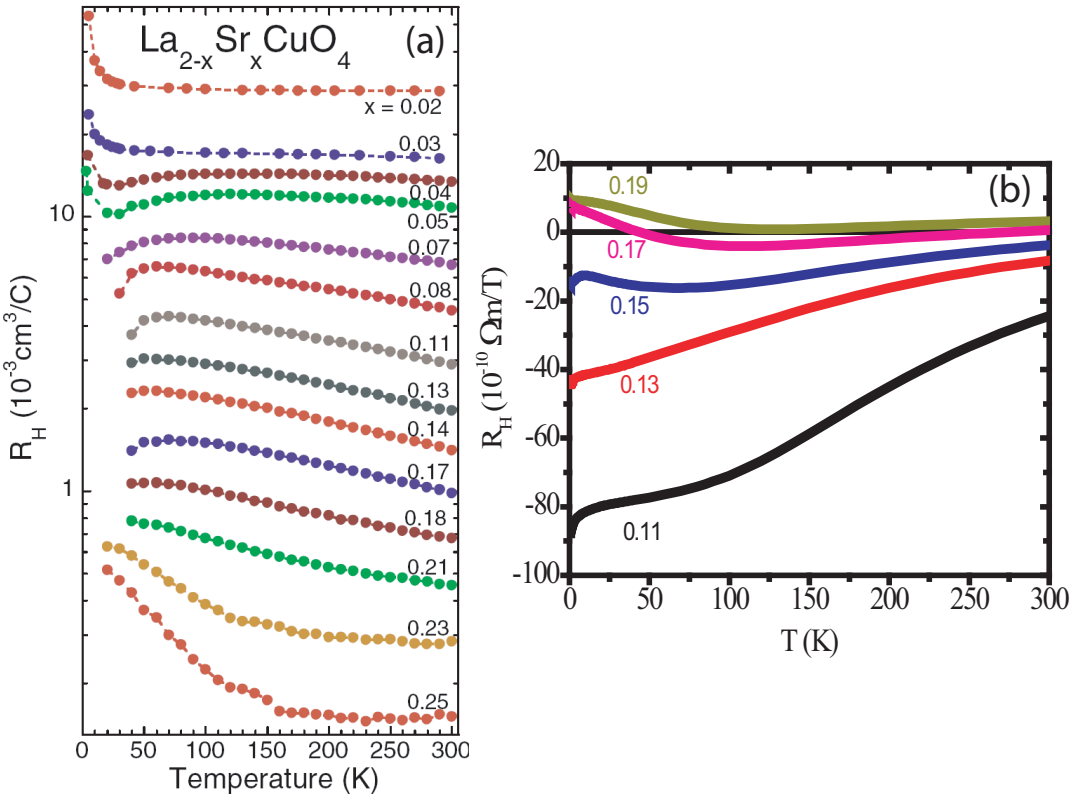

Figure 2.10: R_H versus T for (a) $La_{2-x}Sr_xCuO_4$, taken from Ref. [55], and (b) $Pr_{2-x}Ce_xCuO_{4\pm\delta}$, taken from Ref. [56]. Note: $1\text{cm}^3/\text{C} = 1 \times 10^{-6}\Omega\text{m/T}$.

In both the electron and hole-doped cuprates, R_H changes sign with doping (see Fig. 2.11). It is also interesting to note that, while the *hole-doped* cuprate LSCO remains *positive* throughout the doping range that exhibits superconductivity [58] ($0.05 \leq x \leq 0.30$), the *electron-doped* PCCO *does not remain negative throughout the SC doping range* [45] ($0.12 \leq x \leq 0.20$). The crossover doping for PCCO is $x \simeq 0.16$, at low temperatures. This change in sign for PCCO is interpreted as two-band conduction [41, 59], i.e., conduction from both holes and electrons, which becomes more single-band-like (hole-like) with doping.

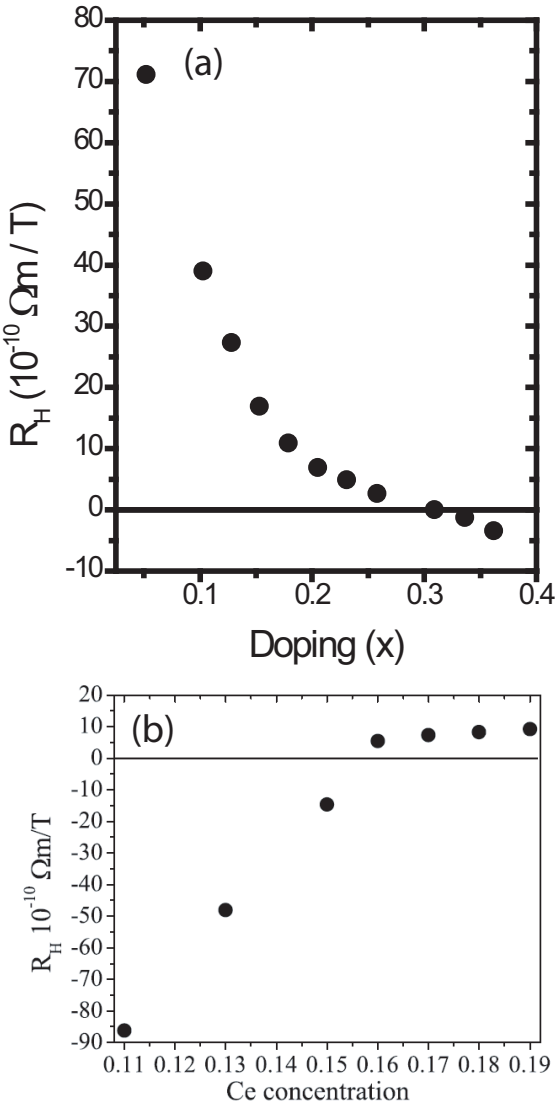

Figure 2.11: R_H versus x for $La_{2-x}Sr_xCuO_4$ and $Pr_{2-x}Ce_xCuO_{4\pm\delta}$. (a) LSCO data at 80 K, adapted from Ref. [58]. (b) PCCO data at 0.35 K, taken from Ref. [45]

Angle-resolved Photoemission Spectroscopy

Angle-resolved photoemission spectroscopy (ARPES) is similar to the photoelectric effect. A photon of known energy enters into a solid and kicks out an electron. ARPES, however, is able to determine the $\vec{k}$ state as well as the energy state (near the Fermi energy) that the electron occupied. In this way, one is able

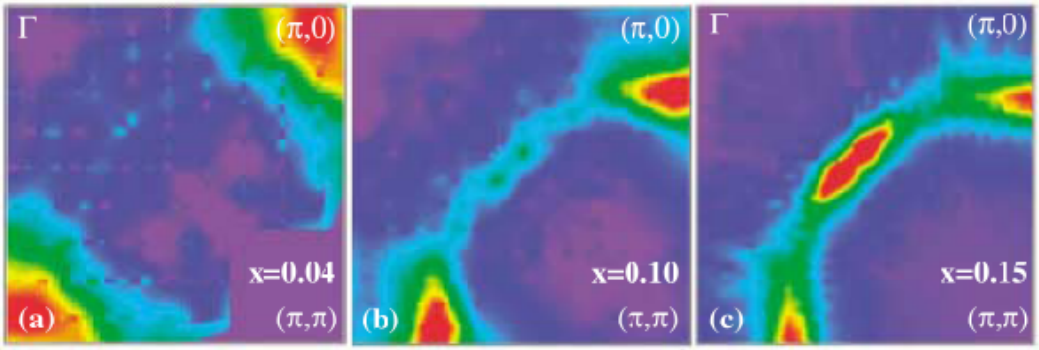

Figure 2.12: ARPES data on $Nd_{2-x}Ce_xCuO_{4\pm\delta}$ for (a) $x = 0.04$, (b) $x = 0.10$, and (c) $x = 0.15$ at T = 25 K, taken from Ref. [60]. Electron pockets are visible in the $(\pi, 0)$ and $(0, \pi)$ corners. As the doping increases to $x = 0.15$, a hole pocket opens in the $(\pi/2, \pi/2)$ region.

to map out the Fermi surface as a function of $\vec{k}$. ARPES measurements [4] on the electron-doped cuprate NCCO has revealed some novel features of the Fermi surface as a function of cerium doping.

In Fig. 2.12(a-c), the doping evolution is shown [5]. At zero doping, the entire Brillouin zone would be empty as we would be looking inside the charge-transfer gap. At low dopings [Fig. 2.12(a)], small electron pockets are seen at the $(\pi, 0)$ and $(0, \pi)$ portions of the Brillouin zone. The red regions indicate quasiparticles with well-defined states near the Fermi energy. The yellow and green regions correspond to progressively "less-well-defined" states. The volume of the pockets at low doping are comparable to the doping level ($\simeq x$). As the doping increases to $x = 0.10$ [Fig. 2.12(b)], quasiparticle states at the Fermi energy can be seen to emerge at the $(\pi/2, \pi/2)$ region of the Brillouin zone (the little green dots). Upon further doping [Fig. 2.12(c)], well-defined quasiparticle states are now observable at the

[4] For a review, see Ref. [29]

[5] These figures are determined by integrating energy dispersion curves (EDC) over an energy window of -40 meV to 20 meV about the Fermi energy

$(\pi/2, \pi/2)$ region. This evolution *can be* interpreted as a closing of the charge-transfer gap [60,61] (Δ in Sec. 2.2). As the charge-transfer gap closes, the hole band (the closest band below the Fermi energy) approaches the Fermi surface. Thus the states at $(\pi/2, \pi/2)$ are due to holes [6]. As doping increases from $x = 0$, two types of quasiparticles are visible in the ARPES spectra: electrons and holes. This is consistent with the change in sign of R_H mentioned above.

As mentioned previously, theories have been relatively successful in describing the cuprates, but only in approaching optimal doping from either the overdoped side ($U \ll t$) or the underdoped side ($U \gg t$), not spanning the entire doping range. An alternative explanation involves an approach from the overdoped side of the phase diagram and interjects a SDW gap [7] [38], dominating the structure of the states at the Fermi surface (at moderate doping levels), in addition to a charge-transfer gap. The regions of suppressed states between the hole pocket and the electron pockets [Fig. 2.12(c)] correspond to an intersection of a hole-like Fermi surface [centered about (π, π)] and the diamond-shaped antiferromagnetic Brillouin zone (Fig. 2.13). The intersection points are frequently referred to as "hot spots" and are portions of the Brillouin zone where antiferromagnetic interactions of the quasiparticles are enhanced. As the gap vanishes (i.e., x increasing), the Fermi surface is just a hole pocket centered about (π, π). As $x \to 0$, two bands are observed if the SDW gap is smaller than the charge-transfer gap. If the SDW gap is larger, then the lower band

[6] The determination of the pockets as either holes or electrons is more rigorous than mentioned in the text. Dispersion relations point to the regions at $(\pi/2, \pi/2)$ as hole pockets and the regions at $(\pi, 0)$ and $(0, \pi)$ as electron pockets

[7] This "gap" corresponds to the amplitude of coherent backscattering at the wave vector $Q = (\pi, \pi)$ due to the AF order. As magnetic order is suppressed with doping, so is the gap.

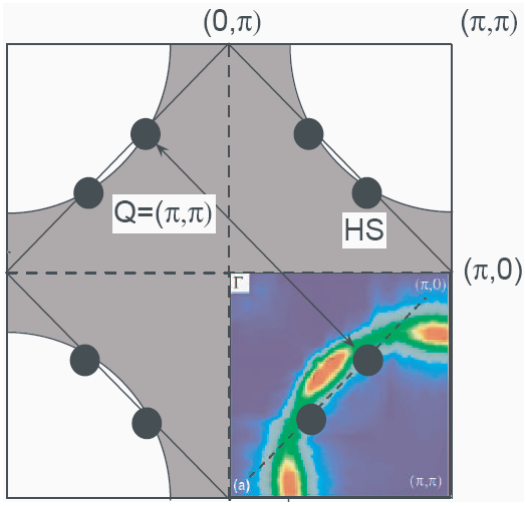

Figure 2.13: Overlay of the Brillouin zone with the antiferromagnetic Brillouin zone (diamond-shaped). The gray areas indicate filled electronic states. The portions where the antiferromagnetic Brillouin zone intersects the Fermi surface (•, or HS) are the "hot spots" and are regions of enhanced antiferromagnetic interactions between quasiparticles and result in a gap at the Fermi surface.

is filled leaving only the upper band (consisting of electrons) at the Fermi surface.

Irrespective of the model, ARPES data on overdoped NCCO ($x = 0.17$) [62] has recently shown that the Fermi surface is indeed a closed hole-like pocket centered about (π, π), with a volume which goes as $1 + x$. A schematic of this result is shown in Fig. 2.14.

This closing of the Fermi surface (between $x = 0.15$ and $x = 0.17$) is consistent with the Hall effect measurements in PCCO, which indicates a dominant hole-like carrier behavior in overdoped samples [Fig. 2.11(b)]. The above mentioned behavior in the transport, ARPES, and magnetic ordering all lead to an interesting coincidence. In particular, the fact that the antiferromagnetic *order* and a reconstruction of the Fermi surface seen in ARPES both occur at a similar doping (i.e., $x \simeq 0.17$) leads us to the last section of this chapter and the motivation for this part of the

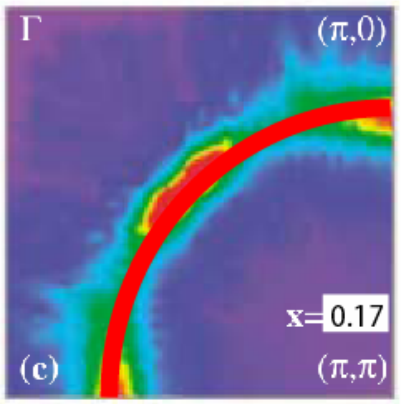

Figure 2.14: Schematic of ARPES data on overdoped NCCO $x = 0.17$ (schematic of data presented by Ref. [62]. The figure is adapted from Ref. [60]. The hole-like Fermi surface (red) is closed, indicating a zero gap in the overdoped compound.

thesis.

Quantum Criticality

Dagan *et al.* [45] demonstrated in PCCO, through measurements of the Hall coefficient and resistivity at low temperatures, evidence for a quantum phase transition at a critical doping $x_c \simeq 0.165$, which is in the vicinity of all the above mentioned phenomena. Before venturing too much further, it is helpful to briefly clarify what is a quantum phase transition [63].

In the ground state ($T = 0$), it is possible for quantum fluctuations to allow a phase transition. If we imagine that the quantum mechanical state, at $T = 0$, can be represented by a ground state and a first excited state (Fig. 2.15), and that we have the ability to tune a parameter of the Hamiltonian (pressure, magnetic field, disorder, doping, *etc.*), then it is possible that the ground state and the first excited state cross at some critical value of the tuning parameter p_c, called the quantum

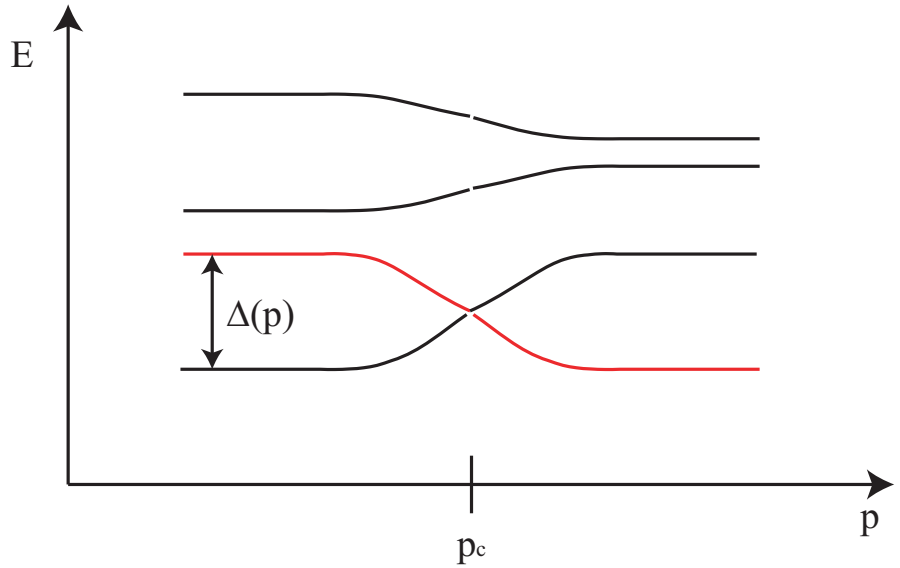

Figure 2.15: Schematic of a quantum phase transition in an energy versus control parameter (see text). For $p < p_c$, the ground state (the lowest energy line) and the first excited state (second lowest energy line) are separated by an energy gap which depends on the control parameter p. As p increases through p_c, $\Delta(p)$ decreases and the ground state and the first excited state cross. The crossing at p_c is called a quantum phase transition, and p_c is called the quantum critical point.

critical point. Typically, this is thought of as a transition from an ordered phase to a disordered phase (ferromagnetism to paramagnetism, for example). So, the quantum phase transition is the $T = 0$ realization of a phase transition from one energetically favorable state to another. This is all fine and dandy, except that the zero temperature limit is not experimentally accessible. Not all is lost, however, as effects of the quantum phase transition are observable at finite temperatures (see Fig. 2.16). The first thing one notes is that a funnel region appears at finite temperatures above p_c. The research community has dubbed this funnel region as a quantum critical region. What is occurring in this region is that the two phases on either side of p_c are thermally mixed at some finite temperature and at some value of p, when $k_B T \gg \Delta(p)$ ($\Delta(p)$ is the energy gap as a function of the tuning

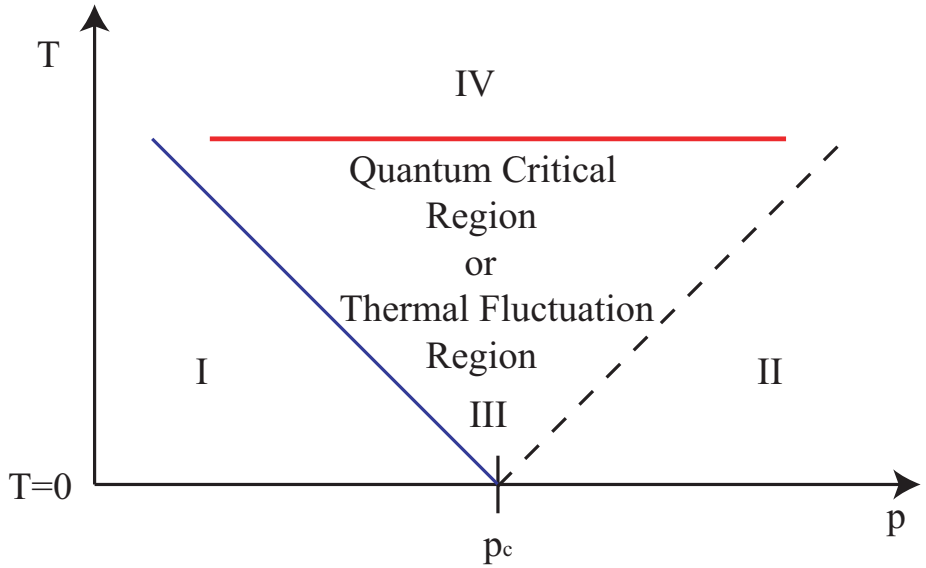

Figure 2.16: Temperature versus control parameter for a quantum phase transition. Region I is dominated by the ground state of the quantum mechanical Hamiltonian. Region II is dominated by the control parameter induced first excited state. Typically, region I is the ordered phase and region II is the disordered phase. Region three represents the region where there is thermal mixing of region I and region II. Region IV represents the temperature above which the system behaves classically.

parameter, depicted in Fig. 2.15). Therefore, rather than calling it a quantum critical region, I prefer the term "thermal fluctuation region." The properties of the system, within this funnel, are thus a mixture of the two phases. Why might this bear any relevance to the cuprates? Current research is investigating whether the unusual normal state properties of the cuprates, in the non-Fermi liquid regime, are the result of a quantum phase transition, and even the high-T_c superconductivity itself.

Now, on to the work by Dagan *et al.* [45], performed on the normal state ($H > H_{c2}$), mentioned at the beginning of this section. Dagan *et al.* [45] show that, as the cerium doping increases in PCCO, fundamental changes in the properties of R_H and ρ(T) occur near a critical doping $x_c \simeq 0.165$. The Hall coefficient displays

an abrupt change as a function of doping, at the lowest temperatures measured ($T = 0.35$ K) [Fig. 2.17(a)]. The low temperature normal state resistivity, expressed as $\rho = \rho_\circ + \mathrm{AT}^\beta$, displays a change in the temperature dependence, i.e., A and β in the above relation as a function of doping. These findings are interpreted in the framework of a quantum phase transition. As the control parameter is adjusted (an increase in cerium doping x), PCCO moves through the thermal fluctuation region, which is centered at $x_c \simeq 0.165$ at T = 0. The doping dependence of R_H is representative of the ground state on either side of x_c, below the thermal fluctuation region. The results of ρ(T) are indicative of moving through the fluctuation region, as the mixing of the two phases results in dependencies not particular to either phase. On the overdoped side (in the absence of a quantum phase transition), one expects a T^2 dependence as PCCO becomes more Fermi liquid-like. On the underdoped side of the phase diagram, the upturn in ρ(T) makes it very difficult to determine β. Focusing on the power dependency β, Fig. 2.17(b) shows the temperature at which β, as a function of doping, deviates from 2. The grey region is where $\beta = 2$ and the white region is where $\beta < 2$. This is consistent with crossing through the fluctuation region, where the control parameter is doping. Dagan *et al.* [45] suggest that the quantum phase transition in PCCO is a transition from an ordered antiferromagnetic state to a disordered magnetic state.

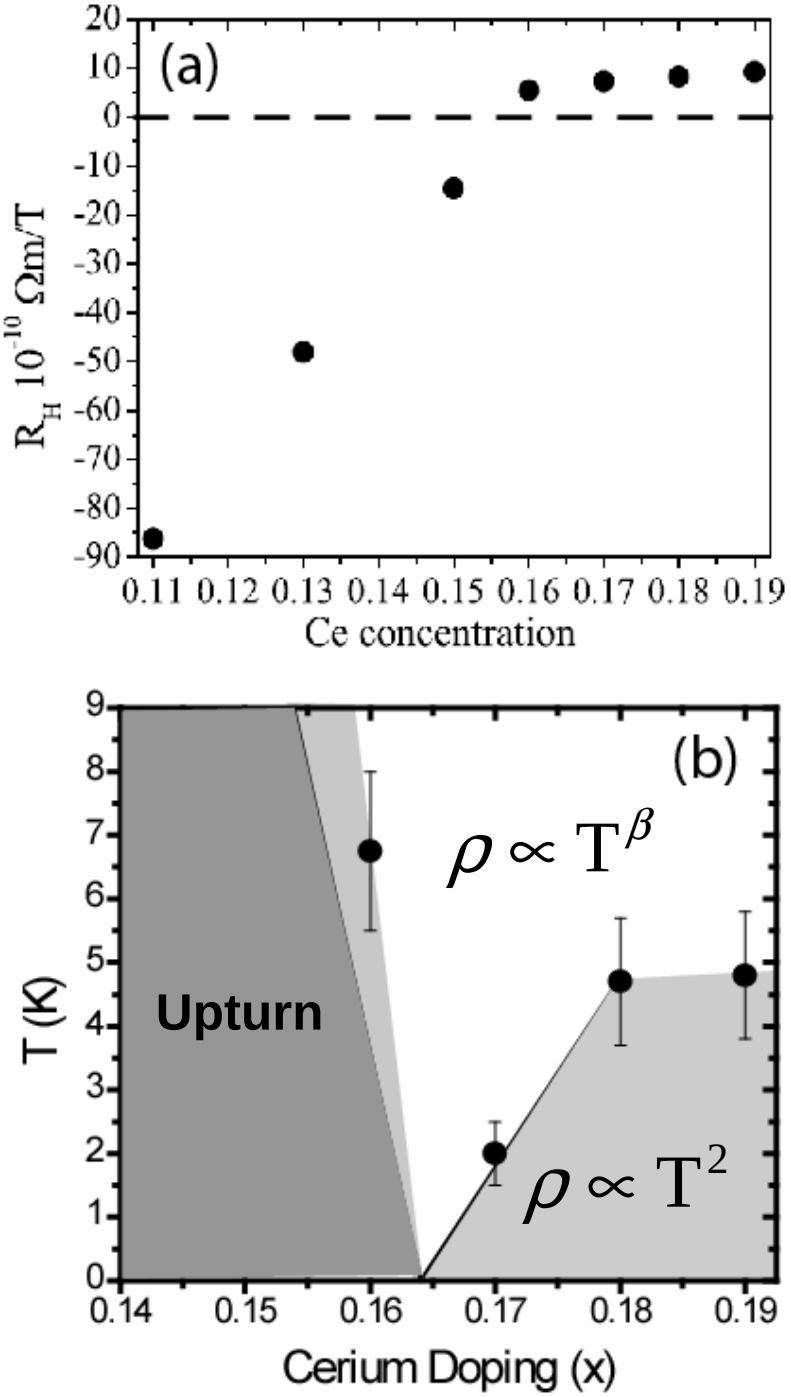

Figure 2.17: Hall and resistivity evidence for a quantum phase transition in $Pr_{2-x}Ce_xCuO_{4\pm\delta}$. (a) Hall measurements at $T = 0.35$ K, taken from Ref. [45]. A kink is clearly visible near $x \simeq 0.165$. (b) Temperature dependence of the resistivity for various dopings, adapted from Ref. [45]. The data points indicate where quadratic behavior is recovered at lower temperatures. This is reminiscent of the "funnel" region of a quantum critical point.

2.4.1 Motivation

The difficulty in using doping as a control parameter for a quantum phase transition lies in the inability to fine tune it. In the case of PCCO, each doping requires an entirely new source for sample growth. The error in the cerium concentration associated with each doping is on the order of $\Delta x \simeq 0.005$. Therefore, with the current methods of changing doping, it is difficult to finely tune the doping in order to more closely examine the proposed quantum phase transition. It is at this point where the original motivation for this part of the thesis developed. Adjusting the oxygen content could be a suitable solution to the doping problem [8]. Most studies on oxygen content and electronic transport in the electron-doped cuprates, however, did not focus on small changes of oxygen near the optimal oxygen content. It is not clear, then, if small changes in the oxygen result primarily in a change in effective doping. Therefore, **the motivation behind this part of the thesis lies in the determination of the feasibility of using oxygen as a dopant control in the vicinity of x_c, in the hopes of further exploring the quantum critical point.**

[8] Oxygen likes to have a -2 valence, so changing the oxygen should change the doping. This is explained in more detail in Sec 4.3.2.

Chapter 3

Transport - Theory

Treatments of Boltzmann transport theory can be found in the texts by Ziman [64], Marder [65], and Ashcroft & Mermin [66]. Treatments on the Hall effect (outside of Boltzmann transport) were adapted from Ref. [67]. Therefore, citations are not given throughout the majority of this chapter. In the cases where other sources are used, citations are given.

3.1 Boltzmann Transport

Boltzmann theory is a semi-classical phenomenological approach to describing the motion of particles and energy through matter. The theory addresses particles, which obey Hamilton's equations, but studies the evolution of their *distribution* subjected to various fields and gradients rather than attempting to describe each particle individually. The advantage of using distribution functions (functions which give the probability of a particle in a particular state) is that it allows one to describe macroscopic behavior without knowing *precisely* the microscopic information of each particle.

We start with a general continuity equation for a particle distribution function $f(x,t)$,

$$\frac{\partial f}{\partial t} = -\sum \frac{\partial}{\partial x_i} v_i(x) f(x,t). \tag{3.1}$$

The parameters x_i could be any parameter of interest, and $v(x)$ is the velocity of the particle. Here we will be using the particle position $\vec{r}$ and wave vector $\vec{k}$, and, utilizing Hamilton's equations ($\dot{r}_i = \frac{\partial \mathcal{H}}{\partial p_i}$, $\dot{p}_i = -\frac{\partial \mathcal{H}}{\partial r_i}$), Eq.(3.1) becomes

$$\dot{f}_{\vec{k}\vec{r}} = -\dot{\vec{r}} \cdot \frac{\partial}{\partial \vec{r}} f_{\vec{k}\vec{r}} - \dot{\vec{k}} \cdot \frac{\partial}{\partial \vec{k}} f_{\vec{k}\vec{r}}, \tag{3.2}$$

where $\frac{\partial f}{\partial t} = \dot{f}$. The first term on the right hand side represents the time rate of change from diffusive movement of carriers moving into and out of a region and can be re-expressed as

$$\dot{f}_{\vec{k}\vec{r}}|_{diff} = -\vec{v}_{\vec{k}} \cdot \frac{\partial}{\partial \vec{r}} f_{\vec{k}\vec{r}}, \tag{3.3}$$

where the vertical line is a label for the process, and $\vec{v}$ is the group velocity of the electron wave packet, i.e. an electron in state $\vec{k}$, defined by

$$\dot{\vec{r}} = \frac{1}{\hbar} \frac{\partial \mathcal{E}_k}{\partial \vec{k}} \equiv \vec{v}. \tag{3.4}$$

The second term in Eq.(3.2) represents changes due to electromagnetic fields, and by noting that the wave vector in an electromagnetic field changes at the rate $\dot{\vec{k}} = \frac{e}{\hbar}(\vec{E} + \vec{v}_{\vec{k}} \times \vec{B})$, this term can be expressed as

$$\dot{f}_{\vec{k}\vec{r}}|_{field} = -\frac{e}{\hbar} \left(\vec{E} + \vec{v}_{\vec{k}} \times \vec{B} \right) \cdot \frac{\partial}{\partial \vec{k}} f_{\vec{k}\vec{r}}. \tag{3.5}$$

From this point, Boltzmann introduced a general term to account for changes in the distribution due to scattering of the particles from one k-state to another. The

entire equation now reads

$$\dot{f}_{\vec{k}\vec{r}} = \dot{f}_{\vec{k}\vec{r}}|_{diff} + \dot{f}_{\vec{k}\vec{r}}|_{fields} + \dot{f}_{\vec{k}\vec{r}}|_{scattering} \, . \tag{3.6}$$

In the steady state, the left hand side of (3.6) is zero. This leaves us with the generalized Boltzmann equation

$$\dot{f}_{\vec{k}\vec{r}}|_{scattering} = \vec{v}_{\vec{k}} \cdot \frac{\partial}{\partial \vec{r}} f_{\vec{k}\vec{r}} + \frac{e}{\hbar}\left(\vec{E} + \vec{v}_{\vec{k}} \times \vec{B}\right) \cdot \frac{\partial}{\partial \vec{k}} f_{\vec{k}\vec{r}}. \tag{3.7}$$

The solution to this equation gives one the ability to calculate many of the electronic and thermal transport properties, such as the electrical conductivity and the Hall coefficient. Flexibility (as well as difficulty) exists in determining the form of the scattering term in (3.7).

A few basic assumptions are frequently made to simplify the Boltzmann equation. In the case where there are no external fields or thermal gradients, the system is in equilibrium and the scattering term, $\dot{f}^{\circ}_{\vec{k}\vec{r}}|_{scattering}$, is identically zero (the open circle denotes equilibrium). If we consider fields and thermal gradients that change the distribution only slightly, then we can view the right hand side as acting on $f^{\circ}_{\vec{k}\vec{r}}$ and represent the change in the equilibrium distribution function on the left hand side from an expansion of f to first order.

$$f_{\vec{k}\vec{r}} \approx f^{\circ}_{\vec{k}\vec{r}} + g_{\vec{k}\vec{r}} \tag{3.8}$$

$$\Rightarrow g_{\vec{k}\vec{r}} = f_{\vec{k}\vec{r}} - f^{\circ}_{\vec{k}\vec{r}} \tag{3.9}$$

A linear relationship is desirable since scattering *attempts* to return the system to an equilibrium state. Put another way, if there was no scattering term, the distribution of particles would continually change and the system would never reach a steady state even for infinitesimally small fields. We know this to be a false assertion from experience. Another assumption made is that the typical time scale for the processes described by the right hand side of (3.7) are slow compared to the time between scattering events. The small change in f then occurs over some timescale, τ, and the repeated process results in a steady state of the system. Boltzmann's equation now reads

$$\dot{f}_{\vec{k}\vec{r}}|_{scattering} \approx \frac{g_{\vec{k}\vec{r}}}{\tau} = \vec{v}_{\vec{k}} \cdot \frac{\partial}{\partial \vec{r}} f^{\circ}_{\vec{k}\vec{r}} + \frac{e}{\hbar}(\vec{E} + \vec{v}_{\vec{k}} \times \vec{B}) \cdot \frac{\partial}{\partial \vec{k}} f^{\circ}_{\vec{k}\vec{r}}. \tag{3.10}$$

Even though these assumptions create an easier equation to solve, problems arise in the effectiveness of τ to describe the scattering processes accurately. As equation (3.10) stands, τ is a constant (or at most dependent on $\vec{k}$ through the energy) and so represents scattering on a constant energy surface (elastic scattering events). Nevertheless, this equation is suitable for rough calculations of general transport dependencies.

3.2 Electronic Transport in Metals

Now that we have a means for determining the distribution function, let us put it to good use and determine the current density from an applied electric field.

We start with the relation

$$\vec{j} = -ne\vec{v} = \sigma\vec{E}, \tag{3.11}$$

and note that the carrier density contributing to current flow in the volume element $d\vec{k}$ is

$$n = \int \frac{g_{\vec{k}\vec{r}}}{4\pi^3} d\vec{k} \tag{3.12}$$

because only the change in the distribution function from its equilibrium value will produce a current. Using equations (3.4) and (3.10) with only an electric field present gives

$$\vec{j} = -e^2 \int \frac{d\vec{k}}{4\pi^3} \vec{v}\tau \left(\vec{E} \cdot \vec{v}\right) \frac{\partial f^\circ}{\partial \mathcal{E}} \tag{3.13}$$

where the distribution function does not depend on position (due to no thermal gradient) and the k-vector dependence is implied. The conductivity tensor can now be determined by using equation (3.11).

$$\sigma_{ij} \equiv \frac{j_i}{E_j} = -e^2 \int \frac{d\vec{k}}{4\pi^3} v_i \tau v_j \frac{\partial f^\circ}{\partial \mathcal{E}} \tag{3.14}$$

In materials of cubic (isotropic) symmetry, this expression is diagonal and reduces to the well known Drude model.

$$\sigma_{ii} = \frac{ne^2\tau}{m^*} \tag{3.15}$$

In the case of a tetragonal lattice, as in PCCO, the conductivity tensor is still diagonal with $\sigma_{ii} = \sigma_{jj} \neq \sigma_{kk}$. The resistivity tensor is just the inverse of the

conductivity tensor, and, for a diagonal matrix, this gives

$$\rho_{ii} = \sigma_{ii}^{-1} = \frac{m^*}{ne^2\tau} \tag{3.16}$$

3.2.1 Matthiessen's Rule

When several different types of scattering processes occur, the total scattering rate is just the sum of the rates from all the different processes.

$$\frac{1}{\tau} = \sum \frac{1}{\tau_i} \tag{3.17}$$

This is known as Matthiessen's rule. It is used to express the total resistivity as the linear sum of resistivities due to different scattering processes.

The resistance of a material can be influenced by many scattering processes. The electrons can scatter off of lattice vibrations (phonons), impurities/defects, other electrons, or anything which adequately alters the regular lattice potential. In the following sections, I will briefly mention a few of these processes and how they contribute to the total resistivity.

3.2.2 Impurity Scattering

In the limit of zero temperature, most of the processes mentioned above no longer contribute to the scattering of electrons. Impurities and defects are the exception. They primarily act as *elastic* scattering centers. They are temperature independent in that the number of defects does not change with temperature nor

do the phonons significantly change the effectiveness of its scattering cross section. Therefore, at low enough temperatures for impurity scattering to dominate, the resistivity tends towards a constant value (this is only correct for non-magnetic scattering). This value is called the residual resistivity, ρ_0. The resistivity in the case of elastic scattering (3.16) has already been determined from the Boltzmann equation (3.10) and we use this expression for ρ_0.

3.2.3 Electron-Phonon Scattering

Vibrations of the ions in the regular crystal lattice (phonons) can also provide a source of scattering. As electrons scatter with phonons, energy is exchanged in the range of $k_B T = h\nu$, provided that the appropriate k-space (for the electron) and phonon mode are accessible. Going back to the Boltzmann equation (3.7), it is necessary to consider a more detailed treatment for the scattering rate than what was previously done. An in-depth calculation can be found in Ref. [64]. Here I give the final result

$$\rho_{e-p} = \frac{3\pi\hbar\mathcal{Q}^6\mathcal{C}^2(0)}{4e^2 m N k_B \Theta \mathcal{R}^4 v_F^2}\left(\frac{T}{\Theta}\right)^5 \int_0^{\Theta/T} \frac{z^5 dz}{(e^z-1)(1-e^{-z})}. \tag{3.18}$$

where $\mathcal{Q}$ is the radius of the Debye zone, $\mathcal{C}(0)$ is the electron-phonon interaction energy, $\mathcal{R}$ is the reduced resistivity (dependent on the Fermi area and the number of electrons per atom), and Θ is the Debye temperature. All other symbols follow the standard nomenclature. The temperature dependence of ρ_{e-p} well above the Debye

temperature ($T \gg \Theta$) is linear.

$$\rho_{e-p} \sim \rho_{\Theta} \left(\frac{T}{\Theta} \right), \tag{3.19}$$

where ρ_{Θ} incorporates all of the prefactors in equation (3.18) which are not explicitly temperature dependent. Well below Θ ($T \leq \frac{\Theta}{50}$) [68], we find [64]

$$\rho_{e-p} \sim 500\rho_{\Theta} \left(\frac{T}{\Theta} \right)^5. \tag{3.20}$$

These processes account for only normal processes. Umklapp processes contribute an additional term [64]

$$\rho_{e-p,U} \sim e^{\frac{-\Theta}{T}}. \tag{3.21}$$

3.2.4 Electron-Electron Scattering

In addition to scattering from the lattice, electrons can scatter off each other. At nonzero temperatures, the distribution function is only fractionally filled at the Fermi energy, with some of the states below $\mathcal{E}_F$ occupying states above $\mathcal{E}_F$. This partial filling, or thermal smearing of the distribution function, only varies appreciably within $k_B T$ about the Fermi energy. Therefore, only electron states within $k_B T$ of $\mathcal{E}_F$ can participate in conduction. As the temperature increases, so does the number of states accessible to electrons. As the number of energy states increases with temperature, then so must the probability of scattering into another state. Since the state of the electron must fulfill the above criteria, both before and after

the scattering, we see that the fraction of accessible processes goes as $(\frac{k_B T}{\mathcal{E}_F})^2$. In a very general sense, the scattering rate from electron-electron scattering should go as T^2.

Lawrence *et al.* [69] calculated from the Boltzmann equation the electron-electron scattering, in the presence of impurity scattering, for a simple metal. They find

$$\rho_{e-e} = \frac{2\pi^2}{3}\left(\frac{m^*}{ne^2\tau_0}\right)\Delta\left(1 - \frac{\Delta}{11.4 + \Delta + 5\beta}\right), \tag{3.22}$$

where Δ represents the relative amount of Umklapp scattering, $\beta = \frac{2\tau_0}{\pi^2\tau_{imp}}$ and represents the relative amount of impurities, τ_{imp} is the relaxation time due to impurities (identical to τ assumed in the Boltzmann section), and $\tau_0 \propto T^{-2}$. We see that ρ_{e-e} has primarily a T^2 temperature dependence. As is evident from (3.22), only Umklapp scattering contributes to ρ_{e-e}. Baber [70] presents a simple explanation for this deduction based on interband scattering. For normal processes (as for e-e scattering between identical particles), momentum is conserved. Since the current relates to the momentum, current is also conserved. For Umklapp processes (as for scattering between dissimilar particles), total momentum is conserved but the current is not. This is due to the different properties of the particles. Even though the change in momentum of one particle corresponds to the change in momentum of the other, the change in current is not equivalent. Even though Umklapp processes are less likely to occur, their effect on the conduction dominates.

There are other calculations for ρ_{e-e}, but they all yield the same temperature dependence and this is due mostly to the argument presented in the beginning of

this section. It is also worth noting that most of these calculations are intended to model simple metals. The temperature at which we expect to see a dominant contribution from e-e scattering is $\sim$ 1 K. In addition, the more complicated the Fermi surface, the more the *magnitude* of ρ_{e-e} changes. For example a system in which scattering between two bands occurs, the magnitude of the electron-electron term increases as the properties of the two bands differ from one another.

3.3 Electronic Transport in Magnetic Fields

3.3.1 Magnetoresistance

The previous sections evaluated the Boltzmann equation (3.10) with only an electric field present. Here we consider the effects of a magnetic field in conjunction with an electric field. The effect of the magnetic field on the longitudinal resistivity (i.e. $\rho_{ii}(B)$) is called the "magnetoresistance" of the system. Equation (3.10) now reads

$$\frac{g_{\vec{k}}}{\tau} = \frac{e}{\hbar}\left(\vec{E} + \vec{v}_{\vec{k}} \times \vec{B}\right) \cdot \frac{\partial}{\partial \vec{k}} f^{\circ}_{\vec{k}}. \tag{3.23}$$

We need to expand the distribution function in the magnetic field term because $\frac{\partial f^{\circ}}{\partial \vec{k}}$ $= \hbar \vec{v} \frac{\partial f^{\circ}}{\partial \mathcal{E}}$ and the magnetic term yields zero. The next term in the expansion of f (3.8), g, is used. Additionally, we represent the equation as a function of the group velocity, rather than the k-vector due to the above result. The end result is that

(3.23) is rewritten as

$$\frac{g(\vec{v})}{\tau} = -\vec{v} \cdot e\vec{E}\frac{\partial f^{\circ}}{\partial \mathcal{E}} - \frac{e}{m^*}\vec{v} \cdot \left(\vec{B} \times \frac{\partial g(\vec{v})}{\partial \vec{v}}\right), \tag{3.24}$$

with $\frac{1}{m^*} \equiv \frac{\partial \vec{v}}{\hbar \partial k}$. A solution for g is

$$g(\vec{v}) = -\tau e \frac{\partial f^{\circ}}{\partial \mathcal{E}}\vec{v} \cdot \frac{[\vec{E} + \alpha^2 \vec{B}\vec{B} \cdot \vec{E} - \alpha \vec{B} \times \vec{E}]}{1 + \alpha^2 B^2}, \tag{3.25}$$

where $\alpha = \frac{e\tau}{m^*}$. Upon inspection of equation (3.25), we see that a magnetic field causes changes in the distribution function along $\vec{E}$ and $\vec{B}$, and perpendicular to both. With this relation for the change in the distribution function, we can calculate the conductivity (or resistivity) tensor according to equation (3.11). Plugging this in, we see that the conductivity tensor contains an integral which is independent of the direction of $\vec{j}$, thus common to all the tensor components. Taking $\vec{E}$ perpendicular to $\vec{B}$, we can write a simple expression for the current density.

$$\vec{j} = \sigma_{\vec{E}}\vec{E} + \sigma_{\vec{B}}(\vec{B} \times \vec{E}), \tag{3.26}$$

where $\sigma_{\vec{E}}$ is the tensor component due to $\vec{E}$ and $\sigma_{\vec{B}}$ is the component due to $(\vec{B} \times \vec{E})$. For clarity, these terms are

$$\sigma_{\vec{E}} = A\frac{1}{1 + \alpha^2 B^2}; \sigma_{\vec{B}} = A\frac{\alpha}{1 + \alpha^2 B^2}, \tag{3.27}$$

where $A = -\frac{1}{3}\int v^2 e^2 \tau(\partial f^\circ/\partial \mathcal{E})\mathrm{d}\vec{k}$ is field independent and shared between the two terms and α is the same as previously defined. From (3.26) we can calculate the conductivity and resistivity tensors, and for simplicity we consider the case where $\vec{E}$ is in the xy-plane and $\vec{B}$ is in the z-direction.

$$\sigma_{ij} = \begin{pmatrix} \sigma_E & -\sigma_B B \\ \sigma_B B & \sigma_E \end{pmatrix} \tag{3.28}$$

$$\rho_{ij} = \sigma_{ij}^{-1} = \frac{1}{\sigma_E^2 + \sigma_B^2 B^2} \begin{pmatrix} \sigma_E & \sigma_B B \\ -\sigma_B B & \sigma_E \end{pmatrix} \tag{3.29}$$

It is straight forward to see that the diagonal components, which relate the current density to the electric field driving that current, is independent of field. The off-diagonal components are anti-symmetric with field and give information about the Hall effect (more detail later in this chapter).

$$\rho_{ii} = \frac{1}{A} = \frac{m^*}{ne^2\tau}. \tag{3.30}$$

This result is identical to the Drude model and shows that a simple metal should have no magnetoresistance. This derivation, however, is assuming a very simple metal, and zero magnetoresistance is not frequently observed. Typically, a B^2 dependence is observed and the easiest way to see how this comes about is from a two-conduction-band model (from here on out, called a two-band model). The two bands are typically thought of as holes and electrons, however the "bands" could refer to a

single sign carrier with parameters which differ within the band (for example, the effective mass may be different in certain regions of the band).

Two-Band Model

Some care needs to be taken with the two-band model. The model frequently quoted in the literature contains very basic assumptions that simplify electron behavior beyond the assumptions made in Boltzmann transport theory. It relies on the Drude model for conductivity and so incorporates an isotropic scattering rate on a spherical Fermi surface (whereas ρ_{e-e} & ρ_{e-p} incorporate anisotropic scattering). The Drude model does not predict temperature dependencies. These are usually manually inserted into the scattering rate. This could cause some difficulty in determining the actual resistivity for the individual bands, as both the elastic (T-indep.) and inelastic (T-dep.) terms need to be taken into account. For instance, one band may have one type of temperature dependence, while the second band may have another. The joining of these two bands *could* result in a third temperature dependence. In this sense, this simple two-band model tends to amplify difficulties. Additionally, it expands the parameter space to the extent that quantitative, experimental determination of the parameters is very difficult. The last important note is that this model *does not* incorporate interband transitions. The two bands operate independently of one another. A better method may be to incorporate different fermi surfaces (and *possibly* two bands) in the Boltzmann transport equations. Despite the difficulties with the two-band model, it can still

yield a qualitative explanation for the behavior of some transport properties which can not be accounted for within simple Boltzmann transport. All in all, this model demonstrates quite nicely how a simple model can take on complex characteristics upon the addition of a second conduction band.

The model starts with the force equation for a charged particle in an electric and magnetic field

$$\frac{d\vec{p}}{dt} = -q\vec{E} - q(\vec{v} \times \vec{B}) - \frac{\vec{p}}{\tau}, \tag{3.31}$$

where q denotes the charge of the particles in the band (-e for electrons and +e for holes), $\vec{p}$ is the particle momentum, and the last term is the damping term (equivalent to the scattering term in the Boltzmann theory). Each band has an equivalent equation, and their conductivities add linearly ($\sigma = \sum_i n_i$). Rather than explicitly derive the relation, I will outline the steps for the most basic model (i.e. both bands are identical except for the carrier concentration). In a magnetic field, the Lorentz force establishes a real-space separation (imbalance) of charges which are subject to an external driving electric field ($\vec{B} \perp \vec{E}$). This separation establishes a transverse electric field, which counteracts the Lorentz force. Thus, in steady state, the force equation is identically zero ($\frac{d\vec{p}}{dt} = 0$) and the current along the transverse electric field vanishes (if we fix the x-direction as the driven current direction, then the current in the y-direction vanishes). With this as the basic boundary condition, we solve equation (3.31) for the velocities of the particles (again, assuming the same orientation of the fields as in the previous section). From there we calculate the current density ($j_x = \sum_i n_i q v_{i,x}$), which gives the resistivity in applied electric and

magnetic fields $\rho_{xx}(B) = \frac{E_x}{j_x}$. The magnetoresistance is given by

$$\frac{\Delta\rho}{\rho} = \frac{\rho(B) - \rho(0)}{\rho(0)} = (\omega_c\tau)^2 \frac{1 - a^2}{1 + a^2(\omega_c\tau)^2}, \tag{3.32}$$

where $a = \frac{n_1 - n_2}{n_1 + n_2}$ is the effective carrier concentration, and $\omega_c = \frac{qB}{m^*}$ is the cyclotron frequency. From this expression, we can clearly see that (for $n_1 = n_2$) the magnetoresistance goes as B^2. As a approaches either band's carrier concentration ($a \to \pm 1$), the magnetoresistance vanishes.

A more general expression, where none of the parameters are considered the same between the bands, can be easily derived from (3.31). From this equation we construct the resistivity tensor for a single band (restricting $\vec{E}$ to the xy-plane and $\vec{B}$ to the z-direction for simplicity) using the relation $\vec{j} = nq\vec{v}$:

$$\rho_{ij} = \begin{pmatrix} \frac{1}{\sigma_0} & -\frac{\omega_c\tau}{\sigma_0} \\ \frac{\omega_c\tau}{\sigma_0} & \frac{1}{\sigma_0} \end{pmatrix} \tag{3.33}$$

where $\sigma_0 = \frac{nq^2\tau}{m^*}$. Since conductivities add in series, we invert this matrix (to obtain the conductivity matrix), and add the conductivities of the two bands. Inverting the resulting matrix gives back the resistivity tensor for the two bands.

$$\rho_{ij} = \frac{1}{(C_1 + C_2)^2 + (C_1\gamma_1 + C_2\gamma_2)^2} \begin{pmatrix} (C_1 + C_2) & -(C_1\gamma_1 + C_2\gamma_2) \\ (C_1\gamma_1 + C_2\gamma_2) & (C_1 + C_2) \end{pmatrix} \tag{3.34}$$

where $C_i = \frac{\sigma_i}{(1+\gamma_i^2)}$, $\gamma_i = \omega_{c,i}\tau_i$, and $\sigma_i = \sigma_0$ with i as the band index. The diagonal

components give the resistivity along the direction of the applied electric field.

$$\rho_{ii} = \frac{C_1 + C_2}{(C_1 + C_2)^2 + (C_1\gamma_1 + C_2\gamma_2)^2} \tag{3.35}$$

Although hidden in γ, factors of H^2 are in the numerator and denominator. The overall behavior of the magnetoresistance has a field dependence for the general two-band model.

3.3.2 Hall Effect

As mentioned in the previous section, when a current is subject to a perpendicular magnetic field, the Lorentz force deflects charge carriers and creates a build up of charge at the boundary of the specimen. This build-up of charge creates an electric field which is transverse to the driven current. In steady state, this transverse field cancels the Lorentz force and a potential drop is established across the sample (perpendicular to the current flow, see Fig. 3.1). This deflection and build-up of charge is commonly called the Hall effect. Because this electric field (Hall field) is perpendicular to the current, the relationship between the two is just the off-diagonal components of the resistivity tensor (3.33). The Hall coefficient (R_H) is the constant of proportionality between these off-diagonal components and the magnetic field.

$$\rho_{ij} = \frac{E_j}{j_i} \tag{3.36}$$

$$\frac{d\rho_{ij}}{dB} = R_H \tag{3.37}$$

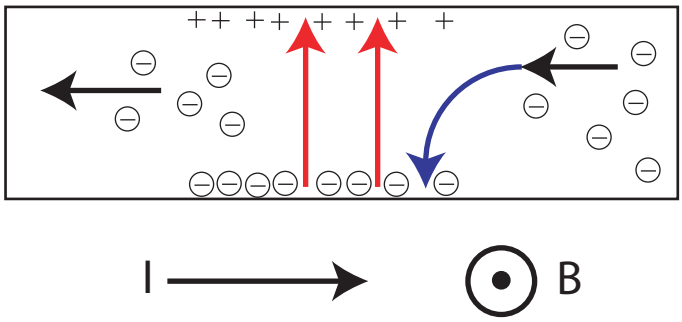

Figure 3.1: Schematic of the Hall effect for electrons. Current flows from the left to right (electrons move oppositely) and the magnetic field is out of the page. The blue arrow represents the Lorentz force felt by the electrons ($q\vec{v} \times \vec{B}$). The red arrows represent the electric force established from the charge imbalance ($q\vec{E}$). In steady state, these two forces sum to provide zero total force on the electrons, and a Hall voltage is established transverse to the current. For positive carriers (holes), the deflection is to the same side of the sample creating an opposite Hall voltage (from the electrons). Therefore, the sign of the Hall voltage gives the sign of the primary charge carrier.

From (3.33), the Hall coefficient in the simple Drude model has the relation:

$$R_H = \frac{1}{nq} \tag{3.38}$$

Thus, R_H yields the carrier concentration in addition to the sign of the carriers.

The same result can be calculated from the Boltzmann equation and most of the work has been done in the previous section for the magnetoresistance. The off-diagonal components of (3.29) give the Hall resistivity. Again, we find for the Hall coefficient:

$$R_H = \frac{\alpha}{A} = \frac{q\tau}{m^*\sigma_0} = \frac{1}{nq} \tag{3.39}$$

where all variables retain their previous definitions. A more general result requires a more general evaluation of the integral in j from the Boltmann equations. This

results in a Hall coefficient which depends on the density of states of the Fermi surface. The more complicated the Fermi surface, the less the Hall coefficient resembles (3.39).

Two-Band Hall Effect

Most of the work has already been done in the two-band section for the magnetoresistance. Again we consider the case where $n_1 \neq n_2$ and all other parameters are the same between the two bands. The derivation follows the same steps outlined in the previous section, and the result is:

$$\frac{E_y}{Bj_x} = R_H = \frac{1}{n|e|} a \frac{[1 + (\omega_c \tau)^2]}{[1 + a^2(\omega_c \tau)^2]} \tag{3.40}$$

where all symbols again retain their previous definitions.

For a more general result, we go back to (3.34) and look at the off-diagonal components.

$$R_H = \frac{\rho_{ij}}{B} = \frac{1}{B} \frac{(C_1\gamma_1 + C_2\gamma_2)}{(C_1 + C_2)^2 + (C_1\gamma_1 + C_2\gamma_2)^2} \tag{3.41}$$

In the low field limit (i.e. $\gamma_i \ll 1$), equation 3.41 reduces to:

$$R_H = \frac{1}{\sigma}[\frac{\sigma_1 q_1 \tau_1}{m_1^*} + \frac{\sigma_2 q_2 \tau_2}{m_2^*}] \tag{3.42}$$

where $\sigma = \sigma_1 + \sigma_2$.

Geometric Interpretations of the Hall Effect

It is worth noting here that interesting work has been done to simplify relations for the Hall effect. The integrals in the Boltzmann equation contain parameters which not only depend on the Fermi surface curvature (as in the effective mass) but also depend on the energy dispersion of the particles (such as v_F). For complicated Fermi surfaces, these integrals are difficult at best.

Ong [71] derived a relation for the Hall conductivity which relies solely on the geometry of the Fermi surface. The basic idea is that as the wave vector ($\vec{k}$) circumscribes the Fermi surface, the k-dependent mean free path, $\vec{l}(\vec{k})$, sweeps out an effective area. The Hall conductivity, σ_{xy}, is related to the amount of magnetic induction contained in this effective area.

$$\sigma_{xy} = \frac{e^2 A_l}{h\pi l_B^2} \tag{3.43}$$

where $l_B = \sqrt{\frac{\hbar}{eB}}$ is the magnetic length, A_l is the area swept out by $\vec{l}(\vec{k})$, and this expression is valid in two dimensions. Lin *et al.* [38] applied this formalism to determine R_H for PCCO as a function of doping in the limit $T \to 0$. Their results were roughly consistent with the trend observed experimentally.

3.4 Disorder in Superconductors

Any change in the material can, in fact, be viewed as disorder. When changing the lattice constituents (as in cation substitution) several effects can be introduced,

either positive or negative or even both (positive in one property but negative in another). Disorder is almost always associated with the negative aspects. Much of this is discussed in the review article by Lee *et al.* [72], and will not be reviewed here outside of what has already been mentioned. Where needed, references are given throughout the text. Rather, I will focus on disorder in superconductors and give a very brief overview.

The suppression of the superconducting transition temperature (T_c) due to impurities has long been used as a tool to probe the superconducting pairing symmetry (the amplitude of the superconducting gap, as well as the phase). Anderson [73] showed that low concentrations of nonmagnetic impurities have no effect on T_c for superconductors with an isotropic (in k-space, both amplitude and phase) s-wave pairing symmetry. The reason is that Cooper pairs are formed from time-reversed eigenstates. The nonmagnetic impurities do not break the time-reversal symmetry. Magnetic impurities, however, do break the time-reversal symmetry even for low concentrations. This breaks the Cooper pairs and suppresses T_c. Anisotropic (for example d-wave[1]) pairing symmetries are more sensitive to nonmagnetic impurities than is the s-wave symmetry. The reason is that the phase of the d-wave pairing symmetry can change sign as the Fermi wave vector (k_F) of the pair changes. As the pair is scattered (i.e., a change in k_F) by nonmagnetic impurities, the time reversal symmetry is broken more easily, due to the change in sign of the phase, and T_c is suppressed. This is primarily what researchers look for when studying the

[1]Most superconductors fall into the category of s or d-wave pairing symmetries. Therefore, I only mention these.

suppression of T_c due to magnetic and nonmagnetic impurities, i.e., whether T_c is suppressed and what it tells us about the pairing symmetry of the Cooper pairs.

Calculations for the suppression of T_c due to magnetic impurities were given by Abrikosov and Gor'kov [74] for isotropic pairing symmetries (this is the well-known AG theory). Openov [75] later expanded on the AG theory to include non-magnetic impurities, as well as anisotropic pairing symmetries, and even mixing of isotropic and anisotropic pairing symmetries (equation 48 in Ref. [75]). The paper by Openov [75] has an extensive list of references for further information.

Chapter 4

Transport in the Electron-doped Cuprates

While electronic transport is relatively straightforward to measure, the results have been difficult to interpret. This is due, in part, to the rich phase diagram of the cuprates resulting in a lack of adequate theories. This chapter is intended to serve as a background for *some* of the current concerns and problems. I will give a brief overview of the resistivity, magnetoresistance, and Hall effect in the electron-doped cuprate PCCO (some of which has been briefly talked about in Ch. 2), with a focus on oxygen non-stoichiometry and additional disorder effects in these properties. In regards to oxygen and disorder, NCCO as well as hole-doped cuprates will also be discussed.

4.1 Resistivity

The resistivity in the electron-doped cuprates shows a significant anisotropy between the c axis and the ab plane. The ratio $\frac{\rho_c}{\rho_{ab}}$ is $\sim 10^4$ and is indicative of a quasi-2D system, with the conduction occurring predominantly in the CuO_2 plane. In the following discussion, the focus will be on ρ_{ab}.

The ab-plane resistivity of the electron-doped cuprates shows a modified quadratic temperature dependence over a wide temperature range [76] and cerium-doping range (Fig. 4.1). The modification is logarithmic and the temperature dependent

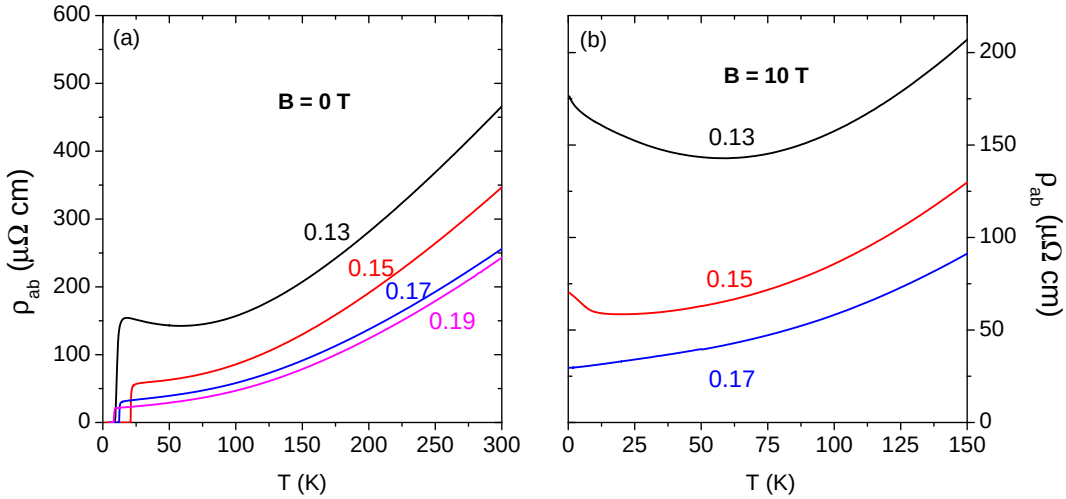

Figure 4.1: ρ_{ab} versus temperature for $Pr_{2-x}Ce_xCuO_{4\pm\delta}$ taken from Ref. [45]. (a) Resistivity in zero applied magnetic field for x=0.13, 0.15, 0.17, 0.19 (b) Resistivity in 10 T magnetic induction. Notice the upturn shifts towards lower temperatures, eventually disappearing, as the cerium content increases.

resistivity fits the form

$$\rho(T) = A_{ee}(\frac{T}{T_F})^2 ln(\frac{T_F}{T}). \tag{4.1}$$

where A_{ee} is a constant, and T_F if the Fermi temperature. This deviation from quadratic behavior occurs at higher temperatures ($T > 200$ K) and is consistent with electron-electron scattering within a 2D Fermi liquid model [51]. Deviations from a T^2 behavior could also arise in a disordered two-band model, where one band has a linear dependence and the second band is quadratic in temperature [53]. However, the magnitude of the temperature dependent part of the resistivity is experimentally much larger than calculations predict [51]. In this regard, it is still not clear why this material shows a nearly T^2 dependence.

The parent compound of PCCO, Pr_2CuO_4, is a Mott-like insulator and becomes metallic upon cerium doping. This is reflected in the resistivity. At low

dopings, the resistivity goes through a minimum and crosses over from a metallic behavior ($\frac{d\rho}{dT} > 0$) to an insulatorlike behavior ($\frac{d\rho}{dT} < 0$) as the temperature decreases. The temperature of this crossover (T_{min}) decreases as the doping increases. For the superconducting compositions ($x \geq 0.14$), the upturn is hidden by the superconducting state, and a magnetic field ($H > H_{c2}$) is needed to quench superconductivity and observe the normal-state resistivity. In the normal state, the occurrence of an upturn persists slightly beyond optimal doping [53] [Fig. 2.9(c)]. Dopings larger than $x \simeq 0.165$ show no upturn[1] and are metallic over the entire temperature range. The temperature dependence of the resistivity upturn is sublogarithmic [53] and, as of yet, unexplained.

The magnetoresistance (MR) in PCCO has several interesting properties. At higher temperatures ($T \gg T_c$), the MR is positive and follows a nearly B^2 dependence. While this behavior is theoretically unusual outside of a two-band model, the B^2 dependence is typically observed in (non-magnetic) materials with MR. For low temperatures, it is negative and seems to follow the behavior predicted by weak localization [77]. Sekitani *et al.* [78], on the other hand, attribute the negative MR to Kondo scattering off of the Cu^{2+} spins. Dagan *et al.* [79] were able to show that there are two distinct components to the MR: an orbital (anisotropic) component, and a spin (isotropic) component. They subsequently show that the spin component vanishes for $x \geq 0.16$. Interestingly enough, the disappearance coincides with the doping at which the upturn in ρ_{ab} (mentioned above) disappears ($T_{min} \rightarrow 0$).

[1] At very low temperatures, a small upturn in ρ (small relative to the upturn in the underdoped samples) exists for $x \geq 0.16$ which is possibly due to disorder from oxygen treatments.

Also, as the temperature increases, the spin component vanishes and this coincides (roughly) with T_{min}. The conclusion one can draw from this is that the upturn in ρ_{ab} is related to the spin MR [79]. This, however, is not a solved issue, and, like the resistivity, is still being investigated.

4.2 Hall Effect

The Hall coefficient in PCCO (and NCCO as well) shows a strong temperature dependence for all dopings [Fig. 2.10(b)]. Considering the values at low temperature relative to room temperature, R_H changes by factors ($\simeq 3-6$) in the doping range $0.11 \leq x \leq 0.19$. The largest change is in the underdoped samples ($x = 0.13, 0.14$).

In addition to the temperature dependence, the Hall coefficient has a doping dependence which evolves from negative values (for $x \leq 0.15$) to positive values (for $x \geq 0.16$) at low temperatures. Within a narrow doping range, $0.16 \leq x \leq 0.18$, R_H even changes sign with temperature [Fig. 2.10(b)]. At higher dopings ($x \geq 0.19$), R_H is purely positive. These are interesting results since cerium doping donates electrons into the conduction band; upon increased electron doping, R_H evolves into a hole-like material. A simple, single carrier Drude model cannot account for the above observation and so the change in the sign of R_H (as well as the temperature dependence) is interpreted as evidence for a two-band model [41,59,80,81]. Peculiar behavior in other transport properties also support the idea of two conduction bands: Positive MR (as mentioned above), a change in the sign of the thermoelectric power with oxygen content [59] and temperature [82], and an anomalous normal-state

Nernst signal [59, 82] all lend additional credence to this claim. Additionally, angle resolved photoemission spectroscopy (ARPES) measurements show that both hole and electron pockets are present at the Fermi surface in optimally doped NCCO [60] (Fig. 2.12). One group [83] quantitatively analyzed NCCO using a two-band model and they show that it can explain their data quite nicely for ρ and R_H, but not as well for the other transport coefficients.

As one may expect, the carrier concentration obtained from $R_H(= 1/ne)$ in the single-band model does not correlate well with the cerium doping. Lin *et al.* [38] demonstrated, at low temperatures, that low dopings follow $n \approx x$ (electronlike occupancy) while high dopings follow $n \approx (1 - x)$ (holelike occupancy), where n is the carrier concentration. The intermediate dopings ($0.12 \leq x \leq 0.16$) do not quite follow either of these behaviors. In the high and low doping range, the experimental results only qualitatively follow the theoretical predictions. One reason proposed by Lin is that the effective doping level in the samples is not precisely known (i.e. the cerium content alone does not determine the effective doping level).

4.3 Oxygen Non-stoichiometry

4.3.1 Hole-doped Cuprates

Conventional carrier doping is achieved by substituting a cation of one valence for a cation of a different valence. For example, in PCCO, Ce^{4+} partially replaces Pr^{3+} introducing additional electrons into the conduction band. Similarly in LSCO, La^{3+} is partially replaced with Sr^{2+} thereby introducing extra holes. In quite a

few of the p-type cuprates, however, superconductivity occurs by carrier doping the insulating parent compound through *oxygen non-stoichiometry*. Since oxygen has a strong affinity for acquiring two additional electrons (giving it a valence of O^{2-}), adjusting the oxygen content will also adjust the number of free carriers. This change in the oxygen content can be viewed as either electron or hole doping, depending on type of free carrier and how you wish to look at the system. By adding oxygen, the number of free electrons decreases, or the number of holes increases. Removing oxygen does just the opposite.

The most well known of the oxygen doped p-type cuprates, is the Y-123 compound $YBa_2Cu_3O_{7-\delta}$ (YBCO), where optimal hole doping is achieved at $\delta \simeq 0.09$ [84]. Another example is the bismuth-based compounds (most notably $Bi_2Sr_2CuO_{6+\delta}$ and $Bi_2Sr_2CaCu_2O_{8+\delta}$), where doping is achieved by adding oxygen. More examples involve several of the Hg- and Tl-based cuprates as well as the rest of the RE-123 cuprates of which YBCO belongs (RE stands for Rare Earth; RE = Y, Nd, Gd, Tm, Yb, Lu).

The p-type compliment of PCCO, LSCO, is an interesting case. The parent compound La_2CuO_4 (LCO) can become superconducting either by partially replacing La^{3+} with Sr^{2+} (i.e., $La_{2-x}Sr_xCuO_4$) [85] or by incorporating extra oxygen (i.e., $La_2CuO_{4+\delta}$) [86–89]. For oxygen-doped LCO, phase separation occurs in the low oxygen doping regime ($\delta \simeq 0.04$), where the two phases are a non-superconducting stoichiometric LCO and a superconducting oxygen-rich phase. At high enough dopings ($\delta \simeq 0.08$)[2], the material becomes a single-phase superconductor [89] with a

[2]The values for δ quoted in the literature for LCO are obtained from thermogravimetric analysis

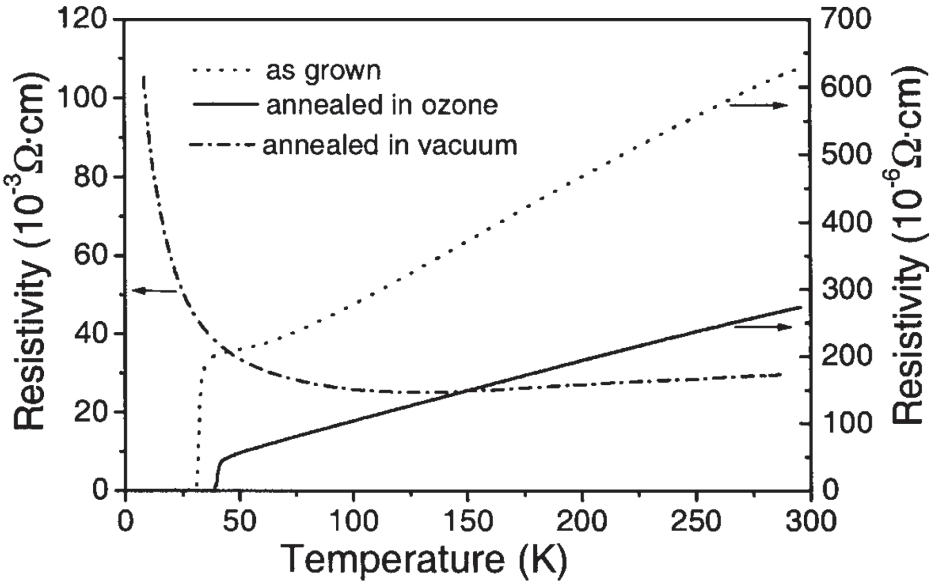

Figure 4.2: ρ_{ab} vs Temperature for $La_2CuO_{4+\delta}$ thin films with different values of δ, taken from Ref. [88]. The vacuum annealed film has the least oxygen, while the ozone annealed film has the most oxygen. Notice the nearly linear temperature dependence of the ozone-annealed film, comparable to optimally Sr-doped LSCO.

$T_c \simeq 40$ K (Fig. 4.2).

Just as in LSCO (for $x \leq 0.16$), T_c increases as the oxygen content increases in LCO. The general consensus is that the added oxygen contributes holes to the CuO_2 plane, which results in superconductivity. Why is it a consensus? Difficulties arise in directly (and quantitatively) relating the oxygen content to an effective doping. This is due to the difficulty in accurately determining the actual oxygen content. Additionally, the fact that the Hall coefficient (R_H) is temperature dependent does not allow for a reliable determination[3] of the carrier density from those measurements. Instead, some groups compare R_H, the thermoelectric power, and T_c of

and iodometric titration, and do not quite agree with each other. Given the difficulty in determining *precisely* the oxygen content, the values of δ should be considered roughly correct. The important information is the trends observed as the oxygen content changes.

[3] R_H does not give a reliable determination of the carrier concentration (n) in the sense that it is unclear how a temperature dependent R_H relates to n in a simple one-band model when the charge carriers are not activated.

different cuprates with that of stoichiometric LSCO (where x is identical to the hole concentration p) [57]. However, I am unaware of any study to determine the change in the carrier concentration of oxygenated LCO. Therefore, since T_c increases with oxygen just as it increases in LSCO with Sr doping, the changes are attributed to a change in the effective doping. Also, the resistivity of oxygen-doped LCO mimics that of LSCO, at least in the region of oxygen which shows an increasing T_c with increasing oxygen. As the oxygen content increases, LCO becomes metallic with a linear ρ_{ab} for T_c's near 40 K. I am unaware of any groups reporting on LCO with oxygen doping that report a dome shape for T_c versus oxygen, i.e., T_c decreases again beyond some optimal oxygen content. At this point it is speculation as to whether or not the resistivity would behave similarly to the other oxygen-doped p-type cuprates, by which I mean that T_c and ρ_{ab} would decrease beyond some optimal doping.

One question begs to be asked: What happens to the disorder as the material moves further away from stoichiometry. This will be addressed in a later section.

4.3.2 Electron-doped Cuprates

The n-type cuprates in the T' structure are a bit different from the p-type cuprates, in particular superconductivity can only occur in the former through a combination of cation substitution *and* oxygen reduction [90]. Either process alone is insufficient. Because of this peculiar property, relative to the other cuprates, it is possible that oxygen reduction plays a more complex role than in the p-type

cuprates. Again I will focus on the resistivity, magnetoresistance, and Hall measurements under various oxygen contents in NCCO and PCCO, and present several proposed explanations for the necessity for oxygen reduction.

In optimally doped NCCO ($x \simeq 0.15$) thin films [81] and single crystals [91], Jiang *et al.* found that oxygen reduction significantly affects ρ_{ab}. In line with other reports [92], the oxygenated samples show an insulator-like behavior, which develops a metallic behavior at higher temperatures as oxygen is removed. The boundary between the metallic high-T region and the insulating low-T region (the minimum in the resistivity) shifts towards lower temperatures as more oxygen is removed. A decrease in the residual resistivity is also apparent. Superconductivity appears and T_c increases, is a maximum at some given reduced oxygen content, and then decreases for higher levels of oxygen reduction [Fig. 4.4(a)]. These trends are reminiscent of optimally reduced cerium-doped samples as the cerium content increases. A dramatic difference in ρ_{ab} occurs when oxygen is reduced beyond the optimal content: The resistivity starts increasing *and* the temperature dependence changes [Fig. 4.3 and Fig. 4.4(a)]. This starkly contrasts with the cerium-doped samples where the resistivity continually decreases beyond optimal doping (Fig. 4.1).

Similarly, the magnetoresistance in NCCO ($x \simeq 0.15$) changes with the oxygen content [Fig. 4.4(b)]. At a temperature of 60 K, far from the superconducting transition, fully oxygenated samples show a negative MR. As the oxygen content decreases, a positive B^2 MR develops, the magnitude of which is a maximum at the same oxygen content as the maximum T_c. As the oxygen is further reduced, the magnitude of the MR decreases and eventually becomes negative again.

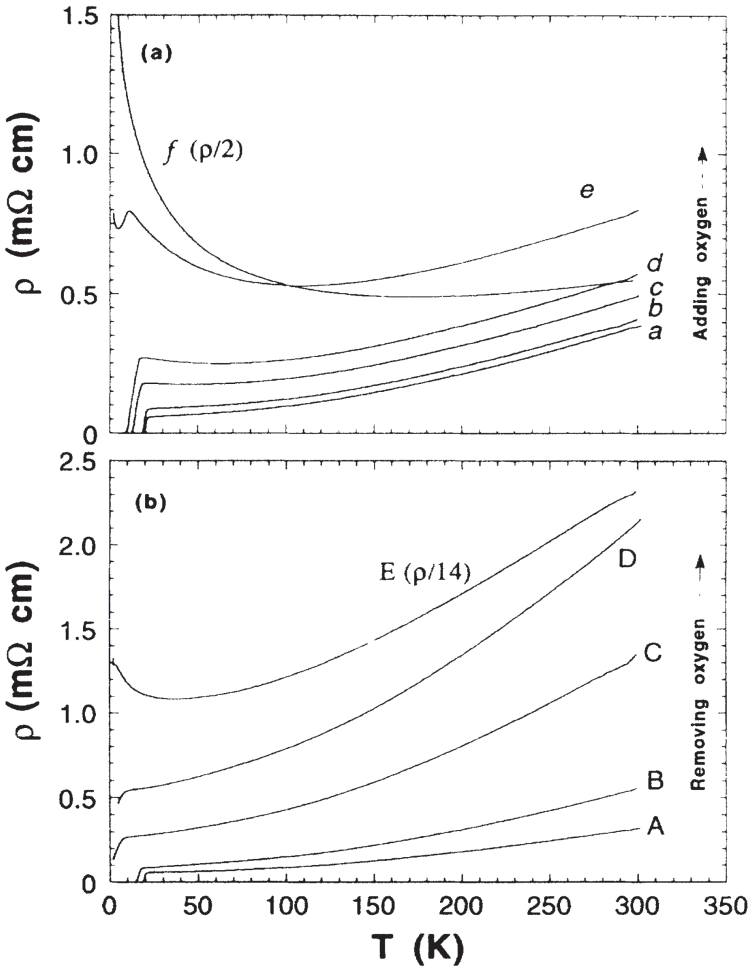

Figure 4.3: ρ_{ab} vs Temperature for various oxygen content δ in $Nd_{1.85}Ce_{0.15}CuO_{4\pm\delta}$ thin films, taken from Ref. [81]. (a) Increasing oxygen content for an optimally annealed thin film. The arrow indicates the order of increasing oxygen. The temperature dependence does not noticeably change in the range of δ which yield a superconducting state, and in the range of T above the resistivity minimum (data sets a, b, c, d). (b) Decreasing oxygen content from an optimally annealed thin film. The arrow indicates the order of decreasing oxygen. In contrast to (a), the temperature dependence changes as oxygen is decreased past the optimal content (B, C, D, E).

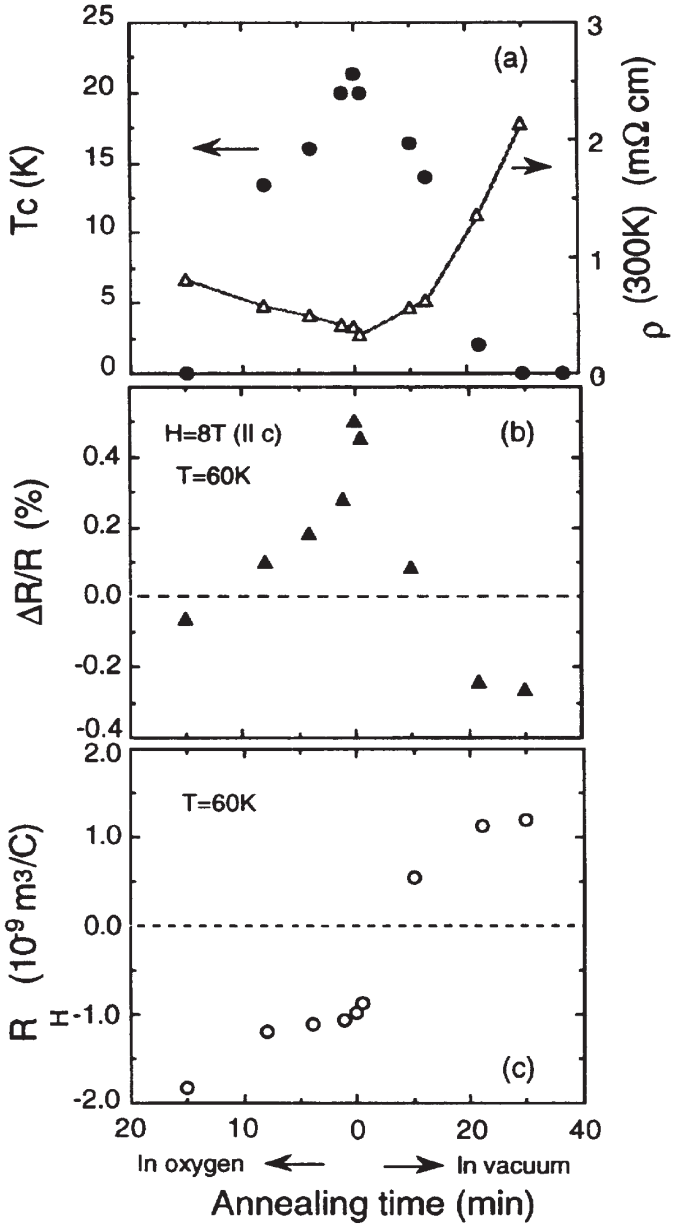

Figure 4.4: T_c, MR, and R_H as a function of oxygen in $Nd_{1.85}Ce_{0.15}CuO_{4\pm\delta}$ thin films, taken from Ref. [81]. (a) T_c and ρ_{ab} at 300 K versus oxygen content. (b) Magnetoresistance at 8 T and 60 K versus oxygen content. (c) Hall coefficient versus oxygen content.

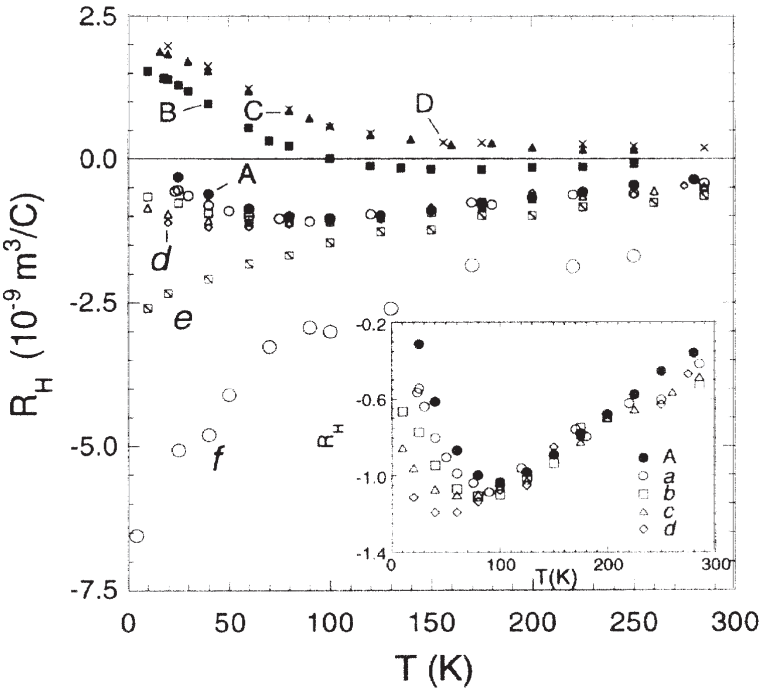

Figure 4.5: R_H as a function of oxygen in $Nd_{1.85}Ce_{0.15}CuO_{4\pm\delta}$ thin films, taken from Ref. [81]. Optimally annealed films are represented by the letters A and a. Oxygen content increases from a to f and decreases from A to E.

The Hall coefficient shows behavior similar to that of cerium doping. In the fully oxygenated $x = 0.15$ samples, R_H is negative and strongly temperature dependent. As the oxygen content is reduced, the magnitude decreases at low temperatures (Fig. 4.5) and the temperature dependence weakens. Upon further reduction, a minimum in R_H versus T develops at low temperatures. In the overly reduced regime, the Hall coefficient actually becomes positive with less of a temperature dependence than in the fully oxygenated case. This behavior, with reducing oxygen content, is qualitatively similar to what is observed in PCCO with increasing cerium content [Fig. 2.10(b)].

These detailed studies were carried out on optimally cerium-doped thin films or crystals. One study examined oxygen in overdoped NCCO ($x = 0.22$) thin

films [93]. The results agree with the data shown above and will not be reiterated here. The only comment I will make is that R_H is negative over the whole temperature range for the fully oxygenated films, while it is wholly positive for optimally reduced films in the same temperature range. Additionally, Fournier *et al.* [94] have demonstrated that the behavior with oxygen reduction shown above is similar in many of the cerium dopings in PCCO, i.e., the way in which ρ_{ab}, T_c, and R_H evolve at a given cerium doping. It is interesting that the oxygen reduction process mimics the behavior of cerium doping, but neither cerium nor oxygen doping alone result in superconductivity.

At this point I will mention some ideas proposed to explain what is happening during oxygen reduction and why it is necessary. The popular idea is that oxygen reduction removes impurity (apical) oxygen thereby reducing scattering and restoring the periodic potential in the CuO_2 plane. This restores the proper stoichiometry and allows superconductivity to exist. This is not the only theory and I will briefly mention a few more. These ideas range from a simple doping standpoint, to minimizing the antiferromagnetic (AF) long-range ordering, to proper *ab*-plane stoichiometry not correlated with apical oxygen.

The most simple and straightforward notion is that adjusting the oxygen content should primarily affect the carrier concentration within the material. Since oxygen likes to have a -2 valence (i.e., O^{2-}), removing oxygen should contribute electrons to the conduction band. This idea is partially supported by the oxygen-dependent behavior presented in the preceding paragraphs. R_H, ρ_{ab}, and T_c all evolve with oxygen reduction in a fashion similar to optimally annealed cerium-

doped samples. One difficulty is that the maximum value of T_c is dictated by the cerium content. By this I mean that one cannot achieve the T_c of optimal-cerium doping ($x = 0.15$, $T_c \simeq 22$ K) by adjusting the oxygen content for $x \neq 0.15$. Xu *et al.* [93] studied an overdoped NCCO film ($x = 0.22$) but did not report a T_c higher than 10 K in their oxygen study. Similarly, Fournier *et al.* [94] have observed a maximum in T_c as oxygen is reduced, [trends reminiscent of Fig. 4.4(a)] for several other cerium concentrations. The maximum in T_c versus O_2 is, however, different for different cerium dopings. Discrepancies also exist between cerium and oxygen doping in the resistivity in that ρ_{ab} shows a minimum with oxygen reduction. The large change in R_H for such a small change in oxygen is also difficult to explain within this picture. Additionally, one cannot achieve superconductivity by oxygen doping alone. These observations make it difficult to believe a purely doping reason for oxygen reduction.

Some studies propose that electrons incorporated through cerium doping are actually localized and do not contribute to conduction. This may be due to a small amount of (excess) oxygen occupying apical (or impurity) sites [91, 95], or it may just be due to the intrinsic effect of cerium doping [92, 96]. In either case, it is necessary to remove the apical oxygen (in the case of the former) or create vacancies near the cerium atoms (of which the apical sites are possible) in order to delocalize the doped electrons allowing them to participate in conduction. It is observed in neutron studies on NCO [97, 98] that the apical site occupancy decreases by $\simeq 0.06$ per copper site while the CuO_2 and the PrO oxygen are relatively unchanged (but slightly oxygen deficient) [97]. This means that oxygen is removed purely from the

apical sites in the parent compound. Iodometric titration and thermogravimetric analysis studies on NCCO show that less total oxygen is removed as the cerium content increases with a $\delta \simeq 0.01$ for $x = 0.15$ (first seven references in Ref. [98]). Schultz *et al.* [98] demonstrate that the reduction in $x = 0.15$ is attributable to the removal of apical oxygen. The reduction process removes these apical oxygen and is suggested to remove any associated disorder, which results in the delocalizing of the doped carriers in the CuO_2 plane. Therefore, in this picture, reduction affects the carrier density as well as the disorder in the system. This attempts to explain why such a drastic change in the electronic transport properties is observed for a small change in oxygen content ($\delta \simeq 0.01$) [91, 95].

Another proposal is that oxygen reduction affects the contributions of the different conduction bands in a two-band (electrons and holes) model. Jiang *et al.* [81] speculate that the majority charge carrier density (electrons) is *relatively* unaffected by reduction. This conclusion is based on the Hall data shown in Figure 4.5. At higher temperatures ($T \geq 100$ K), R_H is relatively unaffected by oxygen treatment. This implies that the majority carrier density is not changing much. If the carrier density changed by a constant amount, one would expect, roughly, some shift over the whole temperature range. This is not observed. Instead, they suggest that the reduction process causes a buckling of the CuO_2 planes which in turn induces a minority hole band. As oxygen is reduced, PCCO goes from an electron-like single band to an electron dominated two-band (at optimal reduction) and then into a hole-like single band in the over-reduced regime. It is further pointed out that superconductivity appears in the regime where two-band conduction is dominant. This

observation (in conjunction with others) leads one to believe that hole conduction is necessary for the occurrence of superconductivity. In the under-reduced regime, superconductivity is prevented by a lack of hole conduction, while significant lattice distortions in the over-reduced regime suppresses superconductivity. Ultimately, in this picture, reduction increases the population (or improves the mobility [94]) of the hole band up to some optimal oxygen content, beyond which the disorder induced in the lattice destroys superconductivity.

Antiferromagnetism has also recently been employed as a reason for oxygen reduction [99–101]. Riou and Richard *et al.* report from Raman spectroscopy measurements that apical oxygen, contrary to popular opinion, is not removed during reduction, but rather it is the CuO_2 plane oxygen which is removed for $x \geq 0.08$ cerium-doped samples. The in-plane vacancies would effectively result in a transfer of electrons onto the copper sites, frustrating the AF order and allowing the competing superconducting phase to appear. This is consistent with the observations of a reduction in T_N as oxygen is removed [37, 102, 103].

The last proposal for oxygen reduction is interesting, if nothing else, and involves an impurity phase frequently observed in the n-type cuprates [102, 104–106]. Kang *et al.* report a copper deficiency ($\sim 1\%$) in their $Pr_{1-x}LaCe_xCuO_{4\pm\delta}$ crystals, which would result in imperfect CuO_2 planes. After the crystals are reduced, they observe an impurity phase (Pr, La, Ce)$_2O_3$ (should be 3.5) which is not present in the as-grown crystals. The oxygen reduction process is then believed to create impurity (Pr, La, Ce)$_2O_3$ precipitates ($\sim 1\%$) in order to restore the proper CuO_2 plane stoichiometry. Maiser *et al.* report spurious peaks in their x-ray diffrac-

tion patterns for PCCO thin films which correspond to peaks for (Pr, Ce)$_2$O$_{3.5}$ or (110) oriented PCCO. They attribute this to misaligned (110) oriented PCCO (which have the same peaks as the impurity phase) because they also observe these peaks in undoped PCO. The impurity peaks disappear during an elevated temperature annealing process ($T \simeq 950$°C) in the thin films (similar to what Kang *et al.* [102] report in their single crystals), however the transition temperature and it's corresponding width degrade significantly relative to values obtained from normal annealing procedures [104]. To be sure, the impurity phase in this class of material is not a settled issue but it is an interesting proposal by Kang *et al.* [102] that is worth mentioning.

4.4 Disorder and Impurity Effects

Disorder and impurity effects in the cuprates has been investigated through several different means. For the most part the electronic properties (i.e., resistivity, magnetoresistance, Hall effect, and T_c) are the focus of research in this area. The disorder may arise intrinsically within the material or may be intentionally introduced. The former has been studied in the context of the Kondo effect [107] and 2D weak localization (2DWL) [72] in the resistivity and magnetoresistance at low temperatures. The latter has been studied by various methods: 1) isovalent cation substitution where the variances of the substituted atomic radii induce lattice distortion, 2) magnetic and non-magnetic ionic substitution which may or may not be isovalent with the substituted ion, 3) high-energy ion irradiation which displaces atoms from

their regular sites and into interstitial sites [4], and 4) oxygen non-stoichiometry. In this section, I will briefly review the current findings in regards to these effects in the cuprates.

4.4.1 Kondo Effect and 2D Weak Localization

The low temperature upturn in ρ_{ab} mentioned in section 4.1 is attributed to mainly two phenomena: 2DWL, or Kondo scattering from magnetic impurities. The reason one may think that either theory explains the low temperature upturn is because of the $\log 1/T$ behavior in ρ_{ab}.

Several groups interpret the low temperature behavior (MR [77, 108, 109], ρ_{ab} [110]) as indicative of 2DWL in the Nd and Pr n-type compounds. Fournier *et al.* [77] find a logarithmic temperature dependence in ρ_{ab} for underdoped NCCO, but a sublogarithmic dependence is observed in underdoped PCCO at the lowest temperatures, which is not predicted by 2DWL (Fig. 4.6). The MR, however, does show a strong orbital effect in both NCCO [77,108,109] and PCCO [77] and this orbital contribution can be fit to predictions of the magnetoconductance in the 2DWL picture (Fig. 4.7). Harus *et al.* [109] also find similar results in the magnetoconductance.

Evidence which supports a Kondo effect comes from Sekitani *et al.* [78]. They find that the logarithmic behavior of ρ_{ab} begins to deviate at low temperatures, in accordance with predictions by the Kondo theory. This deviation also agrees with

[4]The irradiation effects mentioned occur as the *primary* defect at low ion energies. At higher energies, significant lattice defects occur such as columnar defects or even material ablation.

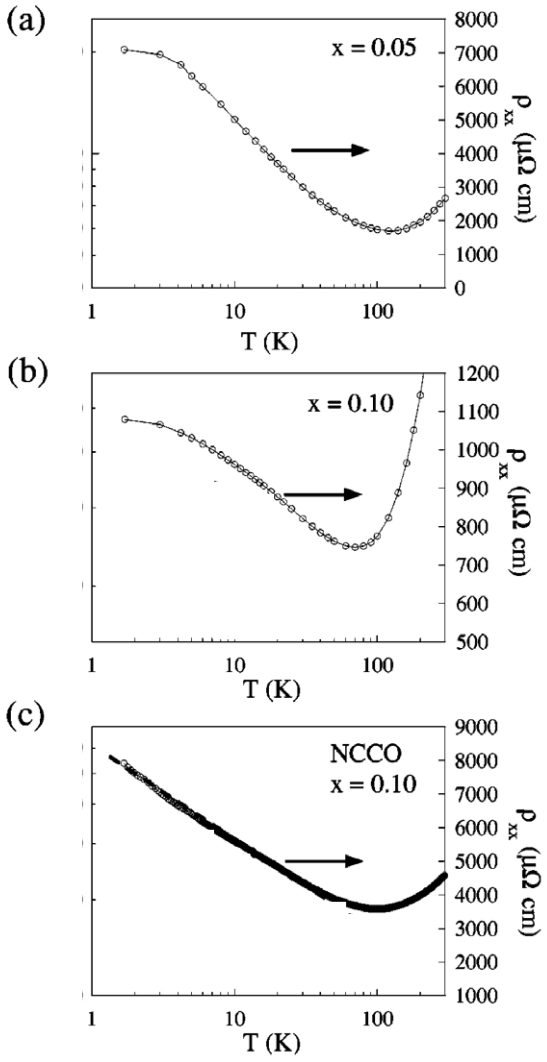

Figure 4.6: Logarithmic temperature divergence of ρ_{ab} in underdoped non-superconducting $Pr_{2-x}Ce_xCuO_{4\pm\delta}$ & $Nd_{2-x}Ce_xCuO_{4\pm\delta}$ thin films in zero applied magnetic field, adapted from Ref. [77]. (a) PCCO $x = 0.05$ (b) PCCO $x = 0.10$ (c) NCCO $x = 0.10$. The departure from logarithmic dependence is observed in PCCO but not in NCCO for these sets of films.

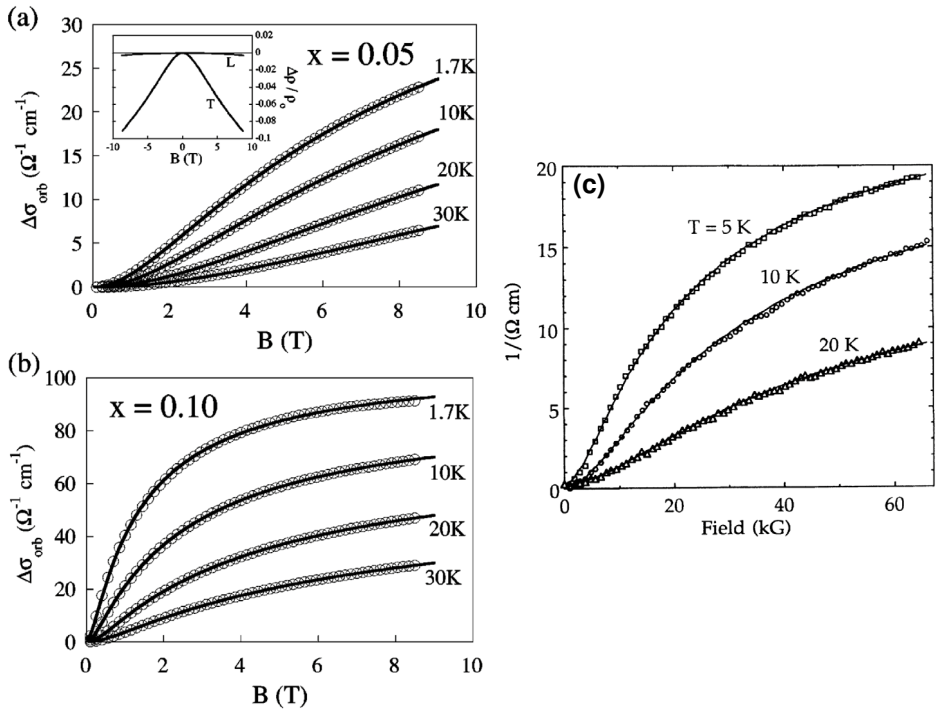

Figure 4.7: Orbital magnetoconductance ($\Delta\sigma_{orb}$) in $Pr_{2-x}Ce_xCuO_{4\pm\delta}$ thin films (from Ref. [77]) and in $Nd_{2-x}Ce_xCuO_{4\pm\delta}$ single crystals (from Ref. [108]). (a) PCCO $x = 0.05$ (b) PCCO $x = 0.10$ (c) NCCO $x = 0.01$. Solid lines are fits to 2DWL. Inset in (a) shows the longitudinal (L) and transverse (T) MR. The longitudinal MR comprises of spin MR where as the transverse MR has both spin and orbital components. In this doping range, orbital MR dominates for these samples.

previous reports [53, 77]. However, they report that LCCO, NCCO, and PCCO all show the same behavior which is different than that reported by Fournier *et al.* [77] (Fig. 4.8). They find that a negative MR is nearly isotropic, which indicates a spin related origin. Additionally, they find that the weak anisotropic MR (orbital MR) does not follow a cosine dependence. Sekitani shows that the resistivity behavior is consistent with a Kondo effect by fitting both the temperature and the field dependent ρ_k (the Kondo contribution to the resistivity) to equations based on the Kondo theory (Fig. 4.9). As a source of the Kondo impurity, they rule out the RE^{3+} ions due to the speculation that the La^{3+} ion in $La_{2-x}Ce_xCuO_{4\pm\delta}$ should not have

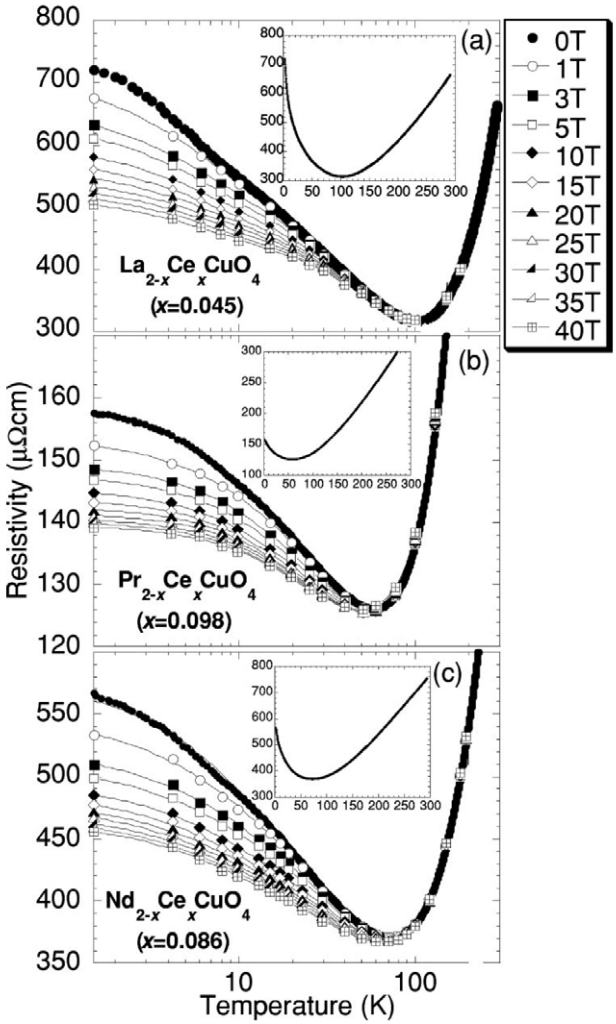

Figure 4.8: Logarithmic temperature divergence of ρ_{ab} in LCCO, PCCO, and NCCO underdoped thin films in zero and non-zero applied magnetic fields, taken from Ref. [78]. (a) LCCO $x = 0.045$ (b) PCCO $x = 0.098$ (c) NCCO $x = 0.086$. Insets show the zero field data on a linear temperature scale.

a spin moment. The Cu^{2+} spin moments are also ruled out as it would be difficult to consider their influence as a "single-impurity" Kondo scattering center. They do suggest that the Kondo scatterers arise from a small amount of residual apical oxygen interacting with the copper sites, resulting in impurity moments.

Care must be taken when considering either of these theories. While the low

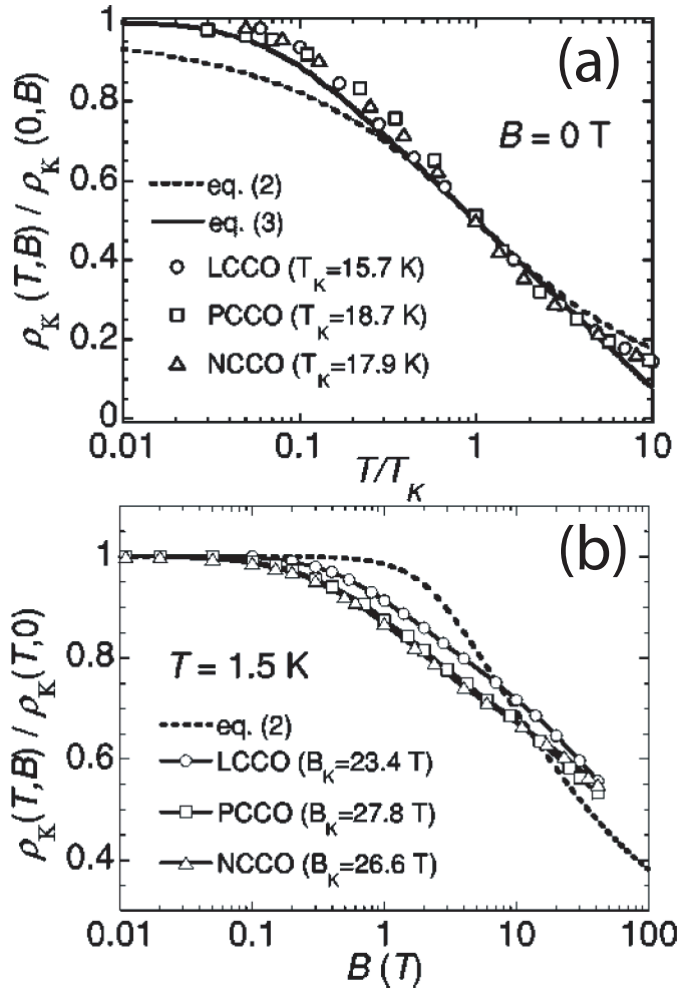

Figure 4.9: Kondo fits to $\rho_k(B,T)$ in LCCO, PCCO, and NCCO underdoped thin films, taken from Ref. [78]. ρ_k is defined by $\rho_{ab} = \rho_\circ + \rho(T^2) + \rho_k$. (a) Zero magnetic field temperature dependence fit, and (b) low temperature field dependence fit for LCCO, PCCO, and NCCO.

temperature ρ_{ab} shows a logarithmic behavior, a deviation into sublogarithmic behavior develops at the lowest temperatures. This deviation is not observed by every group, although it may still occur below the temperature range of the experiment. Again, this deviation is not predicted by 2DWL. Additionally, there is some discrepancy in the magnitude of the orbital MR (relative to any spin MR) and its field dependence reported in the literature. This may imply that the MR is very

sensitive to the sample growth conditions and that samples may or may not have a dominant spin component. On this note, Sekitani *et al.* [78] find that 2DWL fits to the logarithmic temperature dependent upturn yield inconsistent values for the logarithmic term's coefficient between different dopings and materials.

The last interesting thought is provided by Ando *et al.* [40] on the *p*-type cuprate LSCO in that the same logarithmic dependence observed in the *ab* plane is also observed in the *c* direction. The ratio of these resistivities below T_c is nearly temperature independent, which indicates a 3D insulating state rather than one consistent with 2DWL. This behavior is also seen in the *n*-type cuprates [111].

The feeling that one should take away from all this is that neither theory completely predicts the low temperature behavior in both ρ_{ab} and MR. This is one of the unsolved problems in the transport of the HTSC cuprates.

4.4.2 Cation Disorder

What is necessarily meant by cation disorder is a change in some of the regular cation sites by simple substitution which can have several effects. The substitution may be isovalent, meaning that the doping level is held constant, and one may be interested in how lattice strains induced by the different atomic radii affect certain transport properties. Isovalent substitutions may also be magnetic or non-magnetic with the idea that spin scattering may be important. Substitutions may not be isovalent and would affect doping to some extent. Since electronic transport within the cuprates occurs predominantly in the CuO_2 plane, copper substituted with mag-

netic and non-magnetic $3d$ transition metal elements will be briefly reviewed. This is followed by out-of-plane disorder, i.e. cation substitution in the "charge reservoirs."

One reason for looking at in-plane Cu substitution (other than the fact that conduction occurs primarily in the CuO_2 plane) is to help determine the pairing mechanism of the cuprates as well as possibly some clues to the mechanism of superconductivity in the high temperature superconductors. In s-wave superconductors, pair-breaking occurs when the electrons scatter from magnetic impurities, whereas non-magnetic impurities have relatively little effect (assuming weak scattering and low impurity levels [112]). The pair-breaking from magnetic scatterers is well described by the Abrikosov-Gor'kov (AG) theory for conventional (isotropic) BCS superconductors. For d-wave superconductors, pair-breaking can occur from both magnetic and non-magnetic scattering centers. Although a lot of work has been on Cu substitution in YBCO, that particular lattice structure has two sites into which the Cu substitution can take place (the CuO_2 plane and the CuO chain). In this respect, substitutions for copper will be mentioned for the single CuO_2 layer cuprates $La_{2-x}Sr_xCu_{1-y}M_yO_4$ (M:LSCO) and $RE_{2-x}Ce_xCu_{1-y}M_yO_{4\pm\delta}$ (M:RECCO) (RE = Nd, Pr; M = Ni, Fe, Co, Zn), as well as the double CuO_2 layer cuprate $Bi_2Sr_2Ca_1Cu_{2-y}M_yO_{8+\delta}$ (M:BSCCO), where there exists only one lattice site for copper. This potentially "simplifies" things.

P-Type Cuprates - In-plane Substitution

M:LSCO, either polycrystalline or single crystals, was studied with Zn [113–116], Ni [115] and Co [115], and M:BSCCO was studied with Zn, Ni, and Fe [117]. Karpińska *et al.* [118] studied Zn:LSCO thin films. Most experiments were made on optimally doped compounds. The above mentioned elements enter into the lattice with a plus 2 valence [115, 117] (Zn^{2+}, Ni^{2+}, Fe^{2+}) and no intentional chemical doping is done (copper is Cu^{2+}, nominally). Thus, these elements help examine the effects of magnetic (Ni, Co, and Fe) and non-magnetic (Zn) impurities.

T_c is suppressed in M:LSCO at a rate $dT_c/dy \simeq -10$ K/at.% [Fig. 4.10(a)], while in double layer M:BSCCO the rate is $dT_c/dy \simeq -5$ K/at.%. The difference may be due to the fact that BSCCO has pairs of CuO_2 planes separated by charge reservoirs rather than only one plane, as in LSCO. These rates are *independent* of the magnetic state of the doped atoms. While the above statement is, for the most part, true, Zn doping decreases T_c *slightly* faster than Ni doping [Fig. 4.10(a)]. Although Zn is non-magnetic, it is found to induce local moments in the Cu sites[5] ($\simeq 0.8\,\mu_B$/Zn independent of concentration), however this moment is less than that observed for Ni ($\simeq 1-2\,\mu_B$/Ni depending on concentration) and does not account for the stronger suppression of T_c. The observation that all the dopants affect T_c similarly implies that pair-breaking from magnetic impurities is not a the dominant mechanism in the suppression of T_c in these hole-doped systems. This behavior is *qualitatively* consistent with pair-breaking within the AG theory for *d*-wave superconductors, in which magnetic and non-magnetic impurities cause pair-breaking. The lattice

[5] Zn^{2+} is non-magnetic with a filled *d* shell (d^{10}).

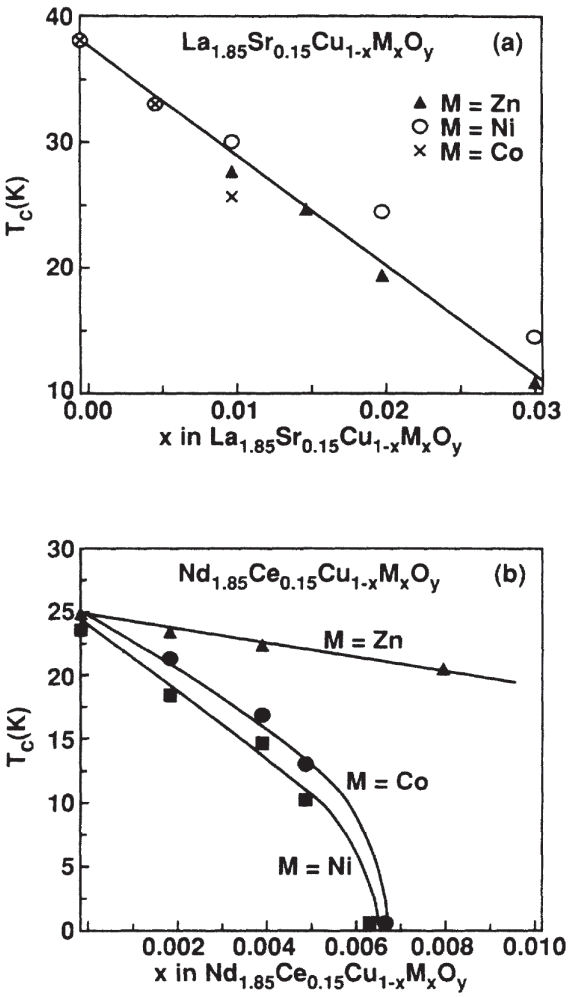

Figure 4.10: T_c versus magnetic and non-magnetic substitution for copper in $La_{1.85}Sr_{0.15}Cu_{1-y}M_yO_4$ and $Nd_{1.85}Ce_{0.15}Cu_{1-y}M_yO_{4\pm\delta}$ polycrystalline samples, taken from Ref. [119]. (a) LSCO with Zn, Ni, and Co substitution. Both magnetic and non-magnetic elements reduce T_c in nearly the same fashion. Notice that non-magnetic Zn suppresses T_c *slightly* faster than magnetic Ni. (b) NCCO with Zn, Ni, and Co substitution. The rate of suppression for Zn is nearly half of what is observed in LSCO. The effect of Ni and Co is *much* stronger than in LSCO, suggesting that LSCO *might* be in a strong coupling limit and NCCO *might* be in a weak coupling limit.

parameters (a and c axes) do change upon doping. In particular, for the case of Zn substitution, the c axis decreases and the a axis increases as the Zn concentration increases. This is attributed to a Jahn-Teller (JT) effect. Zn^{2+} (d^{10}) is not a JT ion, whereas Cu^{2+} (d^9) is a JT ion. The JT effect creates a distortion in the CuO_2 octahedral. As Cu is replaced with Zn, this distortion is relaxed. The lattice distortion (or the alleviation of distortion) does not appear to be a major contributor to the changes in T_c because all of the dopants, both JT and non-JT, reduce T_c by a similar amount. The Hall coefficient also changes with substitution, however this change is not attributed to any change in the carrier concentration in the case of Zn doping [114]. They rule out a change in n because Zn goes in as a 2+ and the oxygen content is managed so as not to change with Zn doping. Additionally, if one assumes that Zn adds either holes or electrons, then the opposite trend in R_H observed in Zn:NCCO demonstrates that the number of carriers is not changing (Fig. 4.11). Additionally, elastic pair-breaking is ruled out by Westerholt *et al.* [117] because Fe strongly affects the resistivity compared to the other dopants, but T_c is still affected by the same amount. This is telling us that the increase in the scattering rate of the quasiparticles does not break Cooper pairs. Tarascon *et al.* [115] point out that the sensitivity of T_c to disorder is consistent with pairing induced by antiferromagnetic interactions (RVB model), and that this material may be in the strong coupling limit [119].

In the under to optimally Sr-doped M:LSCO, Fukuzumi *et al.* [116] find that the substitutions drive a superconductor to insulator transition (as $T_c \rightarrow 0$) at a sheet resistance very near to the value of $h/(2e)^2$. The overdoped samples show

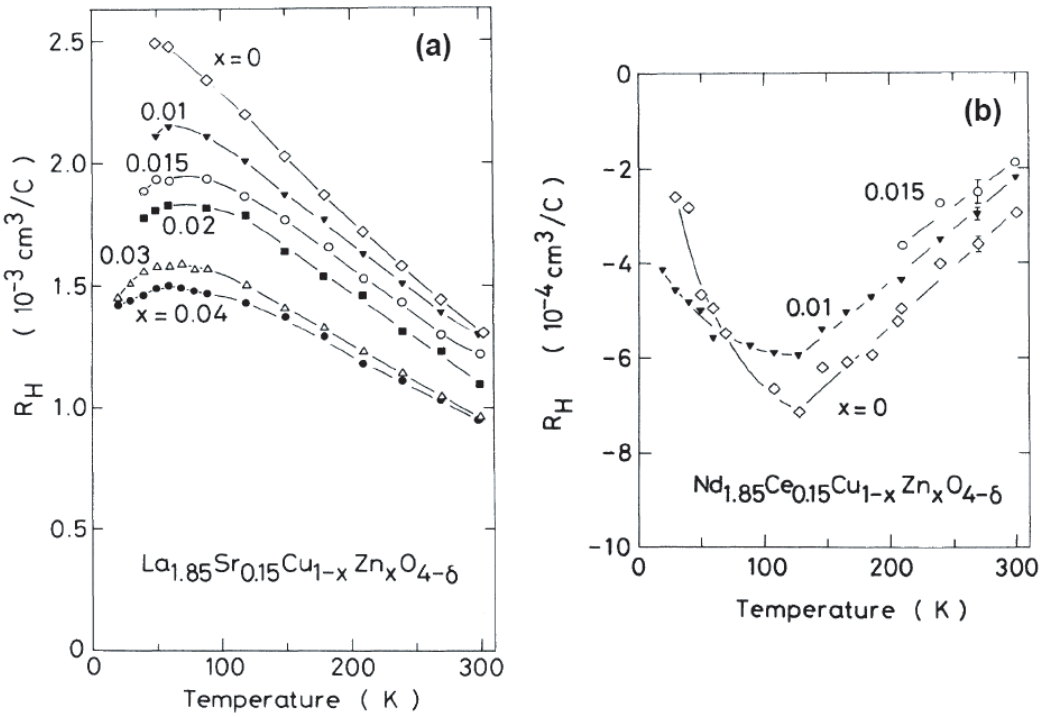

Figure 4.11: Evolution of R_H versus Temperature in $La_{1.85}Sr_{0.15}Cu_{1-y}Zn_yO_4$ and $Nd_{1.85}Ce_{0.15}Cu_{1-y}Zn_yO_{4\pm\delta}$ polycrystalline samples, taken from Ref. [114]. (a) Zn doped LSCO. (b) Zn doped NCCO. The opposite trends between (a) and (b) indicate that Zn does not have an effective doping (as it should not). For example, if we assume Zn dopes *holes*, then R_H in LSCO should decrease (as it does), and it should *increase* in magnitude in NCCO (which it does not).

$T_c \to 0$ at sheet resistances much below this value. In this regard they find that Zn acts as a unitary scatterer in the under/optimally doped compounds. They suggest that a two-fluid model (superconducting and normal carriers) can qualitatively account for the lower sheet resistance where T_c vanishes in the overdoped compound. This idea states that the normal carriers are rather insensitive to the additional scattering, compared to the superconducting carriers. So in this model the normal carriers arise from overdoped portions of the sample while the superconducting carriers arise from underdoped portions (kind of like grains, but more appropriately regions). The overdoped compound has, obviously, more overdoped regions and so

more normal carriers. The point at which the underdoped, superconducting regions become normal occurs at a much less *total* sheet resistance than the underdoped compound because there is less normal, higher resistance, underdoped regions compared to the underdoped compound.

Karpińska *et al.* [118] find that Zn can substitute into LSCO upwards of 12% of Cu. They also find that the T_c suppression is fairly well described by the original AG theory, indicating non-magnetic pair-breaking in a d-wave superconductor. At high values of Zn, however, a slight deviation from theory is observed. This may be consistent with Openov's modified AG theory [75] in which a mixing of s and d-wave gaps are considered. Furthermore, a quadratic temperature dependence of the penetration depth is unaffected with increasing Zn concentration, which indicates that the d-wave pairing is unaffected. A very interesting result comes from the in-plane resistivity. At high Zn concentrations (for Zn concentrations where superconductivity is entirely suppressed), a logarithmic behavior is observed. Additionally, this behavior shows a saturation, very reminiscent of the upturn saturation in underdoped PCCO. This is interpreted as due to remnant superconductivity. A metal-insulator transition at $k_F\ell \simeq 1$, which is suggestive of a disorder-induced localization.

While the consensus is that magnetic pair-breaking is not the reason T_c decreases, no significant and agreed-upon conclusions are made.

N-Type Cuprates - In-plane Substitution

The n-type cuprates have significantly different results from the p-type cuprates mentioned above. Most of the work has been done on optimally Ce-doped polycrystalline M:NCCO samples with Zn [114,119–122], Ni [121,122], Co [119,121], and Fe [122] substituting for copper, where again Zn is the only "non-magnetic" dopant. Single crystals of optimally Ce-doped M:PCCO with Ni and Co substitution are investigated by Brinkmann *et al.* [123]. In contrast with the p-type cuprates, the magnetic dopants appear to be entering the lattice in a *3+ state*. Zn is still entering divalently, as well as inducing local moments on the Cu sites similarly to what is observed in the p-type cuprates. In the context of Zn doping, it is found that $\mathrm{d}T_c/\mathrm{d}y$ is about half of what is found in Zn:LSCO and about the same for Zn:BSCCO, i.e., $\mathrm{d}T_c/\mathrm{d}y \approx -5$ K/at.%. What is interesting is that the magnetic dopants (i.e., Co, Ni, Fe) suppress T_c much stronger than what is found in the p-type cuprates, which also means that the magnetic dopants are stronger than the "non-magnetic" Zn [Fig. 4.10(b)]. This has been interpreted within the conventional AG theory for *s-wave* superconductors [115,121,123] (Fig. 4.12). At the time of many of these reports, the n-type cuprates were believed to be s-wave from tunneling [124] and penetration depth [125] measurements. More recent measurements, however, indicate d-wave [126,127] and an unusual non-monotonic d-wave behavior [128,129]. In light of this, I am unsure about the current interpretation of the Zn doping results. The Hall coefficient also act differently between the n and p-type cuprates. If a carrier doping effect is expected, then R_H should evolve in the same fashion

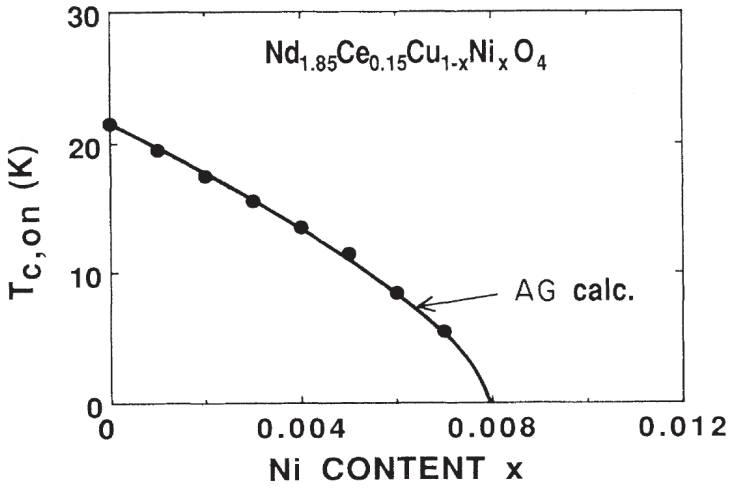

Figure 4.12: Abrikosov-Gor'kov theoretical fit for T_c versus Ni concentration in $Nd_{1.85}Ce_{0.15}Cu_{1-y}Ni_yO_{4\pm\delta}$ polycrystalline samples, taken from Ref. [121]. The points are data and the line is a fit using the AG theory.

for both types of superconductors as more impurities enter the lattice. This is not the case (Fig. 4.11) for Zn doping where the substitution is isovalent and doping effects are ruled out. For the magnetic dopants, where it is not isovalent, Brinkmann *et al.* [123] argue that the large change observed in R_H cannot be attributed to a doping effect. It is true that NCCO and PCCO are sensitive to the oxygen content and that it *may* change with the transition metal dopant concentration, but no significant conclusions are drawn in regards to the non-isovalent substitutions and oxygen defects. Rather, Brinkmann *et al.* [123] suggest that the magnetic impurities may be increasing the scattering rate of electrons more so than holes, within a two-band model, in order to account for the change in R_H. Lattice distortions are also ruled out as a possible mechanism for T_c suppression. This is because the lattice parameters do not change in NCCO with Zn doping [114, 120] as they do in the *p*-type cuprates (due to the JT effect). For NCCO and PCCO, the general consensus

is that magnetic pair-breaking is responsible for the significant suppression of T_c. It would be interesting to see if these results, with the inclusion of the Zn data, fit into the modified AG theory proposed by Openov [75] in which he incorporates d and s-wave symmetries, or a mixing of the two, into the conventional BCS-based AG theory.

P-Type Cuprates - Out-of-plane Substitution

Much focus was initially placed on substitution in the CuO_2 plane due to the fact that electronic conduction takes place in the plane and the substitution is expected to produce strong scattering centers. The out-of-plane substitution was not expected to produce significant results since the atoms between the CuO_2 planes are thought to predominantly act as charge reservoirs which contribute carriers to the plane. However, important results were indeed found. While in-plane T_c suppression is not attributed to lattice distortions, the effect from out-of-plane substitution does have a correlation with lattice distortion.

The objective here is again to probe isovalent substitutions in order to eliminate doping effects. The only literature I am able to find is on the p-type cuprates and so only those will be discussed, and only in a few of the single CuO_2 layer compounds.

Attfield *et al.* [130] produced some very nice work in the $Ln_{2-x}M_xCuO_4$ system (Ln = lanthanides, M = 2+ cations; i.e., LSCO) using polycrystalline samples. The idea is to keep the doping level fixed (by the Ln/M ratio) at $x = 0.15$ and look at

how the T_c changes with various changes in the average atomic radii due to different elements in the A sites [the A sites being the (Ln,M) atoms situated between the CuO_2 planes]. The formulary they use is $La_{1.85-f}Nd_fSr_{0.15-g-h}Ca_gBa_hCuO_4$. In the case of $f = g = h = 0$, we recover the optimal composition for LSCO. By adjusting f, g, and h, the average atomic radii ($< r_A >$) can easily be changed while maintaining a constant doping (Sr, Ca, and Ba go in as 2+ while La and Nd go in as 3+). Three different $< r_A >$ series were made with each series containing several different compositions. In addition to $< r_A >$, the statistical variance $\sigma^2 =< r_A^2 > - < r_A >^2$ (a measure of the lattice disorder due to local variances of atomic radii) is determined and used as a means to rank the compounds within a given $< r_A >$ (least disorder to most disorder). What Attfield *et al.* [130] found was that T_c systematically decreased as σ^2 increased [Fig. 4.13(a)]. Extrapolating each $< r_A >$ series to $\sigma^2 = 0$ gives a "disorder-free" T_c (T_c°) for each series. T_c° was found to *increase* with increasing $< r_A >$ [Fig. 4.13(b)]. They attribute this result to an effective distortion of the CuO_6 octahedral. Suggestions have been made about possible hole trapping [131]. This work shows that disorder (or lattice strain/stress) in the *charge reservoirs* has a significant effect on the superconducting transport properties in the adjacent CuO_2 plane (outside of doping).

Fujita *et al.* [132] find similar results in their work on single crystals of the single layer cuprates $Bi_2Sr_{1.6}Ln_{0.4}CuO_{6+\delta}$ (Ln:Bi2201; Ln = La, Nd, Eu, Gd) and $La_{1.85-y}Nd_ySr_{0.15}CuO_4$ (Nd:LSCO). The Hall coefficient for these systems (R_H and dR_H/dT) is also measured and a similar change occurs as compared to what is seen in the in-plane substitutions (Fig. 4.14). One should note that the Nd:LSCO at

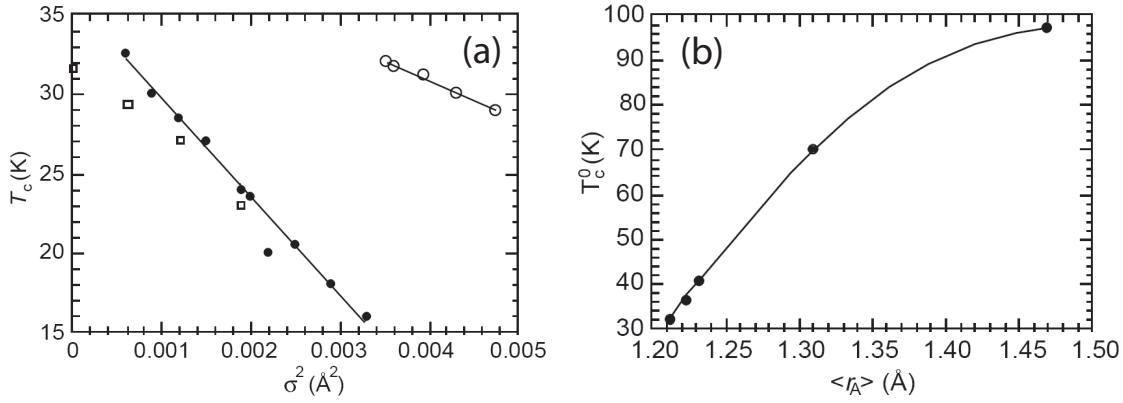

Figure 4.13: T_c versus $< r_A >$ and σ^2 in the $Ln_{2-x}M_xCuO_4$ system, taken from Ref. [130]. (a) T_c decreases as the amount of disorder (σ^2) increases at the A site ($Ln_{2-x}M_x$ site). The three different data sets represent the three different average atomic radii series in the study: $< r_A >= 1.212$Å (open square), 1.223 Å (closed circles), 1.232 Å (closed circles). A linear extrapolation back to $\sigma^2 = 0$ gives the "disorder free" T_c (T_c°). (b) T_c° versus $< r_A >$ for the single layer cuprates. T_c° increases as the average atomic radius increases.

20% substitution is similar to Zn:LSCO at 2% substitution, in regards to the suppression of T_c, showing that out-of-plane impurities are much weaker than in-plane. Resistivity measurements yield almost no change in the temperature dependence while ρ_o changes significantly. These observations lend credence to the belief that the carrier concentration does not change with isovalent substitution outside the CuO_2 plane and that holes are actually not trapped, as is suggested in Ref. [131]. They do find that the disorder acts as a weak scatterer. This comes from the calculation of the sheet resistance at the point where T_c vanishes. This value is significantly lower than what is observed by Fukuzumi *et al.* [116] upon in-plane Zn substitution (Fig. 4.15) for optimally Sr-doped Zn:LSCO, but it is similar to what Fukuzumi *et al.* find in their overdoped samples. For a relatively small change in ρ_o (compared to the unitary scattering of Zn), T_c vanishes. These effects are not attributed to

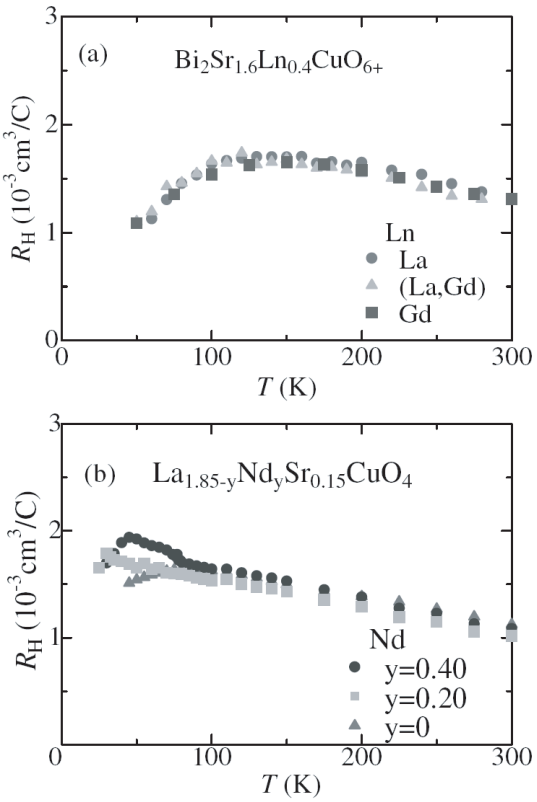

Figure 4.14: R_H versus Temperature for out-of-plane disorder in the $Bi_2Sr_{1.6}Ln_{0.4}CuO_{6+\delta}$ and $La_{1.85-y}Nd_ySr_{0.15}CuO_4$ single crystals, taken from Ref. [132]. (a) $Bi_2Sr_{1.6}Ln_{0.4}CuO_{6+\delta}$ where the disorder comes from the different lanthanide ions having different atomic radii. (b) $La_{1.85-y}Nd_ySr_{0.15}CuO_4$ The disorder in this system is from the different atomic radii between La and Nd. Changing the ratio changes the amount of disorder.

magnetic pair-breaking because T_c is reduced more for non-magnetic Eu than for magnetic Nd in the Ln:Bi2201 system. It is *suggested* that the local distortions in the lattice, from the out-of-plane disorder, affect the transfer integrals (the overlap of the neighboring atoms' wavefunctions) which suppresses superconductivity.

If it interests the reader, more studies can be readily found in the references of Ref. [130–132]. The more structurally complicated system (the bilayer Bi2212) can also be found in the references of Ref. [133] which also addresses the sites that are more likely to cause significant T_c effects, as well as structural considerations of

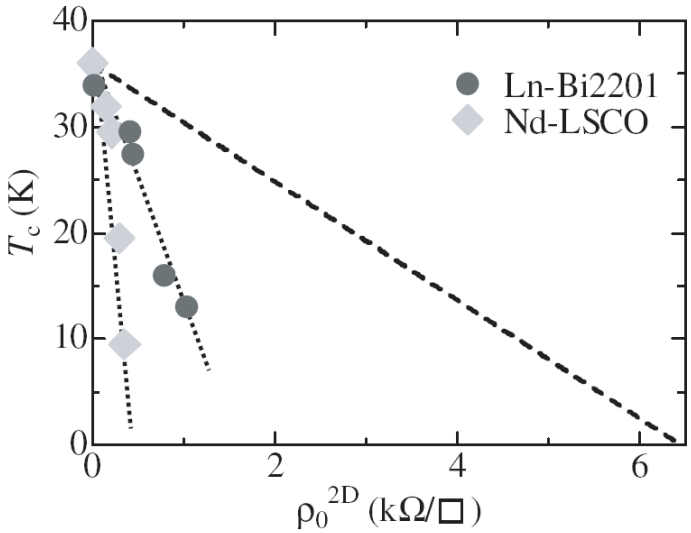

Figure 4.15: T_c versus Sheet Resistance in the disordered $Bi_2Sr_{1.6}Ln_{0.4}CuO_{6+\delta}$ and $La_{1.85-y}Nd_ySr_{0.15}CuO_4$ systems, taken from Ref. [132]. The dashed line represents the results of Fukuzumi *et al.* [116] for their optimally Sr-doped Zn-LSCO samples.

even more complex systems.

4.4.3 Irradiation

Disorder by irradiation (both ion and electron) on the cuprate superconductors has been extensively researched. A very good review on the results of these experiments is given by Weaver *et al.* [134]. I will briefly cover the relevant aspects in the cuprates.

Weaver *et al.* [134] show that irradiation suppresses T_c similarly for a very broad range of cuprates and incident particles. In Fig. 4.16, the decrease of T_c with irradiation fluence $dT_c/d\phi$ is plotted versus the Nonionizing Energy Loss (NIEL, a measure of the number of defects) for many different irradiation experiments on the cuprates. A linear relationship is apparent. This result starkly contrasts results on low temperature superconductors in which little or no systematic trend is

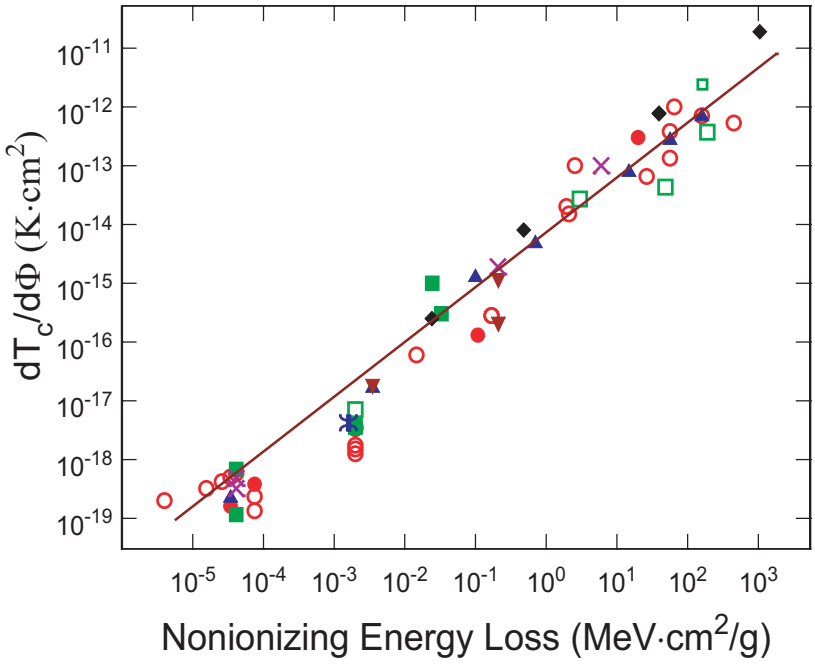

Figure 4.16: $\frac{dT_c}{d\phi}$ versus Nonionizing Energy Loss (NIEL), taken from Ref. [134]. The solid line represents a linear fit to the data. The data points are: (Open/Closed Circles) YBCO; (Open/Closed Squares) Bi-based materials; (Triangles) EuBCO; (Down Triangles) GdBCO; (Diamonds) Tl-based materials; (Xs) LSCO and NCCO; (Asterisk) HgBCO.

found [134]. This linear relationship implies that T_c suppression by irradiation is determined by the defect concentration and *not* by material composition or complexity, the initial T_c of the material, incident particle type or energy, the irradiation environment, the sign or density of the charge carriers, or even whether the sample is crystalline (film or single crystal) or not [134, 135].

Several groups (references 64, 93, and 100-105 in Ref. [134]) demonstrate that the only theory, which is insensitive to much of the material's chemical makeup, is the depairing theory for high temperature superconductors provided by Abrikosov- [136], which incorporates anisotropic gaps. It is therefore the conclusion that pair breaking for a *d*-wave superconductor (and not an anisotropic *s*-wave [135]) drives

T_c suppression in the irradiated cuprates. Tolpygo *et al.* [135], however, show that phase fluctuations can also account for T_c suppression by irradiation.

Interestingly enough, Weaver *et al.* [137] draw the conclusion that oxygen vacancies in the CuO_2 plane are responsible for the depairing. This is based on a few observations: 1) the common structural property of all the cuprates is the CuO_2 plane, 2) suppression of T_c is determined by defect concentration, and 3) oxygen is the lightest (common) element and is the largest recipient of radiation effects. The reason that it is in-plane oxygen rather than out-of-plane oxygen is because experiments targeted at oxygen vacancies in the CuO chain in YBCO show an order of magnitude smaller effect on T_c (per defect) than do irradiation experiments [137] targeted at the in-plane oxygen sites. Experiments on NCCO [138] irradiated with 4 MeV He^{++} ions demonstrate that apical oxygen are not important, as the same trends are observed in NCCO (no apical oxygen) as in all the other cuprates.

Woods *et al.* [139] irradiated NCCO thin films with either 200 keV Ne^{+} ions ($x = 0.15$), or with 200 keV He^{+} ions ($x = 0.14$). Resistivity measurements show that low irradiation doses contribute only an elastic, temperature independent term, i.e., the residual resistivity. At higher doses, superconductivity is destroyed and $\rho(T)$ begins to change, demonstrating variable range hopping conduction (VRH) induced by disorder [140] [Fig. 4.17(b)]. They find that T_c vanishes at a sheet resistance $\simeq 5 - 12$ kΩ, in the neighborhood of $h/4e^2 \simeq 6.5$ kΩ. They interpret this result as disorder destroying the pair amplitude in a 2D superconductor. The most interesting result, however, is in regards to the Hall coefficient. They find that the magnitude of R_H gets slightly smaller with irradiation at low doses (shifts towards more positive

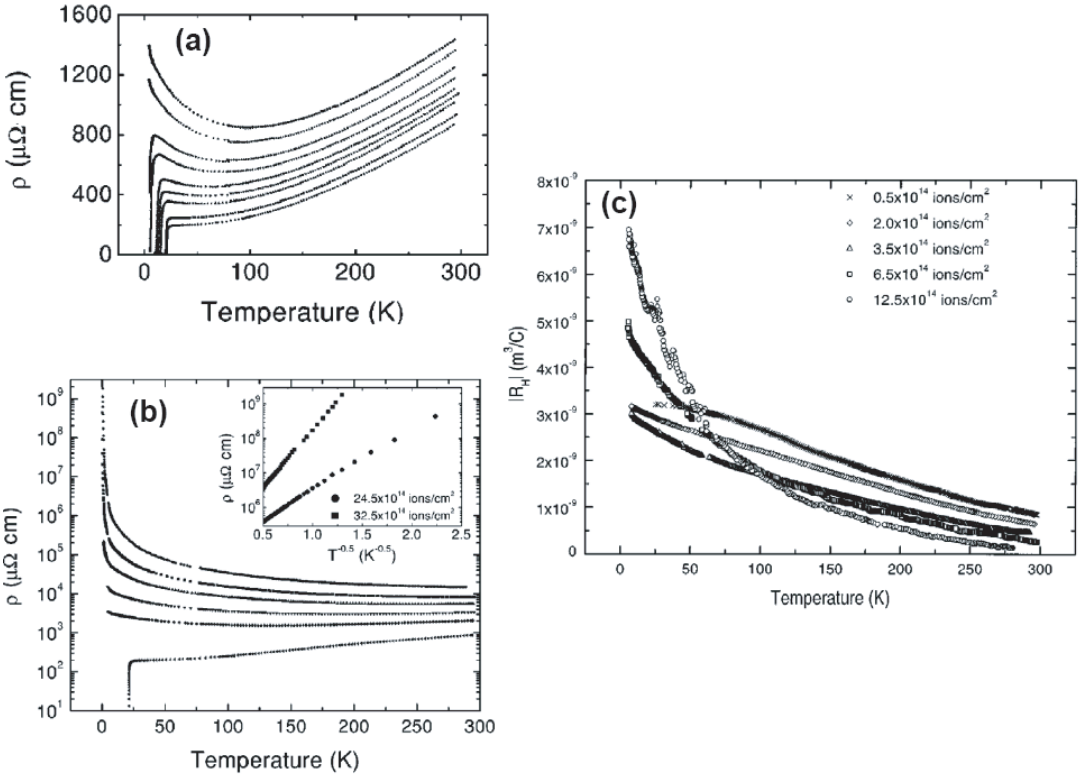

Figure 4.17: Resistivity and Hall on He^+ irradiated $Nd_{1.86}Ce_{0.14}CuO_{4\pm\delta}$ thin films. (a) Resistivity showing parallel shifts in ρ with increasing irradiation, indicating contributions only to $\rho_\circ$. The doses, from bottom to top, are: 0, 0.5, 1, 1.5, 2, 2.5, 3, 4, 4.5×10^{14} ions/cm^2 (taken from Ref. [140]). (b) Continuation of (a) at higher doses, from bottom to top: 0, 6.5, 12.5, 18.5, 24.5, 32.5×10^{14} ions/cm^2. Inset demonstrates VRH ($\rho \propto exp[(T_\circ/T)^{0.5}]$) in the two most irradiated samples. (c) Absolute value of the Hall coefficient for several irradiation doses. R_H is negative for all doses and all temperatures. From bottom to top (at 300K): 12.5, 6.5, 3.5, 2, 0.5×10^{14} ions/cm^2. At low doses, irradiation drives R_H towards positive values. At high doses irradiation drives R_H larger and more negative.

values). Near the point where superconductivity is destroyed, $|R_H|$ increases and starts to develop a strong temperature dependence, diverging as $T \to 0$. A two-band model is invoked to explain this behavior [140].

Rullier-Albenque *et al.* [141] electron-irradiated (2.5 MeV) overdoped Tl_2Ba_2-$CuO_{6+\delta}$ single crystals. They find that the high temperature resistivity increases in a parallel fashion, indicating that the residual resistivity is mostly affected at low

doses. At higher doses, an upturn in the resistivity occurs after superconductivity is destroyed. The temperature dependence is interpreted in the theory of 2DWL. A negative transverse MR, which decreases with increasing temperature, qualitatively supports the idea. However, data is not presented and no mention is made about whether this is orbital or spin MR.

4.4.4 Oxygen Non-stoichiometry

It is easy to see that oxygen non-stoichiometry introduces disorder into the lattice, at least in the sense of structural disorder. If oxygen is added to the system, then it is inserted interstitially. If oxygen is removed, then vacancies are created at regular lattice sites. These two phenomena introduce additional strain, and scattering centers, which may or may not cancel the doping aspect.

In $La_2CuO_{4+\delta}$, it is observed that phase separation exists and disappears as oxygen increases beyond $\delta \simeq 0.045$ [87]. The phases are from oxygen rich and poor regions. In the oxygen poor region, the CuO_6 octahedra are tilted, whereas the tilting is locally disrupted by interstitial oxygen in the oxygen rich regions. The structural differences result in elastic stress at the boundaries between the regions. This results in a martensitic phase transition at some temperature T_m. Beyond $\delta \simeq 0.045$, LCO is a single phase superconductor as the interfacial stress is relieved. In addition to the different phases, the lattice constants also change. Radaelli *et al.* [89] report that the a, b, c lattice constants change by $\simeq -0.4\%, 0.5\%$, and 0.1%, respectively as δ goes from 0.08 to 0.12 (room temperature values). So it is apparent

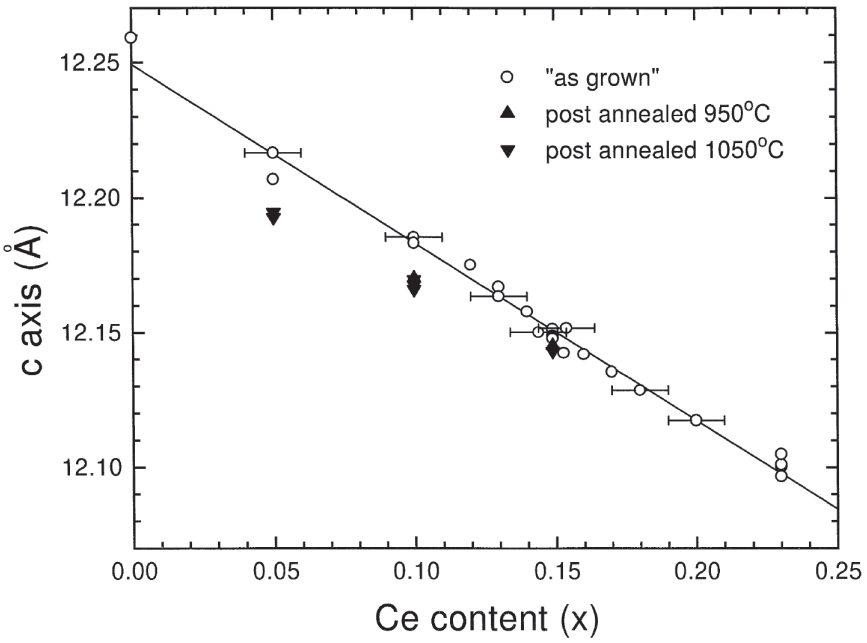

Figure 4.18: c-axis lattice parameter of $Pr_{2-x}Ce_xCuO_{4\pm\delta}$ before and after post-deposition annealing of thin films, taken from Ref. [104]. The c axis decreases as oxygen is removed during annealing. The amount of decrease is less as the cerium content increases (see text).

that adding oxygen to LCO causes structural changes, or a sort of "disorder."

In PCCO, Maiser *et al.* [104] report that the c-axis lattice parameter decreases upon oxygen reduction in thin films. The amount the c axis changes decreases as the cerium content increases (Fig. 4.18). This may be due to a compensation from the smaller atomic radius of the Ce^{4+} relative to the Pr^{3+} ions, thus allowing interstitial oxygen's (excess oxygen?) existence or removal to have nominally no affect on the c-axis length. Tsukada *et al.* [142] also report a decrease in the c-axis lattice parameter in nominally "non-doped" $La_{1.85}Y_{0.15}CuO_{4+y}$ as oxygen is removed. The amount the c axis changes is consistent with what is observed in optimally doped PCCO. This is attributed to the removal of apical (interstitial) oxygen. It is therefore fairly clear that altering the stoichiometry of oxygen in the cuprates induces structural changes

which can be interpreted as a type of structural disorder due to stress or strain.

Recently, McElroy *et al.* [143] demonstrate using scanning tunneling microscopy that local structural disorder from oxygen doping correlates with local electronic disorder in the p-type cuprate $Bi_2Sr_2CaCu_2O_{8+\delta}$. They find a suppression of superconducting coherence peaks and an impurity peak in the tunneling conductance at -0.96 eV, all in the vicinity of oxygen dopant atoms (Fig. 4.19). These features are all absent far away from the structural disorder of the oxygen dopants. They therefore attribute the majority of electronic inhomogeneity to the structural inhomogeneity from the dopant oxygen.

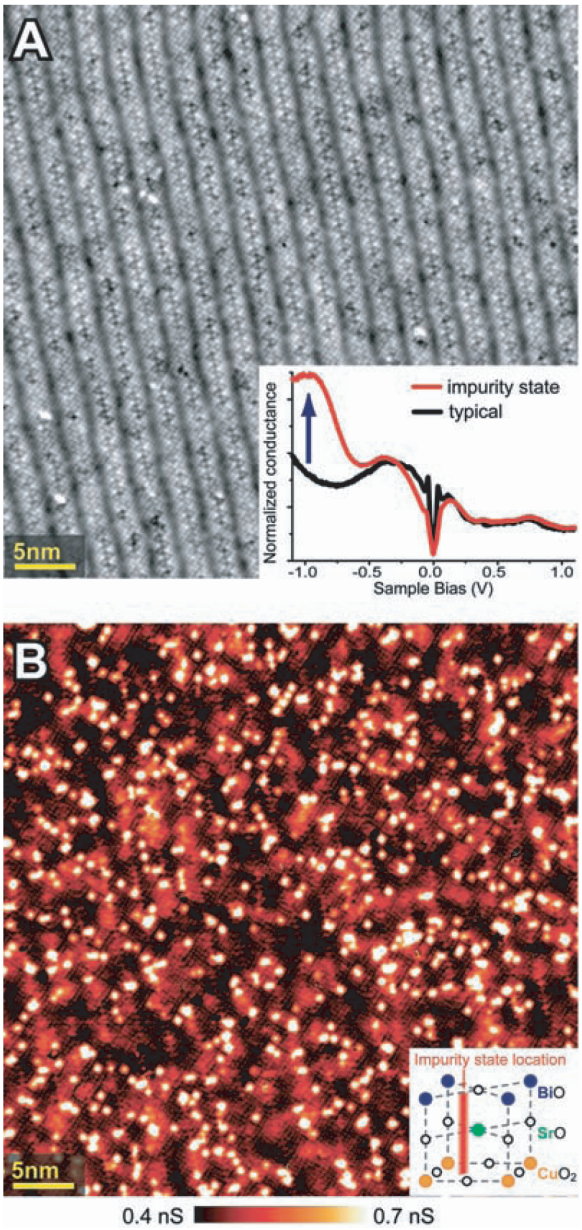

Figure 4.19: STM images of oxygen dopant defects in $Bi_2Sr_2CaCu_2O_{8+\delta}$ single crystals, taken from Ref. [143]. (a) Topographic image of the exposed BiO layer. (B) Differential tunneling conductance measured at -0.9 V. The bright spots correspond to impurity states of the dopant oxygen atoms. Both (a) and (b) display the same area of the crystal. The inset of (a) shows conductance curves at the bright spot and away from the bright spot. The arrow points to the enhanced conductance due to the impurity. Suppressed coherence peaks are also observable in the impurity curve.

Chapter 5

Sample Fabrication

Thin films of overdoped PCCO ($0.12 \leq x \leq 0.19$) were made using a pulsed laser deposition technique. The focus of this work is a specific doping, $x = 0.17$. This technique consists of focusing a high energy density laser beam onto a stoichiometric target inside of a vacuum chamber with a controlled gas environment. The interaction between the laser and the target creates a plasma which is ejected from the surface of the target. The plasma maintains the elemental proportions of the target and deposits onto a single crystal substrate. Under the right conditions, the deposition results in an epitaxial thin film with the same composition as the target.

5.1 Growth and Annealing

The target used for depositions was made using a traditional solid state process. High quality powders of Pr_6O_{11}, and CeO_2, CuO (either four or five 9's pure) were dried and weighed out to give a total target mass of $\sim$ 15 grams with the proper proportion of powders (i.e., to get $Pr_{1.83}$, $Ce_{0.17}$, Cu_1 and the oxygen content takes care of itself). The powders were then mixed thoroughly using an agate pestle and mortar. The mixture was put in an alumina crucible, covered with an alumina lid, and then heated to 900°C at a rate of 100°C/hour in a furnace with an air environment. After 24 hours, the mixture was cooled at the natural rate of the furnace

and then ground to make a fine powder (no visible granules). The powder was re-heated, this time to 1050°C, at a rate of 300°C/hour and stayed at this temperature for 24 hours. After the mixture cooled, it was finely ground, pressed into a pellet, and sintered at 1100°C for 24 hours. This procedure results in a polycrystalline, non-superconducting PCCO sample which we use as a target in the film deposition.

The thin film growth utilizes a pulsed laser deposition technique (PLD) and involves depositing onto a single crystal substrate. A detailed description of growth conditions are available in Ref. [104]. Here I will cover some general information as well as reasons for some of the film growth preparations. The first layers of the deposition mimic the lattice structure of the substrate and it is therefore important to find a substrate which matches the lattice parameters of bulk PCCO. The substrate used in these experiments was (100) oriented $SrTiO_3$ (STO). The structure of STO is cubic with a lattice constant $a = 3.905$ Å. The in-plane lattice constants for PCCO are $a = b \sim 3.953$ Å and the lattice mismatch with STO is $\sim 1.2\%$. Therefore, by choosing a substrate which matches the in-plane PCCO lattice, c-axis oriented (c axis normal to the film surface) crystalline thin films are grown.

The vacuum chamber used for depositions is prepared by cleaning the substrate heater and the target before every deposition. Both are polished using fine grit sandpaper (400 and 600 grit) and a circular motion, clockwise and counterclockwise, in order to reduce the possibility of gouging the surface. Other parts of the chamber require cleaning, but not necessarily before each deposition. The optical window is cleaned, with a colloidal solution followed by solvents, every five or so depositions in order to remove any build up of material. The walls of the chamber are also wiped

down every few weeks. This removes loose dust that may potentially fall on the substrate during preparation/deposition. With the chamber cleaned, the substrate is rinsed (using the solvents acetone, methanol, and isopropanol), dried (using N_2 gas), and affixed to the heater using silver paint and allowed to dry (covered) in air.

The laser used for the deposition is a Lambda Physik LPX 300, 248 nm KrF excimer laser. The beam profile of the laser is another component in the deposition process that needs to be monitored. Changes in the profile could drastically alter the quality of the film. The beam exits the laser and passes through an aperture designed to cut down the cross section of the beam and to give the beam a well-defined rectangular shape. The beam profile is checked after this aperture using laser alignment paper. The desired profile has sharp edges and a uniform burn mark. Due to the high energy of the beam, it is necessary to check the profile uniformity with the alignment paper held at an angle relative to the aperture. This spreads out the beam over a larger area on the paper and allows for an easier visual reading of the homogeneity of the profile, due to a reduced energy density on the paper. Problems with the profile are sometimes caused by too high or too low of a laser operating voltage, as well as misalignment of the laser's internal optics. With a good profile, the beam's total energy is measured with an energy meter and the average energy density is calculated by measuring the laser spot size at the target (again using laser alignment paper).

The deposition of the films is rather straight forward. Once the chamber is closed, we evacuate the chamber until the pressure is below 1×10^{-5} Torr. After adequate vacuum is reached, a preablation procedure is used to "clean" the surface

Table 5.1: Deposition and annealing conditions for PCCO thin films used for oxygenation and irradiation

Sample	Total Energy (mJ)	Spot Size (cm x cm)	Energy Density (J/cm^2)	Dep. Time (min.)	Anneal Pressure (Torr)	Anneal Time (min.)
JP17-2	107	0.12 x 0.47	1.90	15	1×10^{-4}	16
JP17-4	109	0.12 x 0.46	1.97	15	1×10^{-3}	14
JP17-6	110	0.12 x 0.45	2.04	15	2.3×10^{-1}	15
JP17-24	87	0.115 x 0.42	1.8	15	optimal	13

of the target. The conditions for the preablation are identical to the deposition conditions except for the duration (3-5 minutes), the temperature of the substrate, T_s ($T_s \leq 100$°C), and a shutter is used to prevent any deposition onto the substrate. The gas environment used is 230 mTorr N_2O at a flow rate of 100 standard cubic centimeters per minute (sccm). The repetition rate of the laser is 10 Hz. For the deposition, the temperature of the substrate is raised to 770°C at 50°C/minute in vacuum. At temperature, the N_2O environment is reintroduced and the deposition proceeds with the conditions listed in table 5.1. Heating in vacuum rather than a gas environment reduces the time needed to evacuate the chamber for the annealing portion of the film growth (described below). A schematic for the chamber and laser is given in Fig. 5.1.

After deposition, the film is annealed in order to remove oxygen. This is done prior to removing the sample from the deposition chamber. The substrate temperature is lowered to 720°C at the natural rate of the heater ($\simeq$ 30 seconds),

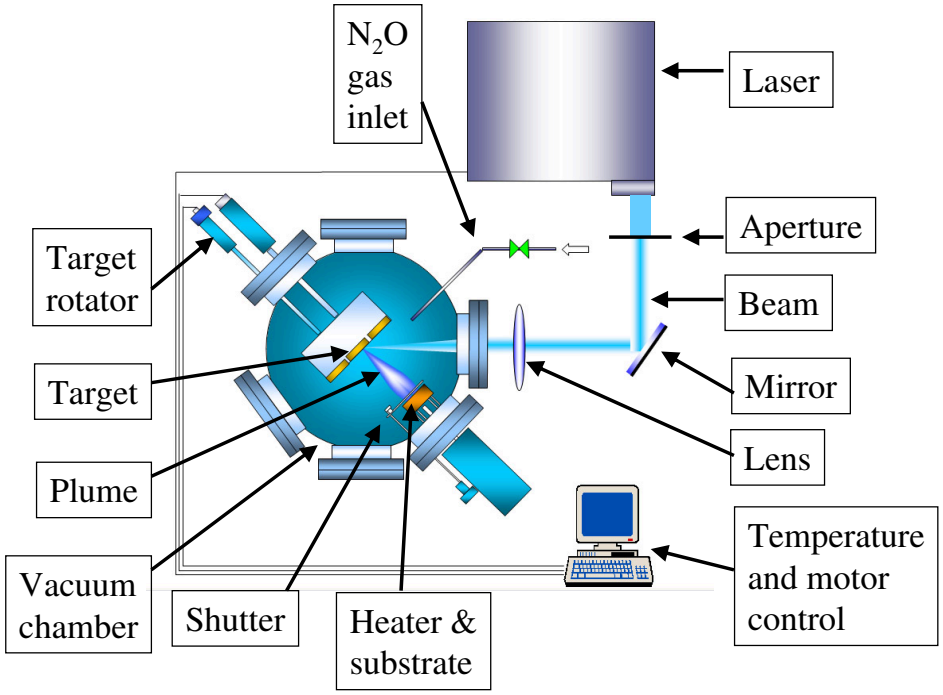

Figure 5.1: Schematic for PLD film growth. The frequently adjusted/maintained components are labeled.

while the N_2O pressure is maintained at 230 mTorr. At temperature, the pressure is reduced (few minutes to reach pressure) and the time of the anneal is monitored once pressure is reached. Two slightly different methods were employed for annealing the thin films and the sample prepared for irradiation was annealed using an "optimal" annealing process. In the first method (optimal anneal), the time of the anneal starts when the pressure in the chamber reaches 1×10^{-4} Torr. The pressure continues to decrease until it reaches 3×10^{-5} Torr ($\simeq$ five minutes) where it is maintained for the duration of the annealing (between ten and 15 minutes).

For the oxygenated films, the annealing is slightly different. In order to increase the oxygen concentration relative to the "optimally" annealed film, the pressure of N_2O is increased from the "optimal" annealing condition. In actuality, oxygen is

not reincorporated into the oxygenated films, rather these films do not have as much oxygen removed. To see how an increase of N_2O pressure results in more oxygen in the film, consider the following [144]. At non-zero temperatures, N_2O will dissociate into N_2 and O_2 (other dissociation results are possible but, for simplicity, we restrict ourselves to only this consideration without loss of generality). The reaction we consider is then

$$2N_2 + O_2 \rightleftharpoons 2N_2O, \tag{5.1}$$

or

$$2N_2 + O_2 - 2N_2O \rightleftharpoons 0. \tag{5.2}$$

For dissociations, the law of mass action states that the product of the reactants is a function solely of temperature. Eq. 5.2 can be expressed as

$$[N_2]^2[O_2][N_2O]^{-2} = \frac{[N_2]^2[O_2]}{[N_2O]^2} = K(\tau), \tag{5.3}$$

where $K(\tau)$ is the equilibrium constant, $\tau \equiv k_BT$, and the brackets denote the concentration. This simply states that as the number of N_2O molecules increases, the number of molecular oxygen also increases. We are concerned, however, with atomic oxygen and not molecular oxygen and we take advantage of dissociation again.

$$2O - O_2 \rightleftharpoons 0 \longrightarrow [O]^2[O_2]^{-1} = \frac{[O]^2}{[O_2]} = K(\tau) \tag{5.4}$$

Therefore, by increasing the N_2O pressure, the number of N_2O molecules increases (from the ideal gas law with T and V held constant) and the number of atomic oxygen in the chamber increases. This increase results in an increase of the chemical potential of oxygen (as well as all other species) inside the chamber.

$$\mu = \tau log(\frac{p}{\tau n_Q}), \tag{5.5}$$

where p is the pressure, and $n_Q \equiv (M\tau/2\pi\hbar^2)^{2/3}$ is the quantum concentration (M is mass). Because we are interested in an equilibrium state between the oxygen in the film and the gas environment, the atomic oxygen chemical potential in the chamber must be equivalent to the chemical potential of the atomic oxygen in the film. Hence, we have a change in the oxygen concentration within the film by changing the N_2O pressure for the annealing process. Previous methods for changing the oxygen concentration involved adjusting the *duration* of the anneal. Since the removal of oxygen is a diffusive process, adjusting the time would not guarantee equilibrium and could result in an inhomogeneous distribution of oxygen within the film.

The annealing for the oxygenated films was done in higher N_2O pressures, where the pressure was maintained for the entire anneal. Table 5.1 gives the annealing conditions. After annealing, the film cools to room temperature at the natural rate of the heater and in the annealing pressure ($\simeq$ 2 hours).

Four thin films were used in this study; three films with different oxygen concentrations, and one optimally annealed film subjected to varying degrees of irradiation.

5.2 Characterization

The films were primarily characterized using ac magnetic susceptibility measurements and visual inspection using an optical microscope. X-ray diffraction (XRD) was performed primarily on films made using new targets, or when deposition conditions significantly changed. A typical XRD pattern is given in Fig. 5.2. Fig. 5.2 shows that the film is dominantly c-axis oriented (c-axis peaks are labeled). There are additional peaks are frequently observed, which are labeled (110) and (220). These peaks are attributed to misaligned PCCO grains in the film [104] and occur during non-optimal growth. They are attributed to these grains rather than an impurity phase of $(Pr,Ce)_2O_{3.5}$ because: 1) the latter does not form under normal solid state reaction conditions, and 2) the peaks are also observed in *undoped* PCO.

Optical microscopy was used to ensure three things: 1) that the film did not have excessive amounts of pinholes, 2) that the film did not have excessive decomposition, and 3) that the film did not show grains. Excessive, in this context, is defined as more than six - ten of any feature within a 200 μm field of view. Pinholes ($\simeq$ 1 micron size holes in the film), we believe, form from dust on the substrate during deposition. Decomposition (black dots typically surrounding transparent "holes", but may occur without the holes) arise from the deterioration of the film during

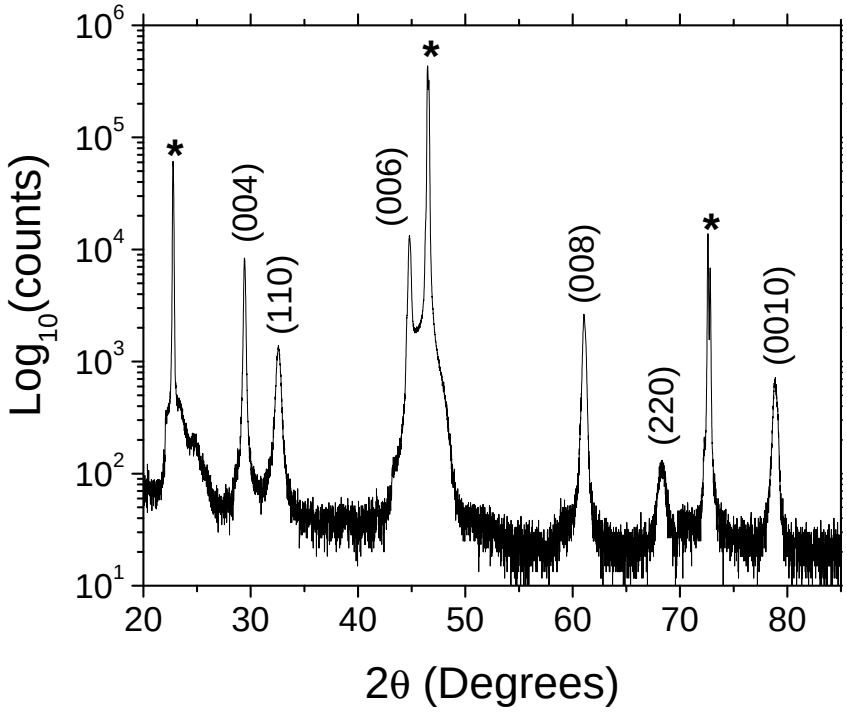

Figure 5.2: X-ray diffraction pattern for an $x = 0.17$ PCCO thin film, sample ID JP17-7, deposited on an $SrTiO_3$ substrate. This particular sample is not annealed. The substrate peaks are identified by an asterisk ($\star$). The other peaks are from the PCCO thin film. While the film is mostly c-axis oriented, "impurity" peaks are frequently observed [labeled (110) and (220)].

the growth/annealing process. This primarily occurs in the cerium optimally and overdoped samples and can be reduced by ensuring a clean substrate (decomposition spots tend to occur around pinholes or dirt) and minimizing the length of time the film is kept at high temperatures. Grains occur from a slow growth rate and look like needles that align along specific directions. Examples of these features (except for grains) can be seen in Fig. 5.3.

The magnetic susceptibility, $\chi(= \frac{dM}{dH})$, is the relation of the material's magnetization to an applied magnetic field and can be expressed as a complex quantity, where the real component (χ') represents the amount of magnetic flux penetration

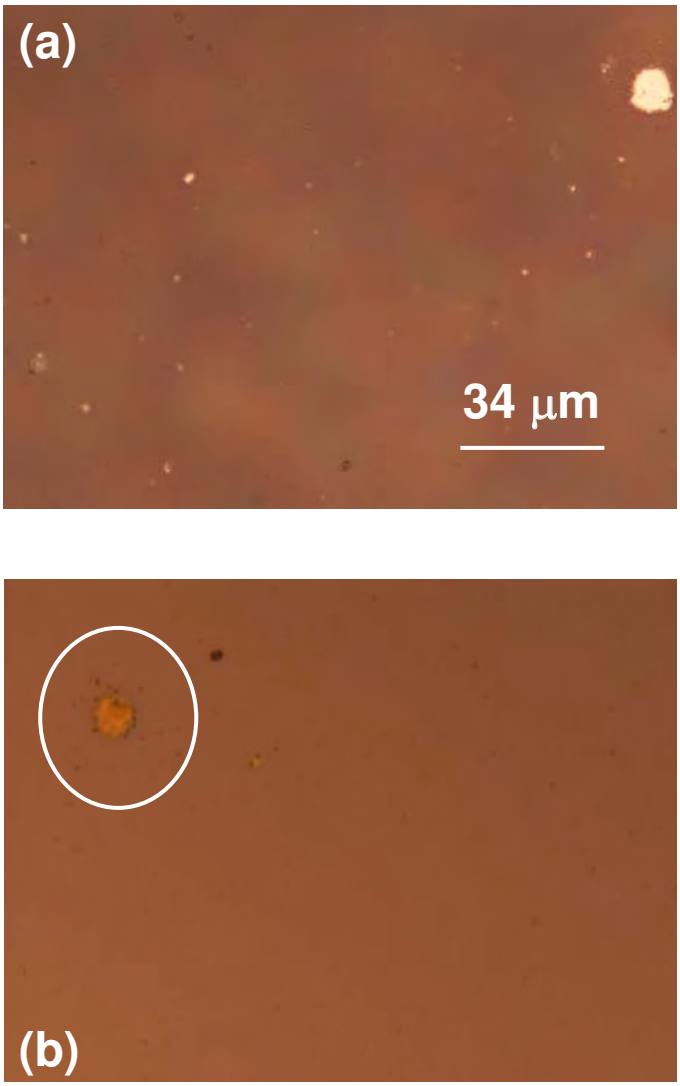

Figure 5.3: Optical microscope images showing visible deterioration of $Pr_{2-x}Ce_xCuO_{4\pm\delta}$ thin films. (a) Example of "pinholes" which develop during film growth (sample JP15-17). The pinholes are the small white spots scattered around the viewing area. (b) Example of decomposition circled in white (sample JP19-17). The light tan colored spot (inside the white circle) is surrounded by black pepper looking spots. The black pepper spots are also seen without the light tan spot, but with much less frequency.

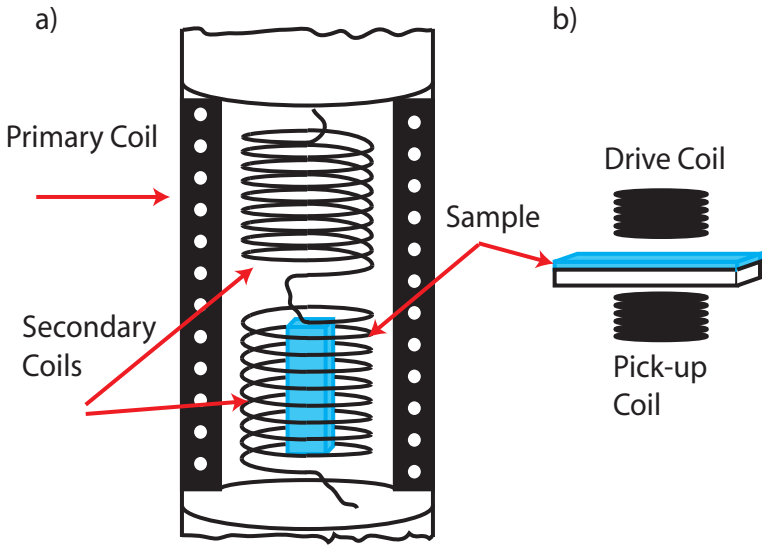

Figure 5.4: AC susceptibility. (a) Traditional susceptometer design. Two counter-wound secondary coils are used to eliminate emf's induced by the primary coil. (b) Design used to measure the temperature dependence of χ in thin films. The film shields the magnetic field from the pick-up coil depending on the susceptibility of the film.

and the imaginary component (χ'') represents the magnetic flux which is 90° out of phase with the applied field. This can be derived from a complex relative permeability [145]. In other words, the real part of the susceptibility represents the magnetic penetration and the imaginary part represents "ac losses" in the sample[1]. As a material transitions into the superconducting state, $\chi' \rightarrow -\frac{1}{4\pi}$ (perfect diamagnestism) and χ'' shows a small peak. These measurements are used to determine the T_c and the width of the transition, ΔT_c, in the films.

AC susceptibility measurements were performed using a homemade ac suscep-

[1]This phrase is in quotes because it is frequently used as an explanation, however its true meaning is lost on me. To the best of my knowledge, the Meissner state has a non-linear response (with magnetic field) that can be represented as a linear plus higher order terms. In this measurement, the linear term is monitored. Therefore, as the material transitions, this linear term becomes non-linear and the imaginary component increases (the shielding of the sample becomes out of phase with the driving field). As the material fully passes through the transition, linearity is again restored in the leading term of the Meissner effect and the sample's response is again in phase with the driving field. This is why a peak is observed in the ac susceptibility measurements.

tometer. This probe is slightly different from a traditional ac susceptometer in which a secondary pick-up coil is concentric within a primary drive coil and the sample is placed inside the secondary coil [Fig. 5.4(a)]. This susceptometer, however, has a drive coil and a pick-up coil *separated* from each other along the common z-axis. The thin film is placed *between* the coils, and the response of the pick-up coil is monitored relative to the drive coil using a lock-in amplifier [Fig. 5.4(b)]. Because the probe is arranged in this fashion, we actually measure how much the pick-up coil is shielded by the sample rather than the true χ of the sample. The temperature dependence of this response is still the same as the temperature dependence of χ. The idea is that the magnetic field of the drive coil induces a magnetic moment in the sample. By applying an ac signal to the drive coil and changing the temperature, we can directly measure the temperature dependence of the sample's susceptibility ($\chi=\frac{dM}{dH_{ac}}$) through the pick-up coil. The changing field provided by the drive coil produces an emf in the pick-up coil, which is monitored. The magnetic state, or transitions between magnetic states, of the sample between the coils affects the magnetic field seen by the pick-up coil. Hence, the pick-up coil's response relative to the applied signal is proportional to the sample's magnetization, i.e. the susceptibility. In the normal state, $T > T_c$, the material shows a very small paramagnetic susceptibility and the signal registered by the pick-up coil is large and positive due to the relatively small shielding of the material between the coils. As the temperature is lowered through the transition, the material begins to screen the magnetic field as it enters the Meissner state, and the magnitude of the signal (the real part of the susceptibility) seen by the pick-up coil decreases towards zero. Because the

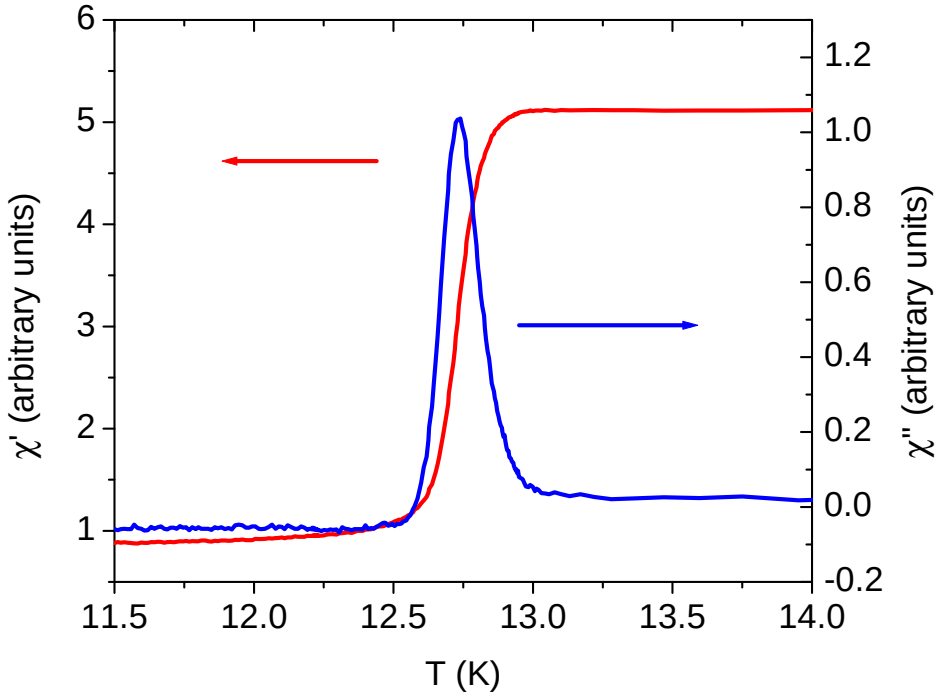

Figure 5.5: AC susceptibility measurement on sample JP17-24 (used for irradiation). The T_c is determined from the peak in χ'' and ΔT_c is determined from the full width at half maximum in χ''.

shielding is nonlinear in the mixed state, the phase lag between the pick-up coil and the drive coil increases and then decreases as the material passes through the mixed state. This peak in the phase is the imaginary component of the susceptibility that we measure. In addition to T_c and ΔT_c, these measurements can yield additional information about the quality of the sample. In particular, a smooth and sharp transition in both χ' and χ'' indicate a single phase superconductor with good homogeneity. Macroscopic inhomogeneity in either the cerium or oxygen concentration typically yield deviations in the shape of χ. A typical ac susceptibility measurement is given in Fig. 5.5.

5.3 Patterning

For measurements of the Hall effect and resistivity, the thin films are patterned (or "cut") into Hall bar geometries. The pattern used for the oxygenated samples is called an eight-contact Hall bar and is schematically shown in Fig. 5.6(a). This configuration passes current down a center pathway (bridge) and voltage measurements are made through the voltage "legs" that are perpendicular to the bridge. The method for patterning this configuration consists of using a mechanical mask and an ion-mill. The mechanical mask is made of stainless steel and covers the parts of the film which we do not want removed (i.e. the Hall bar). The film sits in a holder (made of nickel) and the mask is secured over the surface of the film using screws. The film holder and mask apparatus is placed inside an ion-mill, where a collimated beam of argon ions is accelerated toward the film. The high-energy ions etch away the parts of the film which are exposed to the beam.

The thin film used for irradiation was patterned in a slightly different way. This sample was designed to have multiple, separate Hall pads along a common bridge, which would be irradiated with varying doses. This setup allows a single thin film to contain multiple irradiation samples. Rather than using a mechanical mask, photolithography was used to make the pattern for the film. This technique allows the use of smaller patterns as the features can be as small as 2 μm x 2 μm. The principle concept is that a uv sensitive polymer (resist) is uniformly spread (spun) onto the film. A pattern is used to cover the portions of the film which will ultimately be kept (i.e., the Hall bar). The sample (film, resist, pattern) is

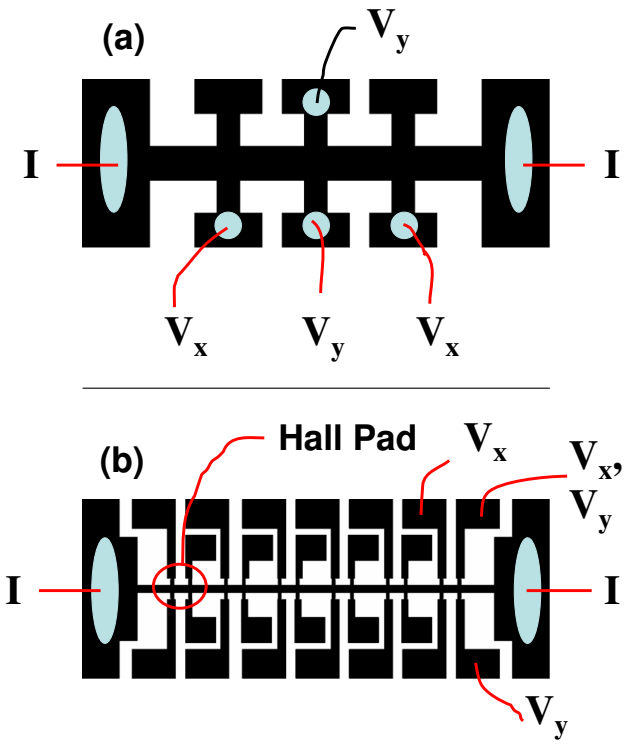

Figure 5.6: Hall Bar Schematics. Current pads are at the left most and right most side of the patterns. The voltage pads connect to the center "bridge" via "legs" and are situated on both sides of the bridge. (a) Eight contact pad pattern used for the oxygenated thin films. The two outermost voltage pads (on the same side of the bridge) are used to measure the longitudinal resistance ($R_{xx} = V_x/I_x$) , while the two (opposing) center voltage pads are used to measure the transverse (Hall) resistance ($R_{xy} = V_y/I_x$). (b) A variation of a six pad Hall bar geometry used for the irradiated sample. The design allows up to six "Hall pads" (circled in red) along a common current path. Both patterns are designed to fit on a 5 mm x 10 mm thin film.

exposed to uv light, which changes the chemical bonds of the resist. The sample is then soaked in a developer and rinsed. The developer removes the resist that was exposed to the uv light, whereas the resist which was covered by the pattern remains on the film. The sample is baked in order to harden the resist and the ion-mill is again used to etch away the unwanted material. Because some of the resist is etched away during milling (along with everything in the ion mill), care needs to be taken that a thick enough layer of resist is used. The etch rate of the resist is slightly less

than half that of PCCO. A schematic of the pattern used for the irradiated sample is shown in Fig. 5.6(b).

5.4 Irradiation

The irradiation was performed at the Naval Research Laboratories by Dr. B. D. Weaver. The sample (JP17-24) was irradiated with 2 MeV H^+ ions (protons) at doses of 0, 1, 2.5, 8, and 32 x 10^{15} ions/cm^2, with different Hall pads subjected to different doses.

The following brief description comes from a review on radiation damage in the cuprates [134]. The effects of irradiation performed on this sample fall into the category of non-ionizing radiation, meaning that any spatially charged regions created by the protons either do not have long lifetimes or do not influence transport properties[2]. The non-ionizing radiation damage primarily causes atoms to be displaced from their regular lattice sites into irregular lattice sites, creating *vacancies* and *interstitials*. A secondary effect is that these defects may also form clusters. In the energy range used to irradiate our sample (2 MeV), the protons are able to fully pass through the thin film and any scattering processes with atoms in the lattice are Rutherford in nature. Figure 5.7 shows the non-ionizing energy loss (NIEL) versus incident particle energy in the p-type cuprate YBCO. The NIEL is a measure of the rate at which the irradiating proton loses energy to displaced lattice atoms. The linear portion of the proton curve shows the regime in which Rutherford interac-

[2]Ionizing effects from gamma-irradiation experiments have been found to have almost no consequences on the electronic properties of the cuprates, at least in comparable energy ranges. Therefore, all observed behavior is attributed to non-ionizing effects.

tions occur. As the curve becomes nonlinear and flattens out, nuclear effects occur and need to be considered. In this regime, the protons are able to penetrate deep into the electron cloud and interact more directly with the nucleus (6-8 MeV), and at high enough energies (15 MeV) can break the nucleus apart. Several spectroscopy studies have shown that these defects have strain fields which are several nanometers in size. Therefore, one defect could affect several unit cells of PCCO. Additionally, since the amount of energy that the protons can impart to the lattice atom is inversely proportional to the mass of the lattice atom, the lighter atoms will be affected more easily than the heavier atoms. In the case of the cuprates, this means that the oxygen atoms are the dominant recipient of irradiation damage.

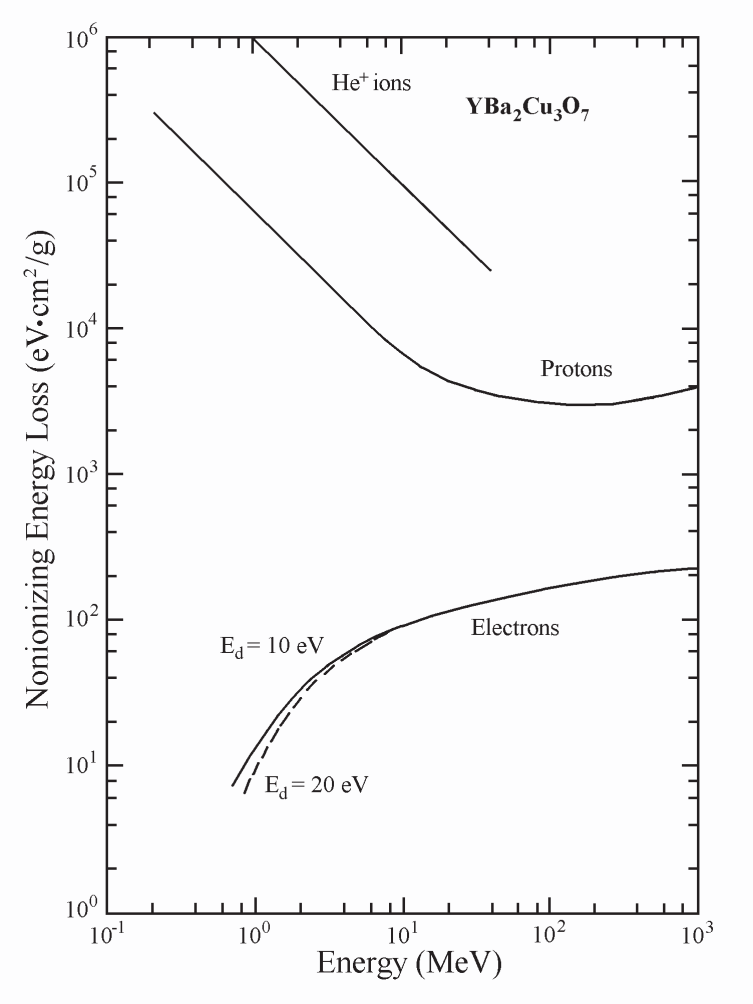

Figure 5.7: Non-ionizing energy loss versus incident particle energy for YBCO, taken from Ref. [134]. The linear portion of the proton curve represents the regime of Rutherford scattering.

Chapter 6

Transport Measurements and Analysis

Up to this point, this thesis has reviewed some of the issues regarding the resistivity, magnetoresistance (MR), and Hall coefficient (R_H) in $RE_{2-x}Ce_xCuO_{4\pm\delta}$ (RE = Nd, Pr) (NCCO, PCCO), as well as these properties when the material is intentionally disordered. The main objective of this chapter is to clarify the role of oxygen reduction in these n-type cuprates.

Originally, Dagan *et al.* [45] found evidence for a quantum critical point (QCP) in PCCO, where the control parameter was cerium doping. It is difficult to finely tune through the QCP in PCCO using doping as the control parameter, because this entails making entirely new deposition targets for each incremental change in doping. This is different from systems in which the tuning parameter may be a magnetic field or even pressure, parameters which are relatively easily tuneable.

For PCCO, the question arose as to the practicality of using oxygen as a dopant. Adjusting the oxygen near the level of optimal reduction may have allowed us to finely tune the carrier concentration as the primary effect. However, adjusting the oxygen content has an overshadowing disorder component, never resulting in an increase of T_c. Instead, we compare the effects of adding oxygen to optimally reduced PCCO with the disorder created from ion irradiation. By using the irradiated sample as a disorder standard, we attempt to determine the doping and disorder

contribution to a changing oxygen content.

6.1 Overview of the Measurements

Note: Throughout this chapter, I frequently interchange ρ_{ab} and ρ_{xx}, as they are equivalent. Both nomenclatures are found in the published literature.

The measurements (ρ, MR, and R_H) are performed using a commercially available Quantum Design Physical Property Measurement System (PPMS). The PPMS is capable of temperatures between 0.35 K and 400 K, and magnetic fields up to $\pm$14 T. The measurements are made using current polarity switching, in order to minimize any thermal voltages due to temperature gradients in the leads running from room temperature down to the sample. At low temperature, measurements of ρ(T) are taken by stepping the temperature. At each temperature, several data points are averaged together. At higher temperatures, data is taken while sweeping the temperature at a slow rate (i.e., data is taken while the temperature continually changes) without any averaging. Measurements of ρ(H) (i.e., MR) are taken while sweeping the field at a slow rate ($\simeq$ 30 Oe/sec). The resistivity is calculated by

$$\rho_{xx} = \frac{R_{xx} \cdot \mathrm{w} \cdot \mathrm{t}}{\mathrm{L}} \tag{6.1}$$

where w, t, and L are the width of the current bridge, the thickness of the sample, and the length between voltage legs, respectively.

Hall measurements are taken with the magnetic field perpendicular to the ab plane ($H \| c$ axis, or $H \perp ab$ plane) and in one of two ways: 1) at a constant tem-

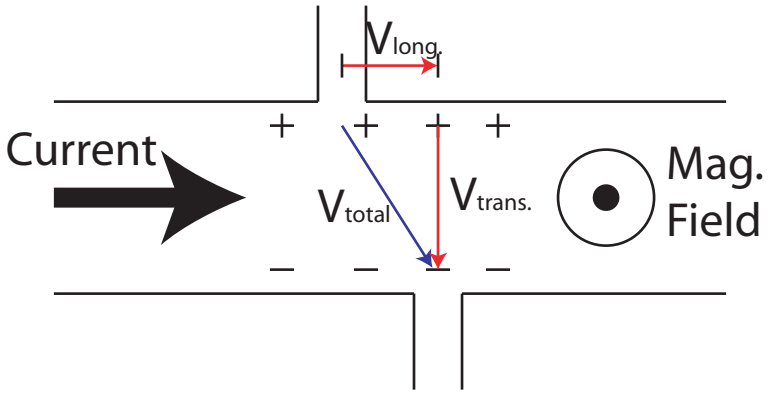

Figure 6.1: Schematic Hall bar voltage leg offset. The displacement of the Hall voltage legs along the current path yields a non-zero voltage ($V_{long.}$) in zero applied magnetic field (similar to measuring the longitudinal resistance). This "offset voltage" is symmetric in field (as MR typically is), whereas the Hall voltage ($V_{trans.}$) is asymmetric with field. By subtracting the voltages, measured between these two legs, in negative magnetic field polarity from positive field polarity, the transverse voltage is isolated from V_{total}.

perature, the magnetic field is swept ($\simeq$ 30 Oe/sec) from positive (negative) fields to negative (positive) fields; 2) at a constant field, the temperature is swept. Both positive and negative field polarities are important for determining R_H because the voltage legs are never perfectly lined up across from each other, hence a longitudinal resistance will be measured in addition to the transverse resistance (typically corresponding to a 1 μm longitudinal offset), schematically shown in Fig. 6.1. This results in a non-zero resistance at zero magnetic field, as well as an MR due to this offset. In order to remove the longitudinal resistance and its MR (which is symmetric with magnetic field), the transverse resistance from the negative magnetic polarity is subtracted from the transverse resistance from the positive polarity. This leaves the asymmetric Hall resistance. For both methods, the Hall resistivity ρ_{xy} is

calculated by

$$\rho_{xy} = \left[\frac{\mathrm{R}_{xy}(B_+) - \mathrm{R}_{xy}(B_-)}{2}\right] \cdot \mathrm{t}. \tag{6.2}$$

where t is the thickness of the sample, and $\mathrm{R}_{xy}(B_\pm)$ is the transverse resistance at positive or negative magnetic fields, and $\mathrm{R}_{xy} = \mathrm{V}_y/\mathrm{I}_x$. All other sample dimensions cancel in the following way.

$$\rho_{xy} = \frac{E_y}{J_x} = \frac{V_y}{w}\frac{wt}{I_x} = R_{xy}t \tag{6.3}$$

In the first case, where the field is swept at constant temperature, R_H is determined by taking the slope of $\rho_{xy}(B)$, i.e., $R_H = \frac{d\rho_{xy}}{dB}$. In the second case, $R_H = \frac{\rho_{xy}}{B}$. Both methods should be identical in the regime where R_H is linear in field. Differences in fitting ρ_{xy} versus B (i.e., forcing the fit through $B = 0$, or allowing a non-zero intercept) can yield values of R_H which differ from each method by as much as 4%. All values of R_H, by magnetic field sweeps, presented in this chapter are obtained with a linear fit which allows for non-zero offsets.

6.2 Oxygenation versus Ion Irradiation

Overdoped thin films of PCCO ($x = 0.17$) are deposited and patterned following the methods described in Section 5.1. Overdoped samples were initially chosen due to the QCP ($x \simeq 0.165$) being on the slightly overdoped side of the phase diagram. This side of the T_c versus doping phase diagram is also convenient for exploring doping effects, because a decrease in the effective doping should increase

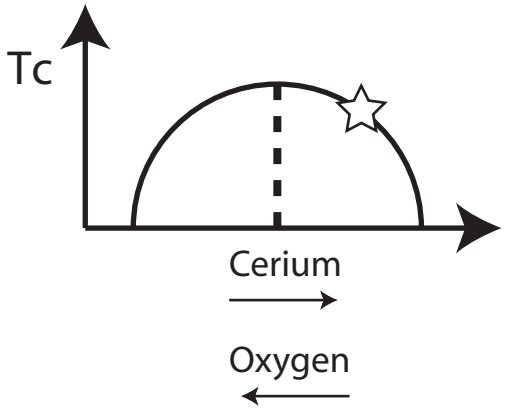

Figure 6.2: T_c versus doping phase diagram (schematic) for $Pr_{2-x}Ce_xCuO_{4\pm\delta}$. Dashed line indicates optimal cerium doping ($x \simeq 0.15$). The star on the diagram indicates the Ce doping presented in this chapet. Electron carrier concentration increases to the right with cerium content. Increasing oxygen concentration decreases the electron carrier concentration and is represented by moving to the left. Upon cerium doping, the material becomes more metallic and the residual resistivity *decreases* as one moves to the right in the diagram.

T_c, whereas an increase in the effective doping will decrease T_c (Fig. 6.2). In order to analyze disorder from impurities, it is important to be able to determine the residual resistivity $\rho_\circ$. This is the second incentive for using overdoped compositions, as the resistivity upturn observed in the underdoped compositions is "absent" in the overdoped compositions. The lack of an understanding of the origin of the resistivity upturn makes it difficult to subtract out the upturn, due mostly to the fact that it is unclear at which temperature the phenomena, which drives the upturn, becomes influential in ρ(T). The absence of an upturn allows for an easier determination of $\rho_\circ$.

The samples made are outlined in Section 5.1, but, just to reiterate, three thin films (t $\simeq$ 3000 Å) are grown with different oxygen content, and one thin film is grown for ion irradiation (2 MeV H^+). The film grown for irradiation accommo-

dates several Hall pads which are disordered with different doses, as mentioned in Chapter 5.

6.2.1 Data

First we look at the resistivity of the oxygenated and irradiated samples (Fig. 6.3). The black data [Fig. 6.3(a) and (b)] is from a sample annealed in 1×10^{-4} Torr, which is very close to the optimal annealing conditions. The arrow indicates the order of increasing oxygen content (annealing pressures of $1 \times 10^{-3}, 2.3 \times 10^{-1}$). The oxygenated samples show an increase in the residual resistivity as oxygen in increased from a nearly optimally reduced oxygen content. This can be seen by expressing the resistivity as $\rho_{ab} = \rho_\circ + \rho(\mathrm{T})$. If the temperature dependent resistivity is not changing, and plots are shifted by a constant, then the contribution is primarily due to the temperature independent $\rho_\circ$. The same behavior is observed in the irradiated samples, where again the arrow indicates the order of increasing irradiation (doses: $0, 1, 2.5, 8, 32 \times 10^{15}$ ions/cm^2) and the black data is from the non-irradiated Hall pad on the same sample [Fig. 6.3(c) and (d)].

The residual resistivity is determined by fitting the normal state resistivity, which is achieved by quenching superconductivity in a magnetic field of 10 T, applied perpendicular to the ab plane (i.e., $B \| c$ axis). Figure 6.4 shows the normal state resistivity of the irradiated and oxygenated samples. The arrows indicate the order of increasing oxygen or irradiation. There is one thing to note: a small upturn develops and shifts towards higher temperatures with oxygenation or with irradiation.

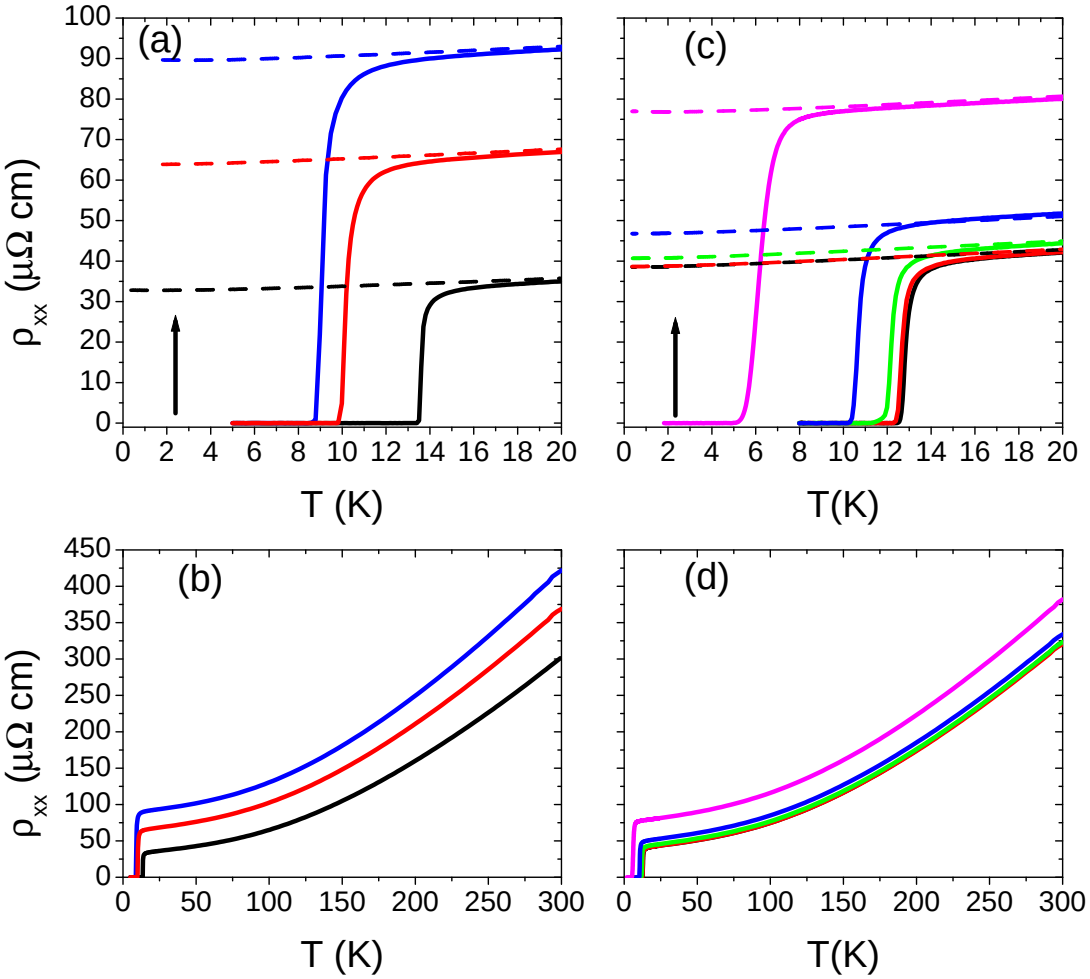

Figure 6.3: ab-plane resistivity versus Temperature for $x = 0.17$ cerium-doped PCCO thin films. Solid lines are data taken in zero applied magnetic field. Dashed lines are taken in a 10 T field ($B \parallel c$ axis) and roughly coincide with $B = 0$ T above T_c. Scales for (a) and (c) are the same, as well as for (b) and (d). (a) Films with different oxygen content. The arrow indicates the order of increasing oxygen, and the corresponding post-deposition annealing pressures are: 1 x 10^{-4} (black), 1 x 10^{-3} (red), and 2.3 x 10^{-1} Torr (blue). (b) Full temperature scale for the same oxygenated films presented in (a). (c) A single, optimally annealed, film subjected to increasing irradiation doses. The arrow indicates the order of increasing irradiation corresponding to doses 0 (black), 1 (red), 2.5 (green), 8 (blue), and 32 (magenta) $\times 10^{15}$ ions/cm^2. (d) Full temperature scale for the irradiated film presented in (c). Notice the nearly parallel shifts in the data for increasing oxygen content or for irradiation dose.

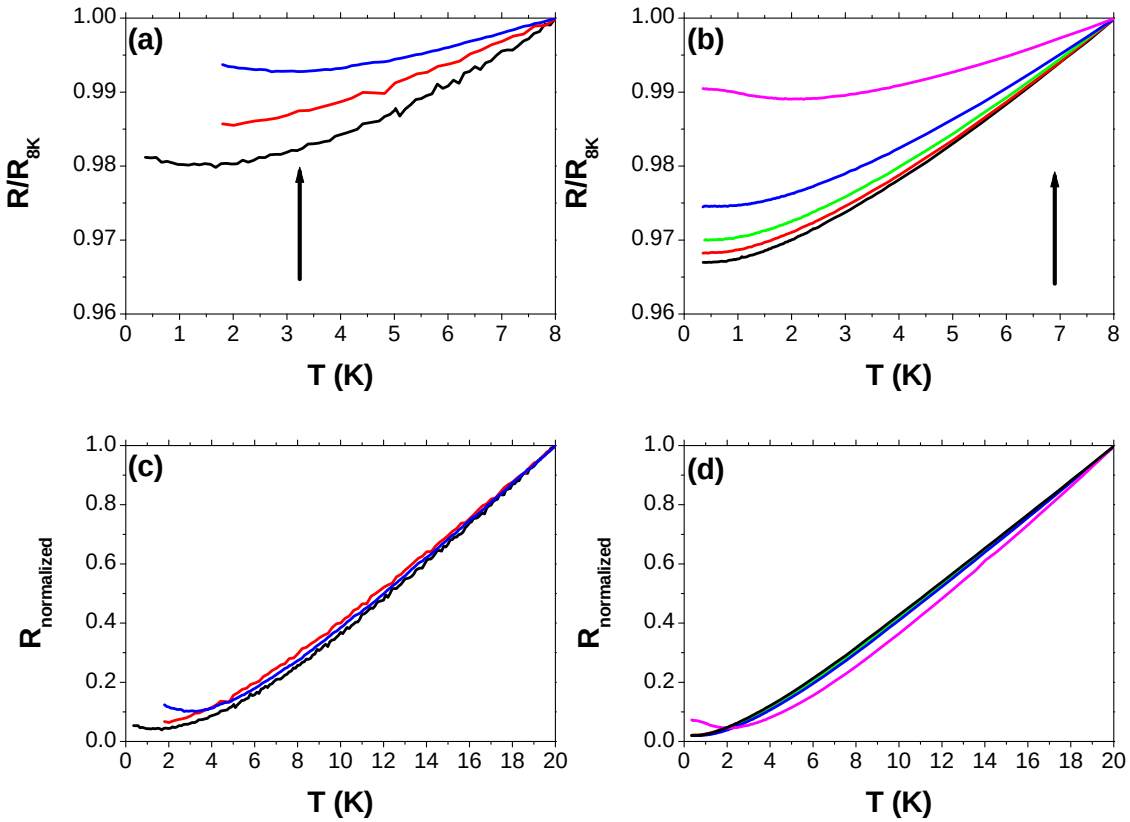

Figure 6.4: Low Temperature resistivity of $Pr_{1.83}Ce_{0.17}CuO_{4\pm\delta}$ thin films subjected to oxygenation or irradiation. Thin films with increasing oxygen content (a) and irradiation dose (b). The arrow indicates the order of increasing oxygen or irradiation dose. The resistivity is normalized by the value at 8 K for ease of viewing. Notice a slight upturn developing with increasing oxygen/irradiation. The most irradiated sample (magenta curve in (b)) shows a slight saturation at low temperatures. This is due to heating and is not intrinsic. (c) and (d) show the normalized resistivity with the residual resistivity subtracted for the oxygenated and irradiated samples ($R_{normalized} = [\rho(T) - \rho_\circ]/\rho_{20K}$). Plotting the data in this way shows that the temperature dependence is not changing within these levels of oxygenation and irradiation (i.e., β in Eq. (6.4) is not changing significantly). The most irradiated sample shows a slight deviation.

This is in addition to the change in $\rho_\circ$. The upturn has been observed by Woods *et al.* [140] when very high doses of irradiation were impinged on the thin films of NCCO. However, at high doses, the upturn is large and follows a variable range hopping model. It is possible that highly oxygenated thin films of PCCO (much more oxygen than done in this study) would have an upturn similar to what was observed by Woods *et al.* [140]. The normal state resistivity is fit to the following relation in the range of $T = 20$ K down to the minimum of the upturn (typically less than 1 K).

$$\rho_{ab} = \rho_\circ + \mathrm{AT}^\beta, \tag{6.4}$$

where $\rho_\circ$, A, and β are free parameters. For this analysis we are interested in the values of $\rho_\circ$, which is relatively insensitive to the fit. An example of this fit is given in Fig. 6.5. The standard deviation for $\rho_\circ$ is taken from the fit.

We are also interested in how T_c changes with either oxygenation or irradiation. The transition temperature is determined from the peak in the derivative plot ($\mathrm{d}\rho/\mathrm{d}T$) of the zero magnetic field data [Fig. 6.3(a) and (c)]. The uncertainty associated with this value is taken to be the full width at half maximum (FWHM). An example of this is given in Fig. 6.6. For both the oxygenated and the irradiated samples, T_c *decreases* as oxygen is added or disorder is induced by irradiation.

One notices from Fig. 6.3 that T_c is suppressed faster, for a given change in $\rho_\circ$, in the irradiated sample than in the oxygenated samples. Figure 6.7 shows this point graphically. The difference between the oxygenated and irradiated samples may be due to an effective doping from the added oxygen. Remember, adding oxygen is

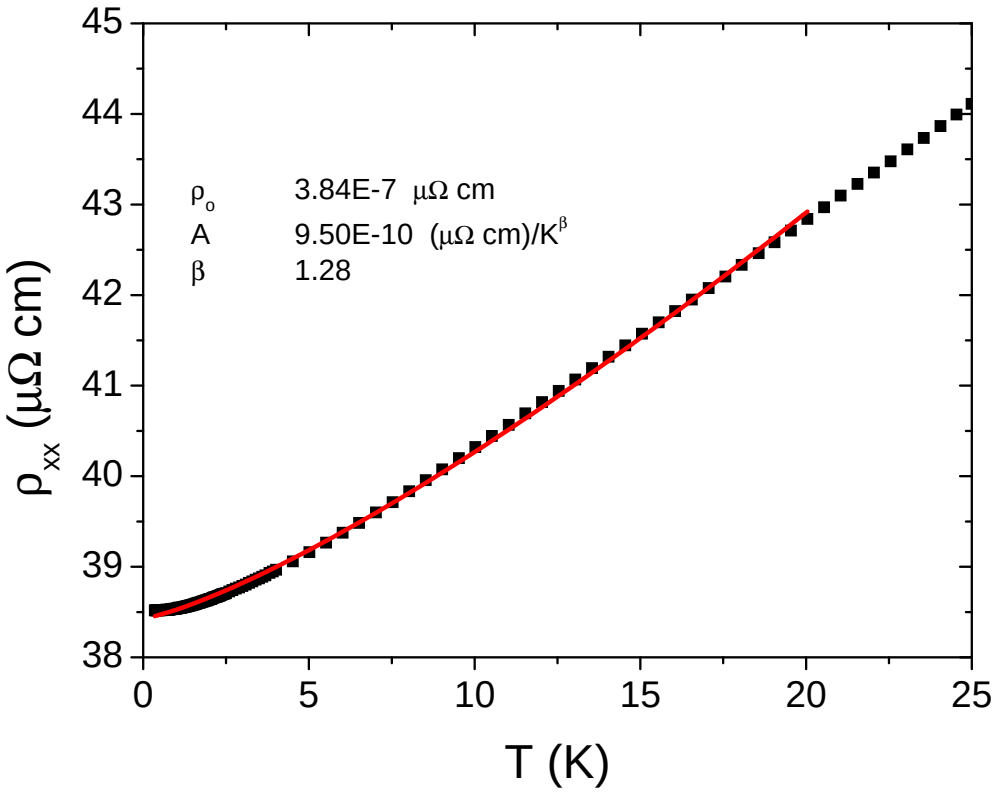

Figure 6.5: Example of fit to the low temperature normal state resistivity of $Pr_{1.83}Ce_{0.17}CuO_{4\pm\delta}$ thin films. This particular fit is from the irradiated sample, JP17-24, on the pad which was not irradiated. The fit is made using Eq. (6.4) and is represented by the red curve.

like removing cerium. Therefore, adding oxygen should shift the effective doping to lower values (moving to the left on the phase diagram, see Fig. 6.2). As the doping decreases (in the case of optimally annealed samples), $\rho_\circ$ increases. Hence, the difference displayed in Fig. 6.7 may be due to doping. The more detailed analysis to follow indeed shows this is the case.

Before venturing into a more thorough analysis, we need to look at the Hall coefficient. Figure 6.8 shows R_H versus Temperature for both the irradiated and oxygenated samples. The Hall coefficient is determined using ± 14 T field sweeps and taking the slope of ρ_{xy} versus Field. For T $\leq T_c$, the high-field range is used ($\mu_\circ H \gg$

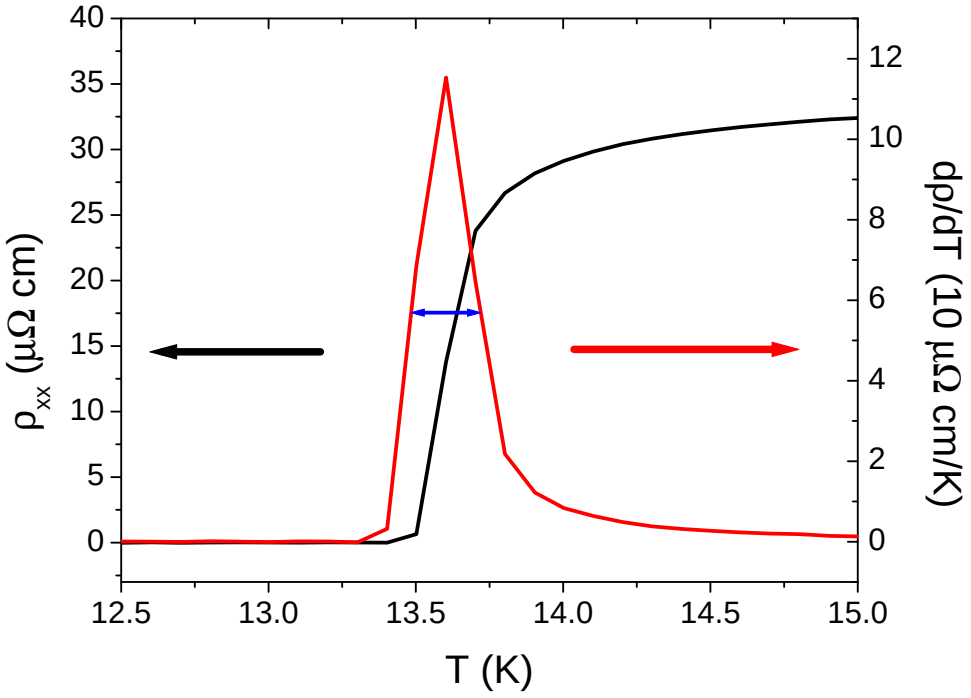

Figure 6.6: Example of the determination of T_c for the $Pr_{1.83}Ce_{0.17}CuO_{4\pm\delta}$ thin films. The zero field resistivity is plotted alongside the derivative plot. The T_c is determined by the peak in the derivative plot and the uncertainty is determined from the FWHM (blue arrow).

$\mu_\circ H_{c2}$). An example is given in Fig. 6.9. The oxygenated samples show a decrease in magnitude of R_H as the oxygen content increases. This trend is consistent with a decrease in cerium doping, from $x = 0.17$ toward $x = 0.16$. The T_c, however, does not increase as would be expected from a purely cerium-doping standpoint (Fig. 6.2). In contrast, the irradiated sample shows an *increase* in R_H with irradiation. Since the relative change in R_H of the irradiated sample is in the direction *opposite* to that observed in the oxygenated samples, we make the assumption that the primary result of irradiation is to induce disorder (i.e. affect scattering) with no effect on the carrier density. An increase in R_H indicates an increase in electron doping, if the increase is attributed to a change in carrier concentration (increasing the cerium

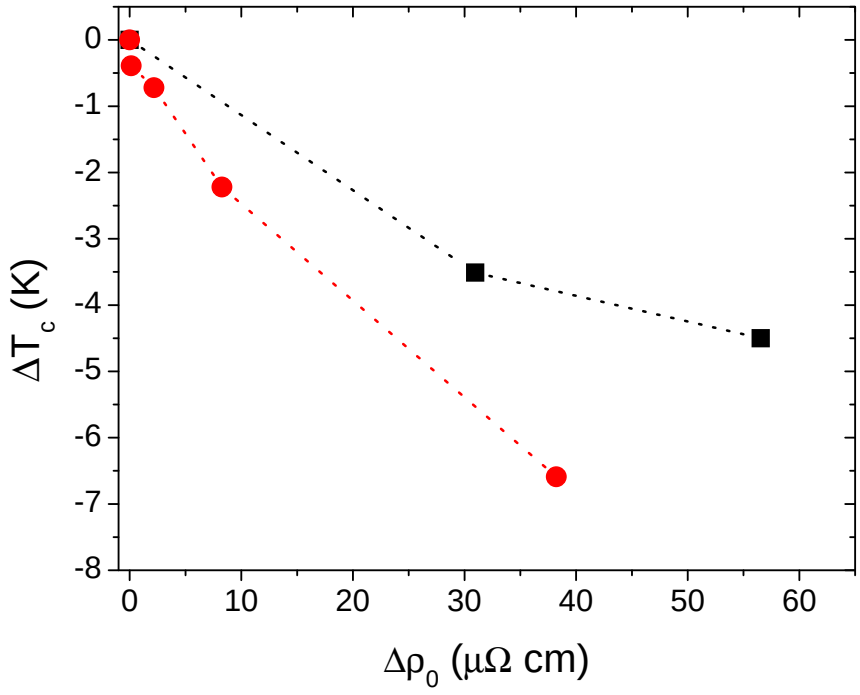

Figure 6.7: ΔT_c versus $\Delta\rho_\circ$ for oxygenated and ion irradiated $Pr_{1.83}Ce_{0.17}CuO_{4\pm\delta}$ thin films. Squares are the oxygenated thin films. Circles are the irradiated thin films.

content - electrons - shifts R_H towards more positive values). This allows us to use the irradiation data as a measure of only the disorder for these samples. This assumption draws on the fact that 2 MeV H^+ ion-irradiation mainly creates oxygen vacancies and interstitials, with no loss of total oxygen. This rearrangement of the oxygen should have little effect on the carrier density [135, 140].

6.2.2 Analysis

The above mentioned observations lead us to the model chosen to analyze the data and to ultimately clarify the role of oxygen in this class of material. The residual resistivity is given by $\rho_\circ = \frac{m^*}{ne^2\tau}$ where m* is the effective mass, n is the carrier density, e is the electronic charge, and τ is the time between elastic scattering

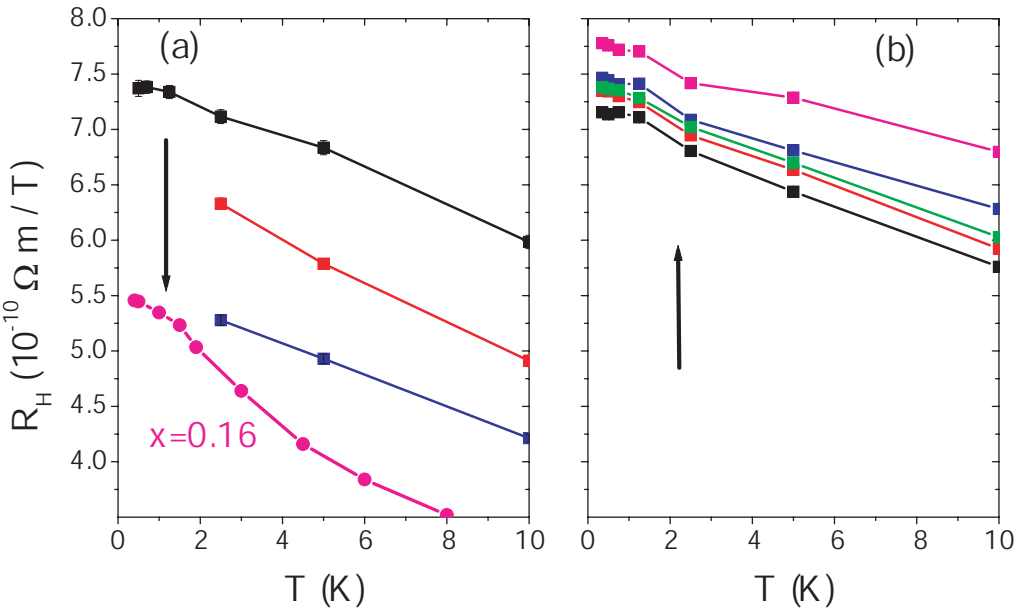

Figure 6.8: R_H versus Temperature for oxygenated and ion irradiated thin films of $Pr_{1.83}Ce_{0.17}CuO_{4\pm\delta}$. Scales for both plots are identical. (a) Films with different oxygen content (arrow indicates order of increasing oxygen). The data labeled x = 0.16 (•) is from an optimally annealed $x = 0.16$ cerium-doped thin film. With increasing oxygen, R_H shifts towards values similar to lower cerium doping compositions. (b) Single (optimally annealed) film subjected to increasing irradiation doses (arrow indicates order of increasing irradiation dose). Notice that the change in R_H is *opposite* to that observed in (a).

events. The Hall coefficient for a simple metal is given by $R_H = \frac{1}{ne}$. PCCO is usually *not* classified as a simple metal and its transport properties have been qualitatively interpreted in terms of a two-band model (Ref.'s [59, 83] and references therein). However, using a two-band model, without expanding the number of measurements, makes quantitative analysis dubious. Thus we restrict ourselves to the one-band Drude model and bear in mind that this model is oversimplified. While we do not attempt to calculate the carrier density from R_H, I do use R_H as an *empirical measure* of the carrier concentration. Since R_H is related to the number of carriers and $\rho_\circ$ to both the number of carriers and impurity scattering, it is possible to

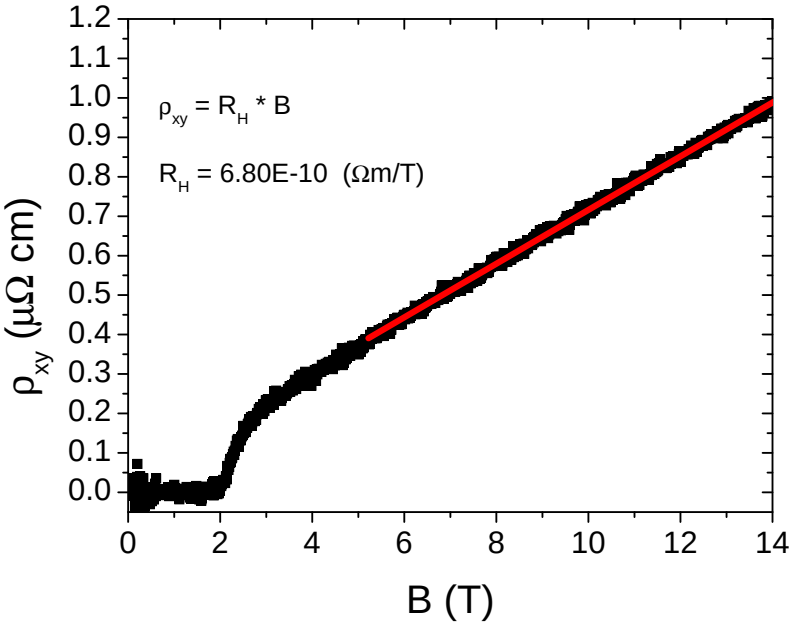

Figure 6.9: ρ_{xy} versus Magnetic Induction for a $Pr_{1.83}Ce_{0.17}CuO_{4\pm\delta}$ thin film. This particular data set is from sample JP17-24 at T= 2.5 K. The sample goes from a superconducting state at low fields into the field-driven normal state at higher fields. The Hall coefficient is determined from the normal state (linear portion at higher fields). A linear fit is shown by the solid red line and is used to determine R_H.

differentiate disorder effects from the carrier concentration effects by measuring $\rho_\circ$ and R_H at low temperatures.

Using these relations for $\rho_\circ$ and R_H, I now determine the contribution to $\rho_\circ$ and T_c due to additional disorder in the oxygenated samples. I then compare the disorder effect on T_c with the measured T_c and we show that the oxygenated samples have an additional, positive contribution to T_c, which has a behavior similar to that of cerium doping. In order to show this, I write the residual resistivity of the oxygenated samples as

$$\rho_\circ(\mathrm{O}_2) = \frac{m^*}{e^2(n+\Delta n)}\left(\frac{1}{\tau_\circ}+\frac{1}{\tau_1}\right), \tag{6.5}$$

where Δn represents any change in the carrier density, $\tau_\circ$ represents the low temperature elastic scattering term inherent in the optimally annealed system, and τ_1 represents the low temperature elastic scattering term due to additional disorder introduced by the extra oxygen. The effective mass is taken to be independent of doping [146, 147] and is a constant in this analysis[1]. After expanding the $(\frac{1}{n+\Delta n})$ factor, we rewrite Eq. (6.5) as $\Delta\rho_\circ(\mathrm{O}_2)$ by subtracting $\rho_\circ$.

$$\Delta\rho_\circ(\mathrm{O}_2) = \frac{m^*}{ne^2}\left[-\frac{\Delta n}{n\tau_0} + \frac{1}{\tau_1}\left(1 - \frac{\Delta n}{n}\right)\right]. \tag{6.6}$$

The first term represents changes in the oxygenated samples due only to changes in the carrier concentration. The second term contains effects from both additional disorder and carrier concentration. To simplify Eq. (6.6), I rewrite it as

$$\Delta\rho_\circ(\mathrm{O}_2) = \Delta\rho_\circ(R_H) + \Delta\rho_\circ(\mathrm{disorder}), \tag{6.7}$$

where we use R_H *as a measure of carrier concentration.*

Equation (6.6) says that we are able to *separate* the effects of oxygen on $\rho_\circ$ *if* we can eliminate $\frac{\Delta n}{n}$ in the second term. I calculate $\Delta\rho_\circ(\mathrm{O}_2)$ for each oxygen sample from the raw data by using the sample annealed at 10^{-4} Torr as the reference $\rho_\circ$. This sample is chosen as the reference because I am interested in looking at the changes due to oxygen within the oxygenated samples, and this sample most resembles the "optimally annealed" sample in terms of R_H and $\rho_\circ$. The doping

[1]The effective mass in optimally doped and overdoped PCCO thin films is calculated from optical conductivity data reported by A. Zimmers *et al.* in Europhys. Lett. **70** (2), 225 (2005) and shows no discernable difference between $x = 0.15$ and $x = 0.17$ cerium-doped films.

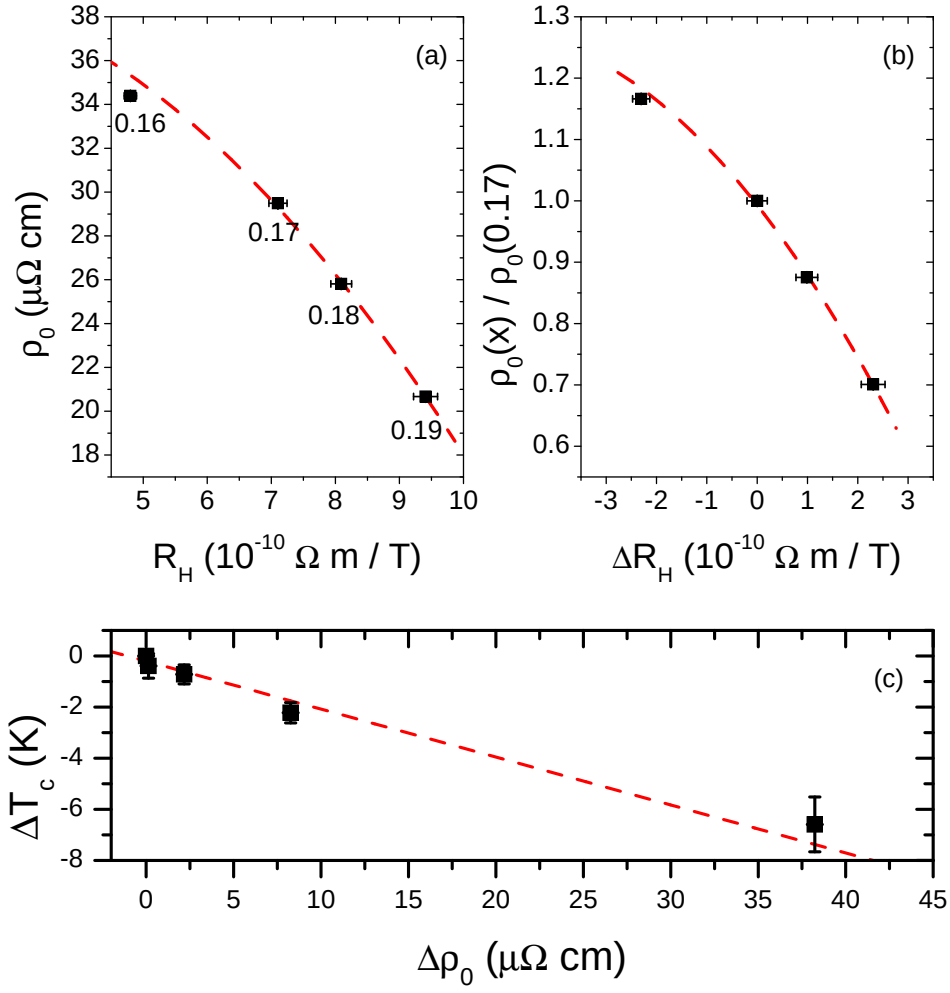

Figure 6.10: (a) Plot of $\rho_\circ$ versus R_H at T= 2.5 K for optimally annealed cerium-doped samples. Cerium concentrations are labeled next to each data point. (b) Carrier concentration correction factor ($\frac{\rho_\circ(x)}{\rho_\circ(0.17)}$) versus change in R_H at T= 2.5 K for optimally annealed cerium-doped samples. (c) ΔT_c versus $\Delta\rho_\circ$ for the irradiated sample. All of the dashed lines are fits to the data.

term [first term in Eq. (6.7)] is determined from previously published data [45] on optimally annealed samples, where the Hall coefficient and residual resistivities for various cerium dopings are known [Fig. 6.10(a)]. From this data I determine the expected change in the residual resistivity for a given change in the Hall coefficient, $\Delta\rho_\circ(R_H)$, using the $x = 0.17$ cerium doping as the reference. I subtract this from

$\Delta\rho_\circ(O_2)$ giving a quantity I will call $\Delta\rho_{\circ,\text{uncorrected}}$(disorder). This term is not quite the disorder term in Eq. (6.7) since I need to eliminate the carrier concentration dependence. I can determine this dependence, $(1 - \frac{\Delta n}{n})$ in Eq. (6.6), by taking the ratios of the residual resistivities of previously reported *cerium-doped* samples and plotting them as a function of the change in R_H from the $x = 0.17$ composition [Fig. 6.10(b)]. This can be seen if I let the residual resistivity of the $x = 0.17$ be $\rho_\circ(0.17) = \frac{m*}{ne^2\tau_\circ}$ and all other *cerium dopings* represented by $\rho_\circ(x) = \frac{m*}{(n+\Delta n)e^2\tau_\circ}$. Here we assume $\tau_\circ$ does not depend on cerium-doping [38]. The $(1 - \frac{\Delta n}{n})$ factor can now be determined from Fig. 6.10(b) for a given ΔR_H within the oxygenated samples. This factor is then divided out of $\Delta\rho_{\circ,\text{uncorrected}}$(disorder). We are now left with the term in Eq. (6.7) due to disorder, i.e., $\Delta\rho_\circ$(disorder). This is the crucial term that is needed in the next step to determine how T_c is affected by disorder in the two more oxygenated films.

I use the irradiation data to make a correlation between $\Delta\rho_\circ$ and the change in T_c (ΔT_c) due to disorder, in order to determine the expected change in T_c of the oxygenated samples due to disorder. I assume that the change in T_c can be written in the same fashion as Eq. (6.7).

$$\Delta T_c(O_2) = \Delta T_c(R_H) + \Delta T_c(\text{disorder}). \tag{6.8}$$

The disorder term on the right hand side is determined from the irradiation data, shown in Fig. 6.3(c) and summarized in Fig. 6.10(c). With this plot it is now possible to determine ΔT_c(disorder) for each $\Delta\rho_\circ$(disorder) calculated in the previous

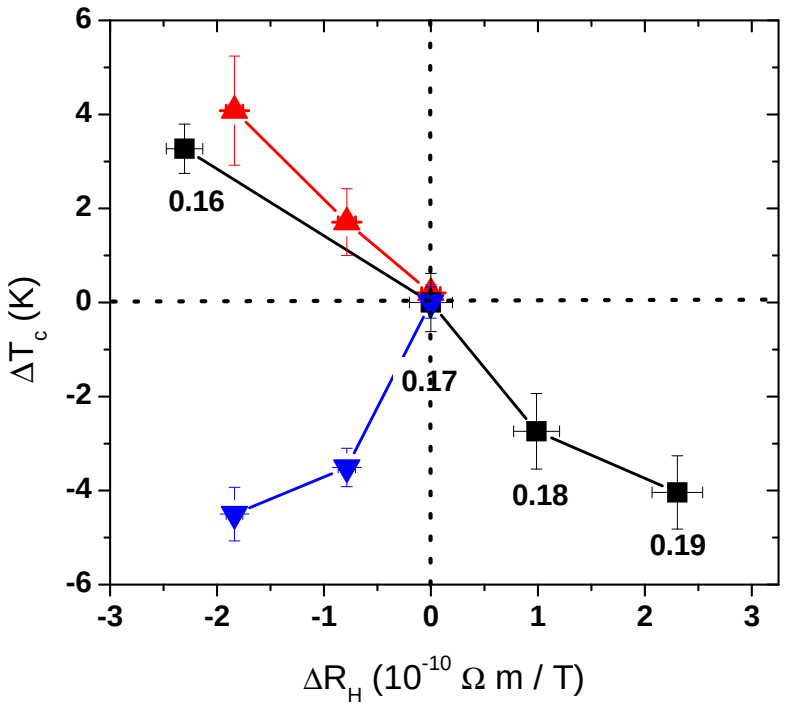

Figure 6.11: Change in T_c versus change in R_H at T = 2.5 K. Doping contributions to the change in T_c, $\Delta T_c(R_H)$, of the $x = 0.17$ oxygenated samples after the analysis described in the text (▲). Optimally annealed cerium-doped samples (■). The raw data from the oxygenated samples are also shown (▼).

paragraph for the two more oxygenated samples. I subtract ΔT_c(disorder) from $\Delta T_c(O_2)$, as determined from Fig. 6.3 using the 10^{-4} Torr sample as the reference, for the two more oxygenated samples. The result is the contribution to the change in T_c of the oxygenated samples from a change in carrier concentration, i.e., $\Delta T_c(R_H)$ in Eq. (6.8). The results are plotted in Fig. 6.11 along with data from optimally reduced cerium-doped samples.

The trend in the oxygenated samples, after the analysis, is consistent with the trend in the cerium-doped samples, i.e., T_c *increases* as R_H evolves toward optimal doping ($x = 0.15$). It can be seen from Fig. 6.11 that the positive contribution to T_c from hole-doping in the oxygenated samples (▲ data) is overshadowed by the

negative contribution due to the disorder introduced by the oxygenation (▼). This result explains why changing the oxygen content in $x \neq 0.15$ samples never results in the maximum T_c (≈ 22 K) of $x = 0.15$ samples.

Interpretation

I have shown that oxygen has an effect on the properties of PCCO that can be separated into two parts: disorder and doping. Based on this result, I will present a possible explanation for the long-standing puzzle of why oxygen reduction is needed to produce superconductivity in the n-doped cuprates. I will speculate on the relation between superconductivity and antiferromagnetism, as well as the lattice sites where oxygen is removed during reduction.

The overall effect of adding oxygen to a superconducting PCCO ($x = 0.17$) sample is similar to ion irradiation, with regards to disorder. However, irradiation and oxygenation are not expected to have the same effect on the antiferromagnetism. It has been clearly shown that T_N increases as the oxygen content increases (from an optimal reduction) [37,102,103] in the n-doped cuprates. In contrast, one would expect T_N to decrease upon irradiation[2]. To that extent, this analysis supports the conjecture that the suppression of T_c by oxygenation is *primarily disorder-driven* and is not related to any competing long-range antiferromagnetic order at this cerium-doping. Conversely, oxygen reduction is necessary to minimize the disorder which is responsible for inhibiting superconductivity.

[2]A lack of literature in regards to experimental results on the effects of T_N upon irradiation leaves no definitive answer as to which direction T_N would actually move, if at all. The conjecture is that T_N would reduce because of a modification of the Cu-Cu exchange interaction energy due to the disruption of the oxygen and copper sublattices created by vacancies in the CuO_2 plane.

This suppression of T_c by disorder gives some insight into where oxygen is removed during the reduction process. Let us look at this problem from the other perspective and consider the case of adding oxygen to a reduced sample. In this case, there are three sites where the oxygen could be entering: the CuO_2 plane, the PrO layer, or the apical sites. The first two sites are regular lattice sites and the reincorporation of oxygen into those sites would restore the regular lattice potential and reduce disorder. The last possibility, the apical site, is most likely to increase disorder as it is predominantly an impurity site in close proximity to the CuO_2 plane. Irradiation, on the other hand, introduces disorder mainly by creating vacancies in the CuO_2 plane [137, 138]. Since oxygen is not removed from the material in this process, it must then be displaced into interstitial sites of which the apical site is a possibility. The disorder from irradiation then comes from both the in-plane and the interstitial sites. The data suggests that this disorder is quantitatively similar to adding oxygen, which brings us to the speculation that changing the occupation of the apical (or interstitial) sites influences the disorder for a given cerium-doping more than disorder from in-plane vacancies or from the PrO layer. This interpretation of the effect of out-of-plane disorder is consistent with Fujita *et al.* [132], who reported a strong suppression of T_c due to out-of-plane disorder in the hole-doped cuprates $La_{2-x}Sr_xCuO_4$ and $Bi_2Sr_2CuO_{6+\delta}$. It is also consistent with the results of McElroy *et al.* [143] who demonstrate that the structural disorder from oxygen non-stoichiometry in $Bi_2Sr_2CaCu_2O_{8+\delta}$ results in an electronic inhomogeneity associated with the oxygen.

6.2.3 Consideration within a Two-band Model

Hall Effect

The analysis of section 6.2.2 utilized a single-band, spherical Fermi surface, Drude model. Although recent results from ARPES show a closing of the Fermi surface in overdoped NCCO ($x = 0.17$), into a single hole-band [62] thus lending credence to the single-band model, it is still rather difficult to explain *all* the measurements using a single-band model, for example the large normal-state Nernst signal or the field dependent R_H [82]. Therefore, I would like to re-examine the Hall effect in the oxygenated and irradiated PCCO thin films from the vantage point of a two-band picture.

Rewriting the equation for the two-band model in terms of the mobility and the carrier density of the two bands and in the low-field limit ($\omega_c\tau \ll 1$), Eq. (3.42) has the form

$$R_H = \frac{n_h|e|\mu_h^2 - n_e|e|\mu_e^2}{(n_h|e|\mu_h + n_e|e|\mu_e)^2}, \tag{6.9}$$

where $n_{h,e}$ is the hole (electron) carrier density, e is the charge of the carrier, and $\mu_{h,e} = e\tau_{h,e}/m^*_{h,e}$ is the mobility of the holes (electrons). For the case of the irradiated samples, we see from Fig. 6.8 that R_H increases as more disorder is introduced through irradiation. In the simple single-band model, this change can only be accounted for by a change in the carrier concentration ($R_H = 1/ne$), however it is not likely that n changes with the irradiation performed on these samples. Rather, it is *more* likely that a change in the scattering rate $1/\tau$ is creating this change.

This can be seen from Eq. (6.9). A *positive* change in R_H can occur if the *electron mobility decreases relative to the hole mobility* ($\frac{\mu_e}{\mu_h}$ decreases), and with the carrier densities held constant. This decrease in the mobility will also cause the resistivity to increase

$$\rho_{ab} = \frac{1}{n_h|e|\mu_h + n_e|e|\mu_e}. \tag{6.10}$$

Qualitatively, the observed change in R_H of the irradiated samples is consistent with a change in the relative mobilities of the two bands, for a given temperature.

What about the temperature dependence? A quantitative analysis is difficult when considering the two-band model, due to the fact that little is known about the individual bands, let alone their temperature dependencies. Additionally, all of the attempts to quantitatively fit the data to a two-band model yield inconsistent fitting parameters between ρ(T) and R_H(T). However, it is still informative to qualitatively investigate the general temperature dependence of ρ and R_H within the two-band model. Rewriting Eq. (6.10) in terms of the resistivities of the two bands gives

$$\rho_{ab} = \frac{\rho_e \rho_h}{\rho_e + \rho_h}, \tag{6.11}$$

where $\rho_{e,h}$ is the single band resistivity of the electrons (holes), which retain the form given in Eq. (6.4). In the single-band model, a change in the residual resistivity (by changing the temperature independent elastic scattering rate $1/\tau_\circ$) results in a parallel shift in ρ. Another way to think of this is that the coefficient (slope) of the temperature dependence does not change. In the two-band model, a change in $\rho_\circ$ of each band results in more than just a parallel shift in ρ: the slope of the

temperature dependence will also change. This makes sense since we are adding two resistive channels in parallel and a mixing of terms is to be expected. Expanding Eq. (6.11) shows this more clearly.

$$\rho_{ab} = \frac{[\rho_{\circ,e} + \rho_e(T)] \cdot [\rho_{\circ,h} + \rho_h(T)]}{\rho_{\circ,e} + \rho_e(T) + \rho_{\circ,h} + \rho_h(T)}. \tag{6.12}$$

The Hall coefficient is a similar story. The temperature dependence of R_H for the irradiated samples is shown in Fig. 6.12. One notices that R_H changes by more than just a rigid shift. Just as a mixing occurs in the resistivity, the same thing occurs in R_H, thereby creating a significant change in the appearance of the temperature dependence. This can be seen from Eq. (6.9) and a relation for the mobilities of the individual bands

$$\rho = \rho_\circ + \rho(T) = \frac{1}{\sigma} = \frac{1}{n|e|\mu} \Rightarrow \frac{1}{\mu} = \frac{1}{\mu_\circ} + n|e|\rho(T), \tag{6.13}$$

where $\mu_\circ = n|e|\rho_\circ$ is a residual mobility which depends only on the temperature-independent elastic impurity scattering rate. The mixing of the temperature dependent and the temperature independent terms is clear upon inversion of Eq. (6.13). It is quite plausible that the observed change in R_H of the irradiated sample is due entirely to a change in $\rho_\circ$ of the individual bands within a two-band picture.

I should mention here that the change in R_H with cerium doping is different than that observed with disorder. Doping causes a slight shift at high temperatures and a larger shift at lower temperatures. It therefore appears as though R_H is

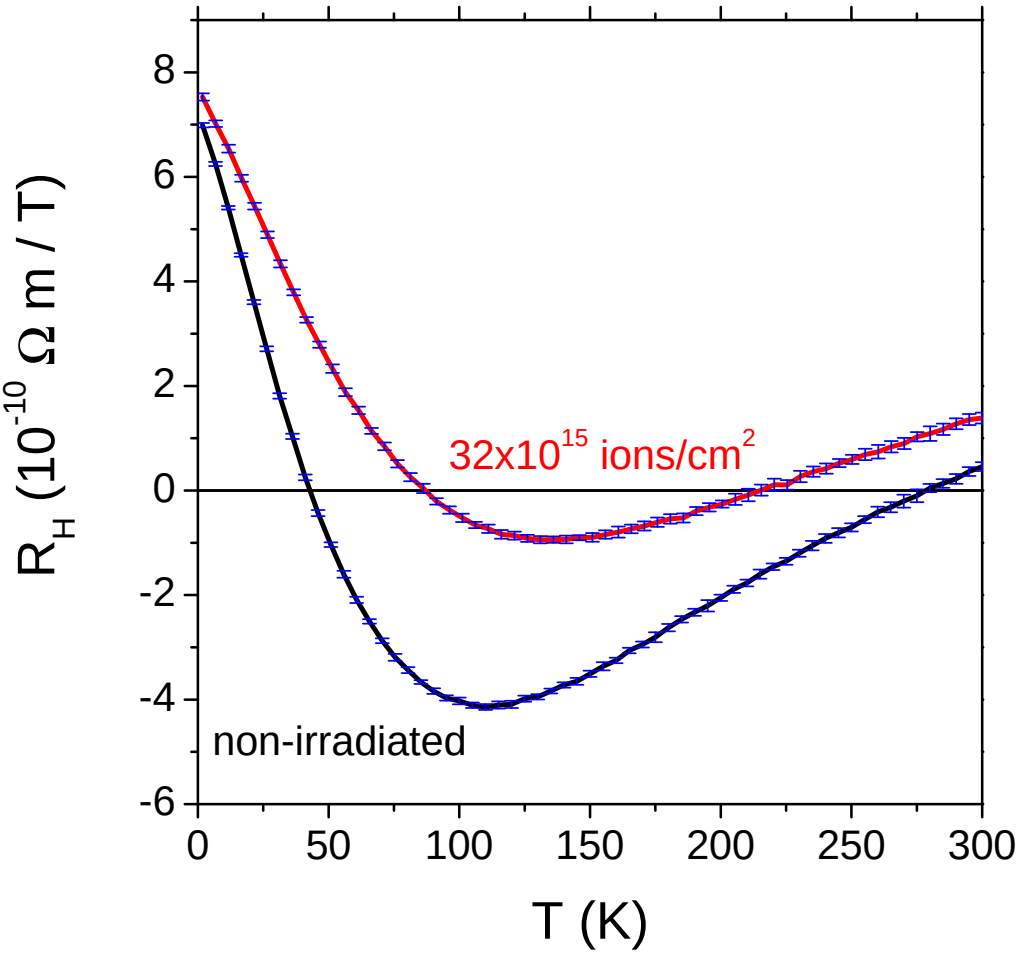

Figure 6.12: R_H versus Temperature for irradiated $Pr_{1.83}Ce_{0.17}CuO_{4\pm\delta}$ thin films. The representative doses are next to each curve. Only two curves are shown; the non-irradiated Hall pad, and the most irradiated Hall pad on JP17-24. This data was taken in $\pm$10 T magnetic fields, while waiting for temperature stability at each temperature.

rotated about the high temperature values as the cerium content changes.

As mentioned above, quantitative fits do not yield consistent parameters for ρ(T) and R_H(T). This most likely stems from the fact that these models are for the simple case of a spherical Fermi surface. From the ARPES data (Fig. 2.12), the electron pocket is cube-like and the hole pocket is ellipsoidal. A more complicated Fermi surface should be incorporated, and an analysis of R_H similar to that of

Ong [71] and Lin *et al.* [38] should be utilized in order to obtain quantitative results.

Now that there is good reason to believe that a change in the elastic scattering rate $\tau_\circ$ can account of the positive changes observed in the irradiated samples, how does this affect the analysis presented in Sec. 6.2? Since the disorder in the oxygenated samples is quantitatively similar to the disorder induced by irradiation, that means that R_H of the oxygenated samples has an additional *positive* contribution due to a change in $\tau_\circ$, albeit for a given change in T_c the positive contribution to R_H is outweighed by the negative contribution from a decrease in n. To this extent, ΔR_H determined in the previous section is *underestimated* for the oxygenated samples. Therefore, if it were possible to quantitatively account for a change in $\tau_\circ$ in R_H, the data presented in Fig. 6.11 (▲) would shift to more negative values of ΔR_H (i.e., to the left in Fig. 6.11), yielding a *better agreement* with the optimally prepared cerium-doped samples (■).

Magnetoresistance

The magnetoresistance of the oxygenated and irradiated samples is complimentary to the qualitative two-band analysis presented for the Hall effect. In the case of the irradiated sample, where we are confident that the carrier density is not changing, the scattering rate increases (τ decreases) with disorder from irradiation. The easiest way to get a feel for how the MR should behave with a change in scattering rate is by looking at the simplest case. In Section 3.3.1, a simple two-band

model gives the MR as

$$\frac{\Delta\rho}{\rho} = (\omega_c\tau)^2 \frac{1-a^2}{1+a^2(\omega_c\tau)^2} \tag{6.14}$$

where $a = \frac{n_1-n_2}{n_1+n_2}$ is the effective carrier concentration, $\omega_c = \frac{qB\tau}{m^*}$ is the cyclotron frequency, and all other properties of the two bands are considered equivalent. The dependence of the MR on τ is similar for all the simple two-band models. Since $\omega_c\tau \ll 1$ and a is a constant, then $\frac{\Delta\rho}{\rho} \propto \tau^2 B^2$. Therefore, at a given temperature, the MR decreases. This is shown in Fig. 6.13(a) for the irradiated sample. The temperature of the data shown in Fig. 6.13 is 50 K. This temperature is chosen so that we are looking in the region of positive MR far away from T_c. Below T_c, the MR is negative. In the region of positive MR, the magnitude decreases with increasing temperature. Therefore, 50 K offers a relatively large magnitude of positive MR. For the oxygenated samples, both the scattering rate and the carrier density are changing. However, the trend in the MR is similar to that of the irradiated samples [Fig. 6.13(b)].

High Field Magnetoresistance

Some interesting data comes from high-magnetic field data obtained from the National High Magnetic Field Laboratory in Tallahassee, Florida. Figure 6.14 shows an optimally annealed, oxygenated (2.3×10^{-1} Torr anneal), and irradiated (32×10^{15} ions/cm^2) thin films in magnetic fields up to 31 T at T $\simeq$ 1.5 K. Each plot in Fig. 6.14 shows data from an increasing magnetic field (field sweep), applied perpendicular to the ab plane ($\mu_\circ H \perp ab$ plane), along with data taken at a constant 31 T while

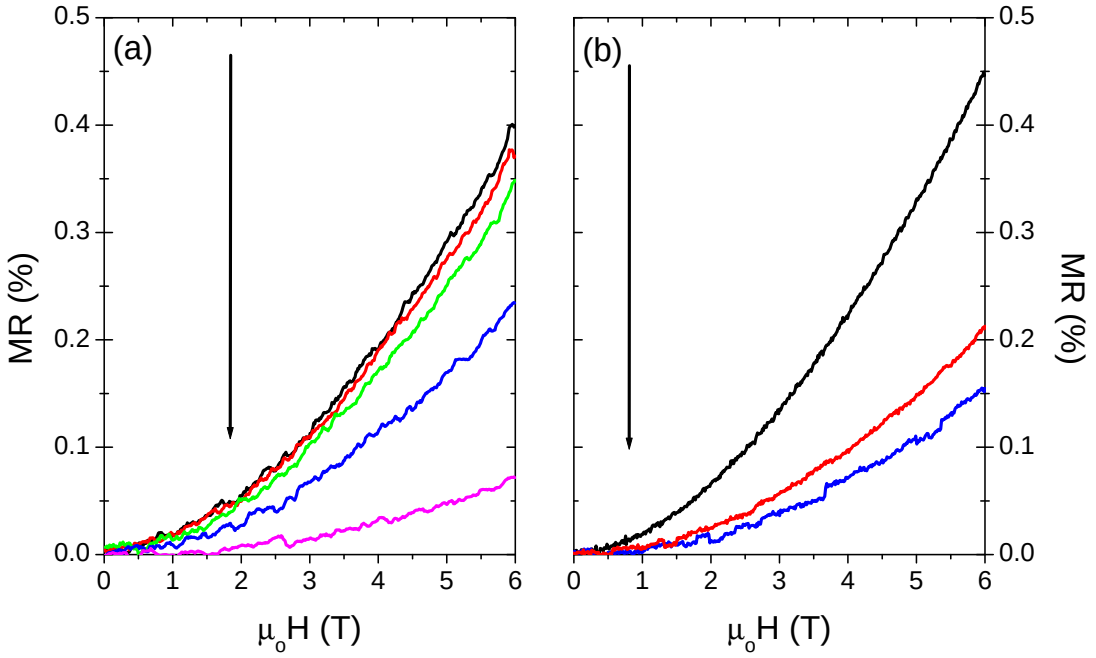

Figure 6.13: Magnetoresistance of (a) irradiated and (b) oxygenated $Pr_{1.83}Ce_{0.17}CuO_{4\pm\delta}$ thin films. The data presented is at T = 50 K. The arrows indicate the order of increasing irradiation/oxygenation. The increasing disorder reduces the lifetime of the quasiparticles, thereby decreasing the MR.

rotating the sample in the field. The idea behind comparing data in this fashion is fairly straightforward and has been reported by Dagan *et al.* [79]. The basic idea is that the spin (isotropic) MR can be isolated from the orbital (anisotropic) MR. When $H \perp ab$ plane, both the spin and orbital MR contribute at the applied field. As the sample is rotated in a fixed field, the spin component sees a constant field (i.e., remains roughly constant) while the effective field that the orbital component sees decreases. If the MR from $H \perp ab$ plane and the rotation in a constant field are the same, then the dominant contribution to the MR is from orbital effects. Dagan *et al.* [79] demonstrated that orbital effects dominate in the doping range $x \leq 0.11$ and $0.16 \leq x$. As one can see from Fig. 6.14, neither oxygenation nor irradiation has changed this observation, at least up to these levels of oxygenation/irradiation.

What one does notice is that the oxygenated sample develops a positive contribution to the MR. This is not observed in the irradiated sample or in the optimally grown sample, in this magnetic field range.

6.3 Magnetic Contributions to the Hall Effect

Due to the antiferromagnetic nature of the parent compound, $Pr_2CuO_{4\pm\delta}$, it is worth considering whether any magnetic spin scattering, due to spin-orbit coupling, is influencing the Hall effect since this has been ignored in all prior analysis of the Hall data on n-doped cuprates. Strongly magnetic systems have a contribution to R_H due to interactions of the free carriers with the magnetic moments in the material. The interesting investigation would be to determine if the antiferromagnetism of the Cu spins affects R_H. However, several experimental observations point out that this may not be happening, *at least in a conventional manner*. One such observation is that ρ_{xy} does not show field dependencies indicative of magnetic spin scattering (i.e., $\rho_{xy} \propto$ Magnetization). The other is not so much an observation, but rather the lack of an observation. The temperature dependence of the antiferromagnetic susceptibility has not been reported in the literature, as far as I am aware. This is not entirely surprising for several reasons. First, for the magnetic field orientation which we are interested in ($B \| c$ axis), it is very difficult to cant the Cu spins (remember, the Cu spins are aligned in-plane) as the tetragonal structure does not provide for easy, out-of-plane canting of the spins [148]. Second, the paramagnetic moment of the Pr ions ($\simeq 3.68\mu_B$ [149]) is roughly an order of magnitude

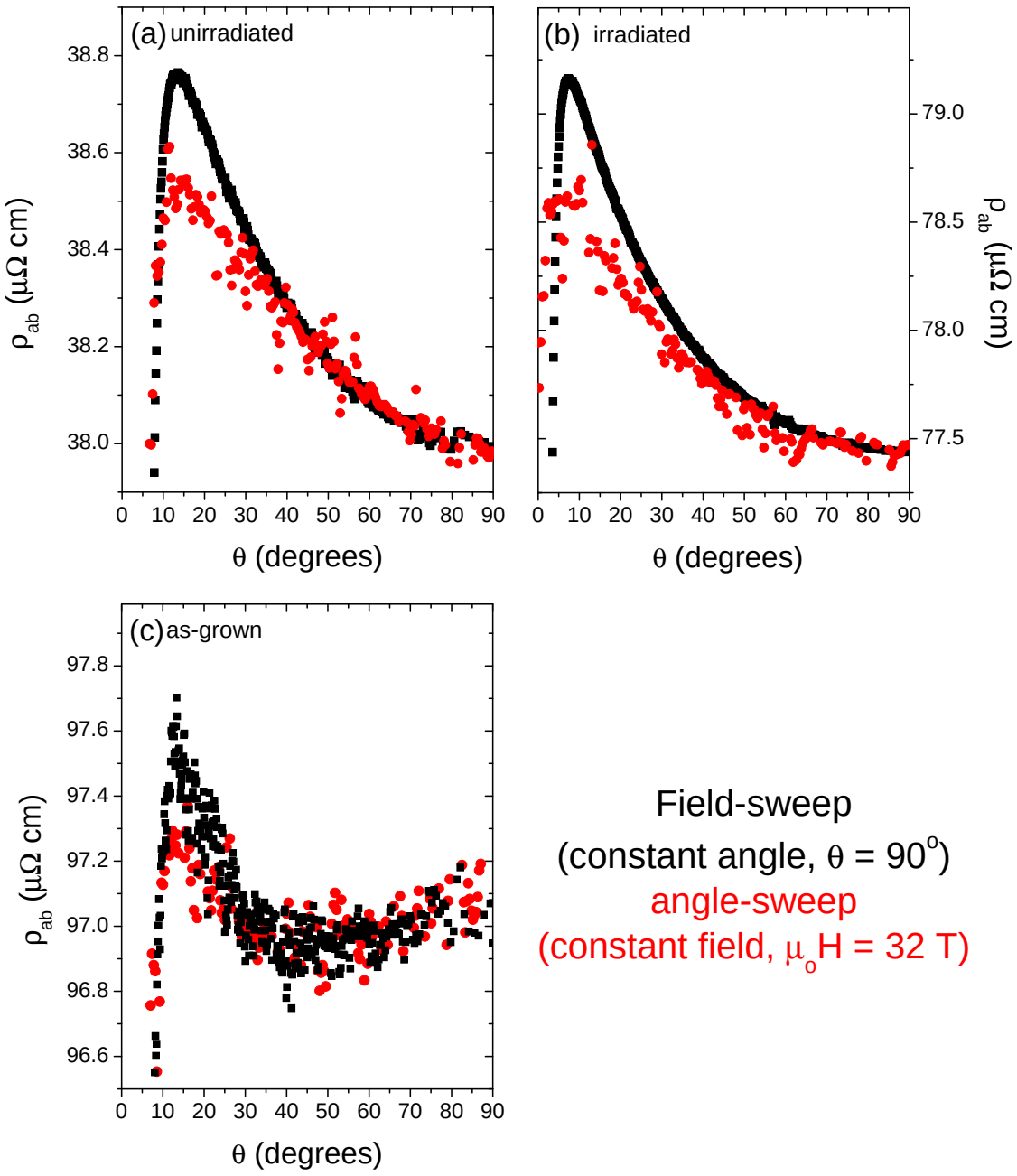

Figure 6.14: Magnetoresistance of irradiated and oxygenated $Pr_{1.83}Ce_{0.17}CuO_{4\pm\delta}$ thin films, taken in high fields. The field of the field-sweep data has been converted into an effective angle between $\vec{H}$ and the *ab* plane. (a) Optimally annealed sample (from JP17-24) (b) Irradiated sample (32×10^{15} ions/cm^2, JP17-24) (c) oxygenated sample (2.3×10^{-1} Torr anneal; sample JP17-6).

larger than any moment determined for the Cu ($\simeq 0.45\mu_B$ [150]) in PCCO. This results in a swamping of any antiferromagnetic susceptibility by the paramagnetic susceptibility of the Pr ions. That being said, is it possible that the paramagnetic moments are influencing the Hall measurements?

The Hall resistivity for a magnetic material can be written as

$$\begin{aligned} \rho_{xy} &= R_\circ \mu_\circ H_{\text{applied}} + [R_s + R_\circ (1 - N)] \mu_\circ M \\ &= R_\circ \mu_\circ H_{\text{applied}} + R_s \mu_\circ M \end{aligned} \tag{6.15}$$

where H_{applied} is the applied magnetic field strength, M is the magnetization of the material, $R_\circ$ is the ordinary Hall coefficient, R_s is the spontaneous Hall coefficient in magnetic materials, and $N = 1$ is the demagnetization factor for samples of thin film geometry (sheets). In the paramagnetic state, the magnetic susceptibility is given by $\chi = M/H_{\text{int}}$ [67] (H_{int} is the interior magnetic field strength), and Eq. (6.15) can be written as

$$\frac{\rho_{xy}}{B} = \frac{\rho_{xy}}{\mu_\circ H_{\text{applied}}} = R_\circ + R_s \chi^*, \tag{6.16}$$

where $H_{\text{applied}} = H_{\text{int}} - NM$, and χ^* is defined by

$$\chi^* \equiv \frac{\chi}{1 + \chi}. \tag{6.17}$$

Assuming that $R_\circ$ and R_s are temperature independent, Eq. (6.16) says that the temperature dependence of $\rho_{xy}/\mu_\circ H_{\text{applied}}$ is dictated by that of the paramagnetic susceptibility. Therefore, one would only need to plot $\rho_{xy}/\mu_\circ H_{\text{applied}}$ versus χ^*

in order to determine $R_\circ$ and R_s. Hundley *et al.* [149] demonstrate that the magnetic susceptibility of single crystals of undoped PCO shows no magnetic ordering from the Cu or Pr ions, consistent with the fact that the paramagnetic moment of the Pr ions dominates the susceptibility. Partial cerium substitution ($x = 0.1$) shows identical temperature dependencies and anisotropies in χ [149] as that of the undoped crystals. Polycrystalline[3] [151] samples show similar results with cerium doping. In this analysis, I will use Hundley *et al.*'s [149] data for the undoped PCO single crystal ($\chi \perp ab$ plane, figure 1 in Ref. [149]). For convenience, the susceptibility data is shown in Fig. 6.15.

The Pr molar susceptibility shown in Fig. 6.15 is in cgs units and I wish to convert it to the volume susceptibility in SI units [which is the form used in Eq. (6.16) and (6.17)]. This is done by the following relation

$$\chi_{\text{Vol., SI}} = \frac{\chi_{\text{mol, cgs}} \cdot 4\pi}{V_{\text{mol}}}, \tag{6.18}$$

where V_{mol} is the molar volume for praeseodymium in PCCO, in units of cm^3/mol (i.e., 1/4 the molar volume of PCCO).

The analysis is rather straight forward, as the objective is to see if the paramagnetic moments of the Pr ions contribute noticeably to the Hall effect. This is done by plotting R_H versus χ^* and seeing if a linear relationship exists, as per Eq. (6.16). This is done for several different dopings ($x = 0.05, 0.15, 0.17, 0.19$). The temperature dependencies of R_H and χ^* are given in Fig. 6.16. Plots of R_H versus χ^* are

[3]The susceptibility of the polycrystalline samples would be averaged between the in-plane and out-of-plane susceptibilities. No significant differences are seen with doping.

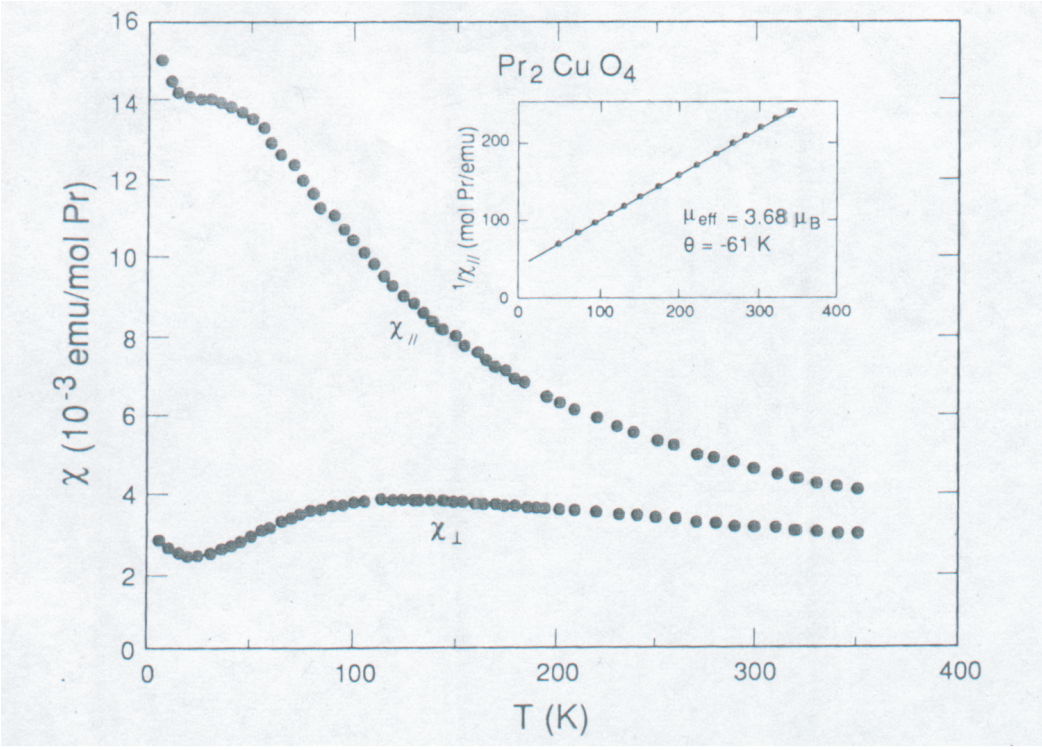

Figure 6.15: Paramagnetic (molar) susceptibility for $Pr_2CuO_{4\pm\delta}$ single crystals, taken from Ref. [149]. The susceptibility relevant to the analysis is $\chi_\perp$ ($\chi \perp ab$ plane) because Hall measurements are made with $\mu_\circ H \perp ab$ plane. The susceptibilities are obtained in a 0.5 T magnetic field.

given in Fig. 6.17. From the plots of R_H versus χ^*, it is apparent that there is not a linear relationship between the two, over the temperature range of the paramagnetic susceptibilities. This indicates one of two things: 1) the paramagnetism of the Pr ions is not responsible for the temperature dependence of R_H, or 2) $R_\circ$ and/or R_s are not temperature independent as assumed. In either case, this implies that the paramagnetic moments do not contribute to R_H according to Eq. (6.16). Wang *et*

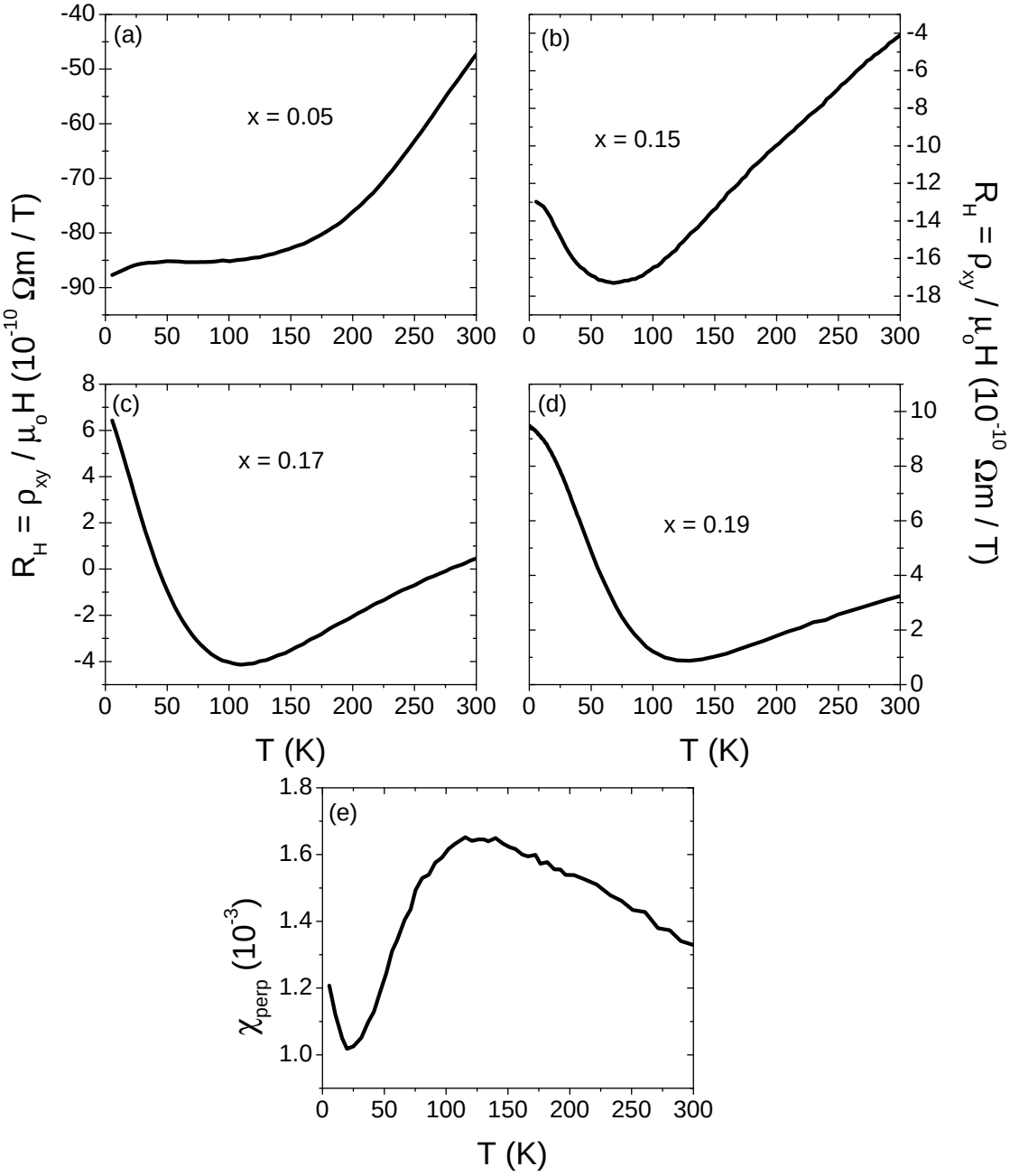

Figure 6.16: Temperature dependencies for χ^* and R_H for $Pr_{2-x}Ce_xCuO_{4\pm\delta}$. All plots have the same temperature range. (e) $\chi^* = \frac{\chi}{1+\chi}$ for undoped PCO, adapted from Ref. [149]. SI units are used here. (a - d) Temperature dependencies for $x = 0.05, 0.15, 0.17, 0.19$ dopings, respectively. The data for (a) is from Ref. [82], (b) and (d) from Ref. [56], (c) from sample JP17-24 (non-irradiated) in this study. The Hall data was taken in 10 T magnetic field.

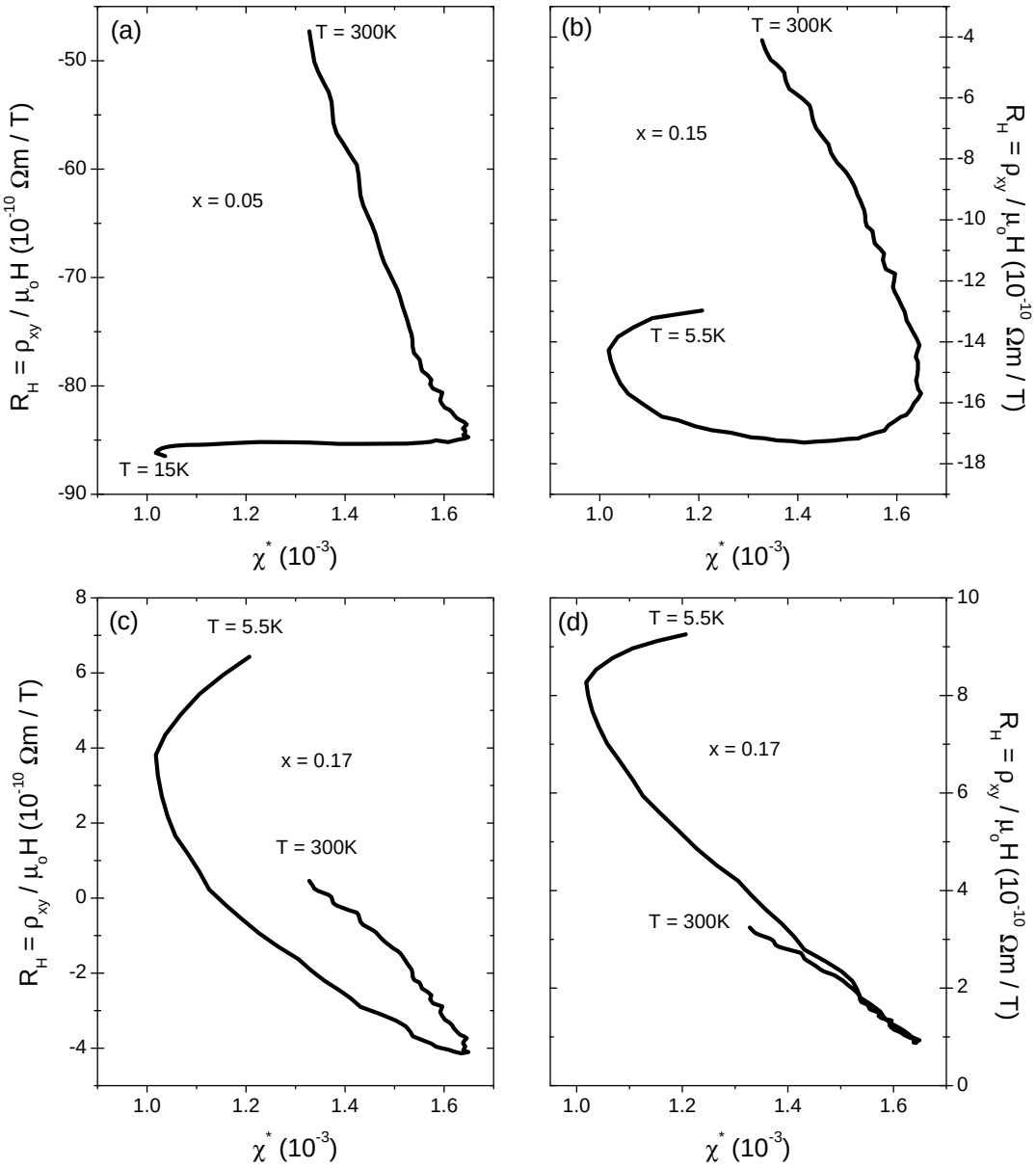

Figure 6.17: R_H versus χ^* for $Pr_{2-x}Ce_xCuO_{4\pm\delta}$ thin films. (a) $x = 0.05$, (b) $x = 0.15$, (c) $x = 0.17$, (d) $x = 0.19$. Notice there is no clear dependence of R_H on χ^*.

al. [41] came to a similar conclusion.

6.4 Future Directions

Although the analysis of the oxygenated and irradiated data does not conclusively indicate which oxygen sites are depopulated during the reduction process, the speculation is that reduction occurs in the apical sites. Planar oxygen has been suggested as the site where oxygen is removed. The rationale behind this notion is that the oxygen vacancies would weaken the antiferromagnetism in the plane, thereby allowing the competing phase of superconductivity to appear, or by reducing the charge-transfer gap. This idea can be tested by irradiating an oxygenated sample. Overdoped samples already have a weakened (or non-existent) charge-transfer gap and the antiferromagnetism is very weak, therefore one would need to chose a doping which inarguably demonstrates antiferromagnetic behavior, such as an $x = 0.12$ sample which is at the boundary between long-range and short-range antiferromagnetism. In the electron-doped cuprates, it is believed that ion irradiation primarily displaces the planar oxygen into interstitial sites (of which the apical site is a possibility). Very low levels of irradiation in an oxygenated sample would then mimic the effect of oxygen reduction, if reduction occurs in the plane. The transition temperature should increase in this scenario. If T_c does not increase, then this would be a clear indication that the removal of planar oxygen during reduction is not the cause for superconductivity. This result would also further confirm the role of apical (or interstitial) oxygen as detrimental to T_c in the electron-doped cuprates.

A test of the model used to separate the doping and disorder effects in the oxygenated samples could be achieved by repeating the experiment on a more cerium overdoped sample, for example an $x = 0.19$ thin film. The reason is that the Fermi surface becomes more and more hole-like as cerium-doping continues farther into the overdoped region. Angle-resolved photoemission spectroscopy has recently shown the Fermi surface in NCCO is nearly closed (hole-like) at $x = 0.17$. Therefore, higher doping should have electronic transport which is dominated by a single-band. If this is indeed the case, irradiation at these higher doping levels would have less of an impact on the Hall coefficient than it did for the x=0.17 samples (since R_H is proportional to 1/ne in a single-band model). In the $x = 017$ sample irradiated for this thesis, a slight positive change in Rh was observed at low temperatures (at the temperatures where the analysis was done). A more dramatic change in R_H, between the non-irradiated and the most irradiated sample, was observed over the entire temperature range. This change in R_H is attributed to a change in residual scattering rates within a two-band model. For higher cerium dopings, one would expect irradiation (at low doses) to have a negligible effect on Rh, again due to a dominating single-band conduction.

The dominant disorder contribution to changes in the oxygen content rule out the possibility of using oxygen as a tuning parameter for investigating the quantum phase transition. Therefore, other control parameters should be considered. A good, initial candidate would be the application of hydrostatic pressure. Pressure *could* have two effects in PCCO. One effect could be a doping effect (change in carrier concentration), similar to what is observed in $YBa_2Cu_3O_{7-\delta}$ [152]. The other effect

could be something else independent of doping. In the first case, applying pressure would offer a fine tuning parameter through the quantum critical point by changing the carrier concentration. In the second case, pressure would be a second control parameter (in addition to doping), and the control parameter phase space for the quantum phase transition would be two dimensional. The quantum phase transition would then occur along a line, rather than a point, and the pressure could be finely adjusted (for any given cerium doping) to observe the transition.

The upturn in the resistivity, which occurs with a decrease in cerium doping, or increased oxygen content, or irradiation, is another project worth considering. There are several possible sources for this upturn (i.e., Kondo effect or 2D weak localization). In particular, the possibility of a superconductor-insulator transition [153] (SIT), induced by disorder through irradiation, is interesting. An SIT basically means that the material is either a superconductor or an insulator in the $T \to 0$ limit. The SIT occurs in 2D superconductors and can be controlled (or fine tuned) by using either disorder [154] or magnetic fields [155]. It is possible that the disorder-driven or magnetic-field-driven quenching of superconductivity in the 2D and $T \to 0$ limit is due to quantum phase transitions [156]. The basic idea is that below some critical control parameter value (either disorder or field), the material is a superconductor with localized vortices and delocalized Cooper pairs. Above the critical control parameter value, the material is an insulator with delocalized vortices and localized Cooper pairs. This is predicted to occur at a sheet resistance corresponding to the quantum resistance for pair of charge carriers $R_\square = h/4e^2 \simeq 6.5$ kΩ. This has been studied in PCCO [157, 158] and its hole-doped sister compound

$La_{2-x}Sr_xCuO_4$ [159]. However, in PCCO, overdoped compositions were used. It would be interesting to study several underdoped PCCO compositions with various disorder (induced by irradiation), and compare with the theoretical predictions. This may give new information about the resistivity upturn.

An SIT could also explain the negative magnetoresistance in PCCO. In the field-driven SIT and for magnetic fields larger than the SIT critical field, the magnetic field depairs the Cooper pairs [155]. Since the Cooper pairs are localized, and the material is insulating, the pair breaking allows quasiparticles to participate in the conduction at high fields. As the field increases, more pairs are broken and more quasiparticles contribute to conduction. This causes a decrease in the resistance (increase in conduction) with an increase in the magnetic field, hence a negative magnetoresistance.

Chapter 7

Introduction to Diluted Magnetic Semiconductors

The next two chapters of this thesis deal with a different project than presented in the previous chapters. The material investigated here belongs to a class of materials called diluted magnetic semiconductors (DMS). In this chapter, I will give the canonical motivation for DMS materials, and the material under investigation here (cobalt-doped TiO_2), followed by some of the models used to describe DMS.

7.1 Spintronics

Conventional solid state electronics work by manipulating the charge of the electrons. But electrons have a spin degree of freedom, and it is the desire to manipulate this aspect which has spurred research in a field called spin-based electronics (spintronics) [160]. Manipulation of the spin of the electrons should have a fantastic outcome in practical application. It is typically easier (from the stand point of energy requirements) to flip spins of the electrons than it is to push charges around. What is meant by manipulating the spin of the electrons? Well, in the few cases I will be covering, a filtering of the electrons with a certain spin orientation (or polarization) is the main idea. A nice parallel occurs in optics. We can polarize light by sending it through a polarizer. We can subsequently send it through another polarizer (analyzer). The analyzer can either allow the light to pass or it can prevent

it from passing, or some fraction thereof. The polarizers are filtering the light, and the presence/absence of light can be the binary states of on and off. The same idea of filtering is used in spintronics. By filtering electrons of a specific spin, we can modify the number of electrons on the one side of the filter, i.e., the current passing through the filter. By incorporating the spin of the electrons, we can effectively double the degrees of freedom in conventional electronics.

7.1.1 Magnetization and Spin Polarization

The point of this section is not to give a rigorous theoretical background for the magnetization and spin polarization. Rather, the objective is to give a somewhat simple perspective as to how these phenomena may occur.

In conducting materials, there are many conduction electrons moving around and their spins are usually "randomly" oriented (roughly equal populations of spin up and spin down electron energy states at the Fermi energy). In order to filter one spin orientation of the conducting electrons, it would be nice if the population of spin up and spin down states was significantly different in the "filtering" material (the reasons will become clear later in this section). Spin polarization is conveniently achieved naturally in ferromagnetic materials.

Magnetization arises from the motion of electrons, and the magnetic moment ($\vec{m}$) of an atom is determined by the configuration of the electrons in the orbitals.

$$\vec{m} = g\mu_B[J(J+1)]^{1/2} \tag{7.1}$$

where

$$g = 1 + \frac{J(J+1) + S(S+1) - L(L+1)}{2J(J+1)} \tag{7.2}$$

is the Landé g-factor, μ_B is the Bohr magneton (the moment associated with an electron), and S, L, J are the quantum numbers associated with the spin, orbital, and total angular momentum of the electrons in the atomic orbitals. The direction of $\vec{m}$ is along $\vec{J}$. The determination of S, L, and J are the same as in basic quantum mechanics classes. Filled orbitals, for example $1s^2$, have zero total angular momentum. So the only orbitals contributing to the magnetic moment are the partially filled orbitals [1].

Ferromagnetism is the tendency of atomic moments to spontaneously arrange themselves (i.e., with no external magnetic field) along a common direction. The result is a net magnetic moment in the absence of a magnetic field. It is this type of magnetism which people encounter most frequently. For example, refrigerator magnets, horseshoe magnets, or any type of permanent magnet exhibits some form of ferromagnetism. The spontaneous ordering of the atomic moments arises primarily through the overlap of wavefunctions of the electrons in the unfilled orbitals of neighboring atoms. In a *very* crude model (a schematic model, if you will), imagine you have two nearby atoms with a half filled d orbital (so all the electrons in either atom have their spins aligned in the same direction). The wavefunctions of these electrons overlap and the Pauli exclusion principle prevents the double occupancy of identical energy states. Since we are dealing with fermions, the total wavefunction needs to be

[1] Filled orbitals, however, still possess a slightly diamagnetic moment, but for all intents and purposes we neglect this fact.

antisymmetric. Since there is significant spatial separation of the atoms, the spatial part of the wave function can be antisymmetric, leaving a symmetric spin part. By this argument, the closer the atoms, the less likely they will have parallel spins. At some point, the spatial portion of the wavefunction will become symmetric and the spins will anti-align, leading to neighboring atoms of oppositely aligned moments (antiferromagnetism). From this we can see that the separation of the neighboring atoms influences what type of magnetic order will occur. Again, this is a model intended only to create the picture of how ferromagnetism may arise. This type of interaction is called "direct exchange", whereby the direct interaction of neighboring local moments influence each other's magnetic orientation. The Hamiltonian for such a system can be written as

$$\mathcal{H} = -\sum_{ij} J_{ij} \vec{\mathrm{S}}_i \cdot \vec{\mathrm{S}}_j \tag{7.3}$$

where J_{ij} is the exchange integral, $\vec{\mathrm{S}}_i$ is the spin at the associated lattice site [2], and the summation is over all atomic sites, excluding $i = j$. The way that Eq. (7.3) is written, positive values of J_{ij} result in ferromagnetism, while negative values result in antiferromagnetism. The exchange integral incorporates the arguments presented above as to how the neighboring moments align.

Now that I've demonstrated how ferromagnetism can occur, I will attempt to show how this can also result in a spin polarized current. Ferromagnetic materials

[2] One should actually be considering the total angular momentum, $\vec{\mathrm{J}}$, which the atomic moment is proportional to as in Eq. (7.1). However, many magnetic material show negligible contribution to $\vec{\mathrm{J}}$ from the orbital angular momentum. Therefore, $\vec{\mathrm{J}} = \vec{\mathrm{S}}$.

such as iron, nickel, or cobalt exhibit what is called itinerant-electron ferromagnetism (or just itinerant ferromagnetism). Each of the above elements contain partially filled d orbitals, along with filled s orbitals. Typically, conduction occurs with the s-orbital electrons. The exchange interaction (or coupling) tells us that there is a significant overlap of the electron wavefunctions. This cannot be entirely the case if the electrons are localized. Therefore, some of the d-orbital electrons must move from atom to atom. As well, the moment of the s-orbital electrons (i.e., spin) must be influenced by the moments of the atom's electron configuration. This is indeed the case and is most evident in the fact that the magnetic moments per atom in Fe, Ni, and Co do not correlate with an integer number of d-orbital electrons. In a ferromagnetic material, with complete saturation of the moments, we have the relation

$$m = g\mu_B S \tag{7.4}$$

where S is the total spin from the electrons in the d orbital (see footnote above). Let us take, for example, Ni. Nickel has a saturation moment $m = 0.616$ and a g-factor of $\simeq 2.185$. We can see from Eq. (7.4) that Ni has a fractional spin alignment, indicating that there are fractional electrons in the d orbital. In the itinerant ferromagnetism model [161–163], the magnetic electrons (d-orbital electrons) and the s electrons are considered to be non-localized. This rationale is able to explain the above result. We can actually determine the electron configuration for Ni using the above numbers. The free atom of Ni has eight $3d$ electrons and two $4s$ electrons for a total of ten electrons. The above numbers indicate that $S = 0.282$ for bulk Ni,

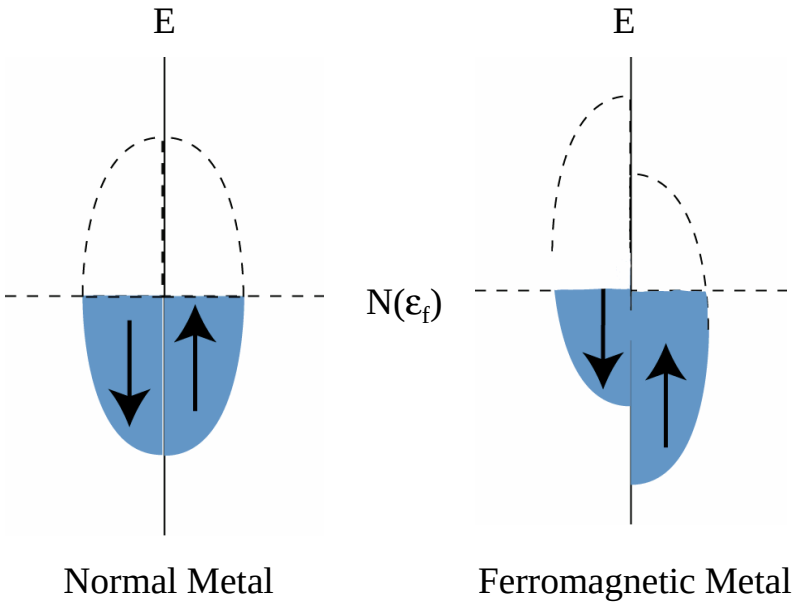

Figure 7.1: Schematic of the Density of States at the Fermi surface N(ε_f) for normal metals and ferromagnetic metals. The ferromagnetic metal has a disproportionate number of available spin-down states at the Fermi surface, as compared to the number of spin-up states. The normal metal has equal numbers of up and down states.

and that there are twice that number in unpaired spins in the d orbital (i.e., 0.564 unpaired spins). This means there are 9.436 electrons in the d orbital and 0.564 electrons in the s orbital. The fact that there are fractional electrons in the orbitals means that electrons are, in fact, moving into and out of these orbitals. This is especially important for the d-orbital electrons since they have a strong correlation with electrons in adjacent atoms. Hence, they play some role in the conduction process. There is experimental evidence in Hall and Nernst measurements which confirms this notion [161]. The discrepancy of spin-up and spin-down states in the d orbital indicate that there is also a discrepancy at the Fermi surface between the up and down states. This is shown schematically in Fig. 7.1. This, in turn, means there is a disproportionate amount of available states with spin-up and spin-down at the

Fermi surface. Hence, the conducting electrons have a preferential spin direction, or polarization. This also means that it is energetically easier to move electrons with the majority spin state, as opposed to the electrons with the minority spin state. It has been experimentally shown that Fe, Ni, and Co have spin polarized current. Tunneling experiments have determined that the amount of polarization is approximately 44%, 34%, and 11% for Fe, Co, and Ni, respectively [164]. In this way, the itinerant ferromagnets can be used as polarizers and as filters, without having to do any extra work.

Of course, the arguments given above don't work for all ferromagnets, but it does give fairly good predictions/results for the transition metal itinerant ferromagnets.

It is worth briefly mentioning how ferromagnets behave in an applied magnetic field. In zero field, a ferromagnet is comprised of domains, within which the spontaneous magnetization causes the spins in the domain to align. Nominally, the domains are oriented randomly with respect to each other, and a small (or zero, which is still small) moment is produced. Upon the application of a magnetic field (Fig. 7.2), the domains begin to align and the moment of the ferromagnet increases. When all the domains are aligned, the moment saturates. When the magnetic field is decreased to zero, the moment of the ferromagnet does not decrease back to near zero. Rather, a moment is maintained. Decreasing the field towards negative values begins to reorient the domains in the material, until they again saturate at large enough fields. Increasing the field towards positive values creates a different path. At large enough fields, the moment saturates again. This "loop", is called a hystere-

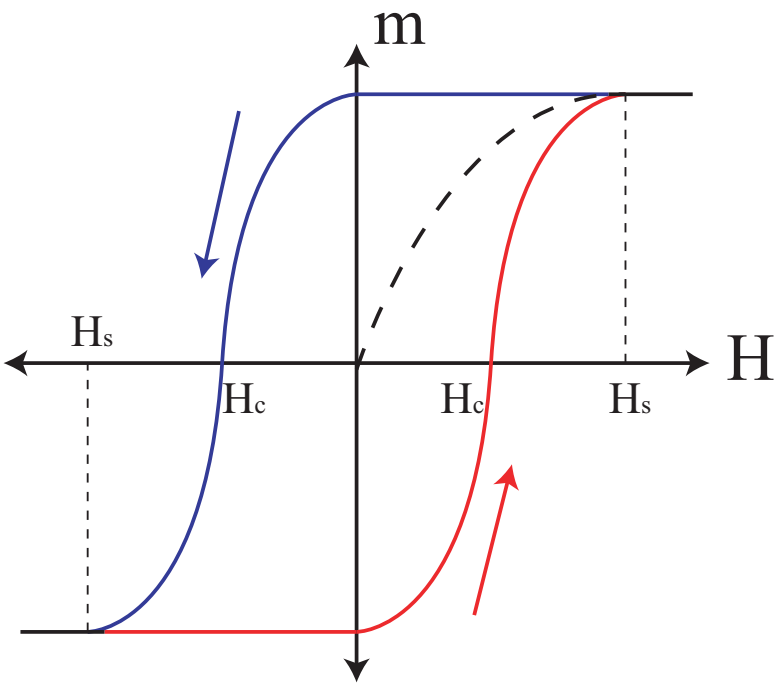

Figure 7.2: Schematic of an $M - H$ curve for a ferromagnet. The dashed line represents the moment due to the initial application of a magnetic field. The right branch (positive field, up arrow) represents the moment in a positively increasing field (after saturation). The left branch (negative field, down arrow) represents the moment in a negatively increasing field. Where the curve levels off is the saturation moment. The field at which this occurs is the saturation field (H_s). The field values at which $m = 0$ is the coercive field (H_c). The field difference between the positive and negative H_c is the coercivity of the ferromagnet. It is used as a measure of how difficult it is to switch the moments (i.e., a "hard" or "soft" magnet

sis loop, or an $M - H$ curve. Continuing back and forth between large positive and negative applied fields retraces the hysteresis loop. The moment can be switched by applying a field large enough to saturate the moments (H_s). If a field lower than H_s is applied, the trace of the $M - H$ curve stays on the same branch. In order to switch branches, $H \geq H_s$. The value of the $M - H$ loop where $m = 0$ is the coercive field (H_c). The field range between the positive and negative H_c is called the coercivity of the ferromagnet. It is a measure of the hardness of the ferromagnet, i.e., how difficult it is to switch the alignment of the moments. If the coercivity of

the material is zero (both branches overlap exactly), then the material is classified as a superparamagnet rather than a ferromagnet.

7.1.2 Two Current Uses of Spintronics in Technology

Spintronics, in the simplest form, has been used in commercial technology since at least the mid 1990's. Thanks to the discovery of giant magnetoresistance [165] (GMR) in superlattices of ferromagnetic materials, IBM proposed and implemented a device called a "spin-valve" [166] as a read head for computer hard disk drives. A schematic of a spin-valve device is given in Fig. 7.3. The spin-valve consists of two ferromagnetic layers separated by a metallic layer, a polarizing layer and a filtering layer. In Fig. 7.3(a), both ferromagnetic layers have their magnetic moment aligned in the same direction. As current enters into the polarizing layer, the current becomes polarized. Since the filtering layer is aligned in the same direction as the first layer, current flows relatively easily through the valve. If the filtering layer is aligned anti-parallel, with respect to the polarizing layer, then it is more difficult for current to pass through the valve [Fig. 7.3(b)], due to the differences in the spin states available at the Fermi surface of each ferromagnetic layer. This results in an increase in resistance, the GMR. The magnetic orientation of the polarizing layer is typically fixed, while the filtering layer can be changed through the application of an external magnetic field.

Another device, similar to the spin-valve, is the magnetic tunnel junction (MTJ). Rather than using a metallic layer between the ferromagnetic layers, as

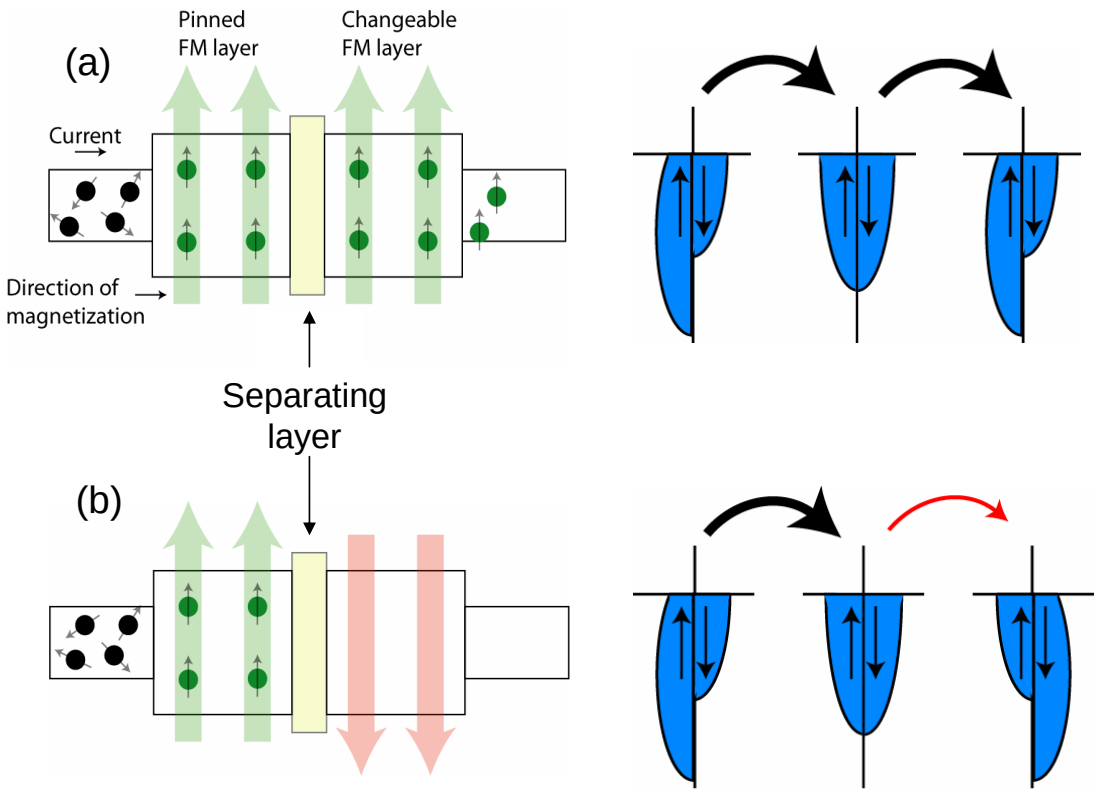

Figure 7.3: Schematic of a spin-valve. (a) Both ferromagnetic layers (polarizer and filter) are magnetically aligned, allowing the spin polarized current to pass through the valve. (b) The filtering layer is aligned anti-parallel with respect to the polarizing layer. The differences of available spin states in the two layers makes it harder to pass current, resulting in a higher resistance. To the right of the valves is a schematic of the density of spin states for the layers in the valve.

in the spin-valve, MTJs incorporate an insulating barrier. This change allows for substantial increases in resistance when the polarizing layer and the filtering layer are anti-aligned (roughly a factor of two when compared to the spin-valve). The exciting aspect of MTJs is their incorporation into technology. Magnetic random access memory (MRAM) appears to be the near future of RAM used in computers. MRAM uses MTJs to store information. Just like the spin-valve, the resistance across the device is the indicator of the state: high-resistance, anti-parallel ferromagnetic layers indicate one state; low-resistance, parallel layers indicate the second

state. The states are controlled by switching the filter layer, through the application of an external magnetic field.

The exciting aspect of MRAM is that it is non-volatile with a long lifetime for rewriting. Traditional RAM relies on manipulation of charge in order to create a bit of memory. In this sense, if power to the RAM is cut off, the memory states are lost. With the MRAM, this is not the case because the ferromagnetic layers do not need external power in order to maintain their alignment. Therefore, turning off the power to an MRAM would not result in a loss of the information stored.

7.2 Diluted Magnetic Semiconductors

The devices mentioned up to this point are composed of ferromagnetic metals. It would also be nice to replace conventional transistors with equivalent spin-based devices. A device proposed by Datta & Das [167] set forth the idea of a spin-based field effect transistor (spin-FET). Rather than modulating the current density in the semiconducting channel of a traditional transistor (i.e., making the channel conductive of insulating), spin-FETs modulate the spin polarization of the current. Modulation of either the current density or the spin polarization allows one to variably change the conductance of the transistor, thereby making it an electronic switch. A schematic of a spin-FET is given in Fig. 7.4. The spin-FET uses a ferromagnetic source and drain on either side of 2D electron gas (2DEG) semiconducting channel. A gate electrode over the channel allows for an electric field to be applied to the channel.

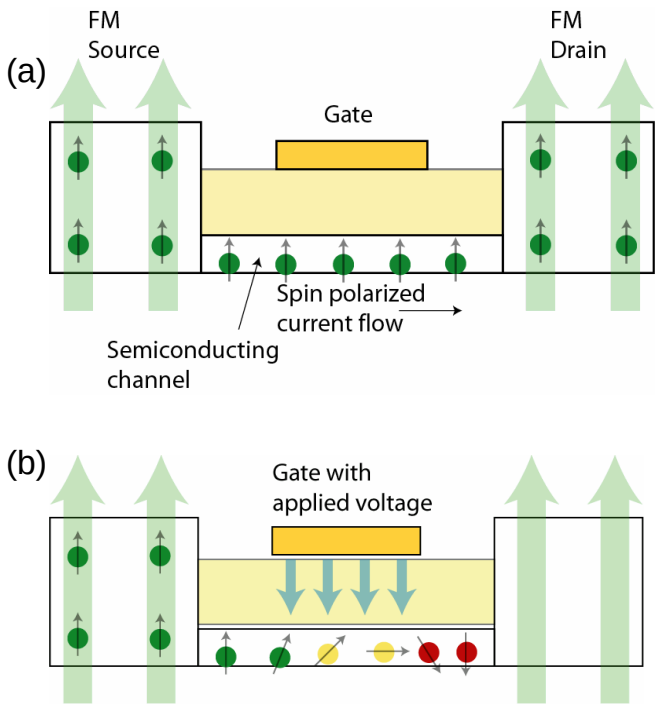

Figure 7.4: Schematic of a spin-FET. (a) Both ferromagnetic layers (source and drain) are magnetically aligned (direction of the arrows), allowing the spin polarized current to pass through the semiconducting channel. (b) A gate voltage is applied across the channel, which causes a procession of the spins in the current. The spin state at the end of the channel is opposite to that of the drain, causing a reduction in the flow of current.

Spin splitting of the conduction band was found to occur in narrow-band semiconductors [168] due to a term in the Hamiltonian, called the Rashba term, which is derived from spin-orbit interactions [169]. The spin-orbit term arises from an electric field due to the interface of the 2DEG with the semiconductor. The Rashba term can be written as

$$\mathcal{H}_{SO} = \eta(\vec{\sigma} \times \vec{k}) \cdot \hat{u}, \tag{7.5}$$

where η is the spin-orbit coupling coefficient, σ are the Pauli spin matrices, k are

the wavevectors, and $\hat{u}$ is in the direction of the interface electric field. The spin-orbit coefficient (η) is proportional to the expectation value of the perpendicular electric field, which is itself inversely related to the band gap of the semiconductor [168]. Therefore, the importance of this term grows with a smaller band gap semiconductor. One of the important aspects of this term in the Hamiltonian is that a differential phase shift [$\Delta\Theta = (k_{\downarrow} - k_{\uparrow})L = 2m^{\star}\eta L/\hbar^2$] is established between the spin-up and spin-down bands. Therefore, if $\Delta\Theta = \pi$, then the majority spin alignment will change orientation and the majority and minority spin bands will switch roles (Fig. 7.4). An alternative description is that the electron spins precess in an effective magnetic field [$\vec{B}_{SO} = (2\eta/g\mu_B)(\vec{k}\times\vec{u})$, g is the g-factor and μ_B is the Bohr magneton] [170]. So, an applied gate voltage can modulate the spin polarization of the current in the spin-FET, and the ferromagnetic source is important for supplying a polarized current, and the drain is important for filtering out the proper orientation. If a sufficient gate voltage flips the spin orientation at the drain, current will be supressed. The advantages of the spin-FET are that it is energetically easier to flip the spins than it is to expel charge in a conventional FET, as well as it is faster to flip the spins [171]. One of the more exciting prospects of the spin-FET is the possibility of using it as memory and as a programmable logic gate [171] (with much longer lifetimes that current programmable gates), by switching the magnetic orientation of either the source or drain (in a similar way as in the MRAM). In this sense, the micro processers in computers could be reconfigured on the fly in order to be optimal for different functions. This is currently not possible with conventional FETs.

One large problem exists in efficiently injecting the spin-polarized current into the 2DEG channel. Due to the conductivity mismatch of the ferromagnetic source/drain (which are metals in the spin-FET proposal) and the semiconducting channel, significant scattering at the boundary nearly eliminates the spin polarization of the current entering the channel [172]. The use of tunnel junctions between the source/drain and the channel has been suggested by Rashba [172], as well as the use of ferromagnetic semiconductors [173]. It is this last idea which is motivating research into diluted magnetic semiconductors.

Ideally, the ferromagnetic semiconductor would be magnetic at room temperature, in order to have a practical application. Traditional ferromagnetic semiconductors have ferromagnetic transition temperatures (Curie temperature T_C) far below room temperature. For example, EuO has a $T_C \simeq 77$ K [174]. Additionally, it would be useful if the ferromagentic semiconductors had semiconducting properties similar to the semiconductors presently used in transistors.

An alternative to conventional ferromagnetic semiconductors is a class of materials called diluted magnetic semiconductors (DMS). Unlike ferromagnetic semiconductors, where the magnetic species resides on every lattice site, DMS systems contain only a small fraction of magnetic species in the unit cell (Fig. 7.5). In the itinerant ferromagnetic systems, the magnetism and spin polarization occurs due to the exchange interaction of neighboring atoms, and the contribution of d-orbital electrons to the conductivity. In the ferromagnetic semiconductor EuO, magnetism arises from an exchange interaction between localized f-orbital electrons. The spin polarization is attributed to a spin-orbit coupling between the delocalized s electrons

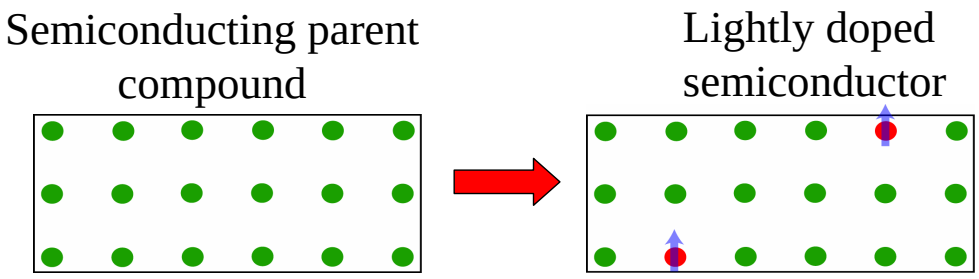

Figure 7.5: Schematic of diluted magnetic doping. The parent compound has a small fraction of magnetic atoms substituted into the matrix. The red dots with the arrows indicate the magnetic atoms.

and the localized f electrons, i.e., a coupling of the spin angular momentum of the s electron with the orbital angular momentum of the f orbitals [175]. DMS systems, however, have magnetic dopants which have significant spatial separation between successive magnetic ions. Therefore, a direct exchange between magnetic ions is not the cause for the magnetism and spin polarization in these systems. Current models used to describe these systems will be briefly mentioned in Sec. 7.3.

The canonical DMS system is $Ga_{1-x}Mn_xAs$, which has a $T_C \simeq 140$ K ($x = 0.06$) for single layer [176] and $T_C \simeq 160$ K ($x = 0.074$) for trilayer [177] structures. One of the desired properties of the DMS systems is that the ferromagnetism interacts with the charge carriers. By this I mean that there is a spin-polarized current. Carriers interacting with the ferromagnetism have been shown in magnetic circular dichroism experiments [178]. Successful injection of spin polarized current has been demonstrated in the $Ga_{0.955}Mn_{0.045}As$ system, where the spin current was injected to a non-magnetic semiconductor $In_{1-x}Ga_xAs$ quantum well [179]. So it appears that we have all the components to make a spin-FET. However, to date there are no reports of the successful construction of a spin-FET.

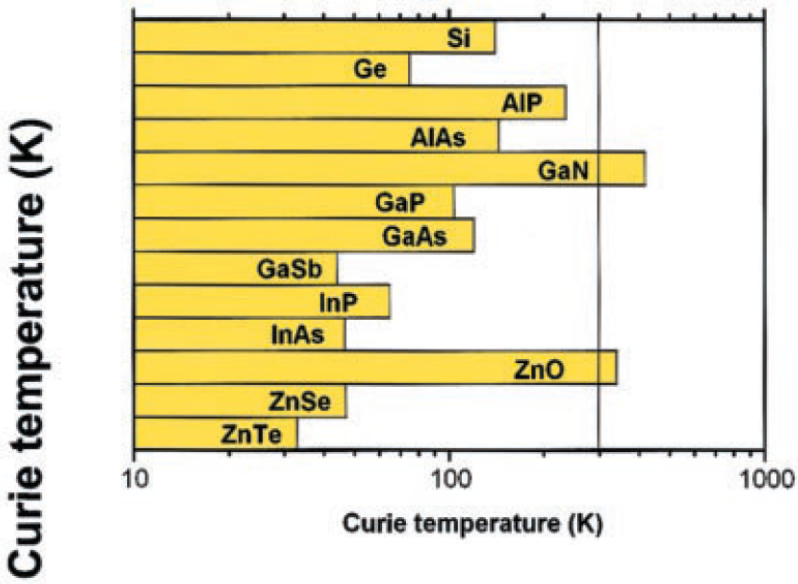

Figure 7.6: Predictions for ferromagnetic transition temperatures in several semiconducting compounds with 5% magnetic substitutions, taken from Ref. [180].

Predictions were made by Dietl *et al.* [180] for semiconductors which could theoretically obtain room temperature ferromagnetism, using a model in which the carriers mediate the interactions between sparse magnetic moments of Mn (5%) within the semiconductors (Fig. 7.6). However, only the oxide ZnO has shown an experimental promise. A report shortly followed that demonstrated ferromagnetism above room temperature in $Zn_{1-x}Co_xO$ [181]. However, the reproducibility of the results was less than 10%. Another group [182] reported above room temperature ferromagnetism in another oxide system anatase $Ti_{1-x}Co_xO_2$. It was beginning to look as though room temperature ferromagnetic semiconductors were possible in the oxide systems.

Most of the initial reports focused on the magnetic properties of the oxides. Very little was reported in terms of transport, which could confirm that the ferro-

magnetism is indeed influencing the charge carriers. This lack of knowledge about the carriers coupling to the ferromagnetism in the oxide DMS systems is the motivation behind this portion of the thesis. In this regard, I used the Hall effect in an attempt to resolve this issue in the case of $Ti_{1-x}Co_xO_2$.

As outlined in Chapter 3, the Hall effect can be influenced by magnetic moments in the material. The Hall resistivity is empirically given by

$$\rho_{xy} = R_\circ B + 4\pi R_s M \tag{7.6}$$

where $R_\circ$ is the ordinary Hall coefficient, R_s is the anomalous Hall coefficient (which is much larger than the ordinary Hall coefficient), and M is the magnetization of the material. The second term in Eq. (7.6) is the anomalous Hall effect. It is believed to arise from a spin-orbit interaction between the spin of the charge carrier and the orbital angular momentum (of the magnetic orbital) of the atoms moment. It is worth noting what are the expected behaviors of the anomalous effect. There are two main features: from Eq. (7.6), the magnetic field dependence of ρ_{xy} will mimic the field dependence of the magnetization of the material (just like the M-H curves mentioned above); the temperature dependence of R_s goes as some power of the longitudinal resistivity ($R_s \propto \rho_{xx}$). An example of what this looks like can be seen in the $Ga_{1-x}Mn_xAs$ system (Fig. 7.7) This feature in the Hall effect is in essence what we are looking for in $Ti_{1-x}Co_xO_2$.

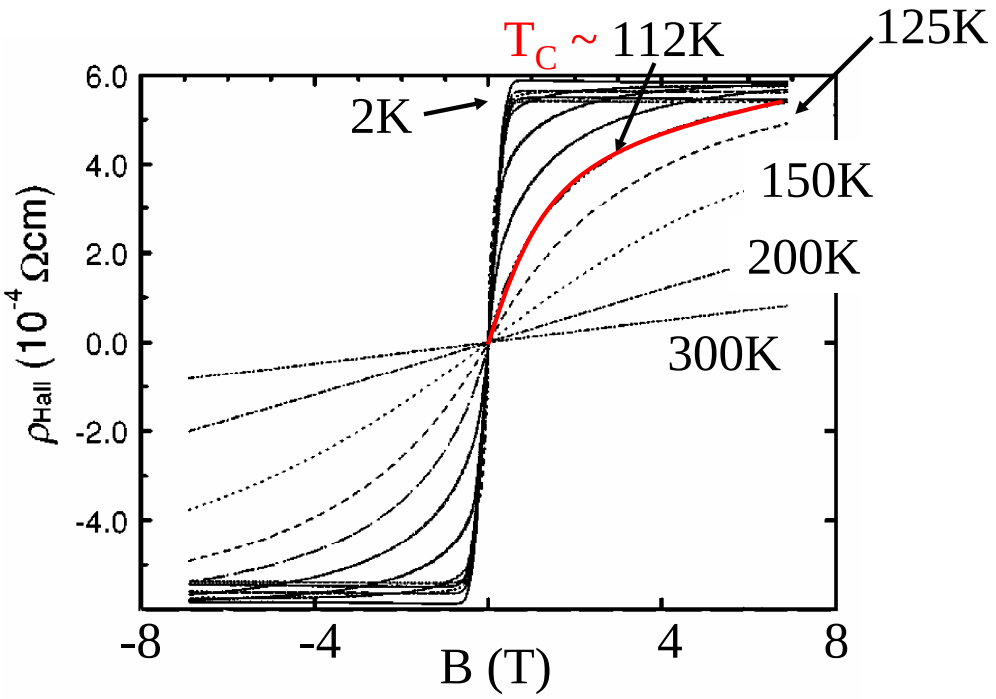

Figure 7.7: ρ_{xy} versus magnetic field for $Ga_{0.947}Mn_{0.053}As$, taken from Ref. [183]. The nonlinear behavior is due to the anomalous Hall effect. The anomalous contribution is much larger than the ordinary contribution. The result is a very sharp increase in ρ_{xy}, as the field increases from zero, which saturates (due to the anomalous contribution). The ordinary contribution is dominant after the saturation of the anomalous part. T_C is indicated on the plot. The anomalous contribution can still be seen above T_C. Below T_C, the anomalous contribution grows as the temperature decreases. This is consistent with the temperature dependence of the resistivity (see text).

7.3 Models for DMS Systems

In Section 7.1.1, I briefly demonstrated how the magnetization and spin-polarization of current occurs in the itinerant ferromagnets. The situation is different in the diluted magnetic semiconductors because there is only a small fraction ($\leq 10\%$) of doped magnetic elements. With this being the case, the magnetic atoms are separated from each other by rather large distances and so a direct exchange between moments cannot explain the ferromagnetism in the DMS systems. I will

give a brief, qualitative glimpse at the popular models used to explain these systems. It is important to note that these systems are semiconductors, and so the carrier concentrations can be varied so as to achieve an insulating material or a conducting material. In either case, it is the doped carriers which are believed to correlate the magnetism throughout the material. Each case has a different picture.

7.3.1 Bound Magnetic Polarons

In an insulating semiconductor, the doped carriers tend to be localized about the dopant cite (not necessarily only on the dopant site). If the area about which the carrier is localized overlaps a magnetic atom, an exchange interaction between the carrier and the magnetic atom correlates the spin of the carrier with the moment of the atom (polarizes the carrier). This is the basic picture of a bound magnetic polaron, which is based on the well-know F-center model. As the density of the magnetic polarons increases, through increased magnetic dopants, overlap of the polarons occurs. Through the overlap, the magnetic moments are now indirectly correlated through the localized carriers (Fig. 7.8). A few overlapping polarons would produce a local, short-range ferromagnetic behavior [3]. With a further increase of the magnetic polaron density, a percolative path can be established, which would then produce a long-range ferromagnetism with some form of spin-polarized carriers (due to the exchange interaction).

[3] As with the magnetism created in the itinerant model, anitferromagnetism as well as ferromagnetism can occur.

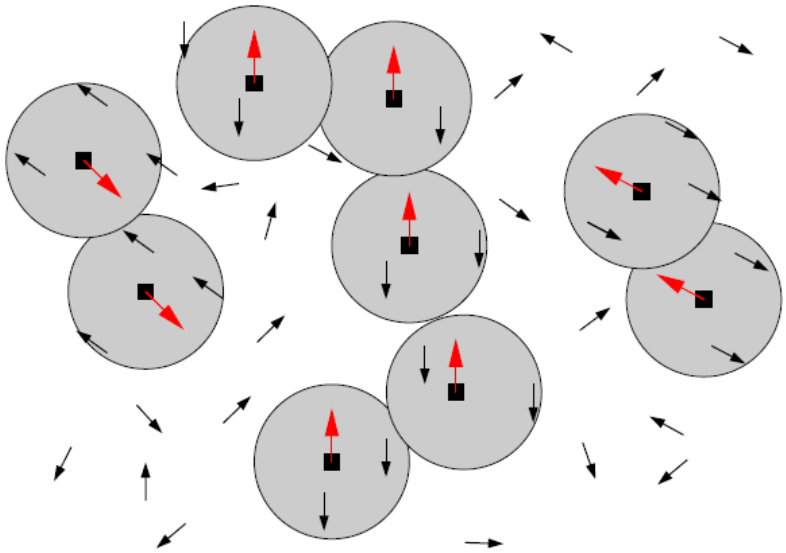

Figure 7.8: Schematic of the bound magnetic polaron model, taken from Ref. [184]. The squares with the red arrows indicate the magnetic moment of the carrier dopant in the semiconducting lattice. In this particular case, the dopant is magnetic. The free arrows represent the spin of the localized carriers. The grey circle represent the area by which the carriers are localized, and in this case the magnetic polaron. The overlap of the polarons leads to long-range magnetic order in the percolating limit.

7.3.2 RKKY Model

The well known Ruderman-Kittel-Kasuya-Yosida (RKKY) model [185–187] is applicable for conducting materials in which the carriers are not localized. The itinerant carriers are temporarily localized around the magnetic moments of an atom, where the spins of the carriers are now determined by the magnetic moment of the atom. As the spin aligned carrier moves through the lattice, it interacts with a second magnetic moment. The two magnetic moments then have an indirect exchange through the itinerant carrier. The process repeats and long-range magnetic order is established through the material.

More details and references on either of these two models can be found in Ref. [184].

Chapter 8

Samples and Measurements

8.1 Introduction to $Ti_{1-x}Co_xO_{2-\delta}$

$TiO_{2-\delta}$ is a wide band-gap semiconductor which occurs in two *primary* structural phases, rutile and anatase. The rutile phase has a band gap of 3.05 eV, and the anatase phase has a band gap of 3.29 eV. Shallow donor levels are created through oxygen vacancies, giving a shallow band-gap of 4.2 meV with n-type carriers of high mobility [188]. Therefore, adjusting the oxygen content allows for easy tunability of the carrier concentration. The lattice structures of the rutile and anatase phases is given in Fig. 8.1. Both structures are tetragonal, and contain TiO_6 octahedra in the stoichiometric form. Titanium has an electron configuration of $[Ar]3d^24s^2$, and oxygen has the configuration $1s^22s^22p^4$. In $TiO_{2-\delta}$, the titanium has a 4+ valence, while oxygen has the typical 2− valence, yielding closed shell for both elements. Cobalt is doped substitutionally into the titanium sites as Co^{2+} [182, 191]. In $Ti_{1-x}Co_xO_{2-\delta}$, there is widespread concern over clustering of the cobalt in the matrix [192–194], especially for $x > 2\%$. There also seems to be disagreement about the solubility limit of cobalt in $TiO_{2-\delta}$ [182, 192–195], however it is generally agreed to be less than 10%.

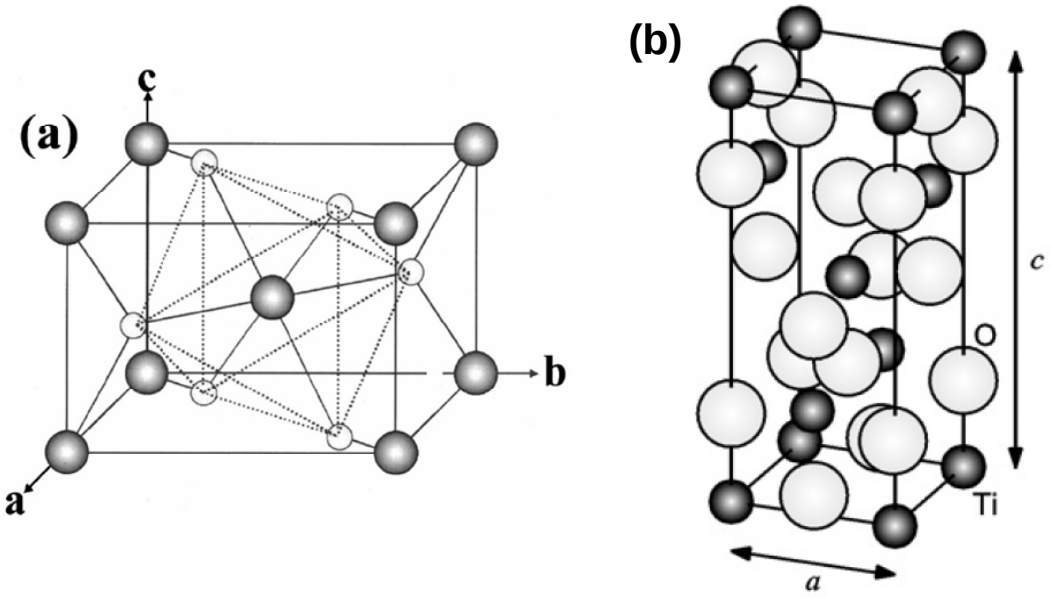

Figure 8.1: Tetragonal lattice structure of rutile and anatase TiO_2 (a) Rutile structure ($a = b = 4.59$ Å, $c = 2.96$ Å) taken from Ref. [189] (b) Anatase structure ($a = b = 3.79$ Å, $c = 9.51$ Å) taken from Ref. [190]

8.2 Sample Growth and Measurements

Initially, cobalt-doped anatase thin films were grown in an attempt to observe an anomalous contribution to the Hall effect. The growth procedures are outlined below, but I would like to motivate the types of films we ultimately measured for the anomalous Hall effect. The initial anatase films showed ferromagnetic behavior at room temperature [193], with a $T_C \simeq 650$ K. Studies of the lattice constant showed a smooth increase of the c axis up to $x \simeq 2\%$, and no change for higher cobalt dopings [193]. Therefore, the solubility limit for cobalt in $TiO_{2-\delta}$ was 2% under the growth conditions outlined below. These films however, showed a linear Hall resistivity with field (Fig. 8.2). Since the Hall coefficient is inversely proportional to the carrier density ($\frac{d\rho_{xy}}{dB} = R_H = 1/ne$, n is the carrier density, e is the

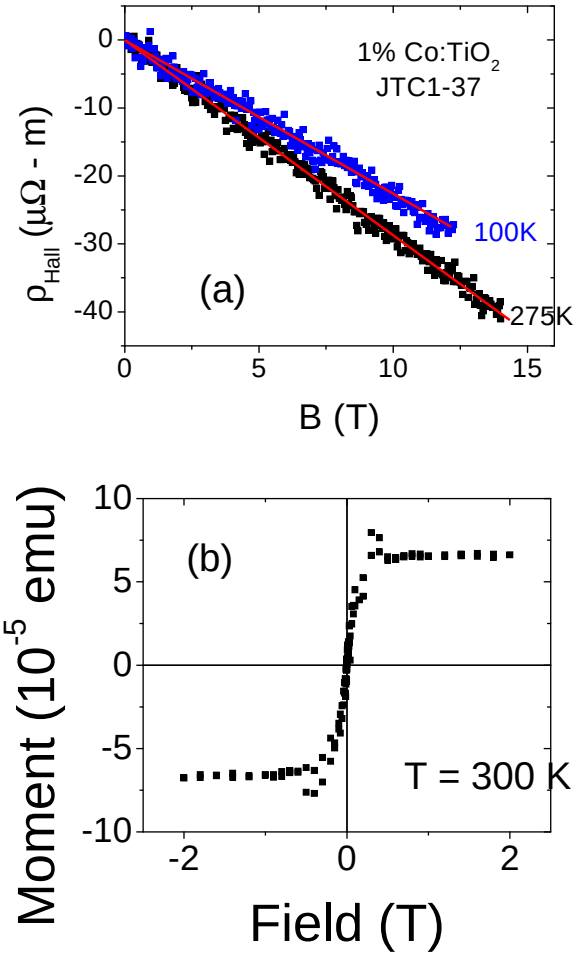

Figure 8.2: (a) ρ_{xy} versus magnetic field for anatase $Ti_{0.99}Co_{0.01}O_{2-\delta}$ (sample JTC1-37) (b) M-H loop for the same sample in (a), taken at 300 K. Notice ρ_{xy} is linear despite clear magnetic behavior.

electronic charge, and R_H is the Hall coefficient), it was believed that the low carrier concentration obtained in these films ($n \simeq 1 \times 10^{18}$ /cm^3) might overshadow a weak anomalous Hall effect because the slope of ρ_{xy} may be too big. Since the carriers originate from oxygen vacancies, further reduction was necessary to reduce the normal Hall resistivity (ρ_{xy}). In fact, as the project was ongoing, two groups reported an anomalous Hall effect; one in highly reduced rutile $Ti_{1-x}Co_xO_{2-\delta}$ [195], and the other in $Ti_{1-x}Fe_xO_{2-\delta}$ [196]. Therefore, the objective was to study highly

reduced samples. All transport measurements were carried out in a Quantum Design Physical Property Measurement System (PPMS), and magnetic measurements were done in a Quantum Design SQUID magnetometer.

The thin films of anatase and rutile $Ti_{1-x}Co_xO_{2-\delta}$ ($x = 0, 0.02$) were grown via pulsed laser deposition [1]. The low cobalt concentration was chosen such that cobalt clusters would be less likely to occur. Stoichiometric ceramic targets and deposited films through a Hall bar shadow mask (similar in dimensions to the eight pad Hall bar in Chapter 5) onto 5 mm × 10 mm $LaAlO_3$ substrates (for anatase films) and 5 mm × 10 mm R-Al_2O_3 ($1\bar{1}02$) substrates (for rutile films). The substrate heater temperature was 700° C and the laser energy density was 1.8 $\frac{J}{cm^2}$ at a frequency of 3 Hz. The thicknesses of all the samples was $\simeq$ 1500 Å.

In order to obtain the anatase structure, films were grown on $LaAlO_3$ in an oxygen environment of 10^{-4} to 10^{-8} Torr. At higher pressures ($P_{O2} \geqslant 10^{-6}$ Torr), the films grew in (001) anatase form and showed room temperature ferromagnetic behavior [193]. Lower pressures resulted in a structure similar to that of rutile $TiO_{2-\delta}$ due to excessive oxygen removal [193]. On R-Al_2O_3 ($1\bar{1}02$) substrates, the rutile structure was stable at lower oxygen pressures than those for the anatase phase ($P_{O2} \ll 10^{-6}$ Torr).

Two approaches have been used to increase oxygen vacancies in rutile Ti_{1-x}-$Co_xO_{2-\delta}$. Sample TC2-86 ($x = 0.02$) was grown in vacuum with a base pressure of 2x10^{-8} Torr. Sample TC2-84 ($x = 0.02$) was deposited using a 15% Hydrogen-Argon mixture at 1 mTorr of pressure. This mixture acts as a getter, and results

[1] This technique is described in Chapter **??**

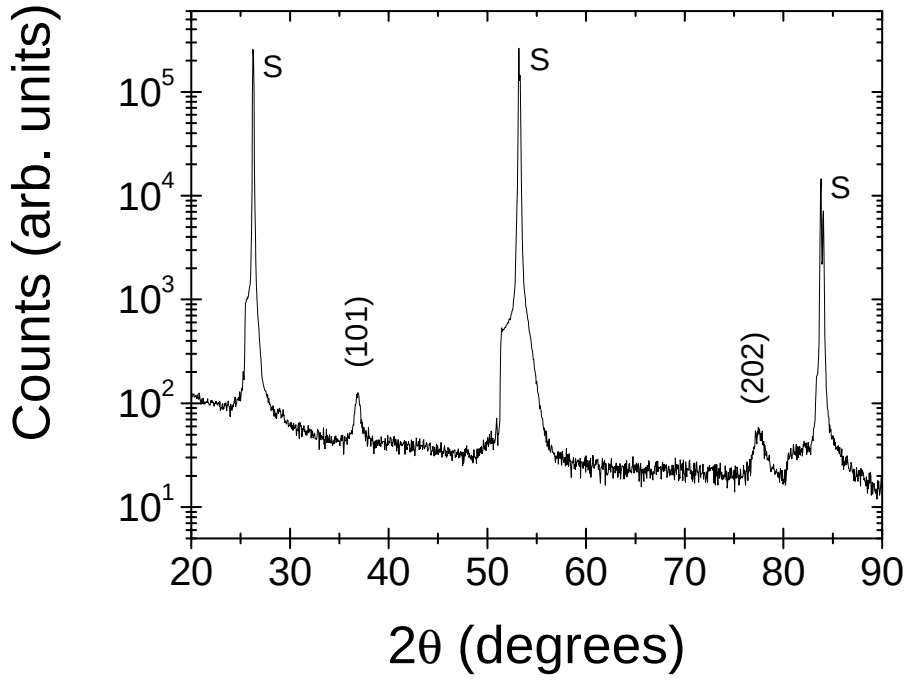

Figure 8.3: X-ray diffraction scan of rutile $Ti_{1-x}Co_xO_{2-\delta}$. The substrate peaks are denoted by 'S'. This particular scan is from sample TC2-86. Sample TC2-84 has a similar XRD scan.

in an effectively lower oxygen partial pressure. Again, the purpose of a reducing environment is to create charge carriers through oxygen vacancies.

X-ray diffraction (XRD) patterns, in Fig. 8.3, show that sample TC2-86 grew in the rutile (101) structure [195, 196]. Sample TC2-84 showed similar XRD patterns. The relatively small intensities of the (101) and (202) peaks are probably due to structural compensation from the oxygen reduction, and will be addressed later in the chapter.

Both films display a relatively high conductivity ($\rho_{300K} = 2.53$ mΩ-cm and 13.4 mΩ-cm for sample TC2-86 and sample TC2-84, respectively), shown in Fig. 8.4. As the temperature decreases, the resistivity of sample TC2-84 increases in an activated manner whereas sample TC2-86 shows an elbow near 140 K. Similar behavior was

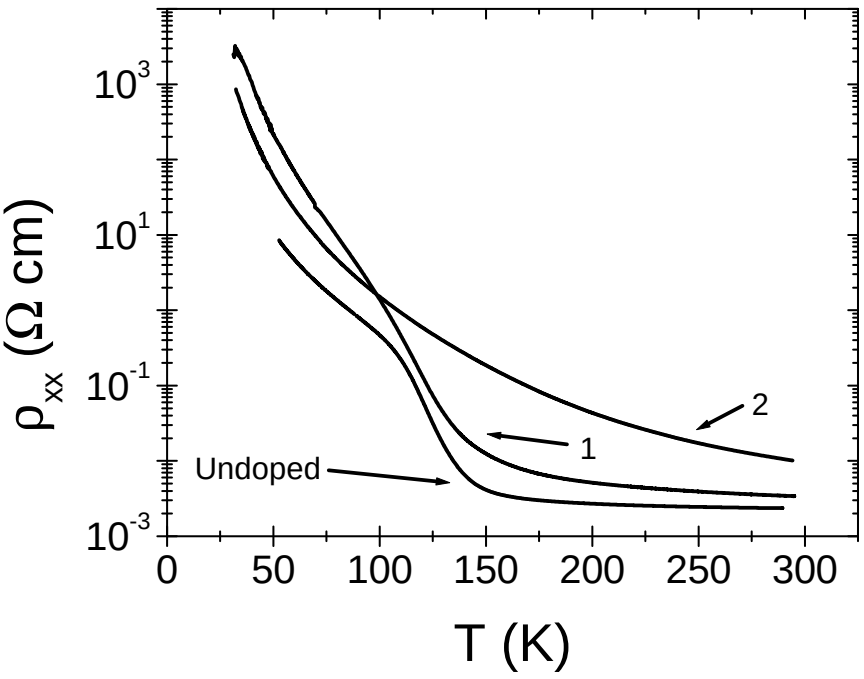

Figure 8.4: Resistivity curves for sample 1 (TC2-86), sample 2 (TC2-84), and an undoped film (TC0-94).

observed by Toyosaki *et al.* [195] and Wang *et al.* [196] for their films in which an AHE was observed. The resistivity of sample TC2-86 is not an expected result due to the elbow, whereas sample TC2-84 displays a temperature dependence similar to bulk $TiO_{2-\delta}$ [193]. The temperature behavior of sample TC2-86, however, matches more closely with the Magnéli phase of this material (Ti_nO_{2n-1}) [197]. This different phase of Ti-O orders in the rutile structure of $TiO_{2-\delta}$, so XRD scans may not be able to differentiate between the Magnéli phases and the rutile TiO_2 phase. We also grew an undoped film (sample TC0-94) in the same manner as sample TC2-86. The resistivity of this sample has a temperature dependence similar to sample TC2-86. Therefore, the temperature behavior of the resistivity of our $TiO_{2-\delta}$ films is influenced by the oxygen deficiency rather than the magnetic dopant (cobalt).

Just as a reminder, the Hall effect arises from the Lorentz force deflecting charges moving in a perpendicularly oriented magnetic field. This establishes an electric field transverse to the current. Typically this effect is linear in field. However, in magnetic materials, the magnetic moment associated with the atoms gives rise to an additive term in the Hall equation, [67]

$$\rho_{xy} = \frac{E_y}{J_x} = R_\circ B + R_s \mu_\circ M_S, \tag{8.1}$$

where ρ_{xy} is the Hall resistivity, E_y is the electric field perpendicular to the current and magnetic field, J_x is the current density, $R_\circ$ is the ordinary Hall coefficient, R_s is the anomalous Hall coefficient, $\mu_\circ$ is the permeability of free space, and M_S is the field-dependent spontaneous magnetization of the material. This anomalous Hall term is conventionally attributed to asymmetric scattering processes involving a spin-orbit interaction between the conduction electrons and the magnetic moments in the material. At low magnetic fields, the behavior of ρ_{xy} is dominated by the field dependence of M_S. Once the material's magnetization is saturated, the ρ_{xy} field dependence is linear and due to the ordinary Hall effect. In many materials, R_s shows a strong temperature dependence, which usually correlates with the electrical resistivity.

The field dependence of ρ_{xy} for sample TC2-86 is shown in Fig. 8.5, measured at 300 K and 200 K. The data were obtained by a simple subtraction in order to eliminate any magnetic field effects which are an even function of field, i.e. magnetoresistance (MR) ($\rho_{xy} = \frac{1}{2}[\rho_{xy}(H^+) - \rho_{xy}(H^-)]$). The inset shows the data before

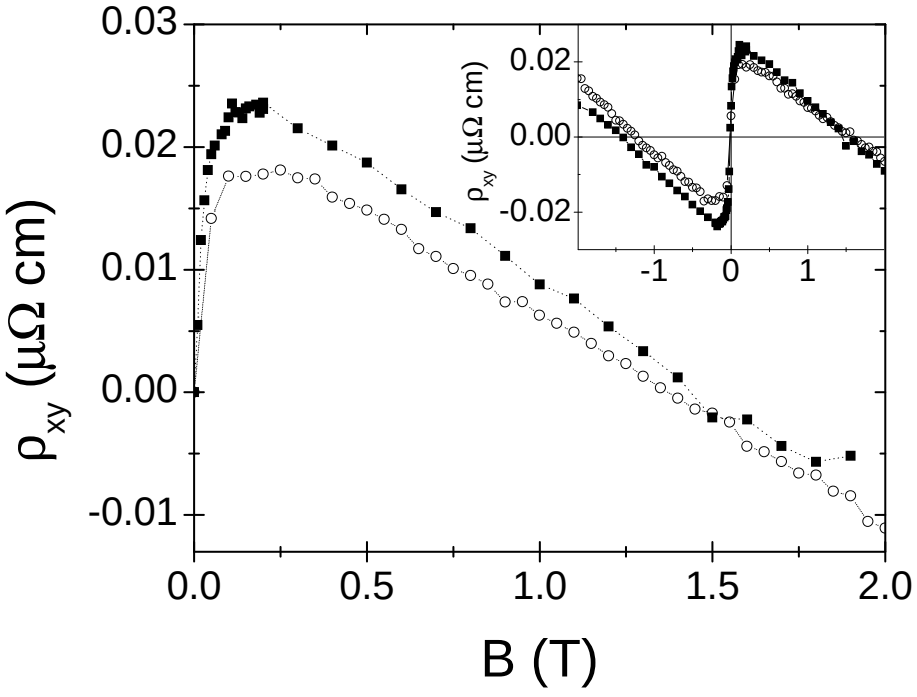

Figure 8.5: Hall resistivity for sample TC2-86. Closed symbols are taken at 300 K, and open symbols are taken at 200 K. The respective resistivities are 2.54 mΩ-cm and 3.22 mΩ-cm. The inset shows both negative and positive magnetic polarities of the raw data.

MR subtraction. These data show a sharp increase in ρ_{xy} at low fields and a linear behavior at higher fields, as expected for ferromagnetic materials. The magnetic hysteresis loop for sample TC2-86, measured with the field perpendicular to the film plane, is shown in Fig. 8.6(a). For comparison, the Hall data is expanded and replotted in Fig. 8.6(b). The field at which the magnetization saturates (~ 0.1 T) coincides well with the change in the low field behavior of the Hall data. Therefore, the rapid increase in ρ_{xy} at low field can be interpreted as an anomalous Hall effect. It is important to note that the negative slope of the high field Hall data indicates n-type carriers. This is in contrast with earlier reports, [196] but is expected for $TiO_{2-\delta}$. The negative slope at high fields gives an effective carrier concentration

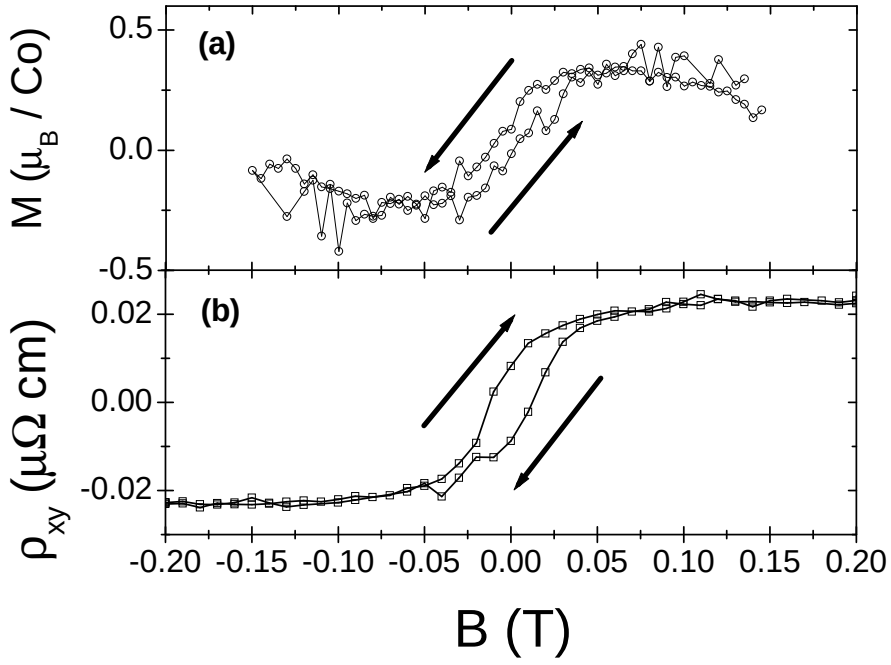

Figure 8.6: (a) Magnetic hysteresis loop at 300 K for sample TC2-86. (b) Expanded view of the Hall resistivity for sample TC2-86 at 300 K. The arrows indicate the direction of increasing/decreasing magnetic field

of $3.3 \pm 0.2 \times 10^{22}/\text{cm}^3$ at 300 K and $3.56 \pm 0.02 \times 10^{22}/\text{cm}^3$ at 200 K. The Hall data for sample TC2-84 is shown in Fig. 8.7. The inset shows the data after MR subtraction. A small but noticeable effect can be seen around zero field. However, if we subtract the ordinary Hall component (leaving the anomalous componenet) from the data (determined from the slope at high fields), a clear effect can be seen near the origin (Fig. 8.8). As in sample TC2-86, sample TC2-84 displays n-type behavior. The effective carrier concentration is $8.0 \pm 0.1 \times 10^{21}/\text{cm}^3$ at 300K and $1.837 \pm 0.005 \times 10^{21}/\text{cm}^3$ at 200K.

The rather large carrier concentration observed in these highly reduced samples raises some questions. It is known that oxygen vacancies contribute shallow donor states in $TiO_{2-\delta}$. A pure rutile film of $TiO_{2-\delta}$, grown by the same method as sample

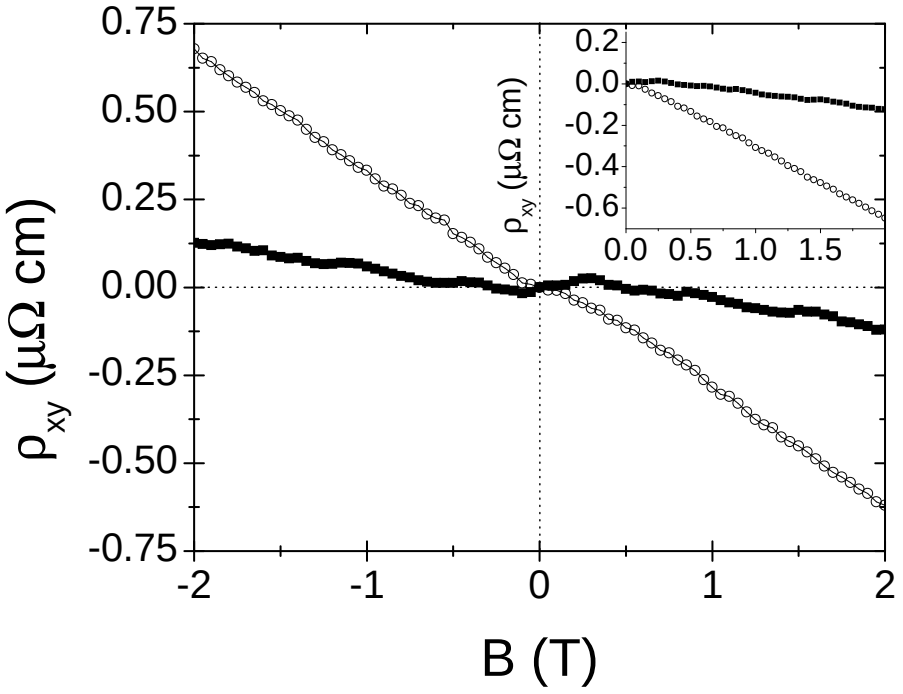

Figure 8.7: Hall resistivity for sample TC2-84 at 300 K (closed symbols) and 200 K (open symbols). The resistivities are 13.4 mΩ-cm and 57.2 mΩ-cm respectively. Inset shows the data after MR subtraction.

TC2-86 (sample TC0-94), gave a carrier concentration of $3.09 \pm 0.02x10^{22}/\text{cm}^3$ at room temperature, consistent with the cobalt-doped samples. This observed carrier density would then suggest the presence of approximately one oxygen vacancy for every unit cell ($\delta \sim 0.5$). This large carrier density, along with the resistivity behavior, suggests that Magnéli phases are present in films made using our growth conditions.

Our Hall measurements give clear evidence for an anomalous Hall effect in the heavily oxygen reduced samples. Is this effect intrinsic to the material, or is it a result of cobalt nanoclusters? First, the low field data changes behavior at nearly the same point that the magnetization of the sample saturates. The magnetic saturation in our films occurs at a field that is significantly lower than that for cobalt metal

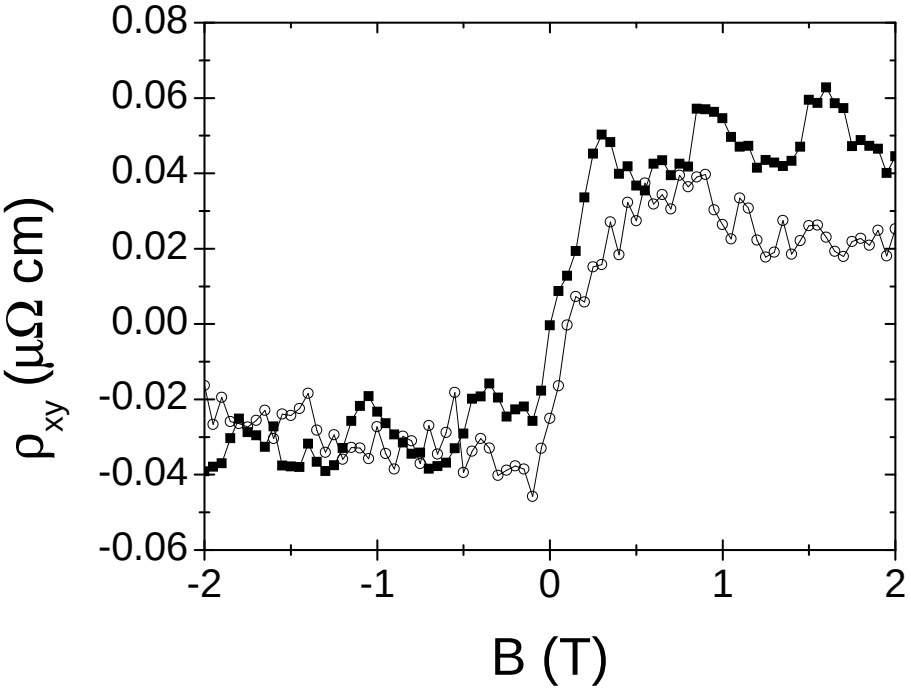

Figure 8.8: Hall resistivity for sample TC2-84 in which the normal Hall contribution is subtracted from the data. Closed symbols are taken at 300 K and open symbols are taken at 200 K.

films ($H \sim 1.5 - 2T$). Second, since the resistivities of each sample remain nearly the same for the two temperatures measured, we expect the anomalous Hall effect to remain relatively constant (in magnitude) for each sample, as is suggested by our measurements. While it is tempting to argue that the encouraging observation of the anomalous Hall effect in the cobalt doped $TiO_{2-\delta}$ system *clearly* testifies to its carrier-induced or intrinsic ferromagnetic character, other material-related possibilities cannot be completely ruled out at this stage. Specifically, the question of cobalt clustering still lingers in view of the absence of a clear theoretical negation of the occurrence of the anomalous Hall effect for such cases. The structural and chemical microstructures formed in samples prepared under highly reduced conditions could be quite complex, especially in view of the known occurrence of Magnéli phases in

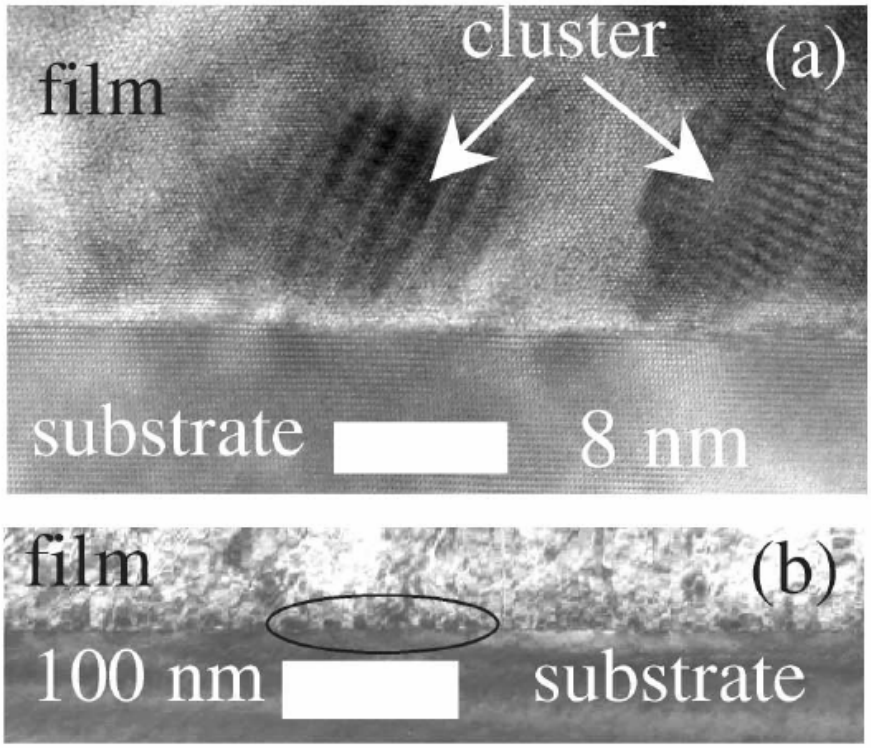

Figure 8.9: Cobalt clusters in highly reduced $Ti_{1-x}Co_xO_{2-\delta}$, taken from Ref. [198]. (a) A zoom-in of the clusters. (b) A wider view of the clusters.

the oxygen-reduced Ti-O system. Indeed, our Transmission Electron Microscopy (TEM) observations [198] on highly reduced samples show the presence of some $\sim$ 10 nm clusters at the interface (Fig. 8.9). Kim *et al.* [194] have also observed cobalt nanoclusters in their anatase Co:$TiO_{2-\delta}$ films when the samples are grown in a low pressure oxygen environment ($\simeq 10^{-7}$ Torr). In addition, Shinde *et al.* [198] demonstrate that the same samples which show an anomalous Hall effect also show superparamagnetism.

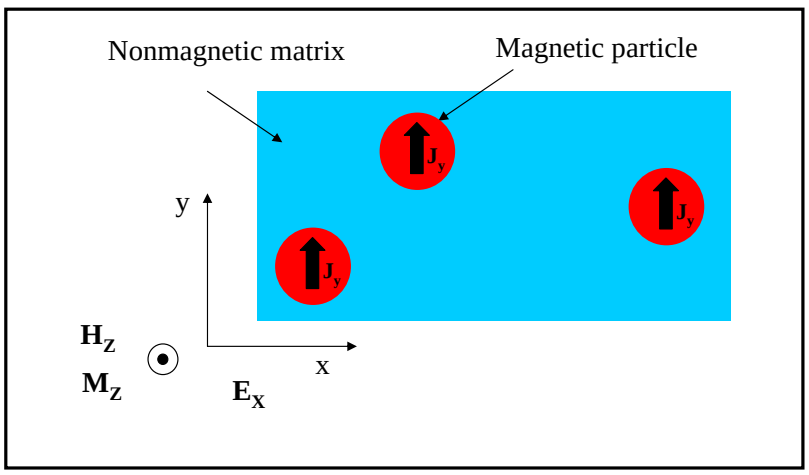

Figure 8.10: Cobalt clusters in an conducting matrix. The electric field in the x direction creates a current density in the y direction within the clusters. This current is injected into the matrix and the charge build-up within the matrix cancels out this current (similar to the Hall effect) leading to an anomalous Hall signal.

8.3 Possible Explanation for the Anomalous Hall Effect

If clusters are occurring in the highly reduced samples, how might the anomalous Hall effect arise. A solution was posed by Shinde *et al.* [198] in which an application of an electric field (E_x) will lead to current density (J_y) in the presence of a magnetic field (B_z). Figure 8.10 shows a schematic of this scenario. The current density in the clusters is proportional to the z component of the particle magnetization ($J_y = \sigma_A M_z E_x$, where σ_A is the anomalous Hall conductivity). Since the surrounding matrix is conducting, each cluster would inject current in the y direction in the TiO_2 matrix. Just in the same way that the current from the Lorentz force is canceled by a build up of charge on the boundaries, so is the additional

current from the clusters. This could yield an anomalous Hall effect in a system in which the magnetic behavior is not correlated with the charge carriers. Despite the fact that an anomalous behavior is observed near zero field in ρ_{xy}, due to the observation of clusters in these samples, it is impossible to attribute this behavior to an intrinsic correlation between the charge carriers and the observed ferromagnetism.

8.4 Future Directions

My work on this material was early on in my graduate career, and I have no plans to pursue this work in the near future. I will outline, though, what is the goal of the scientific community.

While there is widespread reports as to the intrinsic nature of the ferromagnetism in $Ti_{1-x}Co_xO_{2-\delta}$, a complete study on non-clustered ferromagnetic samples has not been reported. In this respect, a single report has not shown all of the following: 1) ferromagnetic behavior, 2) an anomalous Hall effect, 3) optical magnetic circular dichroism, and 4) electric field effects. Since the field of oxide dilute magnetic semiconductors is young, it is imperative to find the proper growth conditions such that all of the above effects are observed within a single sample, without cobalt clusters. Beyond this, the next step would be to incorporate the material into devices.

Chapter 9

Summary

9.1 $Pr_{2-x}Ce_xCuO_{4\pm\delta}$

Resistivity and Hall measurements were performed on overdoped superconducting cuprate $Pr_{2-x}Ce_xCuO_{4\pm\delta}$ (x=0.17) thin films, and comparisons were made between films with added oxygen (from the starting point of optimal reduction) and optimally reduced films subjected to disorder from H^+ ion irradiation. Hall measurements indicate that the primary effect of irradiation is to induce disorder by increasing the elastic scattering rate ($1/\tau_\circ$), whereas the oxygenated samples show a strong doping and disorder effect. Using the irradiated samples as a standard for the suppression of T_c due to disorder, I was able to separate the doping and disorder effects that result from a change in oxygen content, within a simple single-band Drude model. The results show that the modification of the oxygen content has a dominant disorder contribution to T_c, but that a doping contribution is also present, which affects T_c in the same fashion as cerium doping. These results suggest that adjusting the oxygen content in order to fine tune the doping through a quantum critical point is not feasible. Qualitative analysis within a two-band model indicates that the results would not significantly change.

9.2 $Ti_{1-x}Co_xO_{2-\delta}$

In the diluted magnetic semiconductor $Ti_{1-x}Co_xO_{2-\delta}$, it was observed that Cobalt substituted in for Titanium for concentrations $x \leq 0.02$ with no signs of Cobalt clusters, for the deposition conditions used. It was found in the anatase phase that ferromagnetism existed for relatively moderate levels of oxygen reduction. The Hall effect, however, was linear in magnetic field and showed no signs of the ferromagnetism interacting with the charge carriers by means of the anomalous Hall effect. Rutile thin films were grown with high levels of oxygen reduction (higher than those of the anatase films, and thus higher carrier concentrations) showed a non-linear signal in the Hall resistivity. Resistivity measurements displayed behavior which is different from samples with less oxygen vacancies. This behavior was interpreted as a possible Magnéli phase forming under high reduction. Additionally, transmission electron microscopy performed on the samples showing an anomalous Hall effect found 10 nm sized clusters of cobalt. Due to these reasons, it was not possible to conclude that the anomalous Hall effect was intrinsic to the sample, under our growth conditions. An alternative explanation for the occurrence of the anomalous Hall effect, whereby the Cobalt clusters inject a Hall current into the conducting TiO2 matrix, was considered.

Bibliography

[1] H. Kamerlingh Onnes, Leiden Comm. **120b, 122b, 124c**, (1911).

[2] W. Meissner and R. Ochsenfeld, Naturwissenschaften **21**, 787 (1933).

[3] H. London and F. London, Proc. Roy. Soc. (London) **A149**, 71 (1935).

[4] W. S. Corak, B. B. Goodman, C. B. Satterthwaite, and A. Wexler, Phys. Rev. **96**, 1442 (1954).

[5] M. A. Biondi, M. P. Garfunkel, and A. O. McCoubrey, Phys. Rev. **101**, 1427 (1956).

[6] R. E. Glover and M. Tinkham, Phys. Rev. **104**, 844 (1957).

[7] E. Maxwell, Phys. Rev. **78**, 477 (1950).

[8] C. A. Reynolds, B. Serin, W. H. Wright, and L. B. Nesbitt, Phys. Rev. **78**, 478 (1950).

[9] J. Bardeen, L. N. Cooper, and J. R. Schrieffer, Phys. Rev. **108**, 1175 (1957).

[10] J. G. Bednorz and K. A. Müller, Z. Phys. B - Condensed Matter **64**, 189 (1986).

[11] Hidenori Takagi, Shin-ichi Uchida, Koichi Kitazawa, and Shoji Tanaka, Jap. J. Appl. Phys. **26**, L123 (1987).

[12] J. F. Schooley, W. R. Hosler, and Marvin L. Cohen, Phys. Rev. Lett. **12**, 474 (1964).

[13] D. C. Johnston, H. Prakash, W. H. Zachariasen, and R. Viswanathan, Mat. Res. Bull. **8**, 777 (1973).

[14] A. W. Sleight, J. L. Gillson, and P. E. Bierstedt, Solid State Commun. **17**, 27 (1975).

[15] Robert J. Cava, J. Am. Ceram. Soc. **83**, 5 (2000).

[16] R. J. Cava, R. B. van Dover, B. Batlogg, and E. A. Rietman, Phys. Rev. Lett. **58**, 408 (1987).

[17] M. K. Wu, J. R. Ashburn, C. J. Torng, P. H. Hor, R. L. Meng, L. Gao, Z. J. Huang, Y. Q. Wang, and C. W. Chu, Phys. Rev. Lett. **58**, 908 (1987).

[18] P. Dai, B. C. Chakoumakos, G. F. Sun, K. W. Wong, Y. Xin, and D. F. Lu, Physica C **243**, 201 (1995).

[19] Y. Tokura, H. Takagi, and S. Uchida, Nature **337**, 345 (1989).

[20] H. Takagi, S. Uchida, and Y. Tokura, Phys. Rev. Lett. **62**, 1197 (1989).

[21] H. Yamauchi and M. Karppinen, Supercond. Sci. Technol. **13**, R33 (2000).

[22] D. L. Feng, A. Damascelli, K. M. Shen, N. Motoyama, D. H. Lu, H. Eisaki, K. Shimizu, J.-i. Shimoyama, K. Kishio, N. Kaneko, M. Greven, G. D. Gu, X. J. Zhou, C. Kim, F. Ronning, N. P. Armitage, and Z.-X. Shen, Phys. Rev. Lett. **88**, 107001 (2002).

[23] H. Eisaki, N. Kaneko, D. L. Feng, A. Damascelli, P. K. Mang, K. M. Shen, Z.-X. Shen, and M. Greven, Phys. Rev. B **69**, 064512 (2004).

[24] C. W. Chu, IEEE Trans. Appl. Supercond. **7**, 80 (1997).

[25] S. Lösch, H. Budin, O. Eibl, M. Hartmann, T. Rentschler, M. Rygula, S. Kemmler-Sack, and R. P. Huebener, Physica C **177**, 271 (1991).

[26] Elbio Dagotto, Rev. Mod. Phys. **66**, 763 (1994).

[27] Roland Hott, Reinhold Kleiner, Thomas Wolf, and Gertrud Zwicknagl, in *Frontiers in Superconducting Materials*, edited by A. Narlikar (Springer Verlag, Berlin, 2005).

[28] Alexandre Zimmers, Ph.D., ESPCI, 2004.

[29] Andrea Damascelli, Zahid Hussain, and Zhi-Xun Shen, Rev. Mod. Phys. **75**, 473 (2003).

[30] N. F. Mott and R. Peierls, Proc. Phys. Soc. London **49**, 72 (1937).

[31] J. Hubbard, Proc. R. Soc. London, Ser.A **281**, 401 (1964).

[32] V. J. Emery, Phys. Rev. Lett. **58**, 2794 (1987).

[33] C. M. Varma, S. Schmitt-Rink, and E. Abrahams, Solid State Comm. **62**, 681 (1987).

[34] F. C. Zhang and T. M. Rice, Phys. Rev. B **37**, 3759 (1988).

[35] G. M. Luke, L. P. Le, B. J. Sternlieb, Y. J. Uemura, J. H. Brewer, R. Kadono, R. F. Kiefl, S. R. Kreitzman, T. M. Riseman, C. E. Stronach, M. R. Davis, S. Uchida, H. Takagi, Y. Tokura, Y. Hidaka, T. Murakami, J. Gopalakrishnan, A. W. Sleight, M. A. Subramanian, E. A. Early, J. T. Markert, M. B. Maple, and C. L. Seaman, Phys. Rev. B **42**, 7981 (1990).

[36] T. Uefuji, K. Kurahashi, M. Fujita, M. Matsuda, and K. Yamada, Physica C **378-381**, 273 (2002).

[37] P. K. Mang, O. P. Vajk, A. Arvanitaki, J. W. Lynn, and M. Greven, Phys. Rev. Lett. **93**, 027002 (2004).

[38] J. Lin and A. J. Millis, Phys. Rev. B **72**, 214506 (2005).

[39] S. Martin, A. T. Fiory, R. M. Fleming, L. F. Schneemeyer, and J. V. Waszczak, Phys. Rev. B **41**, 846 (1990).

[40] Yoichi Ando, G. S. Boebinger, A. Passner, Tsuyoshi Kimura, and Kohji Kishio, Phys. Rev. Lett. **75**, 4662 (1995).

[41] Z. Z. Wang, T. R. Chien, N. P. Ong, J. M. Tarascon, and E. Wang, Phys. Rev. B **43**, 3020 (1991).

[42] M. A. Crusellas, J. Fontcuberta, and S. Piñol, Physica C **180**, 312 (1991).

[43] P. W. Anderson, in *The Theory of Superconductivity in the High-T_c Cuprates*, edited by Sam B. Treiman (Princeton University Press, Princeton, New Jersey, 1997).

[44] S. Martin, M. Gurvitch, C. E. Rice, A. F. Hebard, P. L. Gammel, R. M. Fleming, and A. T. Fiory, Phys. Rev. B **39**, 9611 (1989).

[45] Y. Dagan, M. M. Qazilbash, C. P. Hill, V. N. Kulkarni, and R. L. Greene, Phys. Rev. Lett. **92**, 167001 (2004).

[46] L. S. Masov, Phys. Rev. B **70**, 054501 (2004).

[47] Yoichi Ando, Seiki Komiya, Kouji Segawa, S. Ono, and Y. Kurita, Phys. Rev. Lett. **93**, 267001 (2004).

[48] G.-H. Gweon, T. Sasagawa, S. Y. Zhou, J. Graf, H. Takagi, D.-H. Lee, and A. Lanzara, Nature **430**, 187 (2004).

[49] J. C. Phillips, Phys. Rev. B **71**, 184505 (2005).

[50] J. P. Hague, Phys. Rev. B **73**, 060503(R) (2006).

[51] Gabriele F. Giuliani and John J. Quinn, Phys. Rev. B **26**, 4421 (1982).

[52] Lian Zheng and S. Das Sarma, Phys. Rev. B **53**, 9964 (1996).

[53] P. Fournier, P. Mohanty, E. Maiser, S. Darzens, T. Venkatesan, C. J. Lobb, G. Czjzek, R. A. Webb, and R. L. Greene, Phys. Rev. Lett. **81**, 4720 (1998).

[54] G. S. Boebinger, Yoichi Ando, A. Passner, T. Kimura, M. Okuya, J. Shimoyama, K. Kishio, K. Tamasaku, N. Ichikawa, and S. Uchida, Phys. Rev. Lett. **77**, 5417 (1996).

[55] Yoichi Ando, Y. Kurita, Seiki Komiya, S. Ono, and Kouji Segawa, Phys. Rev. Lett. **92**, 197001 (2004).

[56] Y. Dagan, (unpublished).

[57] Yoichi Ando, Y. Hanaki, S. Ono, T. Murayama, Kouji Segawa, N. Miyamoto, and Seiki Komiya, Phys. Rev. B **61**, R14956 (2000).

[58] *Strong Correlation and Superconductivity*, edited by H. Fukuyama, S. Maekawa, and A. P. Malozemoff (Springer-Verlag, Berlin, 1989), p. 198.

[59] P. Fournier, X. Jiang, W. Jiang, S. N. Mao, T. Venkatesan, C. J. Lobb, and R. L. Greene, Phys. Rev. B **56**, 14149 (1997).

[60] N. P. Armitage, F. Ronning, D. H. Lu, C. Kim, A. Damascelli, K. M. Shen, D. L. Feng, H. Eisaki, Z.-X. Shen, P. K. Mang, N. Kaneko, M. Greven, Y. Onose, Y. Taguchi, and Y. Tokura, Phys. Rev. Lett. **88**, 257001 (2002).

[61] Kusko C, R. S. Markiewicz, M. Lindroos, and A. Bansil, Phys. Rev. B **66**, 140513(R) (2002).

[62] Takashi Takahashi, *Recent Photoemission Results for the Electron-Doped Superconductors* (March APS Meeting, K3.00003, 2006).

[63] Subir Sachdev, Science **288**, 475 (2000).

[64] J. M. Ziman, *Electrons and Phonons, The Theory of Transport Phenomena in Solids* (Oxford University Press, ADDRESS, 1960).

[65] M. P. Marder, *Condensed Matter Physics* (John Wiley & Sons, Inc., New York, 2000).

[66] N. W. Ashcroft & N. D. Mermin, *Solid State Physics* (Saunders College Publishing, ADDRESS, 1976).

[67] C. M. Hurd, *The Hall Effect in Metals and Alloys* (Plenum Press, New York-London, 1972).

[68] J. Bass, W. P. Pratt, Jr., and P. A. Schroeder, Rev. Mod. Phys. **62**, 645 (1990).

[69] W. E. Lawrence and J. W. Wilkins, Phys. Rev. B **7**, 2317 (1973).

[70] W. G. Baber, Proc. Roy. Soc. London **158**, 383 (1937).

[71] N. P. Ong, Phys. Rev. B **43**, 193 (1991).

[72] Patrick A. Lee and T. V. Ramakrishnan, Rev. Mod. Phys. **57**, 287 (1985).

[73] P. W. Anderson, J. Phys. Chem. Solids **11**, 26 (1959).

[74] A. A. Abrikosov and L. P. Gor'kov, Sov. Phys. JETP **8**, 1090 (1959).

[75] Leonid A. Openov, Phys. Rev. B **58**, 9468 (1998).

[76] C. C. Tsuei, A. Gupta, and G. Koren, Physica C **161**, 415 (1989).

[77] P. Fournier, J. Higgins, H. Balci, E. Maiser, C. J. Lobb, and R. L. Greene, Phys. Rev. B **62**, R11993 (2000).

[78] Tsuyoshi Sekitani, Michio Naito, and Noboru Miura, Phys. Rev. B **67**, 174503 (2003).

[79] Y. Dagan, M. C. Barr, W. M. Fisher, R. Beck, T. Dhakal, A. Biswas, and R. L. Greene, Phys. Rev. Lett. **94**, 057005 (2005).

[80] P. Seng, J. Diehl, S. Klimm, S. Horn, R. Tidecks, and K. Samwer, Phys. Rev. B **52**, 3071 (1995).

[81] Wu Jiang, S. N. Mao, X. X. Xi, Xiuguang Jiang, J. L. Peng, T. Venkatesan, C. J. Lobb, and R. L. Greene, Phys. Rev. Lett. **73**, 1291 (1994).

[82] P. C. Li, (private communication).

[83] F. Gollnik and M. Naito, Phys. Rev. B **58**, 11734 (1998).

[84] Ruixing Liang, D. A. Bonn, and W. N. Hardy, Physica C **304**, 105 (1998).

[85] J. B. Torrance, A. Bezinge, A. I. Nazzal, T. C. Huang, S. S. P. Parkin, D. T. Keane, S. J. LaPlaca, P. M. Horn, and G. A. Held, Phys. Rev. B **40**, 8872 (1989), and references therein.

[86] P. M. Grant, S. S. P. Parkin, V. Y. Lee, E. M. Engler, M. L. Ramirez, J. E. Vazquez, G. Lim, R. D. Jacowitz, and R. L. Greene, Phys. Rev. Lett. **58**, 2482 (1987).

[87] Jian Ding Yu, Yoshiyuki Inaguma, Mitsuru Itoh, Masaharu Oguni, and Tôru Kyômen, Phys. Rev. B **54**, 7455 (1996), and references therein.

[88] I. Bozovic, G. Logvenov, I. Belca, B. Narimbetov, and I. Sveklo, Phys. Rev. Lett. **89**, 107001 (2002).

[89] P. G. Radaelli, J. D. Jorgensen, A. J. Schultz, B. A. Hunter, J. L. Wagner, F. C. Chou, and D. C. Johnston, Phys. Rev. B **48**, 499 (1993).

[90] Y. Tokura, H. Takagi, and S. Uchida, Nature **337**, 345 (1989).

[91] Wu Jiang, J. L. Peng, Z. Y. Li, and R. L. Greene, Phys. Rev. B **47**, 8151 (1993).

[92] S. Kohiki, J. Kawai, T. Kamada, S. Hayashi, H. Adachi, K. Setsune, and K. Wasa, Physica C **166**, 437 (1990).

[93] X. Q. Xu, S. N. Mao, Wu Jiang, J. L. Peng, and R. L. Greene, Phys. Rev. B **53**, 871 (1996).

[94] P. Fournier, (private communication).

[95] Hiroyuki Oyanagi, Yuko Yokoyama, Hirotaka Yamaguchi, Yuji Kuwahara, Toshikazu Katayama, and Yoshikazu Nishihara, Phys. Rev. B **42**, 10136 (1990).

[96] J. E. Hirsch, Physica C **243**, 319 (1995).

[97] P. G. Radaelli, J. D. Jorgensen, A. J. Schultz, J. L. Peng, and R. L. Greene, Phys. Rev. B **49**, 15322 (1994).

[98] A. J. Schultz, J. D. Jorgensen, J. L. Peng, and R. L. Greene, Phys. Rev. B **53**, 5157 (1996).

[99] G. Riou, P. Richard, S. Jandl, M. Poirier, and P. Fournier, Phys. Rev. B **69**, 024511 (2004).

[100] P. Richard, G. Riou, I. Hetel, S. Jandl, M. Poirier, and P. Fournier, Phys. Rev. B **70**, 064513 (2004).

[101] P. Richard, M. Poirier, S. Jandl, and P. Fournier, Phys. Rev. B **72**, 184514 (2005).

[102] H. J. Kang, Pengcheng Dai, H. A. Mook, D. N. Argyriou, V. Sikolenko, J. W. Lynn, Y. Kurita, S. Komiya, and Y. Ando, Phys. Rev. B **71**, 214512 (2005).

[103] R. P. S. M. Lobo, N. Bontemps, A. Zimmers, Y. Dagan, R. L. Greene, P. Fournier, C. C. Homes, and A. J. Millis, SPIE Optics and Photonics conference proceedings, 31 July - 4 August 2005, to be published.

[104] E. Maiser, P. Fournier, J.-L. Peng, F. M. Araujo-Moreira, T. Venkatesan, R. L. Greene, and G. Czjzek, Physica C **297**, 15 (1998).

[105] P. K. Mang, S. Larochelle, A. Mehta, O. P. Vajk, A. S. Erickson, L. Lu, W. J. L. Buyers, A. F. Marshall, K. Prokes, and M. Greven, Phys. Rev. B **70**, 094507 (2004).

[106] D. Prasad Beesabathina, L. Salamanca-Riba, S. N. Mao, X. X. Xi, T. Venkatesan, Appl. Phys. Lett. **62**, 3022 (1993).

[107] J. Kondo, Prog. Theor. Phys. **32**, 37 (1964).

[108] S. J. Hagen, X. Q. Xu, W. Jiang, J. L. Peng, Z. Y. Li, and R. L. Greene, Phys. Rev. B **45**, 515 (1992).

[109] G. I. Harus, A. N. Ignatenkov, A. I. Ponomarev, L. D. Sabirzyanova, and N. G. Shelushinina, JETP **89**, 933 (1999).

[110] Yoshikazu Hidaka, Yukimichi Tajima, Kiyoshiro Sugiyama, Futoshi Tomiyama, Akio Yamagishi, Muneyuki Date, and Makoto Hikita, J. Phys. Soc. Jpn. **60**, 1185 (1991).

[111] W. Yu, (private communication).

[112] Rostam Moradian and Hamzeh Mousavi, condmat/0505092 (2005).

[113] Gang Xiao, A. Bakhshai, Marta Z. Cieplak, Z. Tesanovic, and C. L. Chien, Phys. Rev. B **39**, 315 (1989).

[114] S. Ikegawa, T. Yamashita, T. Sakurai, R. Itti, H. Yamauchi, and S. Tanaka, Phys. Rev. B **43**, 2885 (1991).

[115] J. M. Tarascon, L. H. Greene, P. Barboux, W. R. McKinnon, and G. W. Hull, Phys. Rev. B **36**, 8393 (1987).

[116] Y. Fukuzumi, K. Mizuhashi, K. Takenaka, and S. Uchida, Phys. Rev. Lett. **76**, 684 (1996).

[117] K. Westerholt and B. vom Hedt, J. Low Temp. Phys. **95**, 123 (1994).

[118] K. Karpińska, Marta Z. Cieplak, S. Guha, A. Malinowski, T. Skośkiewicz, W. Plesiewicz, M. Berkowski, B. Boyce, Thomas R. Lemberger, and P. Lindenfeld, Phys. Rev. Lett. **84**, 155 (2000).

[119] J. M. Tarascon, E. Wang, S. Kivelson, B. G. Bagley, G. W. Hull, and R. Ramesh, Phys. Rev. B **42**, 218 (1990).

[120] C. Barlingay, Valentín García-Vázquez, Charles M. Falco, S. Mazumdar, and S. H. Risbud, Phys. Rev. B **41**, 4797 (1990).

[121] Jun Sugiyama, Shinya Tokuono, Shin-ichi Koriyama, H. Yamauchi, and Shoji Tanaka, Phys. Rev. B **43**, 10489 (1991).

[122] B. Jayaram, H. Chen, and J. Callaway, Phys. Rev. B **52**, 3742 (1995).

[123] Matthias Brinkmann, Heinrich Bach, and Kurt Westerholt, Phys. Rev. B **54**, 6680 (1996).

[124] Q. Huang, J. F. Zasadzinski, N. Tralshawala, K. E. Gray, D. G. Hinks, J. L. Peng, and R. L. Greene, Nature **347**, 369 (1990).

[125] D. H. Wu, J. Mao, S. N. Mao, J. L. Peng, X. X. Xi, T. Venkatesan, R. L. Greene, and S. M. Anlage, Phys. Rev. Lett. **70**, 85 (1993).

[126] C. C. Tsuei and J. R. Kirtley, Phys. Rev. Lett. **85**, 182 (2000), and references therein.

[127] J. David Kokales, Patrick Fournier, Lucia V. Mercaldo, Vladimir V. Talanov, Richard L. Greene, and Steven M. Anlage, Phys. Rev. Lett. **85**, 3696 (2000).

[128] G. Blumberg, A. Koitzsch, A. Gozar, B. S. Dennis, C. A. Kendziora, P. Fournier, and R. L. Greene, Phys. Rev. Lett. **88**, 107002 (2002).

[129] H. Matsui, K. Terashima, T. Sato, T. Takahashi, M. Fujita, and K. Yamada, Phys. Rev. Lett. **95**, 017003 (2005).

[130] J. P. Attfield, A. L. Kharlanov, and J. A. McAllister, Nature **394**, 157 (1998).

[131] J. A. McAllister and J. P. Attfield, Phys. Rev. Lett. **83**, 3289 (1999).

[132] K. Fujita, T. Noda, K. M. Kojima, H. Eisaki, and S. Uchida, Phys. Rev. Lett. **95**, 097006 (2005).

[133] H. Eisaki, N. Kaneko, D. L. Feng, A. Damascelli, P. K. Mang, K. M. Shen, Z.-X. Shen, and M. Greven, Phys. Rev. B **69**, 064512 (2004).

[134] B. D. Weaver and G. P. Summers, in *Studies of High Temperature Superconductors* (Nova Science, New York, 2003), Vol. 47, p. 1.

[135] Sergey K. Tolpygo, J.-Y. Lin, Michael Gurvitch, S. Y. Hou, and Julia M. Phillips, Phys. Rev. B **53**, 12454 (1996).

[136] A. A. Abrikosov, Physica C **214**, 107 (1993).

[137] B. D. Weaver, E. M. Jackson, G. P. Summers, and E. A. Burke, Phys. Rev. B **46**, 1134 (1992).

[138] B. D. Weaver, G. P. Summers, R. L. Greene, E. M. Jackson, S. N. Mao, and W. Jiang, Physica C **261**, 229 (1996).

[139] S. I. Woods, A. S. Katz, M. C. de Andrade, J. Herrmann, M. B. Maple, and R. C. Dynes, Phys. Rev. B **58**, 8800 (1998).

[140] S. I. Woods, A. S. Katz, S. I. Applebaum, M. C. de Andrade, M. B. Maple, and R. C. Dynes, Phys. Rev. B **66**, 014538 (2002).

[141] F. Rullier-Albenque, H. Alloul, and R. Tourbot, Phys. Rev. Lett. **87**, 157001 (2001).

[142] A. Tsukada, M. Noda, H. Yamamoto, and M. Naito, Physica C **426-431**, 459 (2005).

[143] K. McElroy, Jinho Lee, J. A. Slezak, D.-H. Lee, H. Eisaki, S. Uchida, and J. C. Davis, Science **309**, 1048 (2005).

[144] C. Kittel and H. Kroemer, in *Thermal Physics*, 2nd ed. (W. H. Freeman and Company, New York, 1980), Chap. 9.

[145] Martin Nikolo, Am. J. Phys. **63**, 57 (1995).

[146] W. J. Padilla, Y. S. Lee, M. Dumm, G. Blumberg, S. Ono, Kouji Segawa, Seiki Komiya, Yoichi Ando, and D. N. Basov, Phys. Rev. B **72**, 060511 (2005).

[147] A. Zimmers, (private communication).

[148] J. W. Lynn, (private communication).

[149] M. F. Hundley, J. D. Thompson, S-W. Cheong, Z. Fisk, and S. B. Oseroff, Physica C **158**, 102 (1989).

[150] D. E. Cox, A. I. Goldman, M. A. Subramanian, F. Gopala-Krishnan, and A. W. Sleight, Phys. Rev. B **40**, 6998 (1989).

[151] C. Mennerich, D. Baabe, D. Mienert, F. J. Litterst, P. Adelmann, and H.-H. Klauss, Journal of Magnetism and Magnetic Materials **272-276**, 162 (2004).

[152] B. Lorenz and C. W. Chu, cond-mat/0410367 (2004).

[153] Allen M. Goldman, and Nina Marković, Physics Today **Nov.**, 39 (1998).

[154] D. B. Haviland, Y. Liu, and A. M. Goldman, Phys. Rev. Lett. **62**, 2180 (1989).

[155] Matthew P. A. Fisher, Phys. Rev. Lett. **65**, 923 (1990).

[156] Kedar Damle and Subir Sachdev, Phys. Rev. B **56**, 8714 (1997).

[157] Satoshi Tanda, Minoru Honma, and Tsuneyoshi Nakayama, Phys. Rev. B **43**, 8725 (1991).

[158] Satoshi Tanda, Shigeki Ohzeki, and Tsuneyoshi Nakayama, Phys. Rev. Lett. **69**, 530 (1992).

[159] M. A. Steiner, G. Boebinger, and A. Kapitulnik, Phys. Rev. Lett. **94**, 107008 (2005).

[160] S. A. Wolf, D. D. Awschalom, R. A. Buhrman, J. M. Daughton, S. von Molnár, M. L. Roukes, A. Y. Chtchelkanova, and D. M. Treger, Science **294**, 1488 (2001).

[161] C. Herring, in *Magnetism*, edited by G. T. Rado and H. Suhl (Academic Press, New York, 1966), Vol. IV, Chap. Exchange interactions among itinerant electrons.

[162] John Crangle, *Solid State Magnetism* (Van Nostrand Reinhold, New York, 1991).

[163] Amikam Aharoni, *Introduction to the Theory of Ferromagnetism* (Clarendon Press, Oxford, 1996).

[164] Gary A. Prinz, Physics Today **April**, 58 (1995).

[165] M. N. Baibich, J. M. Broto, A. Fert, F. Nguyen Van Dau, F. Petroff, P. Eitenne, G. Creuzet, A. Friederich, and J. Chazelas, Phys. Rev. Lett. **61**, 2472 (1988).

[166] Ching Tsang, Robert E. Fontana, Tsann Lin, D. E. Heirn, Virgil S. Speriosu, Bruce A. Gurney, and Mason L. Williams, IEEE Trans. Magn. **30**, 3801 (1994).

[167] Supriyo Datta and Biswajit Das, Appl. Phys. Lett. **56**, 665 (1990).

[168] G. Lommer, F. Malcher, and U. Rössler, Phys. Rev. Lett. **60**, 728 (1988).

[169] E. I. Rashba, Sov. Phys. Solid State **2**, 1109 (1960).

[170] Emmanuel I. Rashba, cond-mat/ 0507007 (2005).

[171] David D. Awschalom, Michael E. Flatté, and Nitin Samarth, Scientific American **May 13**, (2002).

[172] E. I. Rashba, Phys. Rev. B **62**, R16267 (2000).

[173] M. Oestreich, J. H´ubner, D. H´agele, P. J. Klar, W. Heimbrodt, W. W. R´uhle, D. E. Ashenford, and B. Lunn, Appl. Phys. Lett. **74**, 1251 (1999).

[174] B. T. Matthias, R. M. Bozorth, and J. H. Van Vleck, Phys. Rev. Lett. **7**, 160 (1961).

[175] S. von Molnar, IBM J. Res. Dev. **14**, 269 (1970).

[176] K. W. Edmonds, K. Y. Wang, R. P. Campion, A. C. Neumann, N. R. S. Farley, B. L. Gallagher, and C. T. Foxon, Appl. Phys. Lett. **81**, 4991 (2002).

[177] D. Chiba, K. Takamura, F. Matsukura, and H. Ohno, Appl. Phys. Lett. **82**, 3020 (2003).

[178] B. Beschoten, P. A. Crowell, I. Malajovich, and D. D. Awschalom, Phys. Rev. Lett. **83**, 3073 (1999).

[179] Y. Ohno, D. K. Young, B. Beschoten, F. Matsukura, H. Ohno, and D. D. Awschalom, Nature **402**, 790 (1999).

[180] T. Dietl, H. Ohno, F. Matsukura, J. Cibert, and D. Ferrand, Science **287**, 1019 (2000).

[181] Kenji Ueda adn Hitoshi Tabata and Tomoji Kawai, Appl. Phys. Lett. **79**, 988 (2001).

[182] Yuji Matsumoto, Makoto Murakami, Tomoji Shono, Tetsuya Hasegawa, Tomoteru Fukumura, Masashi Kawasaki, Parhat Ahmet, Toyohiro, Chikyow, Shin ya Koshihara, and Hideomi Koinuma, Science **291**, 854 (2001).

[183] F. Matsukura, H. Ohno, A. Shen, and Y. Sugawara, Phys. Rev. B **57**, R2037 (1998).

[184] M. J. Calderón and S. Das Sarma, cond-mat /0603182 (2006).

[185] M. A. Ruderman and C. Kittel, Phys. Rev. **96**, 99 (1954).

[186] Kei Yosida, Phys. Rev. **106**, 893 (1957).

[187] T. Kasuya, Prog. Theor. Phys. **16**, 45 (1956).

[188] F. A. Grant, Rev. Mod. Phys. **31**, 646 (1959).

[189] T. Umebayashi, T. Yamaki, S. Yamamoto, A. Miyashita, S. Tanaka, T. Sumita, and K. Asai, Journal of Applied Physics **93**, 5156 (2003).

[190] Akira Sasahara, Timothy C. Droubay, Scott A. Chambers, Hiroshi Uetsuka, and Hiroshi Onishi, Nanotechnology **16**, S18 (2005).

[191] S. A. Chambers, S. Thevuthasan, R. F. C. Farrow, R. F. Marks, J. U. Thiele, L. Folks, M. G. Samant, A. J. Kellock, N. Ruzycki, D. L. Ederer, and U. Diebold, Appl. Phys. Lett. **79**, 3467 (2001).

[192] S. Chambers, T. Droubay, C. Wang, A. Lea, R. Farrow, L. Folks, V. Deline, and S. Anders, Appl. Phys. Lett. **82**, 1257 (2003).

[193] S. R. Shinde, S. B. Ogale, S. Das Sarma, J. R. Simpson, H. D. Drew, S. E. Lofland, C. Lanci, J. P. Buban, N. D. Browning, V. N. Kulkarni, J. Higgins, R. P. Sharma, R. L. Greene, and T. Venkatesan, Phys. Rev. B **67**, 115211 (2003).

[194] D. H. Kim, J. S. Yang, K. W. Lee, S. D. Bu, D.-W. Kim, T. W. Noh, S.-J. Oh, Y.-W. Kim, J.-S. Chung, H. Tanaka, H. Y. Lee, T. Kawai, J. Y. Won, S. H. Park, and J. C. Lee, J. Appl. Phys **93**, 2003 (2003).

[195] Hidemi Toyosaki, Tomoteru Fukumura, Yasuhiro Yamada, Kiyomi Nakajima, Toyohiro Chikyow, Tetsuya Hasegawa, Hideomi Koinuma, and Masashi Kawasaki, Nature Material **3**, 221 (2004).

[196] Z. Wang, W. Wang, and J. Tang, Appl. Phys. Lett. **83**, 2003 (2003), and references therein.

[197] H. Ueda, K. Kitazawa, H. Takagi, and T. Matsumoto, J. Phys. Soc. Jpn. **71**, 1506 (2002).

[198] S. R. Shinde, S. B. Ogale, J. S. Higgins, H. Zheng, A. J. Millis, V. N. Kulkarni, R. Ramesh, R. L. Greene, and T. Venkatesan, Phys. Rev. Lett. **92**, 166601 (2004).

Curriculum Vitae

List of Publications

J. S. Higgins, Y. Dagan, M. C. Barr, B. D. Weaver, and R. L. Greene, *Role of oxygen in the electron-doped superconducting cuprates*, Phys. Rev. B **73**, 104510 (2006).

Darshan C. Kundaliya, S. B. Ogale, Lianfeng Fu, S. J. Welz, **J. S. Higgins**, G. Langham, S. Dhar, N. D. Browning, and T. Venkatesan, *Interfacial characteristics of a Fe_3O_4/Nb(0.5%):$SrTiO_3$ oxides junction*, Journal of Applied Physics, accepted for publication.

Anjali S. Ogale, S. R. Shinde, V. N. Kulkarni, **J. Higgins**, R. J. Choudhary, Darshan C. Kundaliya, T. Polleto, S. B. Ogale, R. L. Greene, and T. Venkatesan, *Oxygen-deficient $(La_{0.6}Pr_{0.4})_{0.7}Ca_{0.3}MnO_{3-\delta}$ thin films: Towards a first-order metal-insulator transition*, Phys. Rev. B **69**, 235101 (2004).

S. R. Shinde, S. B. Ogale, **J. S. Higgins**, H. Zheng, A. J. Millis, V. N. Kulkarni, R. Ramesh, R. L. Greene, and T. Venkatesan, *Co-occurrence of superparamagnetism and anomalous Hall effect in highly reduced cobalt-doped rutile $TiO_{2-\delta}$ films*, Phys. Rev. Lett. **92**, 166601 (2004).

S. R. Shinde, S. B. Ogale, **J. Higgins**, R. J. Choudhary, V. N. Kulkarni, and T. Venkatesan, H. Zheng and R. Ramesh, A. V. Pogrebnyakov, S. Y. Xu, Qi Li, and X. X. Xi, J. M. Redwing, D. Kanjilal, *Modification of critical current density of MgB_2 films irradiated with 200 MeV Ag ions*, Appl. Phys. Lett. **84**, 2352 (2004).

J. S. Higgins, S. R. Shinde, S. B. Ogale, T. Venkatesan, and R. L. Greene, *Hall effect in cobalt-doped $TiO_{2-\delta}$*, Phys. Rev B **69**, 073201 (2004).

Y. G. Zhao, S. R. Shinde, S. B. Ogale, **J. Higgins**, R. J. Choudhary, V. N. Kulkarni, R. L. Greene, and T. Venkatesan, S. E. Lofland and C. Lanci, J. P. Buban and N. D. Browning, S. Das Sarma, A. J. Millis, *Co-doped $La_{0.5}Sr_{0.5}TiO_{3-\delta}$: Diluted magnetic oxide system with high Curie temperature*, Appl. Phys. Lett. **83**, 2199 (2003).

S. B. Ogale, R. J. Choudhary, J. P. Buban, S. E. Lofland, S. R. Shinde, S. N. Kale, V. N. Kulkarni, **J. Higgins**, C. Lanci, J. R. Simpson, N. D. Browning, S. Das Sarma, H. D. Drew, R. L. Greene, and T. Venkatesan, *High temperature ferromagnetism with a giant magnetic moment in transparent Co-doped $SnO_{2-\delta}$*, Phys. Rev. Lett. **91**, 077205 (2003).

S. R. Shinde and S. B. Ogale, S. Das Sarma, J. R. Simpson, and H. D. Drew, S. E. Lofland and C. Lanci, J. P. Buban and N. D. Browning, V. N. Kulkarni, **J. Higgins**, R. P. Sharma, R. L. Greene, and T. Venkatesan, *Ferromagnetism in laser deposited anatase* $Ti_{1-x}Co_xO_{2-\delta}$ *films*, Phys. Rev. B **67**, 115211 (2003).

A. Biswas, P. Fournier, V. N. Smolyaninova, H. Balci, **J. S. Higgins**, A. R. C. Budhani and R. L. Greene, *Tunneling spectroscopy of the electron-doped cuprate superconductor* $Pr_{2-x}Ce_xCuO_4$, International Journal of Modern Physics B **16** (20-22), 3175 (2002).

Amlan Biswas, P. Fournier, V. N. Smolyaninova, R. C. Budhani, **J. S. Higgins**, and R. L. Greene, *Gapped tunneling spectra in the normal state of* $Pr_{2-x}Ce_xCuO_4$, Phys. Rev. B **64**, 104519 (2001).

P. Fournier, **J. Higgins**, H. Balci, E. Maiser, C. J. Lobb, and R. L. Greene, *Anomalous saturation of the phase coherence length in underdoped* $Pr_{2-x}Ce_xCuO_4$ *thin films*, Phys. Rev. B **62**, 11993 (2000).